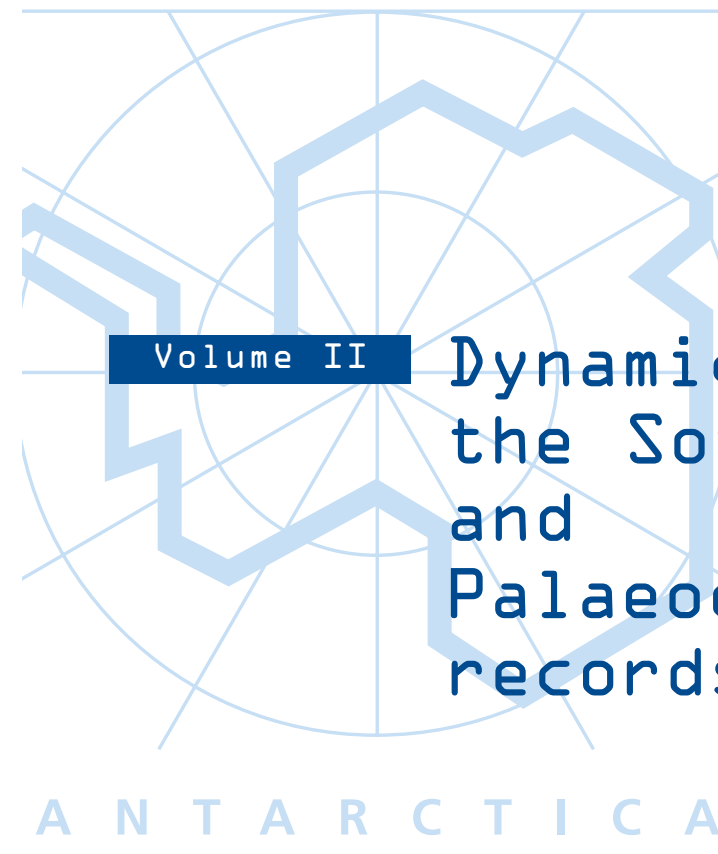




Phase 4 (1997-2001)

Scientific results



Volume II

Dynamics of the Southern Ocean and Palaeoenvironmental records

A N T A R C T I C A

PPS SCIENCE POLICY 

WETENSCHAPSSTRAAT 8, RUE DE LA SCIENCE
B-1000 BRUSSELS
BELGIUM

TEL : +32 (0)2 238 34 11

FAX : +32 (0)2 230 59 12

HTTP://WWW.BELSP0.BE/ANTAR

BELGIAN RESEARCH PROGRAMME ON THE ANTARCTIC
SCIENTIFIC RESULTS OF PHASE IV (1997-2001)

Volume II Dynamics of the Southern
Ocean and
Palaeoenvironmental records

LEGAL NOTICE

Neither the Belgian Federal Public Planning Service Science Policy nor any person acting on behalf of the Service is responsible for the use which might be made of the following information.

No responsibility is assumed by the Publisher for any injury and/or damage to persons or property as a matter of products liability, negligence or otherwise, or from any use or operation of any methods, products, instructions or ideas contained in the material herein.

The authors of each of the contributions are responsible for the content of their contributions and their translations.

No part of this publication may be reproduced, stored in a retrieval system, or transmitted in any form or by any means, electronic, mechanical, photocopying, recording, or otherwise, without the prior written permission of the Publisher.

Additional information on the Belgian Research Programme on the Antarctic is available on Internet: (<http://www.belspo.be/antar>)

Contact person:

Mrs Maaïke Vancauwenberghe (vcou@belspo.be)

Secr.: + 32-2-238.36.49

D/2003/1191/9

Published by the Belgian Federal Public Planning Service Science Policy

Brussels, Belgium

FOREWORD

This Volume presents the scientific results of research projects in the area of **“Dynamics of the Southern Ocean and Paleoenvironmental records”** funded under the **Fourth Phase of the Belgian research programme on the Antarctic (1997-2001)**. The achievements of the research projects in the other areas of the Programme are represented in the first Volume “Marine biota and Global change”.

In 1985, the Belgian Government took the initiative of setting up a structured scientific research programme regarding Antarctica with a manifest view to maximally integrate with the activities of the Antarctic Treaty System. The research programme has continued uninterrupted up to today, with the following broad objectives:

- Maintain and strengthen Belgium's relevant expertise;
- Increase Belgium's visibility within the Antarctic Treaty System;
- Contribute to a rational management of the Antarctic environment and its natural resources;
- Determine the global consequences of the natural processes that take place in Antarctica and its surrounding oceans.

Four major research areas can be distinguished:

- Marine biology and biological geochemistry;
- Glaciology and climatology;
- Hydrodynamics and sea ice;
- Marine geophysics.

The research takes the form of four-year projects that are entrusted to research teams of universities or (federal) scientific institutions. The emphasis is on a multidisciplinary approach of the dynamics of the major Antarctic natural systems' comprehensive functioning, development and interactions. The research themes and priorities fully tie in with other important international projects and programmes, such as ANTOSTRAT (Antarctic Offshore Stratigraphy Project), EPICA (European Project on Ice Coring in Antarctica), IGBP (International Geosphere-Biosphere Programme),...

As Belgium has no infrastructure of its own in Antarctica (base, appropriate research ships,...), the necessary fieldwork is conducted through participation in scientific expeditions set up by other countries.

All research costs are defrayed by the Federal Scientific Policy, which is also in charge of the financing, management, co-ordination and dissemination of the Programme. The scientific link with the Antarctic Treaty System also lies within the scope of the Federal Scientific Policy.

The fourth phase of the programme (1997–2000) was integrated into the 'Scientific Support Plan for a Sustainable Development Policy – PODO I'. Although sustainable development as such is not explicitly mentioned neither in the objectives nor in the strategy of the Treaty System, the underlying concept is in full keeping with the System. This can be gathered from the System's numerous measures and actions aimed at preserving the fauna and flora, establishing protected areas, preventing ocean pollution, eliminating waste or protecting

endemic animal species. As Antarctica is recognized by the Madrid Protocol as a 'natural reserve', in which all human activities are closely monitored, it can model for the broad-scale implementation of the sustainable development concept.

Apart from the budget for research projects within this phase, which amounted to about 6 MEUR, Belgium also contributed 0,5 MEUR to the cost of working of the European Project on Ice Coring in Antarctica (EPICA).

Contents

Dynamics of the Southern Ocean and Palaeoenvironmental records

1 STUDY OF CONVECTIVE MOVEMENTS IN THE SOUTHERN OCEAN

A. Norro

ABSTRACT	1
1. STATE-OF-THE-ART	2
2. GOALS AND STRATEGY	5
3. MATERIALS AND METHODS	6
3.1. Sea ice modelling	6
3.2. Data and Climatologies available for the Weddell Sea	23
4. RESULTS AND DISCUSSION	45
4.1 High-resolution simulation	45
4.2. Annual sea ice cycle	47
4.3. Sea ice evolution	48
4.4. Sea surface temperature	51
4.5. Oceanic heat flux	53
5. OVERALL CONCLUSIONS	55
Acknowledgments	55
References	56

2 MASS BALANCE OF THE ANTARCTIC ICE CAP (A CONTRIBUTION TO EPICA)

J. Naithani et al.

PREFACE	
ABSTRACT	1
1. MARINE AIR INTRUSION	1
1.1. Introduction	2
1.2. Model description	4
1.3. Results of simulations	5
1.4. Discussion and conclusions	23
ACKNOWLEDGEMENTS	28
REFERENCES	28
2. STRONG WIND EVENTS	34
2.1. Introduction	35
2.2. Observations	39
DISCUSSIONS AND CONCLUSION	59
ACKNOWLEDGEMENTS	64
REFERENCES	64

3

BASAL ICE FROM EAST ANTARCTICA (EPICA)

R. Lorrain, et al.

ABSTRACT	1
KEY-WORDS	1
1 GOALS AND STRATEGY	2
2 MATERIALS AND METHODS	4
3 STATE-OF-THE-ART	4
4 RESULTS AND DISCUSSIONS	5
4.1 Study of basal ice in the Dry Valleys of South Victoria Land	5
4.2 Study of ice formed at or near the grounding line in Terra Nova Bay area	20
4.3 Study of lake ice at the bottom of the Vostok ice core	33
5 OVERALL CONCLUSIONS	50
ACKNOWLEDGEMENTS	52
REFERENCES	53

4

DYNAMICS OF THE ANTARCTIC ICE CAP AND CLIMATE CHANGES (A CONTRIBUTION TO EPICA)

F. Pattyn and H. Declerq

ABSTRACT	1
1. INTRODUCTION	2
2. MATERIALS AND METHODS	4
2.1 Development of the ICE2D model	4
2.2 Ice dynamics inferred from radar interferometry	13
3. RESULTS	18
3.1 The variability of Antarctic ice-sheet response to the climatic signal	18
3.2 High-resolution modelling: focus on the grounding zone	27
3.3 Preliminary results of model experiments along a flowline in western Dronning Maud Land	33
3.4 Shirase Glacier dynamics inferred from ERS-SAR interferometry	35
4. DISCUSSION	46
4.1 The variability of Antarctic ice-sheet response to the climatic signal	46
4.2 High-resolution modelling: focus on the grounding zone	47
4.3 Shirase Glacier dynamics inferred from ERS-SAR interferometry	49
5. CONCLUSIONS	51
ACKNOWLEDGMENTS	52
REFERENCES	53

M. De Batist en J.-P. Henriët

ABSTRACT	1
GOALS, STRATEGY AND ACHIEVEMENTS	2
LATE-GLACIAL MASS-WASTING PROCESSES ON THE TRINITY PENINSULA MARGIN, ANTARCTIC PENINSULA	4
1. The Trinity Peninsula margin in Central Bransfield Basin	4
2. Data and methods	6
3. Description of the data	7
4. Evidence for a multi-phase instability event	14
5. Age of the Gebra Slide	15
6. Possible trigger mechanisms	17
A SUB-GLACIAL SEDIMENTARY SYSTEM ALONG THE NORTHERN ANTARCTIC PENINSULA FROM SEA-FLOOR AND SUB- SEA-FLOOR EVIDENCE	20
1. Study area and data set	20
2. Sea-floor morphology	21
3. Model of the sedimentary system	27
DEVELOPMENT OF A NEW DEEP-TOW REFLECTION SEISMIC ACQUISITION SYSTEM	29
1. Introduction	29
2. Description	29
3. Testing and sea trials	37
4. Recent developments	56
OVERALL CONCLUSIONS	56
ACKNOWLEDGEMENTS	57
REFERENCES	58

Contents of VOLUME I

Marine biota and global change

MEIOBENTHIC BIODIVERSITY AND FLUXES
WITHIN THE ANTARCTIC
BIOGEOCHEMICAL ENVIRONMENT

S. Vanhove et al.

STRUCTURAL AND ECOFUNCTIONAL
BIODIVERSITY OF THE AMPHIPOD
CRUSTACEAN BENTHIC TAXOCOENOSSES
IN THE SOUTHERN OCEAN

C. De Broyer et al.

AN INTEGRATED APPROACH TO ASSESS
CARBON DYNAMICS IN THE SOUTHERN
OCEAN

F. Dehairs et al.

SOUTHERN OCEAN GLOBAL ECOSYSTEM
RESPONSE TO PHYSICAL AND TROPHIC
CONSTRAINTS

J.-H. Hecq et al.

A4/36/HO1

**STUDY OF CONVECTIVE MOVEMENTS IN
THE SOUTHERN OCEAN**

A. NORRO

**MANAGEMENT UNIT OF THE NORTH SEA MATHEMATICAL
MODELS (MUMM)
Gulledelle 100
B-1200 BRUSSEL**

TABLE OF CONTENTS

ABSTRACT	1
1. STATE-OF-THE-ART	2
2. GOALS AND STRATEGY	5
3. MATERIALS AND METHODS	6
3.1. SEA ICE MODELLING	6
3.2. DATA AND CLIMATOLOGIES AVAILABLE FOR THE WEDDELL SEA ..	23
3.2.2. WATER CURRENT DATA	35
3.2.3. WIND STRESS DATA	41
3.2.4. SEA ICE CONCENTRATION AND THICKNESS DATA.....	42
3.2.5. BATHYMETRY	44
4. RESULTS AND DISCUSSION	45
4.1 HIGH-RESOLUTION SIMULATION	45
4.2. ANNUAL SEA ICE CYCLE	47
4.3. SEA ICE EVOLUTION.....	48
4.4. SEA SURFACE TEMPERATURE	51
4.5. OCEANIC HEAT FLUX	53
5. OVERALL CONCLUSIONS	55
ACKNOWLEDGMENTS	55
REFERENCES	56

ABSTRACT

In the Southern Ocean, the formation of deep water and the convective movements are influenced by the high-temporal variability of ice production in the area. The study of these phenomena therefore needs an accurate representation of the atmosphere/ocean interface generally occupied by the ice pack.

With this aim in view, a sea ice model based on Semtner's approach is coupled to a three-dimensional hydrodynamical model. The heat and salt fluxes between ice and water column are explicitly taken into account. The domain of application is the Weddell Sea sector of the Southern Ocean.

Available data sets are used to identify zones of convection as well as to initialise models and providing boundary conditions.

The model has a maximum resolution of $1^\circ/12$ in both latitude and longitude. A zooming procedure applied to the results of a given simulation permits to focus on specific zone of the domain. Such procedure is applied to presents results on the Maud Rise region.

The model is run with a set of climatological forcing to reproduce the ice formation during a year and the results are compared with available observations. This work is the first step of a coupled ocean circulation/sea ice model developed for the entire Southern Ocean.

Key words: sea ice; rheology; modelling; Southern Ocean; high-resolution simulation.

1. STATE-OF-THE-ART

The Southern Ocean plays a key role in the world circulation and therefore influences the earth climate (Alekseev, 1994). First, this ocean is unique among the world's oceans because the configuration of land and water permits a circumpolar oceanic flow. The Antarctic continent provides the southern boundary while the northern boundary may be considered to be 50° S. That is the approximate position of the Antarctic polar-front zone. This zone is characterised by relatively large meridional gradients of temperature, salinity, and density associated with the Antarctic circumpolar current.

Secondly, specific oceanographic processes characterize this ocean. In particular, the Weddell Sea (Fig. 1), the Atlantic sector of the Southern Ocean, has been identified, together with the Greenland Sea in the Arctic Ocean, as one of the main sources of dense water that supply the world ocean and one of the rare oceanic regions presenting a deep vertical mixing (Roth *et al.*, 1993).

The Weddell Sea sector (60°W to 20°E) contains relatively cold ocean waters distributed among three main water types: the Antarctic bottom water, the Antarctic surface water and the most abundant one, the circumpolar deep water renamed Weddell deep water (WDW) when it penetrates into the Weddell Sea. The water circulation is influenced by a large-scale cyclonic gyre and the topographic barrier of the Antarctic Peninsula (Zwally *et al.*, 1983). The prevailing easterly winds near the continent and the prevailing westerly winds farther north are responsible for the formation of the Antarctic divergence. Typically, air temperature has a meridional gradient, increasing with latitude, except in the vicinity of the Antarctic Peninsula.

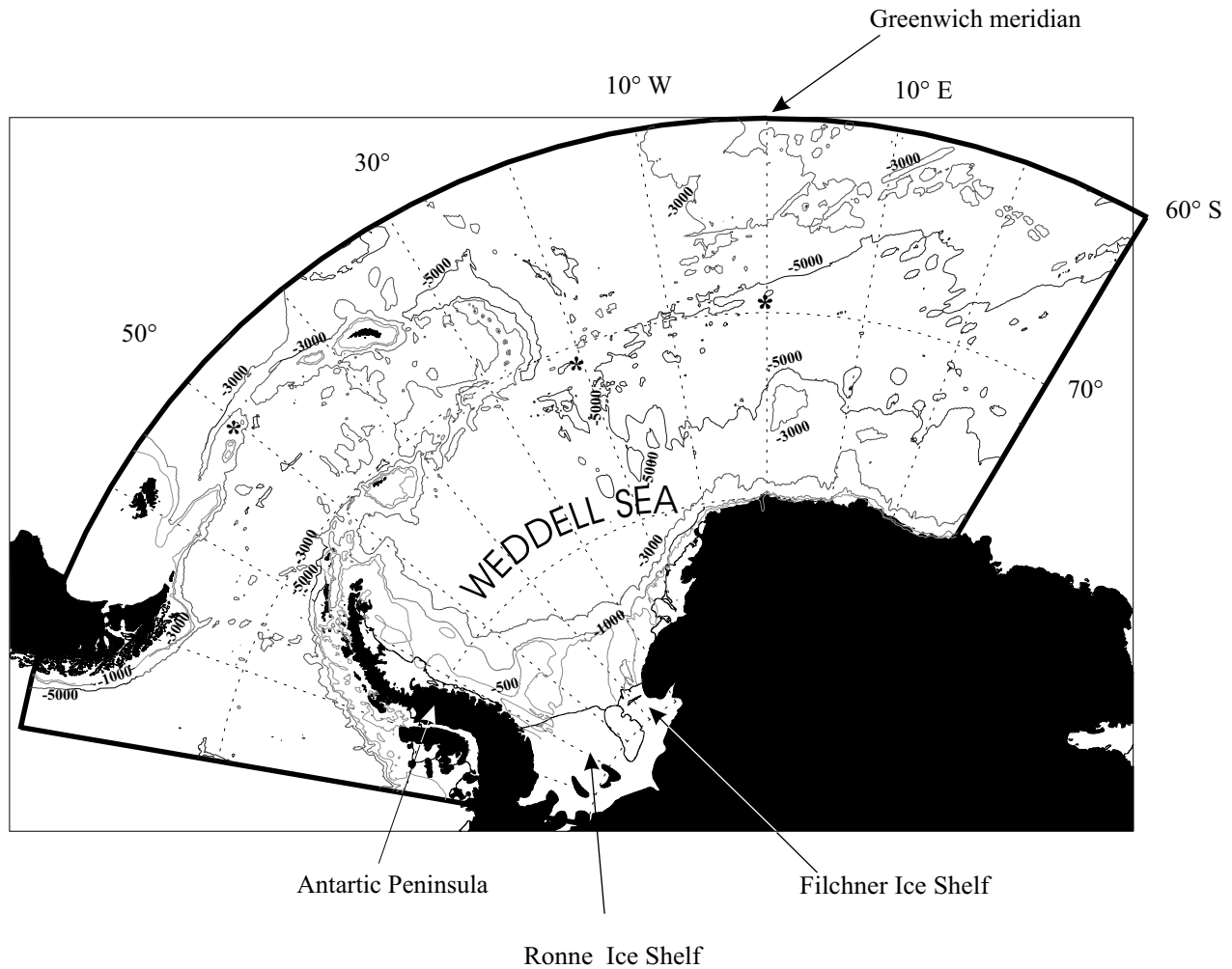


Figure 1 The Weddell Sea Bathymetry and surrounding area (depth data from ETOPO5).

* shows the location of current meter moorings

Although the implied mechanisms are not yet known in detail, the formation of deep water is probably very influenced by the high spatio-temporal variability of ice production in the area (Gloersen *et al.*, 1992). This dense water, generated by complex processes related to geometry, presence of an ice pack and to the resulting heat and salt fluxes, spreads into the world ocean.

These mechanisms are probably influenced by the complex bathymetry of the Weddell Sea. In this respect, observations (Gordon and Huber, 1995) have shown local weakening of the ice pack in the zone around the Maud Rise, a seamount culminating at 1098 m below the sea level located at 65°S to the east of the Greenwich meridian, due to high vertical heat and salt fluxes. (Hunke and Ackley, 2001). Presence of a seamount also modifies the structure of the flow and can modify the stability of the water masses leading to favourable condition for convection (Bersch *et al.*, 1992).

Comparisons between different maps of ice concentration have shown high interannual variations in the ice distribution, attributed to important changes of the atmospheric and oceanic forcing from one year to another. The circumpolar current appears to influence the position of the ice margin.

This paper describes a sea ice formation model connected to a three -dimensional circulation model of the Weddell Sea. For boundary condition reasons, the model domain has been somewhat extended to include the Drake Passage. This modelling approach aims to understand the complex behaviour of the Weddell Sea.

2. GOALS AND STRATEGY

The Southern Ocean is characterised by specific oceanographic processes. More precisely, the Weddell Sea has been identified, together with the Greenland Sea in the Arctic Ocean, as one of the main locations of bottom water formation for the world ocean. The Weddell Sea is also one of the rare oceanic regions presenting deep vertical mixing. The dense water, generated by complex processes related to the geometry, to the presence of ice pack, to meteorological forcing as well as to the resulting heat and salt fluxes, spreads into the world ocean.

To simulate these processes, the approach followed at MUMM is the building of a coupled ocean/ice model at the regional scale of the Weddell Sea. A particular attention is needed for the zones around the Filchner-Ronne Ice shelf and the Maud Rise, which are renowned, one, for contributing to the production of Antarctic bottom water, the other, for undergoing vertical movement (upwelling) of relatively warmer water.

- To reach such a goal,:
- a sea ice model has been coupled to a three-dimensional circulation model.

 - Available data sets have been analysed and relevant information extracted.

Specific meteorological forcing is applied to the model and comparison between results and observation is conducted.

3. MATERIALS AND METHODS

3.1. SEA ICE MODELLING

The model is divided into 4 parts: ice thermodynamics and dynamics, mixed layer and deep ocean evolution. Fig. 2 presents schematically its organisation and the interactions between the four modules, which are described in the following paragraphs.

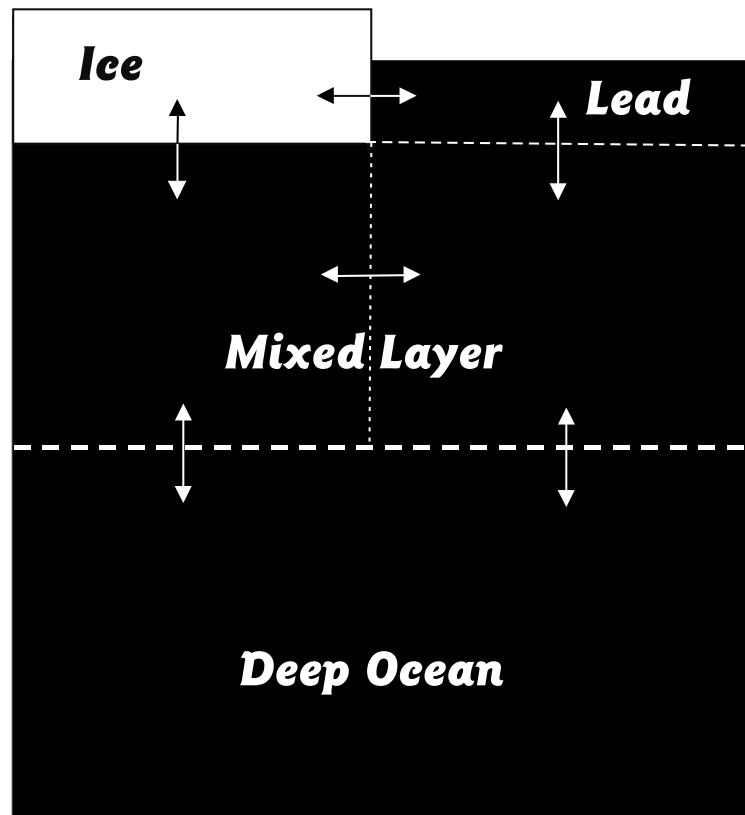


Figure 2 Model scheme.

3.1.1. Ice thermodynamics

The sea ice model, initially based on the so-called “zero layer” model developed by Semtner (1976), computes the annual cycle of sea ice thickness and coverage. This model is divided into two major parts dealing with the thermodynamical and dynamical processes that control the ice and determine its thickness and movement.

The thermodynamical component computes the thickness and the temperature of the ice deduced from heat exchanged vertically through the ice-air and ice-ocean interfaces and horizontally through the leads.

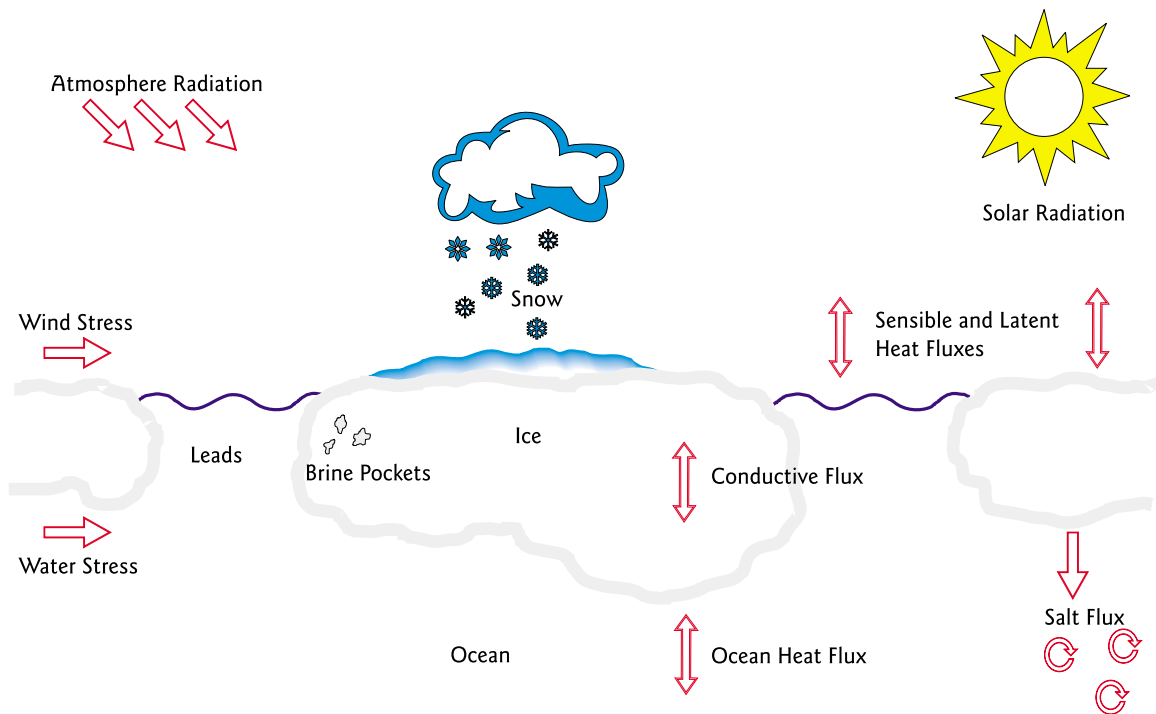


Figure 3 Sea ice formation description.

The sea ice, assumed to be a uniform horizontal slab of ice, develops to balance the heat exchanges between the atmosphere and the ocean (Figure 3). Any imbalance leads to its formation or melting. The energy exchanged through the air-ice interface consists of:

3.1.1.1. Sensible and latent heat flux (Parkinson and Washington, 1979)

Over water

$$e(T_d) = (1.0007 + 3.46 \cdot 10^{-8} p_a) 611.21 \exp \left[17.502 \left(\frac{T_d - 273.15}{T_d - 32.19} \right) \right] \quad (1)$$

$$e_s(T_s) = (1.0007 + 3.46 \cdot 10^{-8} p_a) 611.21 \exp \left[17.502 \left(\frac{T_s - 273.15}{T_s - 32.19} \right) \right] \quad (2)$$

Over ice

$$e(T_d) = (1.0003 + 4.18 \cdot 10^{-8} p_a) 611.15 \exp \left[22.452 \left(\frac{T_d - 273.15}{T_d - 0.61} \right) \right] \quad (3)$$

$$e_s(T_s) = (1.0003 + 4.18 \cdot 10^{-8} p_a) 611.15 \exp \left[22.452 \left(\frac{T_s - 273.15}{T_s - 0.61} \right) \right] \quad (4)$$

Where T_s is the surface temperature (K); T_d the dew point (K); e the vapour pressure of the air over the surface (Pa); e_s the vapour pressure of saturated air at the surface (Pa); p_a the atmospheric pressure (Pa).

$$q = \frac{m_w}{m_a} \frac{e}{p_a - \left(1 - \frac{m_w}{m_a} \right) e} \approx \frac{m_w}{m_a} \frac{e}{p_a} = 0.62198 \frac{e}{p_a} \quad (5)$$

Where q is the air specific humidity; m_a the molecular mass of dry air; m_w the molecular mass of water.

$$F_h = \rho_a c_{pa} C_h U (T_a - T_s) \quad (6)$$

$$F_{le} = \rho_a \left(\frac{L_v}{L_s} \right) C_{le} U [q(T_d) - q_s(T_s)] \quad (7)$$

Where F_h is the flux of sensible heat (Wm^{-2}); F_{le} the flux of latent heat (Wm^{-2}); ρ_a the air density; c_{pa} the specific heat of dry air ($\text{J kg}^{-1} \text{K}^{-1}$); C_h the Stanton number; U the wind speed; T_a the air temperature; L_v and L_h respectively the latent heats of vaporisation and sublimation; C_{le} the Dalton number.

3.1.1.2. Shortwave or solar radiation including the surface albedo effect (Shine, 1984)

$$F_{sw}(clear) = \frac{S_0 \cos mu^2 (1 - \alpha_{clear})}{a \cos mu + (b + \cos mu) 10^{-5} e^{(T_d)} + c} \quad (8)$$

$$F_{sw}(cloudy) = \frac{(53.5 + 1274.5 \cos mu) \cos mu^{1/2} (1 - 0.996 \alpha_{cloudy})}{1 + 0.139 (1 - 0.9345 \alpha_{cloudy}) \tau} \quad (9)$$

Where S_0 is the solar constant (Wm^{-2}); $\cos mu$ the daily mean of the cosine of the zenith angle; τ the cloud optical thickness; α the albedo; a , b and c are empirical parameters.

The total solar radiation available at the surface is given by:

$$F_{sw} = n F_{sw}(cloudy) + (1 - n) F_{sw}(clear) \quad (10)$$

Where n is the fractional cloud cover.

3.1.1.3. Non-solar heat flux gathering the longwave radiation from the atmosphere (Marshunova, 1966)

$$F_{hva} = \sigma T_a^4 (a + b\sqrt{e}) \quad (11)$$

$$F_{hva} = \sigma T_a^4 (a + b\sqrt{e})(1 + rn) \quad (12)$$

Where σ is the Stephan-Boltzmann constant; a , b and r are empirical parameters.

3.1.1.4. Emitted surface longwave radiation

$$F_{hvs} = \varepsilon \sigma T_s^4 \quad (13)$$

Where ε is the surface emissivity.

3.1.1.5. Conductive flux through the ice layer

$$F_c = -k_i \frac{\partial T}{\partial z} \quad (14)$$

Where k_i is the ice heat conductivity; T the ice temperature.

In the presence of snow, the conductive flux is computed the same way by replacing the ice heat conductivity by an effective heat conductivity equal to:

$$k_{eff} = \frac{k_s k_i (h_s + h_i)}{h_i k_s + h_s k_i} \quad (15)$$

Where k_s is the snow heat conductivity; h_i and h_s are respectively the ice and snow thicknesses.

3.1.1.6. Ice formation and melting

The surface water begins to freeze when the atmosphere pumps more energy from the ocean upper layer than the ocean is able to supply throughout F_w ¹. The thermal equilibrium at the sea surface is no longer respected. The energy deficit produces an ice volume, initialising the ice formation process. The sea surface temperature decreases under the water freezing point and an ice layer is formed.

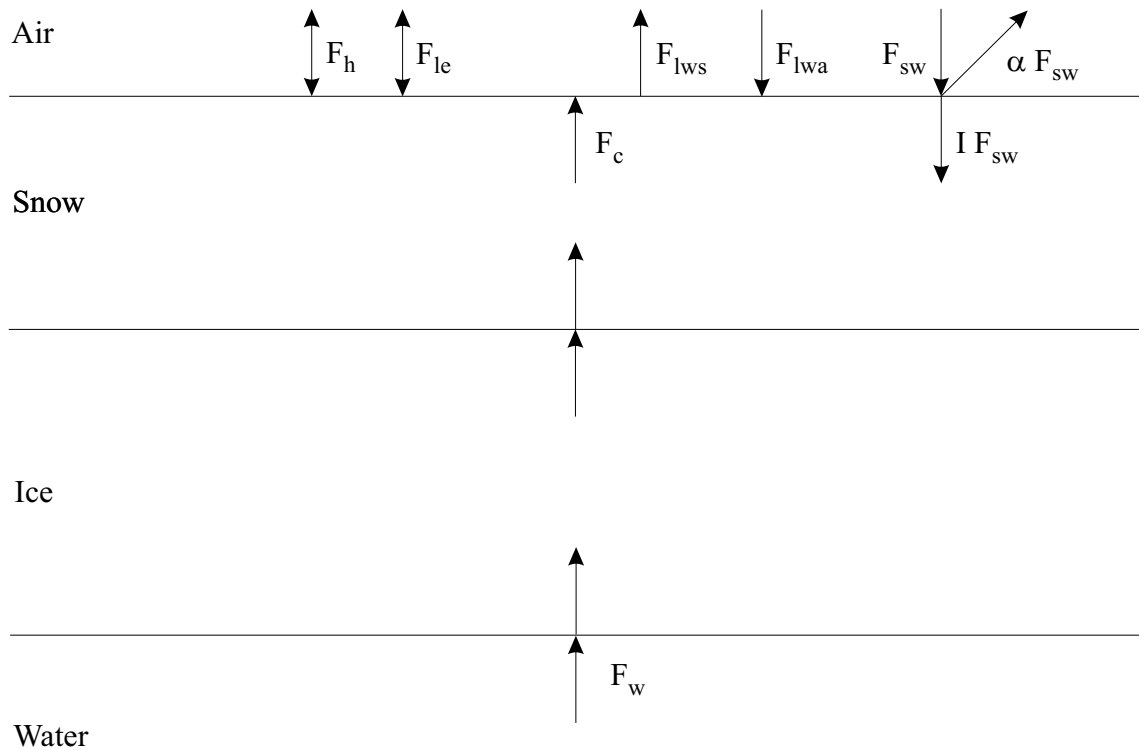


Figure 4 Energy fluxes visualisation

¹ F_w is the deep ocean vertical heat flux

The surface temperature is obtained by iterations on the energy budget (Figure 4) with the Newton-Raphson method. If its value exceeds the melting point (0°C for snow, -0.1°C for ice), the excess of energy is used to melt snow and/or ice. The model takes into account the presence of snow and the formation of meteoric ice (Eicken *et al.*, 1994).

At the ice layer base, the conductive flux within the ice is balanced by the deep ocean vertical heat flux (Figure 4). Any imbalance causes ice to grow or to melt at the bottom. In all calculations, the bottom temperature is supposed to be equal to the freezing temperature, which depends on the salinity.

Horizontally, the heat flux balance at the surface of a lead can modify the sea ice extent.

3.1.1.7.Data

The main parameters are given in Table 1. The air temperature, the dew point, the water and wind stresses, and the pressure are the main inputs to introduce in the model.

The oceanic flux can be imposed from observations or computed by a hydrodynamic model or by a mixed layer model (Petit and Norro, 2000).

Table 1 Main parameters of the sea ice model

Symbol	Definition	Unit	Value
S_0	solar constant	(Wm^{-2})	1368
σ	Stephan-Boltzmann constant	($\text{Wm}^{-2}\text{K}^{-4}$)	5.67051×10^{-8}
k_i	ice heat conductivity	($\text{Wm}^{-1}\text{K}^{-1}$)	2.04
k_s	snow heat conductivity	($\text{Wm}^{-1}\text{K}^{-1}$)	0.31
ρ_i	ice density	(kg m^{-3})	900
ρ_s	snow density	(kg m^{-3})	330
ρ_w	water density	(kg m^{-3})	1027
c_i	ice specific heat	($\text{J kg}^{-1} \text{K}^{-1}$)	2090
c_s	snow specific heat	($\text{J kg}^{-1} \text{K}^{-1}$)	2090
c_w	water specific heat	($\text{J kg}^{-1}\text{K}^{-1}$)	3935

The temporal evolution of the upper ocean temperature T_m and salinity S_m is governed by the three-dimensional hydrodynamical model (see following section)

A specific term in the salinity equation takes into account salt flux resulting from ice formation.

The turbulence closure scheme used in the three-dimensional model does not guarantee the hydrostatic stability. Therefore a strong mixing process² is included in order to restore stable density profiles in case of static unstable stratification due for instance to salt rejection phenomena.

² Such strong mixing process mimics the convection in an hydrostatic formulation

3.1.1.8. The oceanic heat flux F_w

As stated before the oceanic heat flux can be calculated either by a mixed layer model or by the full three-dimensional model.

- **The mixed layer formulation**

A mixed layer model such as the one proposed by Fichet and Gaspar (1988), gives the temperature, the salinity and the thickness of the mixed layer as well as the deep ocean vertical heat flux. The deep ocean is represented by two equations computing the temperature and salinity diffusion below the mixed layer.

The evolution of the upper ocean temperature T_m and salinity S_m integrated over the mixed layer thickness h_m are fixed by the following conservation laws:

$$\rho c_p h_m \frac{\partial T_m}{\partial t} = [1 - J(h_m)] F_{sol,m} + F_{nsol,m} - \rho c_p w_e \Delta T - c_p \rho (K_T \frac{\partial T}{\partial z})_m \quad (16)$$

$$\rho h_m \frac{\partial S_m}{\partial t} = F_{salt} - \rho w_e \Delta S - \rho (K_S \frac{\partial S}{\partial z})_m \quad (17)$$

where ρ , c_p , $J(h_m)$, $F_{sol,m}$, $F_{nsol,m}$, F_{salt} , w_e are respectively the water density, the water specific heat, the fraction of solar radiation penetrating to the depth h_m , the solar and the non-solar radiation available for the mixed layer, the salt flux between the ice and mixed layer, and the mixed layer entrainment velocity; $(K_T \partial T / \partial z)_m$ and $(K_S \partial S / \partial z)_m$ are the heat and salt diffusion fluxes at the depth h_m with the diffusivities K_T and K_S , both fixed at the molecular value of $2 \cdot 10^{-5} \text{ m}^2 \text{ s}^{-1}$. ΔT and ΔS are the temperature and salinity jumps across the bottom of the mixed layer. w_e is the time derivative of h_m .

Below the mixed layer, temperature T and salinity S evolve according to:

$$\rho c_p \frac{\partial T}{\partial t} = F_{sol,m} \frac{\partial J}{\partial z} + \rho c_p \frac{\partial}{\partial z} (K_T \frac{\partial T}{\partial z}) \quad (18)$$

$$\frac{\partial S}{\partial t} = \frac{\partial}{\partial z} \left(K_s \frac{\partial S}{\partial z} \right) \quad (19)$$

Vertically 12 levels are used to solve the temperature and salinity equations (30, 100, 200, 300, 500, 800, 1200, 2000, 3000, 4000, 4750, and 5250 m)

- **The three-dimensional hydrodynamic model formulation**

The time evolution of the thickness of the surface layer of the ocean is now governed by the hydrodynamics and is not anymore explicitly calculated.

The oceanic heat flux is calculated as follow.

$$F_w = \rho_w c_w h_m \frac{\partial T_f}{\partial t} \quad (20)$$

Where

ρ_w is the water density (kg m^{-3});

c_w the specific heat of water ($4.18 \cdot 10^3 \text{ J kg}^{-3} \text{ K}^{-1}$);

T_f the mixed layer temperature;

t is the time.

Björk (1997) uses the following formulation

$$F_w = \rho_w c_w C_b u_i (T_f - T_m) \quad (21)$$

Where

u_i the ice velocity (m s^{-1});

C_b an a-dimensional bulk transfer coefficient ($3 \cdot 10^{-4}$);

T_m the temperature at the lower ice surface at the freezing temperature of the seawater just below the ice.

The Björk formulation includes the ice velocity and therefore does not permit any heat exchange between the ocean and the ice in the case of the sea ice movement stop.

Ebert and Curry (1993) propose a formulation depending on the ice thickness

$$F_w = \rho_w c_w C_{Tb} (T_f - T_m) \quad (22)$$

Where

$$C_{Tb} = 1.26 \times 10^{-4} h_i^{-0.5} \quad \text{if } h_i < 3\text{m} \quad (23)$$

$$C_{Tb} = 7.27 \times 10^{-5} \quad \text{if } h_i \geq 3\text{m} \quad (24)$$

Where h_i is the ice thickness (m).

- **Initialisation of models**
-

The models are initialised with the climatology of Gordon and Baker (1982).

The air temperature, the dew point, the wind stresses and the pressure are computed from the climatological data compiled by Taljaard *et al.* (1969). Parkinson and Washington (1979) have derived the cloudiness from van Loon's works (1972).

3.1.2. Ice dynamics

The dynamical component of the sea ice model provides the ice velocity ensuring the horizontal redistribution of the amount of ice present at the ocean surface. In this process, the conservation of total ice mass per unit area m is given by (Hibler, 1979):

$$m \left[\frac{\partial \mathbf{u}}{\partial t} + \mathbf{u} \cdot \nabla \mathbf{u} \right] = -m f \mathbf{e}_3 \times \mathbf{u} - mg \nabla H + \boldsymbol{\tau}_{air} + \boldsymbol{\tau}_{water} + \mathbf{F} \quad (25)$$

Where \mathbf{u} is the ice velocity vector; m its mass per surface unit; f the Coriolis parameter; \mathbf{e}_3 a unit vector normal to the surface; g the acceleration due to gravity; H the dynamic height of the sea; $\boldsymbol{\tau}_{air}$ et $\boldsymbol{\tau}_{water}$ respectively the wind and water stresses; \mathbf{F} the force due to internal ice constraints.

However, the ice dynamics can be, in first approximation, simplified to an equilibrium between the wind and water stresses (Demuth and van Ypersele, 1989). Unfortunately, this formulation, even improved by an angular correction, does not satisfactorily reproduce the ice ejection from the Weddell Gyre due to earth rotation and fails in locating the perennial ice. The complete formulation (Eq. 5) is therefore used here with satisfactory results to displace the perennial ice northwards along the Antarctic Peninsula, which is closer to the observations.

It is worth noting that the internal ice constraints term can locally become very important and stop the movement of an ice pack under a strong wind as observed in Arctic (Colony, 1990). This term can thus not be neglected.

According to Hibler's theory considering ice as a visco-plastic material, the force due to internal constraints can be developed as follows:

$$F_x = \frac{\partial}{\partial x} \left[(\eta + \zeta) \frac{\partial u}{\partial x} + (\zeta - \eta) \frac{\partial v}{\partial y} - \frac{P}{2} \right] + \frac{\partial}{\partial y} \left[\eta \left(\frac{\partial u}{\partial y} + \frac{\partial v}{\partial x} \right) \right] \quad (26)$$

$$F_y = \frac{\partial}{\partial y} \left[(\eta + \zeta) \frac{\partial v}{\partial y} + (\zeta - \eta) \frac{\partial u}{\partial x} - \frac{P}{2} \right] + \frac{\partial}{\partial x} \left[\eta \left(\frac{\partial u}{\partial y} + \frac{\partial v}{\partial x} \right) \right] \quad (27)$$

Where ζ and η are nonlinear bulk and shear viscosities; P a pressure term depending on ice thickness and concentration; u and v the components of ice velocity.

$$\zeta = \frac{P}{2\Delta} \quad (28)$$

$$\eta = \frac{\zeta}{e^2} \quad (29)$$

$$P = P^* h_i \exp[-C(1 - A_i)] \quad (30)$$

$$\Delta^2 = \left(1 + \frac{1}{e^2}\right) \left[\left(\frac{\partial u}{\partial x}\right)^2 + \left(\frac{\partial v}{\partial y}\right)^2 \right] + e^{-2} \left(\frac{\partial u}{\partial y} + \frac{\partial v}{\partial x}\right)^2 + 2 \left(1 - \frac{1}{e^2}\right) \frac{\partial u}{\partial x} \frac{\partial v}{\partial y} \quad (31)$$

Where e and Δ are, respectively, the eccentricity of the visco-plastic rheology and a function of the strain rate invariants; P^* and C , respectively a strength parameter and a dimensionless strength parameter.

This ice rheology introduced by Hibler (1979) is largely used by other authors (e.g. Oberhuber, 1993). It links internal ice constraints to ice thickness and concentration obtained by the thermodynamic processes. This approach is applicable in a large range of time and space scales. Nevertheless, it is not depending on temperature and salinity, which are supposed to have second order effects.

The ice velocity (Eq. 5) will redistribute the ice mass created at the ocean surface. During this process, the ice and snow mass must be conserved according to the following continuity equations:

$$\frac{\partial h_i}{\partial t} + \nabla \cdot (\mathbf{u} h_i) = \nabla \cdot K_i \nabla h_i + F_{hi} \quad (32)$$

$$\frac{\partial h_s}{\partial t} + \nabla \cdot (\mathbf{u} h_s) = \nabla \cdot K_s \nabla h_s + F_{hs} \quad (33)$$

$$\frac{\partial A_i}{\partial t} + \nabla \cdot (\mathbf{u} A_i) = \nabla \cdot K_i \nabla A_i + F_{Ai} \quad (34)$$

Where \mathbf{u} is the ice velocity vector; h_i and A_i the ice thickness and concentration; h_s the snow thickness; K_i and K_s the diffusivity coefficients; F_{hi} and F_{Ai} are respectively the ice thickness and concentration production-destruction terms and F_{hs} the snow thickness production-destruction term.

The water stress is a function of the water surface current obtained from a three-dimensional model, which computes the hydrodynamic response of the ocean to the wind forcing. This model is described in the next paragraph.

The conservation equations written in spherical coordinates are solved on a computational grid characterised by mesh sizes of 2 degrees in longitude and 1 degree in latitude. The model domain, delimited by the bold line in Fig. 1, extends from latitude 50°S to 80°S and from longitude 80°W to 30°E and includes the southern tip of South America, the Drake Passage, the Weddell Sea and the Falklands Islands.

3.1.3. Circulation Model

A classical three-dimensional primitive equation model is used to simulate the wind driven general circulation on the Weddell sea sector of the Antarctic ocean.

The model includes time-dependent, non linear equations describing the conservation of mass and momentum. Evolution equations for temperature and salinity complete the system of equations.

On the vertical, so-called bottom following σ -transform is applied (Phillips, 1957).

$$\sigma = \frac{z - \eta}{H + \eta} \quad (35)$$

Where $H(x,y)$ denotes the bathymetry and $\eta(x,y,t)$ the surface elevation. $h=H+\eta$ represents the total depth.

The sea surface is thus located at $\sigma=0$ and the sea floor at $\sigma=-1$. That transform presents numerous advantages including a simpler application of boundary conditions at the sea surface and bottom as well as inclusion of all the complexity of the bathymetry inside the equations. Horizontally, a staggered C-grid (Arakawa, 1972) is used.

Classical Boussinesq approximation and hydrostatic assumption are made leading to the following system of equations:

$$\frac{\partial}{\partial x}(hu) + \frac{\partial}{\partial y}(hv) + \frac{\partial}{\partial \sigma} \tilde{w} + \frac{\partial}{\partial t} \eta = 0 \quad (36)$$

$$\frac{\partial}{\partial t}(hu) + \frac{\partial}{\partial x}(hu^2) + \frac{\partial}{\partial y}(hvu) + \frac{\partial}{\partial \sigma}(\tilde{w}u) - fhv \quad (37)$$

$$= -g \frac{\partial \eta}{\partial x} - \frac{1}{\rho_0} \frac{\partial P_a}{\partial x} + Q_1 + \frac{\partial}{\partial \sigma} (v/h \frac{\partial u}{\partial \sigma}) + \frac{\partial}{\partial x} (h\tau_{11}) + \frac{\partial}{\partial y} (h\tau_{21})$$

$$\frac{\partial}{\partial t}(hv) + \frac{\partial}{\partial x}(hv^2) + \frac{\partial}{\partial y}(huv) + \frac{\partial}{\partial \sigma}(\tilde{w}v) + fhu \quad (38)$$

$$= -g \frac{\partial \eta}{\partial y} - \frac{1}{\rho_0} \frac{\partial P_a}{\partial y} + Q_2 + \frac{\partial}{\partial \sigma} (v/h \frac{\partial v}{\partial \sigma}) + \frac{\partial}{\partial y} (h\tau_{22}) + \frac{\partial}{\partial x} (h\tau_{12})$$

$$\frac{\partial}{\partial t}(hT) + \frac{\partial}{\partial x}(hTu) + \frac{\partial}{\partial y}(hTv) + \frac{\partial}{\partial \sigma}(T\tilde{w}) \quad (39)$$

$$= \frac{\partial}{\partial \sigma} (v_T / h \frac{\partial hT}{\partial \sigma}) + \frac{\partial}{\partial x} (\lambda_H / h \frac{\partial hT}{\partial x}) + \frac{\partial}{\partial y} (\lambda_H / h \frac{\partial hT}{\partial y}) + \frac{1}{\rho_0 c_p} \frac{\partial I}{\partial \tilde{x}_3}$$

$$\begin{aligned}
& \frac{\partial}{\partial t}(hS) + \frac{\partial}{\partial x}(hSu) + \frac{\partial}{\partial y}(hSv) + \frac{\partial}{\partial \sigma}(S\tilde{w}) \\
& = \frac{\partial}{\partial \sigma}(v_T / h \frac{\partial hS}{\partial \sigma}) + \frac{\partial}{\partial x}(\lambda_H / h \frac{\partial hS}{\partial x}) + \frac{\partial}{\partial y}(\lambda_H / h \frac{\partial hS}{\partial y})
\end{aligned} \tag{40}$$

Where t denotes the time; u , v and \tilde{w} the (x, y, σ) components of the velocity vector; f the Coriolis parameter; g the gravity acceleration; p_a the atmospheric pressure; ρ_0 the density; ν the vertical eddy viscosity coefficient; v_T and λ_H , respectively, the vertical and horizontal eddy diffusivities related to T and S ; c_p the specific heat of seawater at a constant pressure and $I(x, y, \tilde{w}, t)$ the solar irradiance.

τ_{xy} the horizontal components of the stress tensor defined by:

$$\begin{aligned}
\tau_{11} &= 2\nu \frac{\partial u}{\partial x} \\
\tau_{21} = \tau_{12} &= \nu \left(\frac{\partial u}{\partial y} + \frac{\partial v}{\partial x} \right) \\
\tau_{22} &= 2\nu \frac{\partial v}{\partial y}
\end{aligned} \tag{41}$$

Q_1 and Q_2 are the components of the baroclinic pressure gradient given by the relation:

$$\begin{aligned}
Q_1 &= \frac{\partial}{\partial x}(hq_d) + \frac{\partial}{\partial \sigma}(q_d \frac{\partial z}{\partial x}) \\
Q_2 &= \frac{\partial}{\partial y}(hq_d) + \frac{\partial}{\partial \sigma}(q_d \frac{\partial z}{\partial y})
\end{aligned} \tag{42}$$

In order to solve such an equation system (36)-(41), values for the eddy coefficients are to be provided by a turbulence scheme and a state equation for seawater is required.

Turbulent scheme or closure is provided by two supplementary evolution equations (Mellor and Yamada, 1982) one for q^2 the turbulent kinetic energy and

ℓ a turbulent length scale. The equations read:

$$\begin{aligned} & \frac{\partial}{\partial t}(q^2 h) + \frac{\partial}{\partial x}(h q^2 u) + \frac{\partial}{\partial y}(h q^2 v) + \frac{\partial}{\partial \sigma}(q^2 \tilde{w}) \\ & = \frac{\partial}{\partial \sigma} \left(\frac{\nu_T}{h} \frac{\partial}{\partial \sigma} q^2 \right) + 2\nu/h \left\{ \left(\frac{\partial u}{\partial \sigma} \right)^2 + \left(\frac{\partial v}{\partial \sigma} \right)^2 \right\} + \frac{2g}{\rho_0} \nu \frac{\partial(\rho - \rho_0)}{\partial \sigma} - \frac{2hq^3}{B\ell} + F_q \end{aligned} \quad (43)$$

$$\begin{aligned} & \frac{\partial}{\partial t}(q^2 \ell h) + \frac{\partial}{\partial x}(h q^2 \ell u) + \frac{\partial}{\partial y}(h q^2 \ell v) + \frac{\partial}{\partial \sigma}(q^2 \ell \tilde{w}) \\ & = \frac{\partial}{\partial \sigma} \left(\frac{\nu_T}{h} \frac{\partial}{\partial \sigma} q^2 \right) + E_1 \ell \left\{ \left(\frac{\partial u}{\partial \sigma} \right)^2 + \left(\frac{\partial v}{\partial \sigma} \right)^2 \right\} + E_3 \frac{g}{\rho_0} \nu \frac{\partial(\rho - \rho_0)}{\partial \sigma} \tilde{W} - \frac{hq^3}{B} + F_l \end{aligned} \quad (44)$$

Where $\tilde{W} \equiv 1 + E_2 \left(\frac{\ell}{\kappa L} \right)^2$ with κ the von Karman cste and L defined by

$$1/L = 1/(\eta - z) + 1/(H + z)$$

E_1 , E_2 , E_3 and B_1 are cste (Respectively 1.8, 1.33, 1.0 and 16.6 according to Blumberg and Mellor (1987).

F_l, F_q are horizontal turbulent diffusion terms parameterised analogously as what can be found for T and S in equation 39 and 40.

The state equation for seawater is given by

$$\rho = \rho(T, S) \quad (45)$$

Where the UNESCO(1983) parameterisation is used.

The numerical procedure used to solve equations is based on the Princeton Ocean Model (Blumberg and Mellor, 1987)

The model, applied to the same domain than the ice model (Fig. 1), is used to simulate the wind driven circulation in the Weddell Sea sector. The surface currents are used to compute the ice dynamics. The oceanic heat flux is also an output of the model.

3.2. DATA AND CLIMATOLOGIES AVAILABLE FOR THE WEDDELL SEA

3.2.1. Hydrology and associated parameters

Sets of data and climatologies are available for the Weddell Sea. The World Ocean Atlas 1994³ presents annual, seasonal and monthly climatologies for the entire World Ocean. The atlas continues and extends the 1982 Climatological Atlas by Levitus. Ocean parameters have been analysed in a consistent, objective manner at standard oceanographic analysis levels on a one-degree latitude-longitude grid between the surface and ocean bottom. These climatologies are calculated using a very large number of bottle data and/or profiles even for the Antarctic regions.

The reconstructed fields of temperature and salinities are given at the three-time scale. Oxygen fields (dissolved oxygen, oxygen saturation and apparent oxygen utilisation) exist at seasonal and annual scale. Finally, phosphate, nitrate and silicate are available within the annual climatology.

The climatologies at $\frac{1}{4}^{\circ}$ by $\frac{1}{4}^{\circ}$ based on the 1998 version of the World Ocean Database are foreseen in a near future. At the time of writing, only some parameters exist at that resolution and they are based on the 1994 data set.

Other monthly climatologies exist but do not always cover the Weddell Sea.

The Hydrographic Atlas of the Southern Ocean (Olbers *et al.*, 1992) is a compilation of all available data for the Southern Ocean. The atlas exists in paper format and there is a possible access to data at AWI (Germany).

3.2.1.1. Climatologies

As a general matter, these climatologies are available at different depths. Figure 5 and Figure 6 present respectively the surface temperature and salinity fields for the Weddell Sea and the surrounding area. These fields are extracted from the monthly climatology WOA94, introduced above in this paragraph. They represent typical fields for November (A), December (B), January (C) and February (D). This four-month period corresponds to the melting of the sea ice.

Figure 5 shows typical surface temperatures from November until February. In November, a comparison with the ice pack position (Figure 24) shows that WOA94 proposes very low temperatures for the areas covered by sea ice. Nevertheless, it should be pointed out that there is no information on the number of used field profiles for regions covered by sea ice⁴. When the sea ice melting starts, more contrasted thermal

³ S. Levitus, T. Boyer, R. Burgett, and M. Conkright of the National Oceanographic Data Center, NODC

⁴ One has to note that such kind of information is now available for the new release of that database

fronts appear on the presented climatology inside the Weddell Sea. The salinity and sigma-t fields (Figure 6 and Figure 7) confirm the presence of these frontal structures.

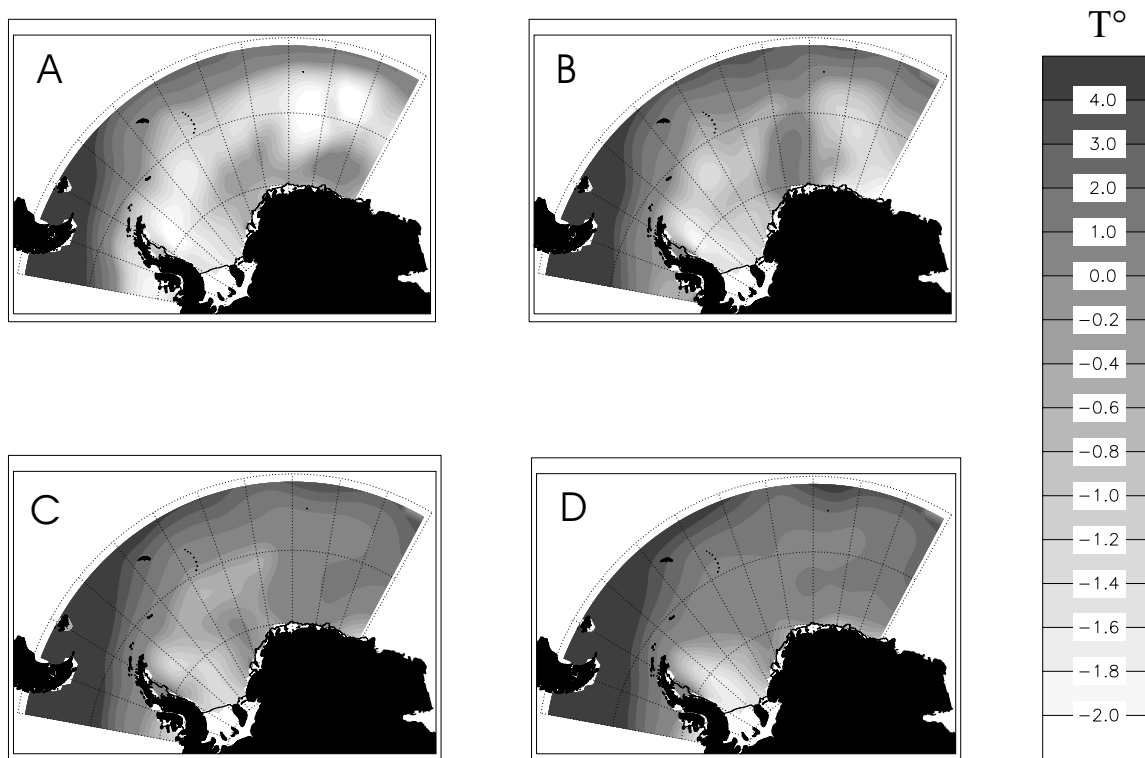


Figure 5. SST fields from World Ocean Atlas 1994 (A to D respectively November until February). One can observe very low temperature in November within the Weddell Sea as well as the existence of a thermal front from December until February.

A warmer water tongue is observed in December (Figure 5B) at the longitude of the Maud Rise, a submarine mount culminating at about 1000 below sea surface. This phenomenon could be the signature of an up-sloping event.

Other fronts are present along the ice pack boundaries. A tongue of colder water appears in the Weddell Sea in January (Figure 5C) and is advected by the Antarctic Circumpolar Current (ACC) (Figure 5D). The origin of the tongue is probably the melting of sea ice as suggested by the January (Figure 5C) and February (Figure 5D) salinity fields. The Antarctic convergence is well represented by the SST field.

The November until February typical sea surface salinity field is presented at Figure 6. Less saline water appears during the melting of the sea ice (Figure 6B to Figure 6 D) And a large scale 'plume' is visible in January (Figure 6C).

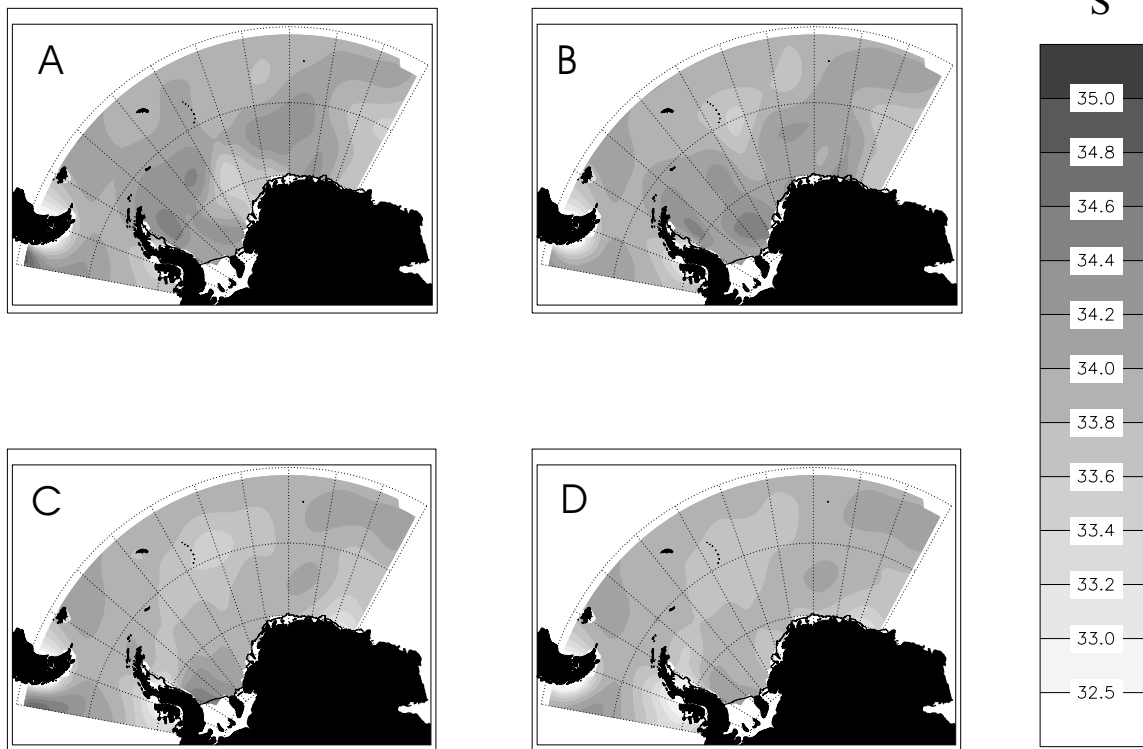


Figure 6 Typical monthly mean sea surface salinity climatology from November (A) to February (D) (WOA94). This figure enhances a tongue of less saline water (C) and (D) due to sea ice melting.

Density is more relevant than temperature or salinity to trace water masses. To be able to extract more information from the hydrological data we calculate surface density fields from the above-presented temperature and salinity climatology using Fofonoff and Millard (1983).

Figure 7 displays the typical density field from November (A) until February (D). Density fronts are present in the Weddell Sea during the period from November until February, although the validity of the density field could be questioned when sea ice coverage is present.

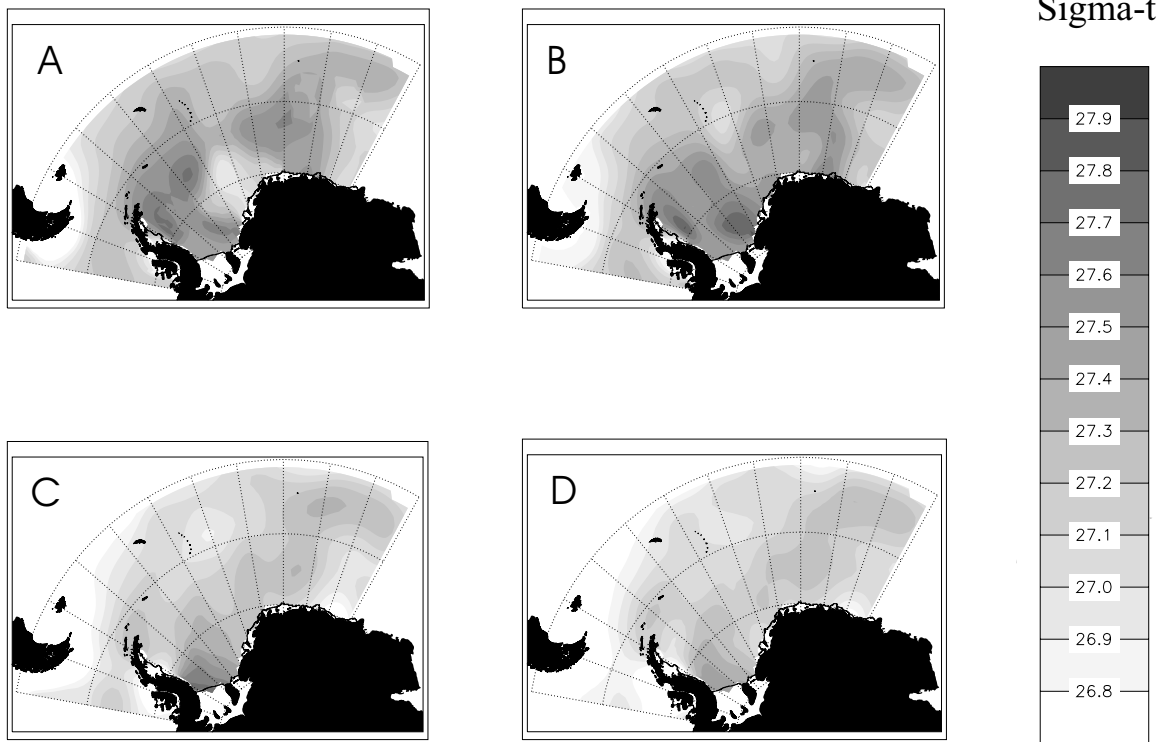


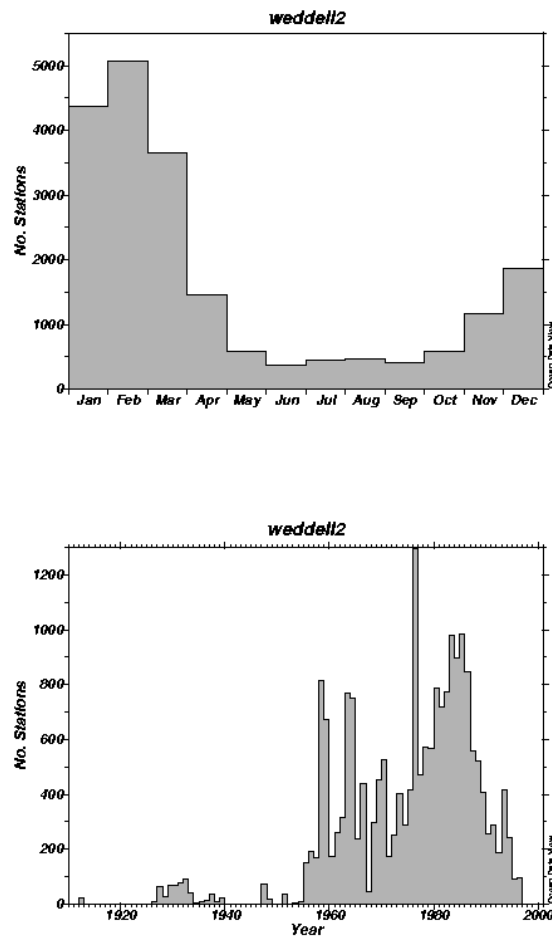
Figure 7. Typical monthly mean climatology of the density (recalculated from temperature and salinity monthly mean using Fofonoff and Millard (1983)).

3.2.1.2. Individual profiles and data

An access to quality controlled⁵ profile data used in the climatologies is some time possible. The World Ocean Database CD-ROM series are available at the National Oceanographic Data Center (NOAA). The NODC database include about $5 \cdot 10^6$ metadata⁶ of while 43000 concern the Weddell sea. Data extracted from that database were used during this research program. We focused on the specific region of the Weddell Sea such as the Maude Rise for physical phenomenon identification and worked at a larger scale for boundary condition purposes. The temporal distribution of data available for the Weddell Sea is summarised at Figure 8 for bottle and CTD data.

⁵ Methods used for the quality control are available in Boyer and Levitus (1994)

⁶ By metadata we mean the complete information for the location. i.e. a complete CTD profile.



ODYS4: D:\Africa_data_archive\ODYS\odys_backData\WOD98\weddell2; D:\Africa_data_archive\ODYS\odys_backData\WOD98\weddell2.ctg - Nov21/2001 11:57:50

Figure 8: Weddell Sea WOD98 available Bottle data

We have to remark that only some data are available during the winter periods when navigation inside the Weddell Sea is impossible.

We were focusing on CTD profile and will therefore work with a subset of the available data presented at

Figure 9 for the spatial localisation and at Figure 10 for a temporal summary.

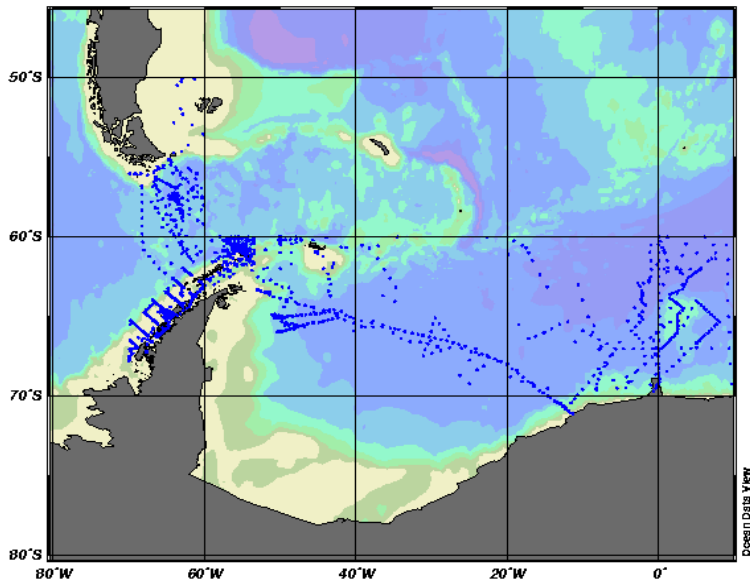
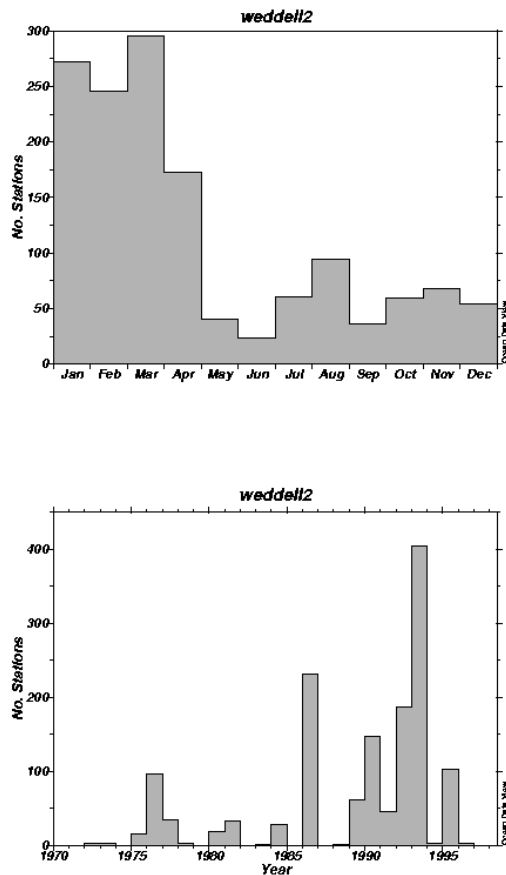


Figure 9: Available CTD profiles within the above mentioned data set (every dot is a CTD Station).

The following sections present⁷ results obtained from the analysis of these data for the Maude rise zone and for the Weddell Sea boundaries.

⁷ Graphical representation of the data are made using the software Ocean Data View (Schlitzer, R, 1999)



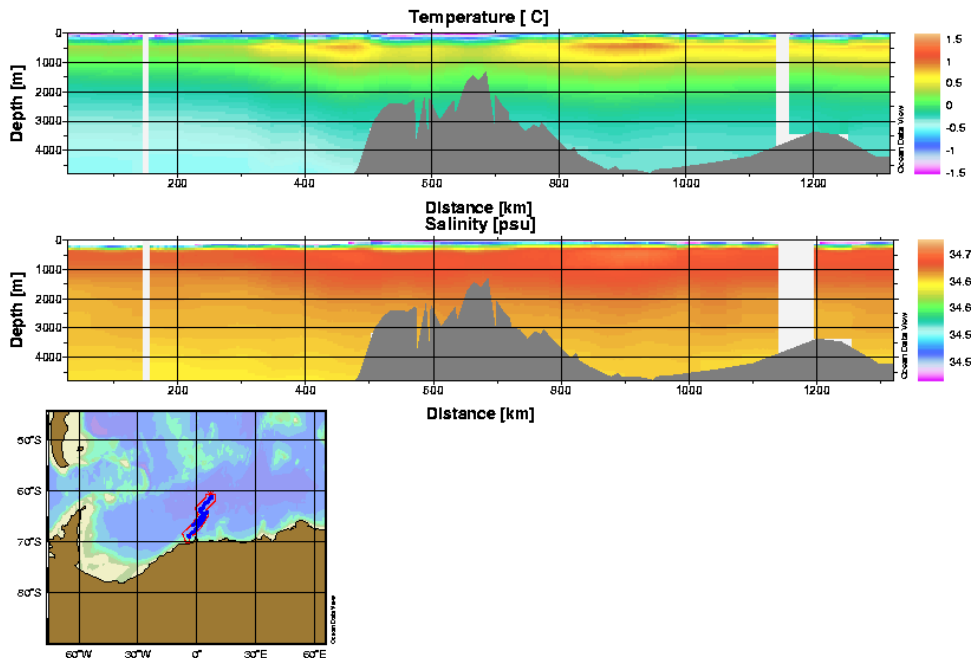
DDYS A: D:\A\Ice\ice_dsts_etcd\dsts\DDV\cdv4_bck\Dst\Save\weddel12; D:\A\Ice\ice_dsts_etcd\dsts\DDV\cdv4_bck\Dst\Save\weddel12.cfg - N

Figure 10 Temporal distribution of available CTD profiles

- **Maude Rise zone**

Data are available from a cruise undertaken in August 1986. Figure 11 shows vertical section reconstructed along the ship track from about sixty CTD profiles.

The seamount located at the centre of the image is the Maud rise. The Maude rise is a place known to be characterised by the presence of warmer water pools of Weddell Deep Water (Gordon and Huber, 1995) influencing the dynamics of the sea ice.

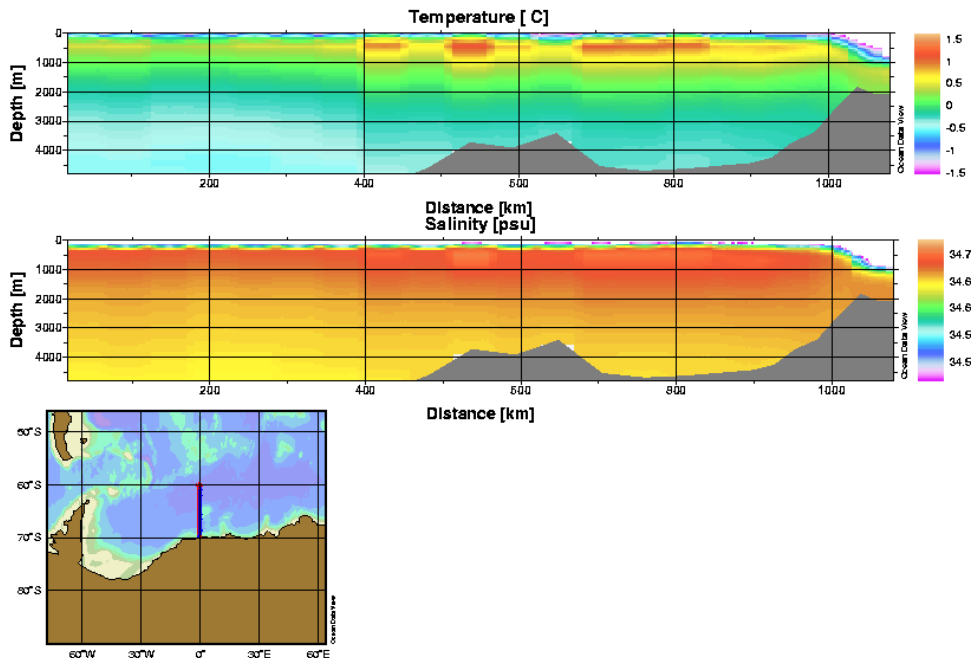


DDV4.0.12: C:\Program Files\Ocean Data View 4.0\Data\Save\weddel; C:\Program Files\Ocean Data View 4.0\Data\Save\weddel.clg; C:\Program Files\Ocean Data View 4.0\Data\Save\weddel_lp3_summer.sec - Ri Dec 03 11:20:30 1999

Figure 11: Temperature and Salinity along track. Reconstructed vertical section. August 1986 data

Figure 11 shows pools of warmer water at about 200 km before and after the Maude rise along the vessel track. Such warm pools are also observed in June 1992. Because both vessel tracks are not the same, localisation of the pools cannot be exactly compared. It is confirmed from Figure 11, Figure 12 and other data sets⁸ from 1977 and 1986 that such pools exist and remain permanently at the vicinity of the seamount.

⁸ Not presented in this document.



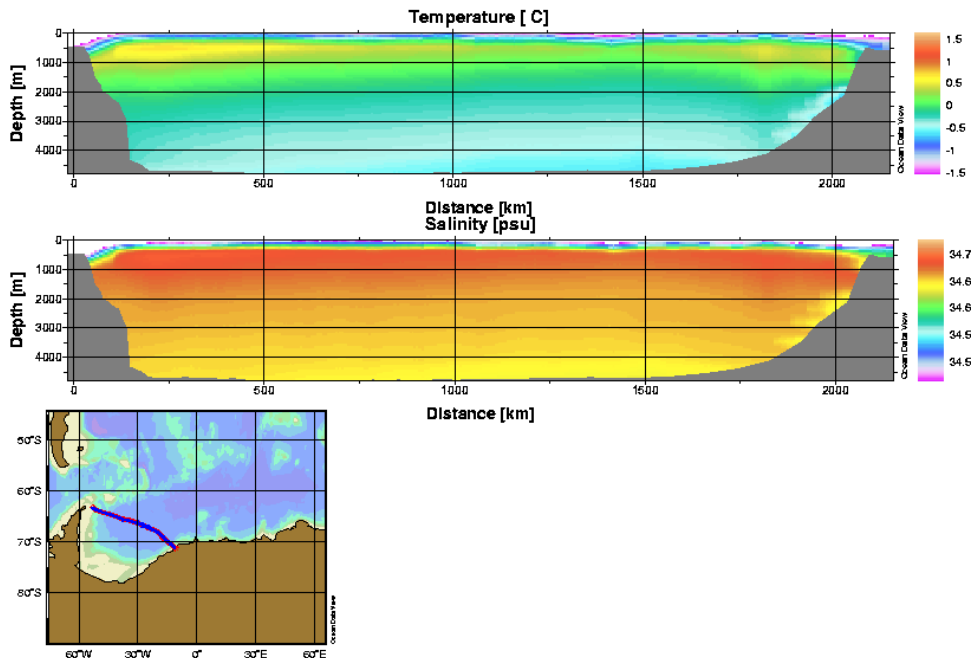
DDV4.0.12: C:\Program Files\Ocean Data View 4.0\Data\Saved\wedell; C:\Program Files\Ocean Data View 4.0\Data\Saved\wedell_at1.clg; C:\Program Files\Ocean Data View 4.0\Data\Saved\wedell.sec - Fri Dec 03 14:16:46 1999

Figure 12: Temperature and Salinity along track. Reconstructed vertical section. June 1992 data

- Boundaries of the Weddell Sea domain.

The NODC database has also been used to gain information at the boundaries of the modelled domain. That is of great importance for boundary condition definition purposes. We present now some of the data used. Figure 13 presents a section through the Weddell Sea oriented from the Antarctic continent to the Antarctic Peninsula. A zone of possible formation of Antarctic bottom-water⁹ (ABW) close to the Antarctic Peninsula is visible as well as the very low salinity characterising the surface waters. A dome in the temperature is also visible at a few hundred km from the Peninsula. The position of the dome is governed by the interaction between Weddell Sea permanent gyre and the Antarctic Circumpolar Current (ACC) (Gouretski and Danilov, 1993).

⁹ ABW, Antarctic Bottom Water is characterized by a temperature $T \sim -0.3$ °c and a salinity $S \sim 34.6$.



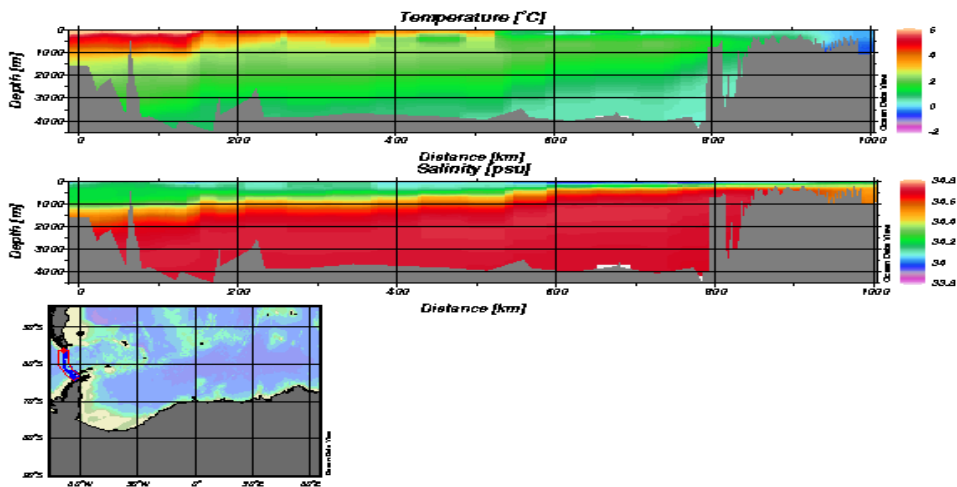
DDV4.0.12: C:\Program Files\Ocean Data View 4.0\Data\Save\weddel; C:\Program Files\Ocean Data View 4.0\Data\Save\weddel.clg; C:\Program Files\Ocean Data View 4.0\Data\Save\weddel_tran1.sec - Fri Dec 03 11:28:41 1999

Figure 13: Temperature and Salinity vertical section along vessel track sailed from the Antarctic Peninsula in November-December 1990 but represented here from the continent to the Antarctic Peninsula.

Just below the surface layer the circumpolar deep water (CDW) characterised by its maximum temperature can be found. Below CDW, Weddell bottom water (WBW) remains. One other data set is available for the Weddell Sea region. That is the WOCE data set presented at Figure 14.

Drake Passage. Intensity of the ACC is ranging from 29 Sv to 290 Sv with a mean accepted value of 139 Sv. (Tomczak and Godfrey, 1994). Current speed is usually low. Values ranges from 0.05 to 0.15 m/s but can reach 1 m/s at some occasion (Tomczak and Godfrey, 1994).

Figure 15 features different water mass in interaction through the Drake Passage. CDW is present from the bottom and predominantly face the Antarctic continent. On the other side of the Drake Passage warmer water masses are found and the vertical structure is in relation with the dynamic of the Antarctic convergence situated between South America and Antarctica.



© DMS4: D:\Msl\mca_data\stord\slr\CCW\slr\4_bach\Date Server\redsh12: D:\Msl\mca_data\stord\slr\CCW\slr\4_bach\Date Server\redsh11.cdg: D:\Msl\mca_data\stord\slr\CCW\slr\4_bach\Date Server\redsh10: Deco 1360001 09:23:22

Figure 15 Temperature and Salinity vertical section along vessel track across the Drake Passage in January 1990.

3.2.2. Water current data

3.2.2.1 Lagrangian data (drifter data)

Drifter¹⁰ data are available for the Southern Ocean. Satellite tracking methods obtain drifter tracks and as a general matter, no drifter tracks enter the Weddell Sea or sails below 60° of latitude South. In addition, some drifters have a temperature sensor fitted.

We present here some tracks relevant for the project. No temperature plots are presented.

Figure 16 shows the long-term tracks of three drifters. Such data permit to extrapolate current speed and direction for the hydrodynamic model boundary conditions. For example, drifter n° 24428 has been tracked during 288 days. About 60° of longitude at mean latitude of 56° S have been covered. This corresponds to a surface current intensity of the order of magnitude of 0.10 to 0.15 ms⁻¹. That kind of data used together with current meter data (next section) permit to deduce the flow at boundaries of the domain.

¹⁰ These data are made available by Donald V. Hansen, Pierre-Marie Poulain, and the Atlantic Oceanographic and Meteorological Laboratory (Miami) for the drifter data. (NOAA)

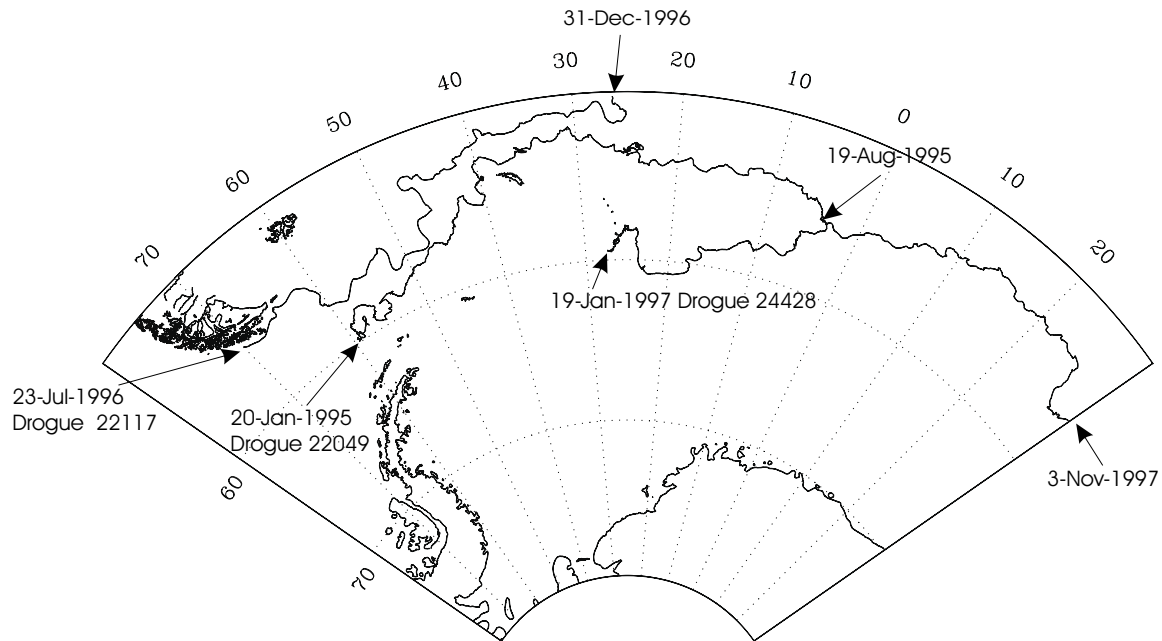


Figure 16 Drifter tracks in the surrounding area of the Weddell Sea. Data from Atlantic Oceanographic and Meteorological Laboratory for the drifter data, NOAA.

3.2.2.2 Eulerian data (Current meter data)

Current meter data of the Weddell Sea are scarce and not widely available. Nevertheless, some are available¹¹ from Alfred Wegener Institute for Polar and Marine Research (AWI) Germany. Relevant data sets are presented at the three following figures. Localisation of the mooring is underlined at Figure 1. Data are available at an hourly or two-hourly rate and are further filtered in order to obtain daily values.

¹¹ Data made available by G.Rohardt. AWI-Germany

72.5567 S; 20.5950 W

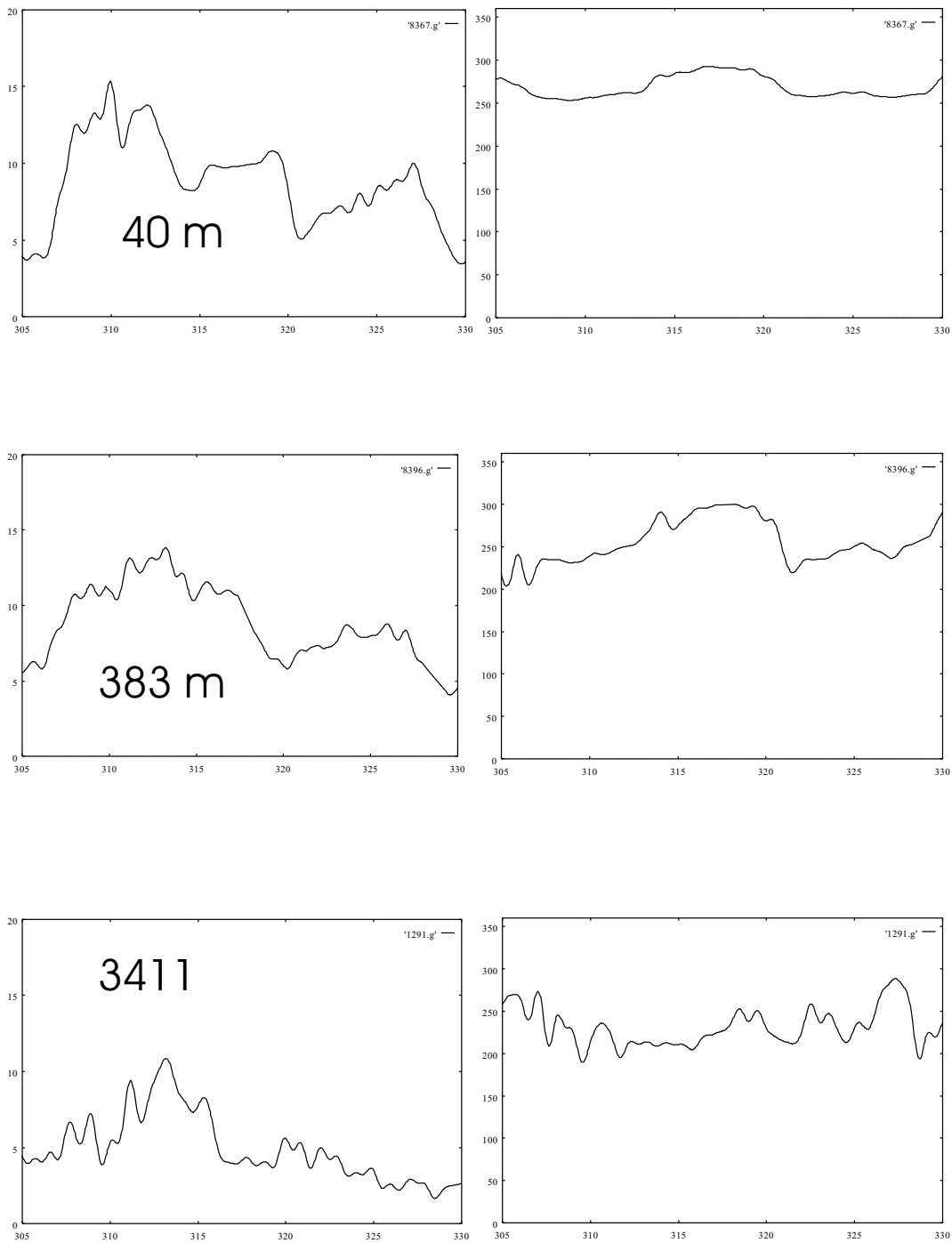


Figure 17 Current meter data from AWI-Bremerhaven. Current at three depths and at the location given

Figure 17 shows 25 days of current data during October-November 1986 approximately at the middle of the domain. Magnitude of the current ranges between 5 to 15 cm/sec for

the entire water column. The current is oriented towards the west at the surface and turn lightly to the south as the depth increases but the vertical shear remains small. Figure 18 and Figure 19 show current speed and direction for two other locations inside the Weddell Sea sector.

Data are presented for a 160 days period starting end February 1997. Variation range of the current velocity remains with the same order of magnitude. The highest value of the current observed at day 38 north of the Maud Rise (Figure 19) is visible for the three depths indicating that the acceleration of the current affects the complete water column. That current acceleration is not visible for the other location close to the western boundary of the domain (Figure 18). The origin of the acceleration is unclear from the only available data but if the signal is strong close to the surface at Figure 18 -297 m-, it is at the noise level for the bottom current meter and an atmospheric cause is the most probable.

The direction of the current at Figure 19 shows a mean westward flow at 297 and 3366 m while two different directions (280° and 255°) characterise the 803m data. Direction recorded at the western mooring shows a flow oriented towards the Southwest.

Figure 18 also features stronger current at depth than at the surface.

Conclusions from this first analysis of current meter records enhance the temporal and spatial variability of the Weddell Sea circulation. If at annual to pluri-annual scale, the circulation appears to be simple and based on the ACC flowing eastward¹², at smaller scale, all complexity of water masses interaction and weather condition prevail and complicate the circulation patterns

¹² See drifter data at Figure 16

63.7217 S; 50.82 W

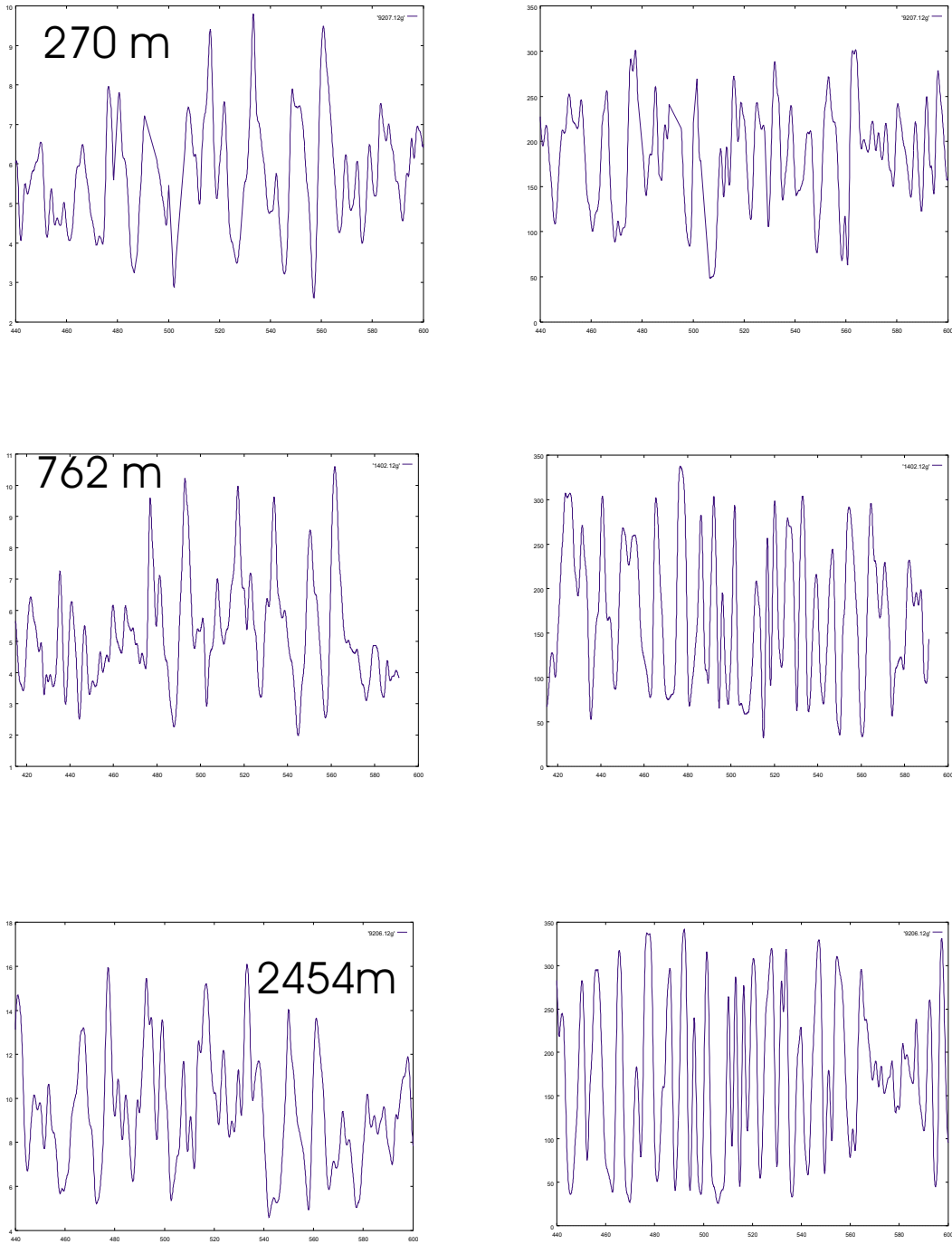


Figure 18 Current meter data from AWI-Bremerhaven. Current at three depths and at the location given

40
69.0 S; 0.00 E

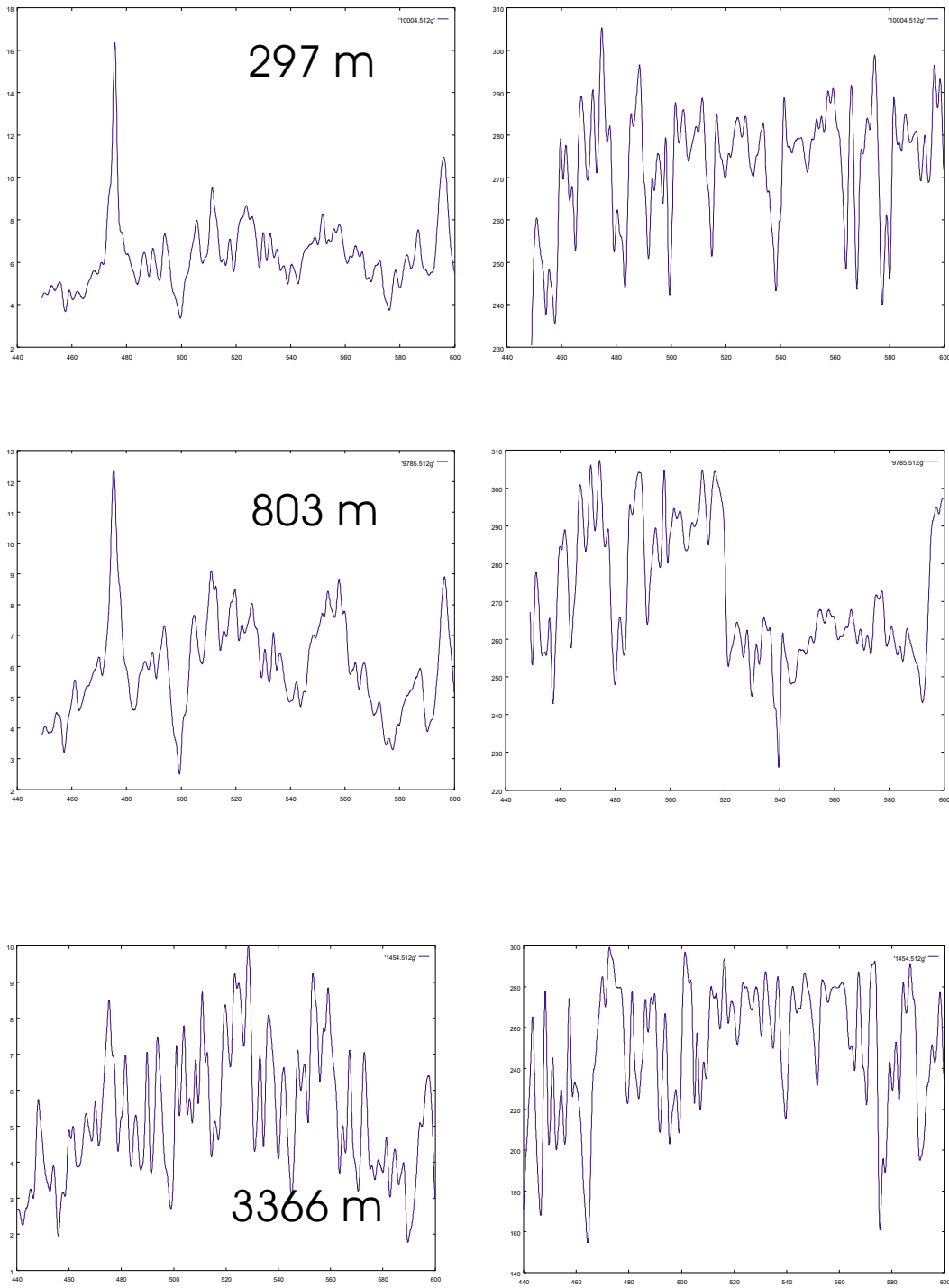


Figure 19 Current meter data from AWI-Bremerhaven. Current at three depths and at the location given

3.2.3. Wind stress data

The Hellerman and Rosenstein (1983) wind stress climatology is mainly used to force the model (Figure 21 and Figure 20).

Other data sets are available for the Weddell Sea and we also used

- Taljaard *et al.* (1969)
- Kottmeier *et al.* (1997)
- Remote sensed data of wind fields are available from CERSAT-IFREMER (France)
- Climatological wind as well as other air-sea interaction parameters are available from the European Centre for Medium-Range Weather Forecasts (ECMWF)

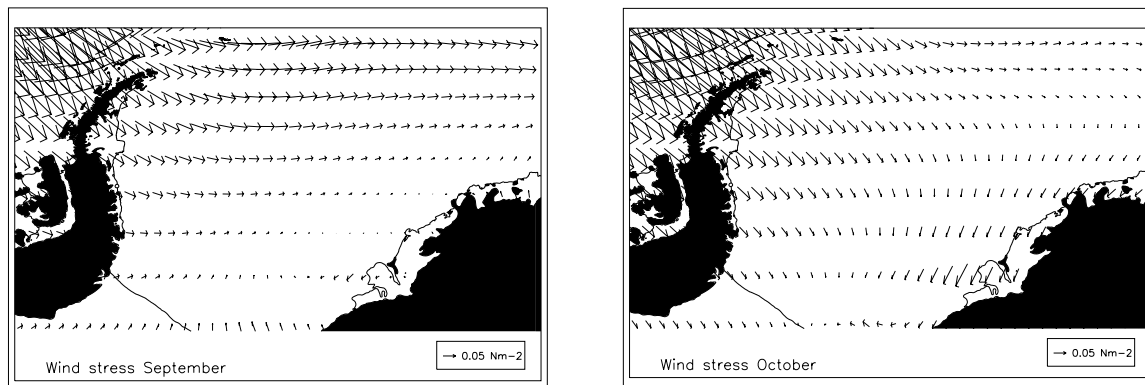


Figure 20 Weddell Sea Wind Stress from Hellerman and Rosenstein, (1983)

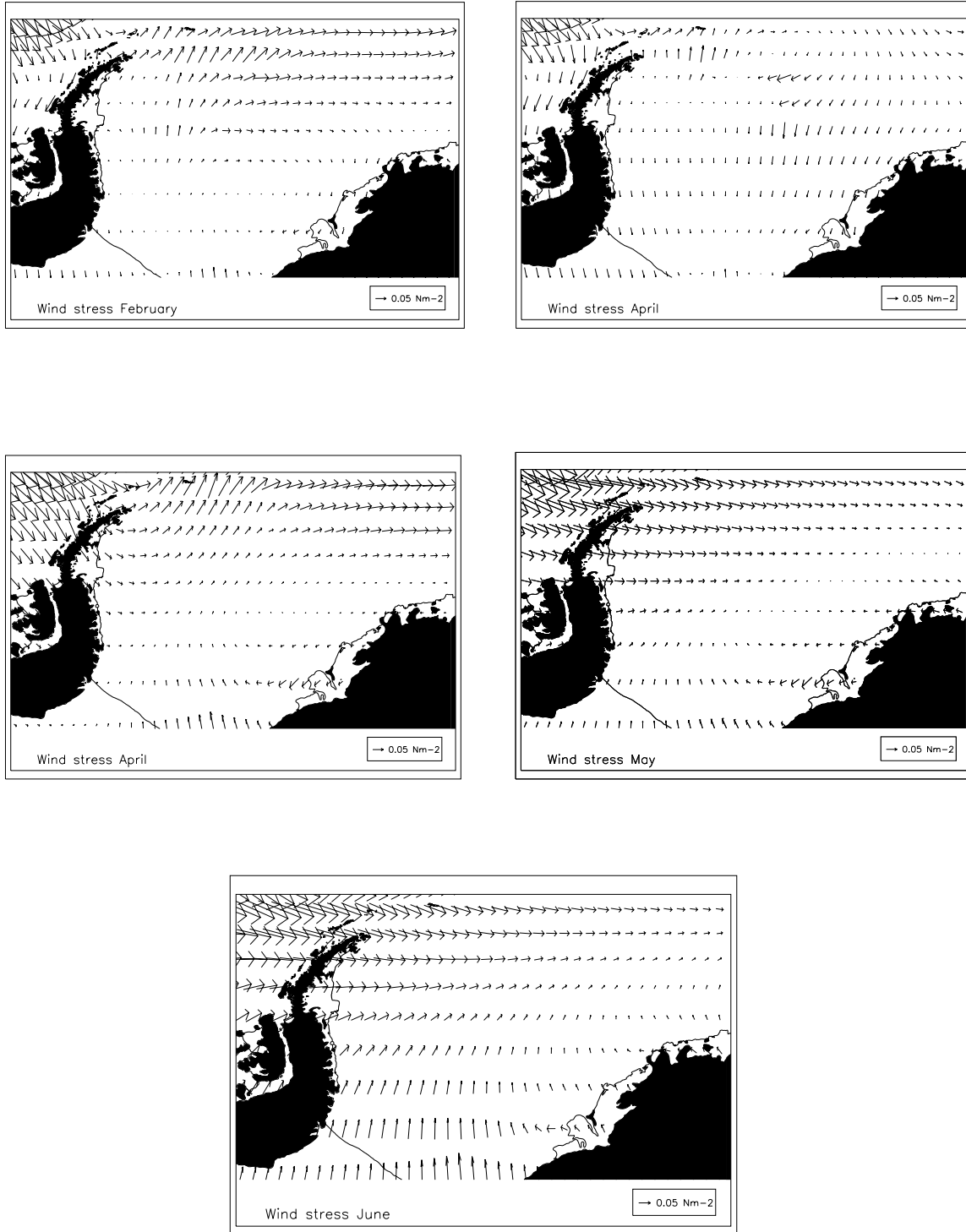


Figure 21 Weddell Sea Wind Stress from Hellerman and Rosenstein, (1983)

3.2.4. Sea ice concentration and thickness data

Sea ice concentration data are used here for the calibration and the validation of the sea ice model. These data are also important for identifying regions of high primary production. A new map of sea ice concentration is made available each day from remote sensing (passive microwave sensor) by the Ocean Modelling Branch of the Environmental Modeling Center (NOAA, Washington, USA).

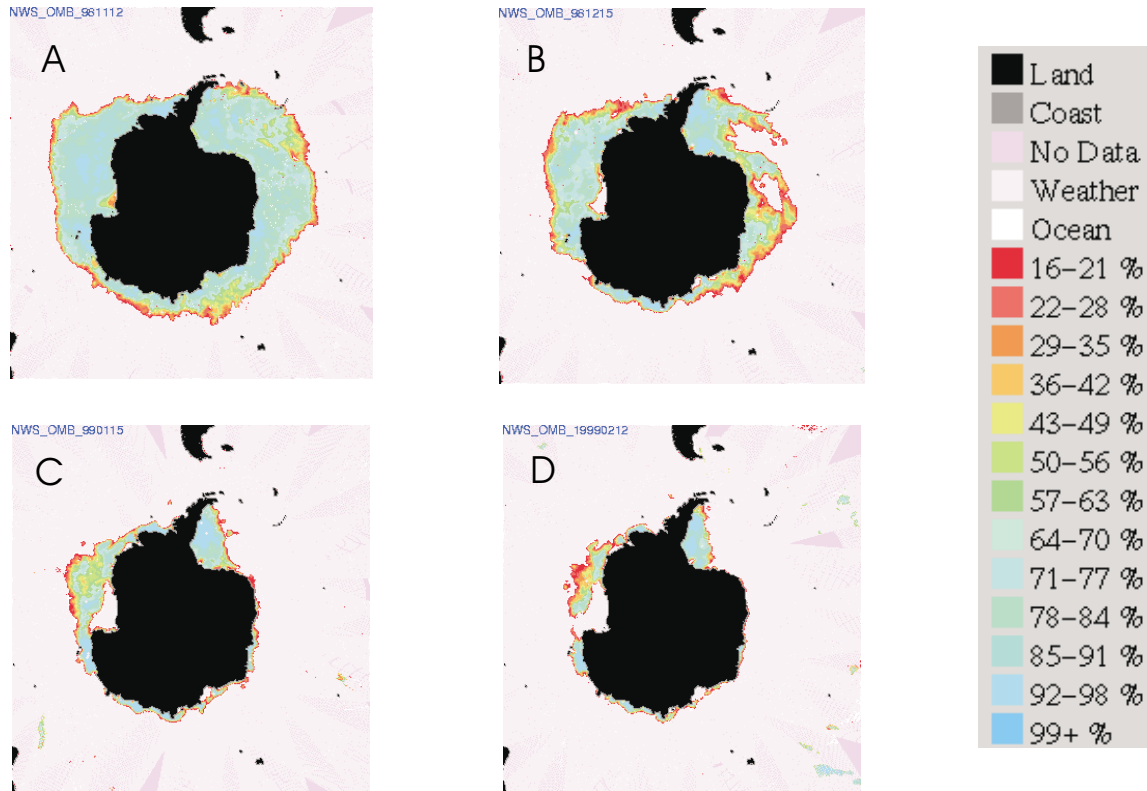


Figure 22 Sea Ice concentration (Ocean Modelling Branch (NOAA)) for November 12, 1998, (A); December 15, 1998, (B); January 15, 1999 (C) and February 12, 1999 (D).

Figure 22 illustrates the melting of sea ice in Antarctic from December until February. One can observe for instance the opening of the Weddell Sea ice pack.

The sea ice model applied to the Weddell Sea is able to reproduce the December ice concentration pattern (Petit and Norro, 1999). Sea ice thickness data are scarce but necessary for calibration and validation of sea ice model. Until now, sea ice thickness is not available from remote sensing.

3.2.5. Bathymetry

The model bathymetry (Figure 1) is based on the ETOPO5 bathymetry. ETOPO5 has a $1/12^\circ$ by $1/12^\circ$ coverage of the entire world. The Weddell Sea is characterized by a large zone along its coast where the depth of water does not exceed 1000 m. The central part of the sea is an abyssal plain where the depth can reach 4500 m. Outside the Weddell Sea, the South Sandwich trench is deeper than 6000 m.

4. Results and Discussion

The models we developed earlier at § 3.1.2 and §3.1.3 have been run on the Weddell Sea domain at various resolutions.

First stage development worked on a grid of 2° in longitude and 1° in latitude. Further refinement included passage to a grid size of $1/2^\circ$ in longitude and $1/4^\circ$ in latitude to finally end with a resolution of $1/12^\circ$ on both latitude and longitude¹³.

4.1 High-resolution simulation

The results of the previously described models on the $1/12^\circ$ latitude and longitude grid are proposed here.

As a general matter, the results at high resolution are compatible with the large-scale circulation obtained earlier with similar models on coarser grids and with results of other model (Beckmann *et al.*, 1999) The interest of the high-resolution simulation is the possibility offered to focus on a specific region such as the Maud Rise for instance.

The zooming strategy is developed at the level of post-processing of the model results providing the main advantage of no interaction with the numerical model itself and therefore no risk of solution contamination.

The Maud Rise region is known to be a region playing a key role in the oceanology of the Southern Ocean (Gordon and Hubert, 1995). Furthermore, that is a region where ice break up takes places in advance almost every year in early spring. Data have been presented showing the presence of upwelled warm WDW in the vicinity of the Maud Rise. In addition, a zone of restricted sea ice cover in duration and thickness has been associated with the vicinity of the Maud rise.

¹³ As an information, for such a refined grid on the specified domain, the size of computer central memory required for a single run of the model is just above 1Gb

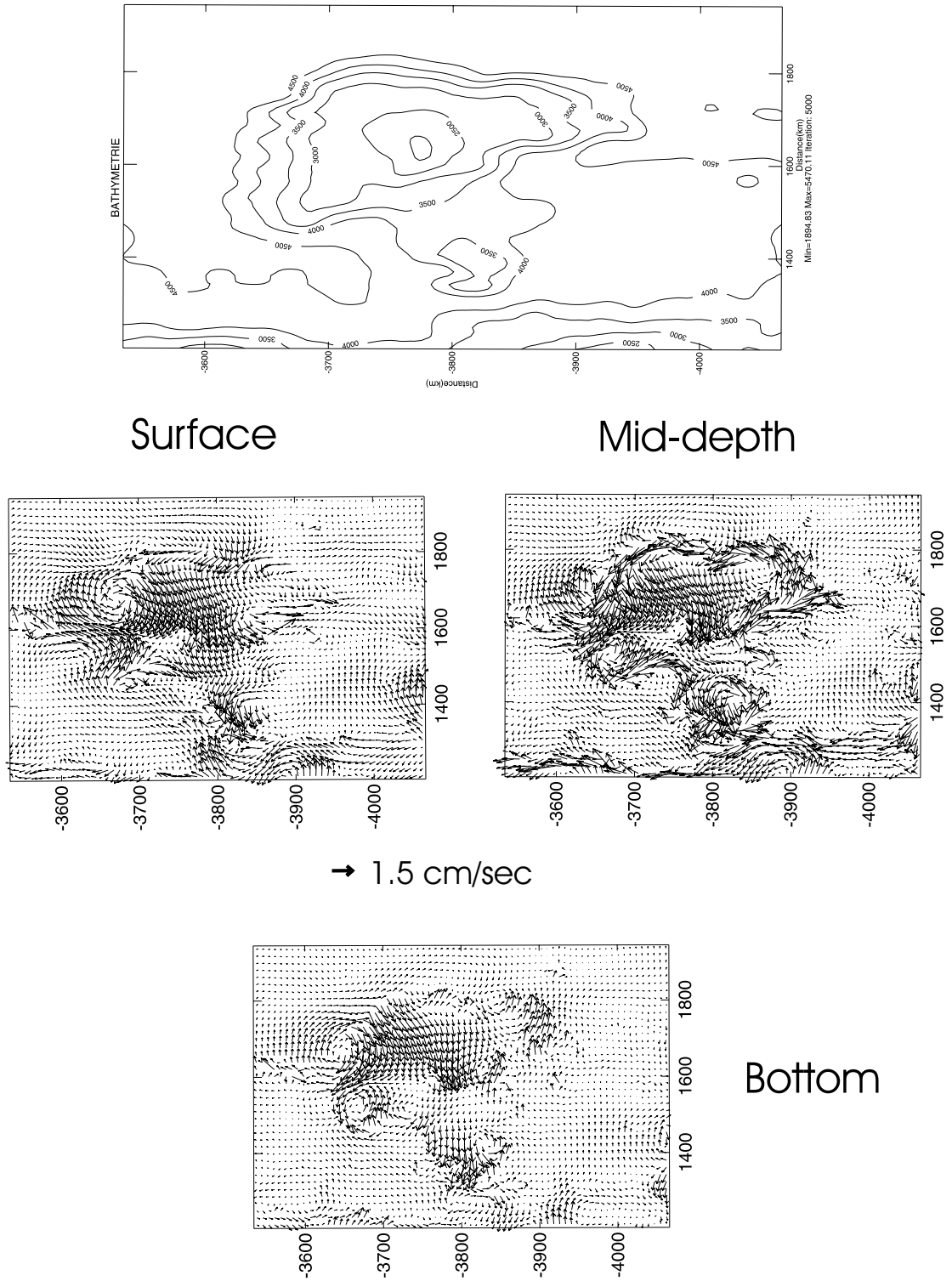


Figure 23 Maud Rise flow pattern at surface , mid-depth and the bottom for a simulation forced by December climatology. (Only one arrow for four grids point)

Model simulations have been conducted to confirm vertical movement of water masses. Figure 23 presents the flow around Maud Rise in December using wind forcing from the

Hellerman and Rosenstein climatology. The model is run for the entire Weddell Sea domain (Figure 1) and zooming is proposed for the region of interest. The flow pattern is represented at the sea surface, at mid depth and close to the bottom. The zone of interest is a rectangle of 600 km in longitude by 800 km in latitude centred on the Maud Rise. Important vertical shear of the horizontal velocity vector is observed emphasising the strong three-dimensional structure of the flow field.

180° rotation in the velocity vector is observed between surface and mid-depth flow pattern. It occurs also between the mid-depth and the bottom solution. Bathymetry modifies considerably the flow in direction and intensity. The velocity remains of the order of magnitude of a few cm/sec. Shear and velocity are completely in accordance with the data presented at section 3.2.2 and with Bersch et al. (1992)

Vertical movements of water are associated with three-dimensional flow pattern and for the present case, the true upwelling velocity¹⁴ can locally be close to 1mm/s. Such enhanced upwelling is located preferably, in our simulation, in the Eastern side of the Maud Rise and could be responsible for the observation of upwelled WBW in the vicinity of the Maud rise.(Bersch et al.,1992). Moreover, the presence of the Maud Rise and the associated upwelling can modify the stability of the water masses and precondition large and deep convection. Relation with large recurring polynyas in 1974 and 1980 are proposed by Comiso and Gordon(1987).

4.2. ANNUAL SEA ICE CYCLE

This section illustrates the application of the model described above. The main parameter values are presented in Table 2

¹⁴ True upwelling velocity represents the flow crossing iso-sigma lines.

Table 2 Parameter values

Symbol	Definition	Unit	Value
c_p	water specific heat	(J kg ⁻¹ K ⁻¹)	3935
K_T	vertical heat diffusivity	(m ² s ⁻¹)	2.10 ⁻⁵
K_S	vertical salt diffusivity	(m ² s ⁻¹)	2.10 ⁻⁵
P^*	strength parameter	(Nm ⁻²)	27000
C	dimensionless strength parameter	-	20
e	visco-plastic rheology eccentricity	-	2
A_h	horizontal eddy viscosity coefficient	(m ² s ⁻¹)	5000
A_v	vertical eddy viscosity coefficient	(m ² s ⁻¹)	0.1

First, the response of the ice pack submitted to monthly-averaged meteorological data during one year is reproduced and compared with observations. Secondly, the interactions between ice and ocean are investigated by studying the evolution of the sea surface temperature and the oceanic heat flux, an important parameter which is difficult to measure *in situ* and mainly influencing the ice formation and melting.

4.3. SEA ICE EVOLUTION

At the end of the short Antarctic summer, the surface water begins to freeze when the atmosphere pumps more energy from the ocean upper layer than the ocean is able to supply. The sea surface temperature decreases under the water freezing point and an ice layer is formed.

In February, the ice pack attains its minimum coverage. With the atmosphere cooling, ice layer forms so that in March, the ice production described in Figure 24 is already intense. From the zones of production, the ice is transported essentially under the influence of the cyclonic wind field blowing over the Weddell Sea (Figure 26). Consequently, the ice pack is affected by a clockwise rotating movement induced by the Weddell gyre combined with a resulting divergent Ekman transport in the surface layer of the ocean (Figure 25). In the south and in the west, the ice can accumulate respectively along the Filchner-Ronne ice shelf and the Antarctic

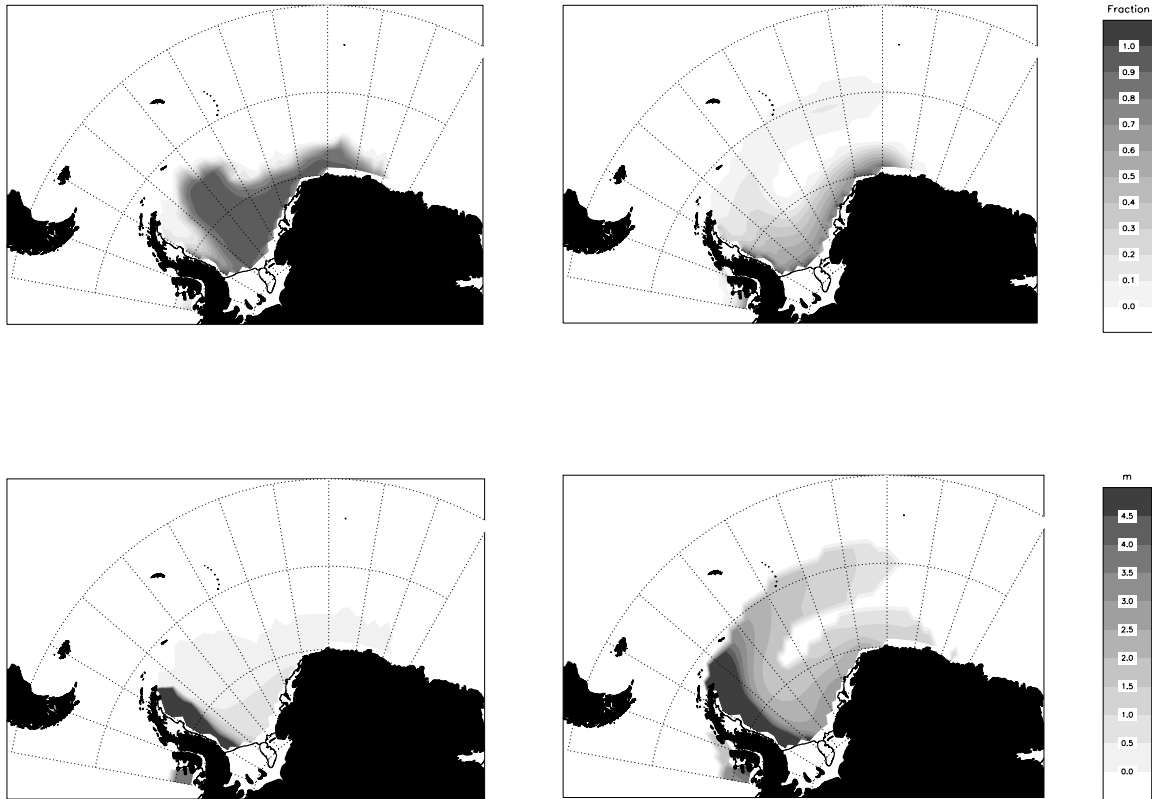


Figure 24. Sea ice concentration in March (0 = no ice, 1 = surface completely covered by ice) (top) and thickness (m) (bottom) and for a typical November (right).

Peninsula, where the ice thickness can become relatively high (Figure 24). The ice pack can widen northwards almost freely. Some ice produced in the southern part of the Weddell Sea is carried northwards in relatively warmer waters where it partly melts or is carried away eastwards by the strong ACC current partly governing the ice margin (Figure 16).

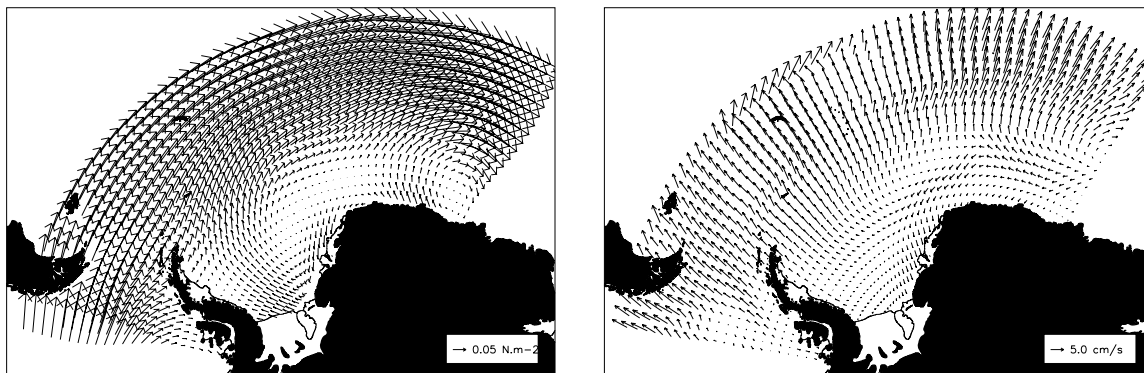


Figure 25. Wind stress field (N m^{-2}) (left; Taljaard et al., 1969) for a typical November (climatology) and computed surface currents (cm s^{-1}) in November (right) (A $1^\circ \times 1/2^\circ$ grid model has been used here).

Some ice can be re-injected in the Weddell gyre by the rotating movement but will rarely be older than two years, contrary to the Arctic ice pack where multiyear ice up to 10 years is a common feature because the Arctic ice pack is surrounded by continents and ice can turn several years before leaving the Arctic ocean through the Bering and the Fram Straits.

In winter when the ocean-atmosphere heat flux is directed towards the atmosphere the leads fill with new ice. In this way new sea ice forms in the interior of the sea ice fields rather than being accreted to the outer edge. While some addition at the edge may be expected, the northward migration of the ice edge may be primarily governed by Ekman velocity (Gordon, 1981). As ice is carried northwards, the local heat balance would induce melting, and a steady-state ice cover is attained, as may be the case from August to October. During this period ice forming in the south is balanced by melting in the north.

Southern Ocean seasonal sea ice thickness is estimated at 1.0 to 1.5 m (Gordon, 1981). Measurements taken in the period July, 18 to September 10, 1986 in the zone between 55°S and 70°S around the Greenwich meridian (Wadhams *et al.*, 1987) have shown that undeformed ice in the eastern Weddell Sea was less than 1m thick. The model results (Figure 24) are in good agreement with these observations. The maximum ice thickness computed with the model of Scheduikat (1996) is located in the southwestern Weddell Sea and amounts to approximately 4.5 m.

The cyclonic wind field induces a weakening of the ice pack (Figure 25 and Figure 26) in the central part of the Weddell Sea. The location of this weakening moves northwestwards along the Antarctic divergence located around 65°S and finally provokes an opening of the ice pack in November accelerating the melting processes. This melting process is reproduced in the model results (Figure 24).

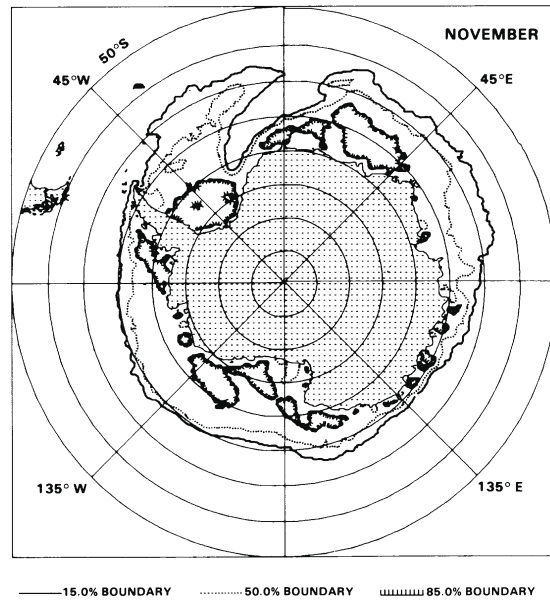


Figure 26. Mean ice concentration satellite observations in November (Zwally *et al.*, 1983).

The sea ice cover undergoes a rapid decrease from mid-November to mid-January (Figure 24). The ice charts of the Navy-NOAA ice center indicate that during this period sea ice virtually disappears over the deep ocean (Gordon, 1981). Ice melting during spring is also influenced by Ekman divergence generating open water or leads and enhancing exchanges between ocean and atmosphere. The open water areas act as heat collectors, which accelerate melting of the surrounding ice pack.

Zwally *et al.* (1983) underline that the persistent low pressure over the Weddell Sea introduces a northwards cold air flow over the western part of the sea, limiting the ice melting along the Antarctic peninsula and even maintaining ice growth at the edge of the Filchner-Ronne Ice Shelf throughout the year.

4.4. SEA SURFACE TEMPERATURE

Figure 27 shows the evolution of the sea surface temperature during the most intense period of the breakup. At the end of October, the footprint of the ice pack on the upper ocean is clearly recognisable by a large zone of cold water between -1° and -2° . The rapid ice melting introduces fresh water in the upper layer of the ocean. This pool of fresh water in equilibrium with the water column can be maintained a long time after the ice break-up as shown in Figure 27.

The Antarctic circumpolar current governs the position of a temperature front located around 50°S , which agrees with the approximate position of the Antarctic polar-front.

The model succeeds in locating the Antarctic polar front and reproducing the general temperature pattern

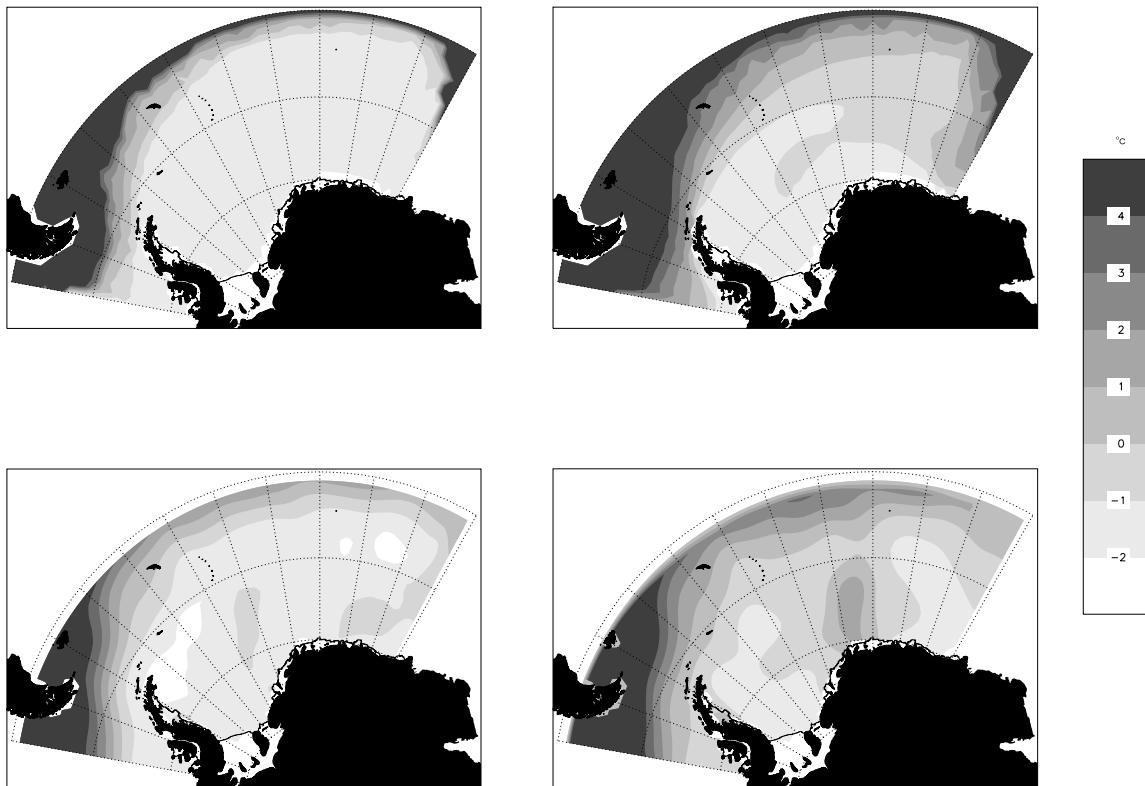


Figure 27. Evolution of the computed (top) and observed (World Ocean Atlas, 1994; bottom) sea surface temperature (degrees Celsius) during the breakup at the end of October (left) and on 15 December (right).

4.5. OCEANIC HEAT FLUX

Gordon *et al.* (1984) has estimated the value of the Weddell Sea oceanic heat flux between 9 and 16 Wm^{-2} . More recent observations have shown that the variation range of this parameter could be larger, which corroborates the results of the model described above.

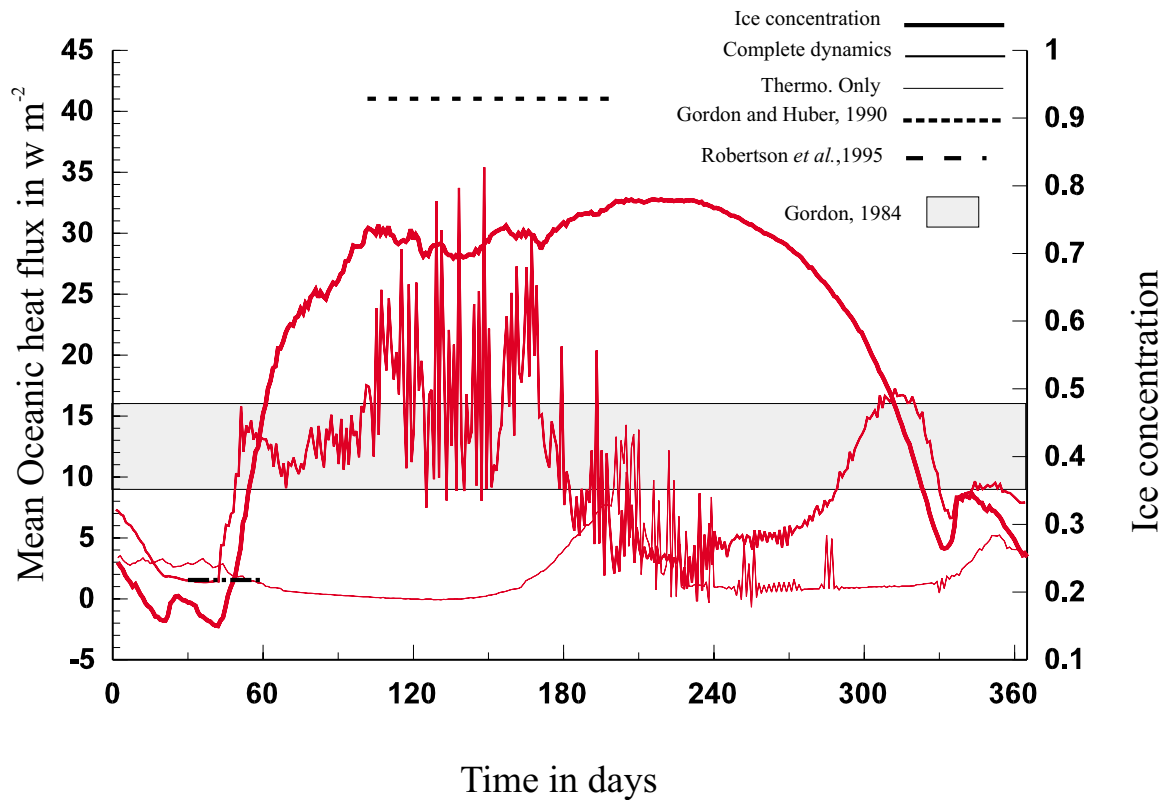


Figure 28. Annual cycle of the mean oceanic heat flux (W m^{-2}).

At the beginning of the year, the ice extent reaches its minimum value. The ice pack is located in the western part of the Weddell Sea. In February, the mean oceanic heat flux also reaches its minimum corresponding to the observations of Robertson *et al.* (1995) who measured values of 1.7 Wm^{-2} in the western Weddell Sea which is in good agreement with Figure 28. Then, the atmosphere cools and begins to pump energy from the ocean provoking the extending of the ice pack. The ocean flux increases to reach a maximum in May. At this time, the model slightly underestimates the value of 41 Wm^{-2} evaluated by Gordon and Huber (1990). In August, the production and the melting of ice are almost in equilibrium. The ice pack reaches its maximum of compactness protecting

the ocean from the atmosphere while the ocean mean flux begins to decrease and reaches a new minimum in September. With the beginning of the break-up, the leads open allowing more energy to penetrate into the water column and the mean oceanic flux increases again to melt the ice. During the short summer, the ocean warms and the ocean/atmosphere system reaches equilibrium. Therefore, the heat exchanges between atmosphere and ocean are reduced.

The daily oscillations of the mean oceanic flux, also observable on the cycle reproduced by Scheduikat (1996), are due to the nature of this flux. It could be decomposed in two parts: a flux at the basis of the ice layer and a flux at the interface between ocean and atmosphere when no ice is present. The advection of ice modifies the proportion of both components of the oceanic heat flux and provokes the daily oscillations reinforced, during the freezing season, by the convective adjustment due to salt rejection into the upper ocean layer. Figure 28 also shows the mean oceanic flux computed by the model run in the thermodynamic mode only. This underlines once again the influence of ice divergence on the heat transfers between ocean and atmosphere.

5. OVERALL CONCLUSIONS

It has been shown that the model satisfactorily reproduces the main characteristics of the annual ice pack evolution: the computed ice thickness is in the range of observed values. This model is a useful tool to investigate the separate roles of each parameter influencing the ice formation.

The model still overestimates the ice thickness along the Antarctic Peninsula because the coastal winds are too weak to push offshore the ice produced in this area. This is because the climatological atmospheric forcing fields fail in correctly representing the strong influence of katabatic winds along the coasts of the Antarctic continent. The climatological dataset of Taljaard *et al.* (1969) underestimates the air temperatures responsible for the overestimate of ice production in the Weddell Sea.

The model simulates an evolution of the oceanic mean flux in good agreement with the *in-situ* observations.

As observed, the perennial ice is located along the Antarctic Peninsula and the Filchner-Ronne ice shelf (the southern part of the Weddell Sea).

The general circulation of the Weddell Sea has been successfully reproduced by the model as enhanced by the analysis of the ice movements. Small-scale simulations have been conducted on the Maude Rise region and permitted to show the strong three-dimensional character of the flow around the seamount. Moreover, strong upwelling velocities have been obtained. Hence no direct measurements of the vertical velocity are available, such results are in good agreement with the presence of warmer upwelled water in the vicinity of the Maud Rise.

Different available datasets (T, S, density, ice concentration and thickness, current meter and drifters, etc...), have been used and analysed to produce maps of the Weddell Sea. Data have also been extracted from these datasets to calibrate and validate the sea ice and hydrodynamic models.

Finally, the analysis of the produced map has allowed to identify regions and periods of water vertical motion.

ACKNOWLEDGMENTS

This research has been conducted under grant A4/DD/H01 within the Programme “Scientific Research on the Antarctic-Phase IV” supported by the Belgian State (The Prime Minister’s Services-Scientific, Technical and Cultural Affairs).” The author would like to thank Mr. Benoit Petit who started the research on that project. Dr Gerd Rohardt, from Alfred Wegener Institute for Polar and Marine Research, Bremerhaven, Germany, has kindly provided current meter data of the Weddell Sea

REFERENCES

- Alekseev, G. 1994. The influence of polar oceans on interannual climate variations. *The Polar Oceans and Their Role in Shaping the Global Environment*, Geophysical Monograph 85, AGU, pp. 327-336.
- Arakawa, A. 1972. Design of the UCLA general circulation model. *Numerical Simulation of Weather and Climate*. Dept of Meteorology, Univ. of California, Los Angeles, Tech. Rep., 7.
- Beckmann A., Hellmer H. and Timmermann R.:1999. A numerical model of the Weddell Sea: Large-scale circulation and water mass distribution. *JGR*, 104, c10, pp 23375-23391.
- Bersch, M., Becker G., Frey, H. and Koltermann K., 1992: Topographic effects of the Maud Rise on the stratification and circulation of the Weddell Gyre. *Deep-sea Research*, vol 39,2, pp 303-331.
- Blumberg, A.F and Mellor, G.L.1987 A description of three-dimensional coastal ocean circulation model, in *Three-Dimensional Coastal Ocean Models*, Vol.4, edited by N.Heaps, pp. 208, American Geophysical Union, Washington, D.C.
- Björk, G., 1997. The relation between ice deformation, oceanic heat flux, and the ice thickness distribution in the Arctic Ocean. *Journal of Geophysical Research*, 102: 18,681-18,698.
- Boyer T and Levitus S., 1994. Quality control and processing of historical oceanographic temperature, salinity and oxygen data. NOAA technical report NESDIS 81. U.S Department of Commerce, Washington D.C. 65 pp.
- Colony, R. 1990. Seasonal mean ice motion in the Arctic Basin, *Proceedings of the International Conference on the Role of the Polar Regions in Global Change*, Fairbanks, Alaska.
- Comiso J., and Gordon A., 1987: Recurring Polynyas over the Cosmonaut sea and the Maud Rise. *JGR*, vol, 92 C3, pp 2819-2833.
- Demuth, C. and van Ypersele, J.-P. 1989. Simulations of the annual sea ice cover in the Weddell Sea. In: S. Caschetto (Editor), *Belgian Scientific Research Programme on Antarctica. Scientific Results of Phase One (Oct.85-Jan.89)*. Volume III: glaciology and climatology. Services of the Prime Minister-Science Policy Office.
- Ebert, E.E. and Curry, J.A., 1993. An Intermediate One-Dimensional Thermodynamic Sea Ice Model for Investigating Ice-Atmosphere Interactions. *Journal of Geophysical Research*, 98: 10,085-10,109.
- ECMWF, 2001: Users Guide to ECMWF forecast products, Anders Persson. ECMWF, 105pp.

- ETOPO5. 1998 Data Announcement 88-MGG-02, Digital relief of the Surface of the Earth. NOAA, National Geophysical Data Center, Boulder, Colorado.
- Fichefet, Th. and Gaspar, Ph. 1988. A model study of upper ocean-sea ice interactions. *Journal of Physical Oceanography*, 18: 181-195.
- Fofonoff N. and Millard Jr. 1983, Algorithms for computation of fundamental properties of seawater, UNESCO technical papers in marine science, N°44.
- Gloersen, P., Campbell, W.J., Cavalieri, D.J., Comiso, J.C., Parkinson, C.L and Zwally, H.J. 1992. Arctic and Antarctic Sea Ice, 1978-1987: Satellite Passive-Microwave Observations and Analysis. Scientific and Technical Information Program, NASA SP-511, Washington D.C.
- Gordon, A.L. 1981. Seasonality of Southern Ocean Sea Ice. *Journal of Geophysical Research*, 86: 4193–4197.
- Gordon, A.L., and Baker, T.N. 1982. Objective contouring and grid point data set. *Southern Ocean Atlas*, Columbia Univ. Press, New York.
- Gordon, A.L., Chen C.T.A., and Metcalf W.G. 1984. Winter mixed layer entrainment of Weddell Deep Water. *Journal of Geophysical Research*, 89: 637–640.
- Gordon, A.L. and Huber B.A. 1990. Southern Ocean winter mixed layer. *Journal of Geophysical Research*, 95: 11,655-11,672.
- Gordon, A.L. and Huber B.A. 1995. Warm Weddell Deep Water west of Maud Rise. *Journal of Geophysical Research*, 100: 13,747-13,753.
- Gouretski V.V. and Danilov, A.I., 1993: Weddell Gyre: structure of the eastern boundary. *Deep-Sea Research I*, Vol. 40 pp 561-582
- Hellerman, S. and M. Rosenstein, 1983. Normal monthly wind stress over the world ocean with error estimates. *Journal of Physical Oceanography*, 13, 1,093-1,104.
- Hibler W.D. 1979. A Dynamic Thermodynamic Sea Ice Model. *Journal of Physical Oceanography*, 9: 815-846.
- Hunke E.C and Ackley S.F. A numerical investigation of the 1997-1998 Ronne Polynya. *Journal of Geophysical Research*, 106: 22373-22382
- IFREMER , Scatterometer off-line wind field, series of CD-ROM, IFREMER-CERSAT, FRANCE.
- Jamart, B.M., Milliff, R., Lick, W. and Paul, J. 1982. Numerical studies of the wind driven circulation in the Santa Barbara Channel. Final Report to Exxon Production Research Company, 126 pp.
- Kottmeier, C., Ackley, S., Andreas, E., Crane, D., Hoeber, H., King, J., Launiainen, J., Limbert, D., Martinson, D., Roth, R., Sellmann, L., Wadhams, P., and Vihma, T. 1997.

- Wind, temperature and ice motion statistics in the Weddell Sea. International Programme for Antarctic Buoys (IPAB). January 1997, WMO/TD-N°797, 48 pp.
- Marshunova, M.S. 1966. Principal characteristics of the radiation balance of the underlying surface and the atmosphere in the Arctic. In: Fletcher, J.O., Keller, B. and Olenicoff, S.M. (Editors), Soviet Data on the Arctic Heat Budget and its Climatic Influence., pp. 51-131.
- Mellor G.L. and Yamada T., 1974. A hierarchy of turbulence closure models for planetary boundary layers, *J. Atmos. Sci.*,31, 1791-1896.
- Oberhuber J.M. 1993. The OPYC Ocean General Circulation Model. Deutsches KlimaRechenZentrum, technical report n°7.
- Ocean Modelling Branch (OMB), R. Grumbine, US Department of Commerce, National Ocean and Atmospheric Administration, National Weather Service, National Centers for Environmental Prediction.
- Olbers, D, Gouretski V.,Seib G., Schröter J., 1992. Hydrographic Atlas of the Southern Ocean, Alfred Wegener Institute, Bremerhaven.
- Parkinson, C.L. and Washington, W.M. 1979. A large-scale numerical model of sea ice. *Journal of Geophysical Research*, 84: 311-337.
- Paul, J.F. and Lick, W.J. 1981. A numerical model for three-dimensional variable density hydrodynamics flows. U.S. Environmental Protection Agency Report, 150 pp.
- Petit, B. and Demuth, C. 1993. Sea Ice Circulation in the Weddell Sea. In: S. Caschetto (Editor), Belgian Scientific Research Programme on the Antarctic. Scientific Results of Phase II (10/1988-05/1992). Volume III: glaciology and climatology. Belgian Science Policy Office.
- Petit, B. and Norro A. 1999. Ice Formation and Hydrodynamics of the Weddell Sea, a modelling approach. In: International Offshore and Polar Engineering Conference. Brest, France, May 30-June4,1999.
- Petit, B. and Norro A. 2000. Seasonal evolution of the sea ice and oceanic heat flux in the Weddell Sea. *Journal of Marine Systems* 27, pp 37-52
- Phillips, N.A. 1957, A coordinate system having some special advantages for numerical forecasting, *J.Meteorol.*, 14, 184-185.
- Robertson R., Padman L., and Levine M.D. 1995. Fine structure, microstructure, and vertical mixing processes in the upper ocean in the western Weddell Sea. *Journal of Geophysical Research*, 100: 18,517–18,535.
- Roth R., Schulze O., Thomas M., Rothe T., and Brandt R. 1993. Sea-ice and Climate – an Approach Using Sar Data. Proceedings of the Second ERS-1 Symposium, Hamburg, Germany, 11-14 October 1993, 1: 323-334.

- Scheduikat, M. 1996. A Coupled Sea Ice Model for the Atlantic Sector of the Southern Ocean. Report of the first ACSYS sea-ice/ocean modelling workshop (Hamburg, Germany, 13-15 December 1993). WCRP Informal Report N° 12/1996.
- Schlitzer, R, 1999. Ocean Data View software. <http://www.awi-bremerhaven.de/GEO/ODV>.
- Shine, K.P. 1984. Parameterization of the shortwave flux over high albedo surfaces as a function of cloud thickness and surface albedo. *Quart. J.R. Met. Soc.*, 110: 747-764.
- Semtner, A.J. Jr. 1976. A model for the thermodynamics growth of sea ice in numerical investigations of climate. *J. Phys. Oceanog.*, 6: 379-389.
- Taljaard, J.J., van Loon, H., Crutcher, H.L. & Jenne, R.L. 1969. *Climate of the Upper Air, I, Southern Hemisphere, Vol.1. Temperatures, Dew Points and Heights at Selected Pressure Levels.* NAVAIR 50-1C-55, U.S. Naval Weather Service, Washington, D.C., 135 pp.
- Tomczak M. and Godfrey S, 1994 *Regional Oceanography: an Introduction*, Pergamon, New York, 1994 (422 pages)
- UNESCO, 1983. Algorithms for computation of fundamental properties of seawater. *Unesco technical papers in marine science vol. 44*, 54 pp.
- Van Loon, H. 1972. Cloudiness and precipitation in the Southern Hemisphere. In: *Meteorology of Southern Hemisphere, Meteor. Monogr. 13*, American Meteorological Society, Boston.
- Wadhams, P., Lange M.A., and Ackley S.F. 1987. The Ice Thickness Distribution across the Atlantic Sector of the Antarctic Ocean in Midwinter. *Journal of Geophysical Research*, 92: 14,535–14,552.
- World Ocean Atlas, US Department of Commerce, National Ocean and Atmospheric Administration, National Environmental Satellite, Data and Information Services, National Oceanographic Data Center, Ocean Climate Laboratory, World Data Center-A for Oceanography.
- Zwally, H.J., Comiso, J.C, Parkinson, C.L., Campbell, W.J., Carsey, F.D., and Gloersen, P. 1983. *Antarctic Sea Ice 1973-1976: Satellite Passive-Microwave Observations.* NASA SP-459, Washington D.C., 206 pp.

RESEARCH CONTRACT N° A4/DD/E01

**Mass balance of the Antarctic ice cap
(a contribution to EPICA)**

by

Jaya Naithani¹, Hubert Gallée², Alexis Dutrieux¹,
and Guy Schayes¹

¹ UCL, Institut d'Astronomie et de Géophysique Georges Lemaître,
Chemin du Cyclotron 2, B-1348 Louvain-la-Neuve, Belgique

² Institut de Recherches pour le Développement, LTHE, BP 53,
F-38041 Grenoble Cedex 9, France

CONTENTS

PREFACE

ABSTRACT.....	1
---------------	---

CHAPTER 1

Marine air intrusion.....	1
---------------------------	---

1.1. INTRODUCTION	2
-------------------------	---

1.2. MODEL DESCRIPTION	4
------------------------------	---

1.2.1. MAR moist physics	5
--------------------------------	---

1.3.3.2. MAR boundary conditions.....	5
---------------------------------------	---

1.3. RESULTS OF SIMULATIONS	5
-----------------------------------	---

1.3.1. Long Term Simulations.....	6
-----------------------------------	---

1.3.2. Grid Point Studies	11
---------------------------------	----

1.3.3. Marine Intrusion Episodes	16
--	----

1.3.3.1. First Week of SOP1.....	16
----------------------------------	----

1.3.3.2. Last Week of SOP1	19
----------------------------------	----

1.3.3.3. Episodes of SOP3	21
---------------------------------	----

1.4. DISCUSSION AND CONCLUSIONS.....	23
--------------------------------------	----

ACKNOWLEDGEMENTS.....	28
-----------------------	----

REFERENCES.....	28
-----------------	----

CHAPTER 2

Strong wind events.....	34
-------------------------	----

2.1. INTRODUCTION	35
-------------------------	----

2.2. OBSERVATIONS	39
2.2.1. Time Series	39
2.2.2. Synoptic Patterns	42
2.2.2.1. 11-17 April 1993	42
2.2.2.2. 6-16 May 1993	44
2.2.2.3. 8-18 July 1993	46
2.2.2.4. 17-22 September 1993	49
2.2.2.5. 1-8 November 1993	50
2.2.2.6. 6-18 December 1993	52
2.2.2.7. 1-11 July 1994	54
2.2.2.8. 25-30 July 1994	56
2.2.2.9. 17-22 September 1995	57
2.2.2.10. 1-10 December 1999	59
DISCUSSIONS AND CONCLUSION	59
ACKNOWLEDGEMENTS	64
REFERENCES	64

PREFACE

This report is divided into two chapters. The first chapter describes the work done during the period from February to November 2000, while the second chapter describes the work done during the extension period, i.e., from december 2000 to May 2001. Both these works have been submitted for publication to the Journal of Geophysical Research. The first one has been accepted and has been submitted in the revised form.

Chapter 1

MARINE AIR INTRUSION

Marine air intrusion and subsequent cloud formation plays a dominant role in the energy budget and mass balance of the Antarctic. However, the intrusion is very difficult to understand using the ground-based measurements alone. In this paper we present simulations of marine air intrusion into the Adelie land, East Antarctica, using the Modèle Atmosphérique Régional (MAR), for July 1994 and January 1995. The model is nested into the ECMWF analyses. The simulations show a strong influence of large-scale disturbances, over the ocean, which helped in the penetration of marine air into the interior and the formation of clouds. Each marine air intrusion episode resulted in cloud formation in July 1994. Blocking anticyclones have also been found to be responsible for much of the moisture transport far into the interior elevated locations. MAR simulations, as well as ECMWF analyses, show influence of cyclones in strengthening and prolonging the surface layer flow. The study also indicated that the influence of depressions on surface winds is pronounced during the period when the depression is approaching the Adelie Land coast.

1.1. Introduction

Marine air intrusion into the Antarctic interior cannot be discussed or introduced without discussing transient eddies or cyclones. The topography of the continent is such that it acts like a barrier to any local penetration. This is particularly true for East Antarctica, where coastal slopes are of the order of 10^{-1} to 10^{-2} . Cyclones can be regarded as forces helping the air mass to rise against topography and penetrate inland. Advection of warm marine air is the only source of moisture into the continent and is very important for the mass balance of the Antarctic ice sheet. Connolley and King [1993] reported that the main contribution to water vapour into the continent is provided by transient eddies. Clouds in the coastal region are associated with major low-pressure systems [Schwerdtfeger, 1984; King and Turner, 1997]. Warm air masses advected by cyclones into the interior of the continent encounter topography, rise adiabatically (due to elevation), cool, condense and result in cloud formation, and often, precipitation in the coastal regions. Extratropical cyclones also advect cloud cover ahead of them as they track eastward. The presence of clouds greatly effects the reflected radiation of the atmosphere. In summer their main impact is to decrease the short wave radiation coming to earth, while in winter, when the solar radiation is not there, they reflect the long wave radiation back to earth, and, therefore, result in temporary heating near the surface. This heating occasionally destroys inversions. The rise in temperature is more pronounced in winter months than in summer. Thus, clouds play an important role, besides inversions and katabatic winds, in the radiation budget of the Antarctic boundary layer, in addition to their significant role in precipitation and mass budget of the continent.

Webster and Stephens [1984] underlined the influence of clouds on key quantities such as earth radiation budget, the heating of the ocean, and the diabatic heating of the atmosphere; they concluded that of all climate parameters, clouds have the largest possible effect on the radiation field. Stone et al. [1989] studied the short-term variation in the surface radiation balance and temperature associated with cloudiness at the South Pole. They reported that clouds tend to heat the surface in snow covered polar regions and the heating increases monotonically with increasing cloud cover and/or cloud optical depth. Ramanathan et al. [1989] presented satellite-based remote-sensing results from the Earth Radiation Budget Experiment, showing that, whereas clouds generally have a net cooling effect on the surface of the earth, they contribute to anomalous surface warming in

high-latitude snow-covered regions. According to them the radiative forcing due to clouds potentially far exceeds that due to gaseous green house warming. Even small changes in the frequency, type or spatial distribution of clouds result in significant climate change on a regional scale [Stone and Kahl, 1991]. Neff [1981] emphasized that the energy balance of the South Polar Plateau depends critically on the structure of the surface temperature inversion and its control by synoptic scale processes.

In coastal regions near 70S, clouds occur throughout the year with little variability and only small decrease during winter months [King and Turner, 1997]. This might be due to the formation of sea ice, which reduces the flux of moisture inland and, to the reduced cyclonic activity in winter [van Loon, 1967]. It is easier and natural for the moist air to penetrate far inland during summer when there is no sea ice and the warmer ocean is nearby. In winter, it should be more difficult as the sea ice is almost up to its maximum extent and the open sea is far north from the continent. The warm marine air moving southwards towards the continent gets cooled while travelling over the sea ice. Therefore, this air is cold to rise adiabatically in winter months. For the marine air to reach the continent and to penetrate far inland against the ice-slopes, the operating mechanism has to be strong to advect the air across the sea-ice into the interior so that the travel time of the warm air over the sea-ice is less. As we go into the interior, the amount of cloud cover decreases. Most of the cloud formation is due to transient eddies, and as these eddies cannot penetrate far inland, the amount of cloud cover in the interior is very low. However, some well-organized depressions do penetrate far into the interior even in winter months [Neal, 1972; King and Turner, 1997; Pook and Cowled, 1999]. Synoptically quiet or high-pressure situations also can cause clouds and precipitation in the coastal region [page 111, King and Turner, 1997; Turner et al., 1995].

The motivation of this paper is to understand the mechanism behind marine air intrusions into the Antarctic interior. In this study we present observations and simulations of marine air intrusions using the Modèle Atmosphérique Régional (MAR) [Gallée and Schayes, 1994 ; Gallée, 1995], over the Adelie Land quadrant of east Antarctica. Analyses of the European Center of Medium-range Weather Forecasts [ECMWF] are used to initialize the model and force its lateral boundaries. For this study we have used July 1994, 15 October to 15 November, 1994 and, January 1995, representing three Special Observing Periods (SOPs) of the Antarctic First Regional Observing Study of the Troposphere (FROST)

project [Turner et al., 1996]. Details of the FROST project and earlier work done can be found in Turner et al. [1996] and in the special issue on FROST project in *Weather and Forecasting*, volume 14, December 1999. Estimation of 500-hPa geopotential heights from station-level observations of pressure and temperature using Phillpot [1991] technique were also a part of the FROST project and have been included in the analyses. This work started with the objective to utilize the comprehensive datasets assembled during the three SOPs. Out of three SOPs, the first SOP showed two very interesting examples of marine air intrusion, more pronounced than the other SOPs. Both cases took place with different synoptic conditions. In this work, we present simulations from the first and last SOP, i.e., SOP1 and SOP3, representing winter and summer months, respectively.

1.2. Model Description

In this study we present simulations using MAR (Modèle Atmosphérique Régional). MAR is a hydrostatic, primitive equation model. Model details can be found in Gallée and Schayes, [1994] and Gallée, [1995]. However, a brief description is given here and in the following sub-sections. In the present version, the model uses 30 sigma levels to represent the vertical structure of the atmosphere ($\sigma = 0.998, 0.997, 0.994, 0.990, 0.980, 0.963, 0.933, 0.886, 0.821, 0.744, 0.667, 0.600, 0.544, 0.497, 0.456, 0.420, 0.385, 0.352, 0.319, 0.287, 0.255, 0.224, 0.194, 0.165, 0.137, 0.111, 0.088, 0.067, 0.048, 0.0321$). The lowest sigma level is approximately 10 m above the surface and the top level is at 0.1 hPa. In the top six sigma levels, horizontal diffusion is more pronounced so as to damp the waves horizontally, i.e. to smooth the vertically propagating gravity waves. This is introduced as an extra term in the horizontal eddy exchange coefficient for the upper levels. This viscous damping layer minimizes the reflection from upper boundary. MAR has been used for studies of the Antarctic atmosphere [Gallée and Schayes, 1994; Gallée, 1995; Gallée, 1996; Gallée et al., 1996]. In previous studies MAR was initialized using soundings. In the present work it is initialized from ECMWF fields for Antarctica [Brasseur, 2001]. High resolution limited area models nested within large scale models have been successfully used for climate studies [Giorgi et al., 1993a,b; Walsh and McGregor, 1996]. The present study will determine the capability of MAR as a nested version in simulating the Antarctic atmosphere.

ECMWF analyses have been used to initialize lateral boundaries of the model. Boundary conditions are updated every 6 hours from ECMWF analyses and interpolated in each direction using a bicubic horizontal interpolation. The horizontal resolution used in MAR is 40 km by 40 km.

1.2.1. MAR moist physics

The hydrological cycle includes a cloud microphysical model, with conservation equations for cloud droplet, raindrop, cloud ice crystal and snowflake concentrations. Blowing snow particles are considered as snowflakes. The representation of the cloud microphysical processes is essentially based on the Kessler [1969] parameterization. In particular, the sublimation of snowflakes is a function of relative humidity of the air, according to Lin et al. [1983, their relation (13) p.1072].

1.2.2. MAR boundary conditions

The temperature, specific humidity, horizontal wind speed and surface pressure at the lateral boundaries of MAR are specified from the analyses. Furthermore MAR variables are relaxed towards the analyses over 5 grid points near the lateral boundaries, using both Newtonian and diffusive relaxation [see e.g., Davies, 1983]. Sea Surface Temperatures (SST) are prescribed from the analyses. Sea ice is assumed in each grid point where the SST is lower than the seawater freezing temperature (271.2K).

1.3. Results of simulations

In this section model output and ECMWF analyses for SOP1 and SOP3, i.e. July 1994 and January 1995 are presented. Figure 1 shows the model domain. The height contours are drawn at 500 m intervals. From the figure it is clear that the model is able to resolve topographical details of the continent to a good approximation. The model domain includes the sea-ice, the nearby ocean and the part of the continent from where winds originate, all at sufficient distance from the domain boundaries. This consideration ensures that the simulation of cyclones and katabatic winds are unbiased from large scale boundary forcings, which are provided at the boundaries and slowly relaxed inwards up to 5 grid points (whereafter, inwards actual model simulation prevails). We will first present the main results of the two one month long simulations (the two SOPs) to show the model's ability to

simulate the circumpolar trough correctly. Later, we will concentrate on the periods exhibiting marine air intrusion.

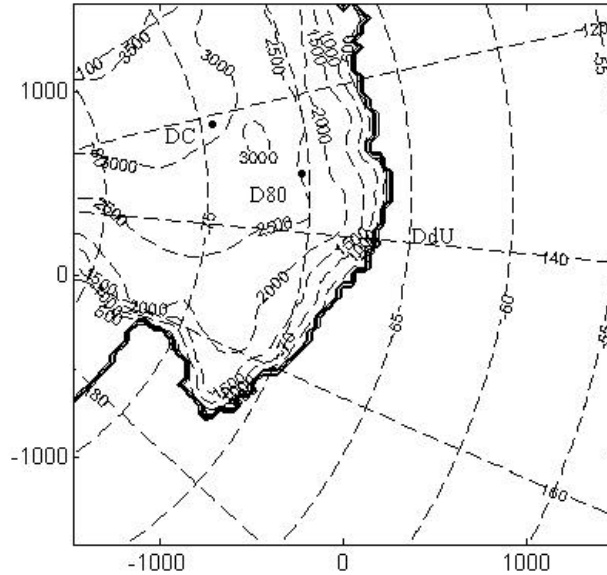


Figure1. Model domain showing the height contours and three grid points discussed in the text.

1.3.1. Long term simulations

Figures 2-3 show the time averaged 500 hPa level geopotential height and mean sea level pressure (MSLP) fields for the model simulations and the difference between the simulated and analyzed MSLP fields, for SOP1 and SOP3, respectively. Results are plotted over the model domain shown in Figure 1. 500 hPa geopotential gradients are weak over the continent as compared to over the ocean in both SOPs (Figures 2a, 3a). Difference between the simulated and analyzed heights are largest along the coastline of the Ross Ice Shelf in both SOPs (Figures 2b, 3b), where the model has underestimated the magnitudes. Nevertheless, the difference does not exceed 65 m. Similar under-prediction of 60 m has been reported by Hines et al. [1995] for the June 1998 averaged 500 hPa simulation by MM4 model. The 500 hPa heights are well represented in the rest of the domain, the difference never exceeding 20 m. Coming to the MSLP plots (Figures 2c, 3c), the circumpolar trough is well represented by MAR. The MSLP has been overpredicted in simulations by 4 hPa over the ocean in both SOPs (Figures 2d, 3d). The maximum overprediction by MAR is in the interior near the coast, being 10 hPa and 4 hPa for SOP1

and SOP3, respectively. The MSLP is underpredicted by MAR over the coastline along the Ross Ice Shelf.

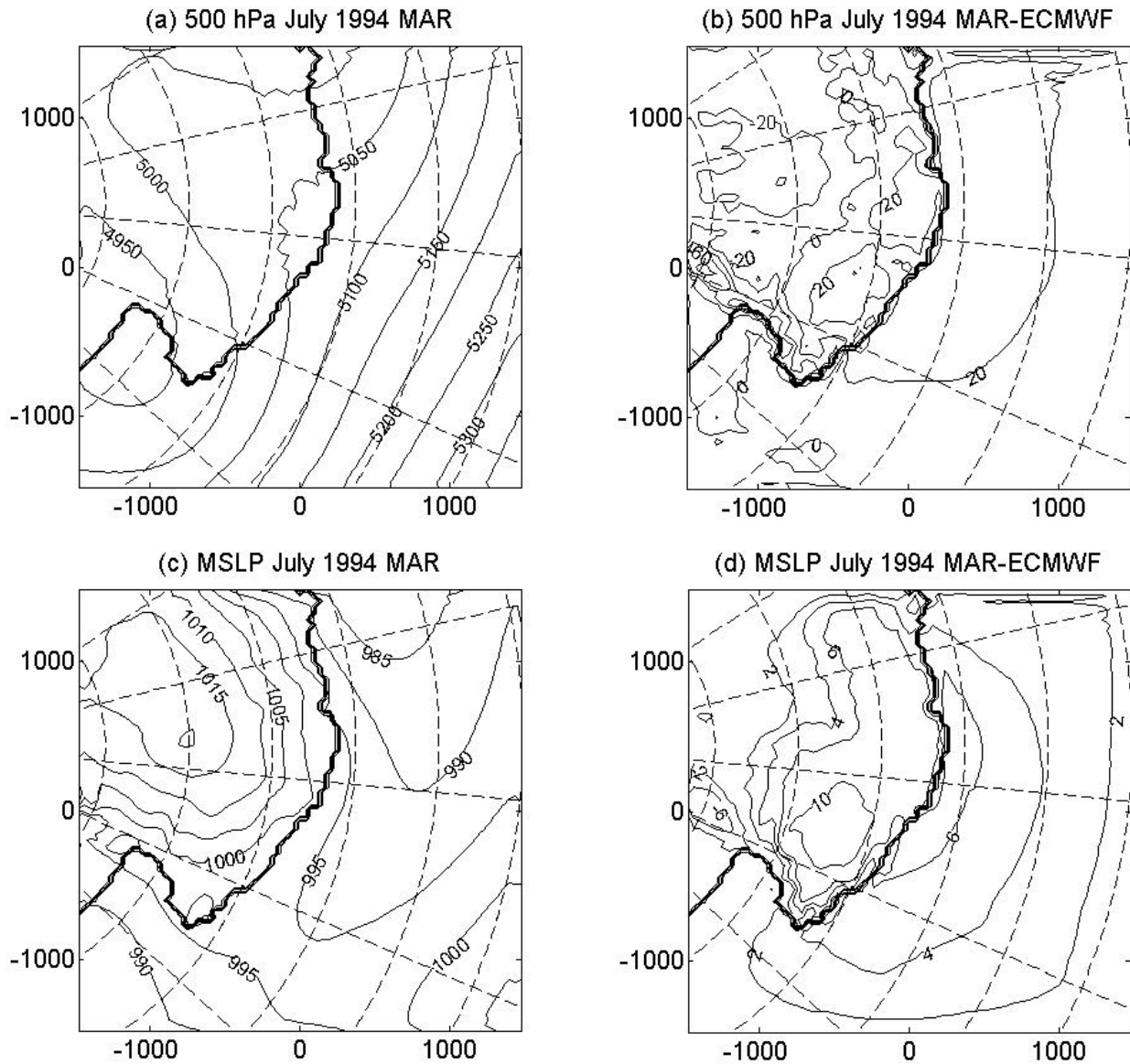


Figure 2. Time averaged 500 hPa height and MSLP fields simulated by MAR and the difference between MAR and ECMWF fields for July 1994.

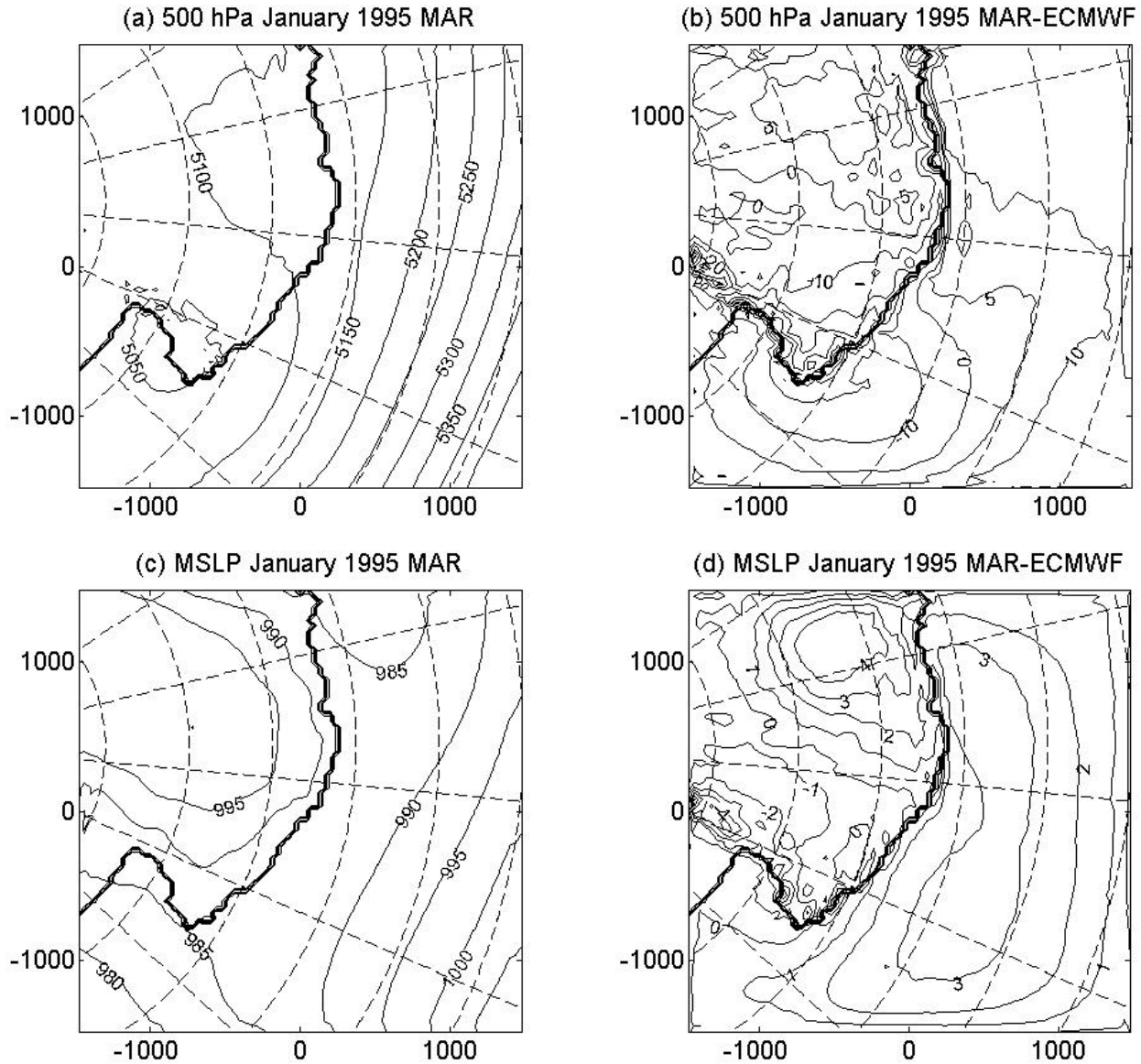


Figure 3. Same as in Figure 2 for January 1995.

Figures 4 and 5 present the temperature and horizontal wind, time averaged over SOP1 and SOP3, respectively, for the lowest model sigma level. Temperatures are overpredicted by MAR in the interior by 6 degrees in July 1994 (Figure 4b) and underpredicted over the Ross Ice Shelf area by 6 degrees. Temperatures are similar to the ECMWF data over the rest of the continent. In January 1995, the positive bias in temperature is 2 degrees (Figure 5b). A negative bias exists along much of the coastline, being a maximum (-5 degrees) over the Ross Ice Shelf coastline. Over the ocean the simulated values are similar to the

analyses. MAR simulated wind speeds are maximum along the coastline (Figures 4c, 5c), which is as expected since the ice slopes are maximum there. The wind speeds are similar for both SOPs over much of the domain (Figures 4d, 5d). The difference in wind speeds between MAR and ECMWF is noticeable only along the coastline, being maximum along the Ross Ice Shelf coast. Surface winds along the coastal area, especially along the Victoria land coast, are underestimated by ECMWF.

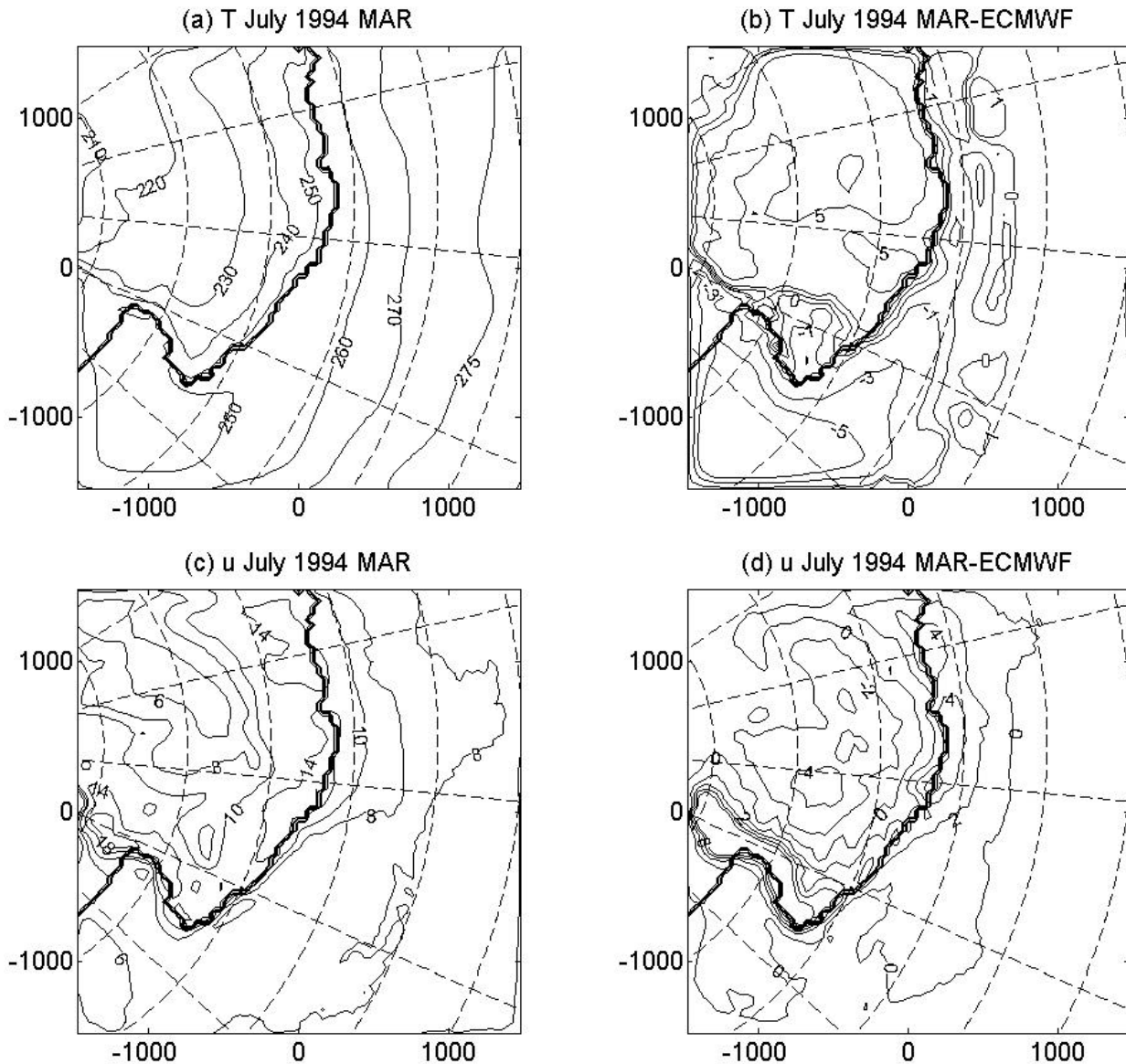


Figure 4. Temperature and wind fields for the first model sigma level averaged over July 1994, MAR simulated and the difference between MAR and ECMWF fields.

From Figures 2-5, we see the high negative bias in 500 hPa, MSLP and temperature fields and a high positive bias in wind speeds between MAR and ECMWF fields over the coastline along the Ross Ice Shelf. Table 1 gives the mean monthly averaged meteorological parameters for Enigma Lake (EL, 74.43S; 164.02E; 210m asl) and Cape Philips (CP, 73.03S; 169.36E; 550m asl) sites over the Ross Ice Shelf. MAR grid points for

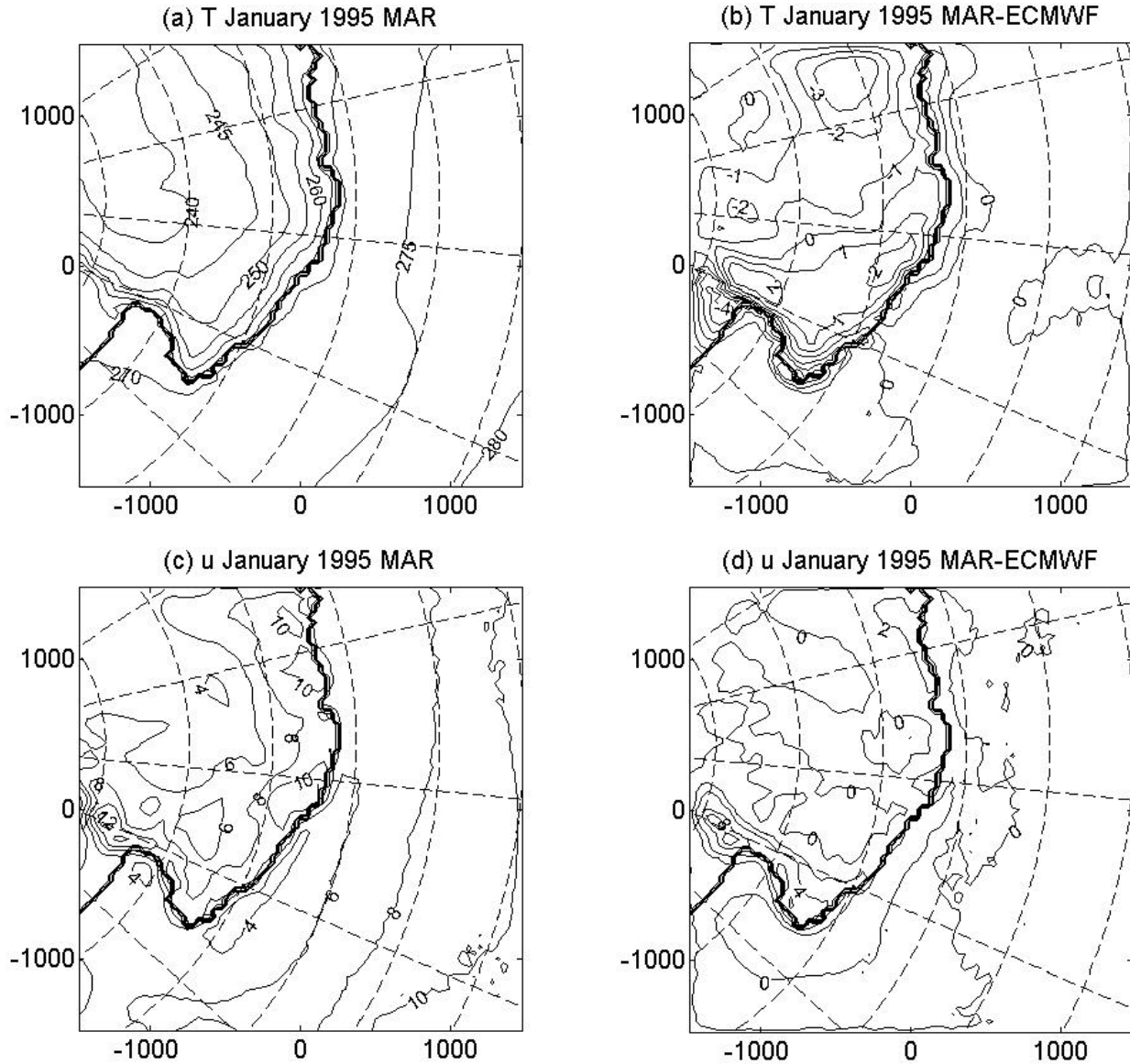


Figure 5. Same as in Figure 4 for January 1995.

these sites are (74.7S; 164.1E; 234m asl) and (72.5S; 169.8E; 569m asl), respectively, making them 31 m and 26 m above the actual elevation, respectively. Average monthly

pressures are similar for both MAR and ECMWF for July 1994 and differ by a maximum of 4 hPa from observations. For January 1995, average pressure predicted by MAR is less than about 3 hPa compared to ECMWF for both sites. Temperature values are underestimated compared to observations by MAR and ECMWF for both SOPs and for both sites. MAR simulated average winds are higher as compared to ECMWF, which predicts extremely low winds at both sites. However, MAR simulated winds are closer to observations for both SOPs. In general, MAR simulations for July 1994 are closer to observations than ECMWF ones.

In the above discussion and Figure 2-5, we see that MAR is able to simulate the synoptic situation and other parameters to a fairly accurate approximation. In the following we will be discussing data obtained from grid points closest to Dumont d'Urville (DdU, 67.7S; 140E; 40 m asl), D80 (70.2S; 134.72E; 2500 m asl) and Dome C (74.5S; 123E; 3280 m asl). The corresponding grid point locations in MAR domain for DdU are 66.4S; 140.7E; 49 m asl, for D80 are 70.01S; 134.4E; 2500 m asl and for Dome C are 74.5S; 122.3E; 3042 m asl. This makes DdU and D80 grid points in MAR, 9 and 7 m above the observational sites, respectively, while the model grid point for Dome C is 228 m below the observational site. These sites are marked on Figure 1. These three stations are chosen as they represent the main direction of the surface layer flow in the Adelie land. Surface winds at DdU mainly originate at Dome C and pass through D80.

1.3.2. Grid point studies

Figure 6 shows MAR simulated, ECMWF analyzed and observed time series of meteorological parameters for DdU and D80 for the two SOPs. While looking into the data and making comparison it should be kept in mind that model grid points, best representing DdU and D80, represent an average for 40 km by 40 km grid box. Results should, therefore, not be expected to be exactly similar to observations. The differences in elevation between the model grid points and the actual observation sites, however, are 9 m for DdU and 7 m for D80. It should be kept in mind that ECMWF analyses are constrained by the radiosonde observations at DdU and can thus be considered as representing the actual conditions at DdU. For both SOPs Dome C results are different. This might be due to large difference in elevation (228 m) between the actual location and model grid point (Dome C results are not shown here). For the first SOP, all three data

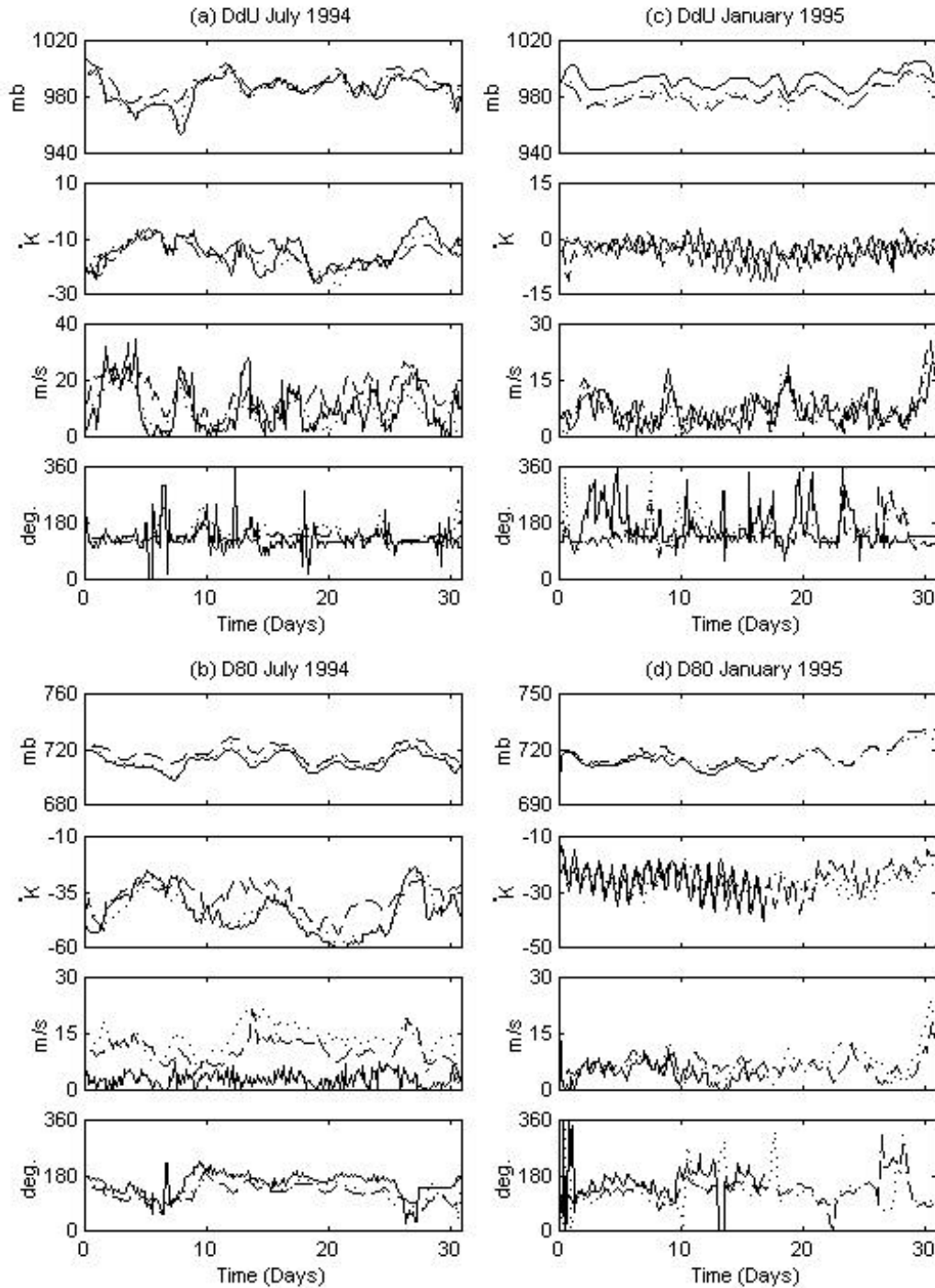


Figure 6. Time series of meteorological parameters for DdU and D80 for July 1994 and January 1995. Observations (solid line), MAR (dashed line) and ECMWF (dotted line).

types (observations, simulations and analyses) show a good correlation except that for D80 and Dome C grid points, ECMWF and MAR overestimate winds in comparison to

observations. For SOP3, time series of MAR simulation and ECMWF analyses match very well with observations except that pressure values are overestimated for DdU and Dome C. For D80, observations are available only up to 17 January 1995.

For SOP1, time series of temperature for all stations show episodes, where a temperature increase of up to 20°C is observed within two-three days. This temperature anomaly is observed in all three stations, being maximum in DdU. The diurnal temperature cycle is underestimated by MAR. The temperature anomaly in the last week of July 1994 builds up gradually for DdU, while for D80 and Dome C the temperature increase is abrupt. The increase in temperature in July 1994 is associated with high winds during the same period, and can be explained by the vertical mixing provided by strong winds between the cold boundary layer air and the warm free atmospheric air. In January 1995, winds along with the temperature depict a diurnal variation. This variation in wind is broken during the passage of low pressure systems. The effect can also be seen in the temperature cycle. In both SOPs, each depression is preceded closely by a high pressure ridge. This high pressure allows strong surface inversions to form and helps in forming cold air supplies feeding the gravity flow during the passage of the depression for longer duration and greater intensity [Murphy, 2000].

Figures 7 - 9 present the time-height variation of wind speed, specific humidity (g/kg) and clouds (g/kg) for two SOPs. Clouds are represented as the sum of ice water and liquid water content. Time-height plots give an idea of the temporal and spatial evolution of the phenomena in each station. Relative magnitudes of each episode in each parameter between stations should be looked upon considering the distance of the station from the sea and their elevation above sea level. The sea ice extent is approximately up to 63S in July 1994, which was similar to the maximum extent in September 1994. The sea-ice extent made the sites further away from the open ocean. Sea-ice continued to extend to an average of 63S between 145E and 170S and a polynya (open water) existed in the Ross Ice Shelf area in January 1995.

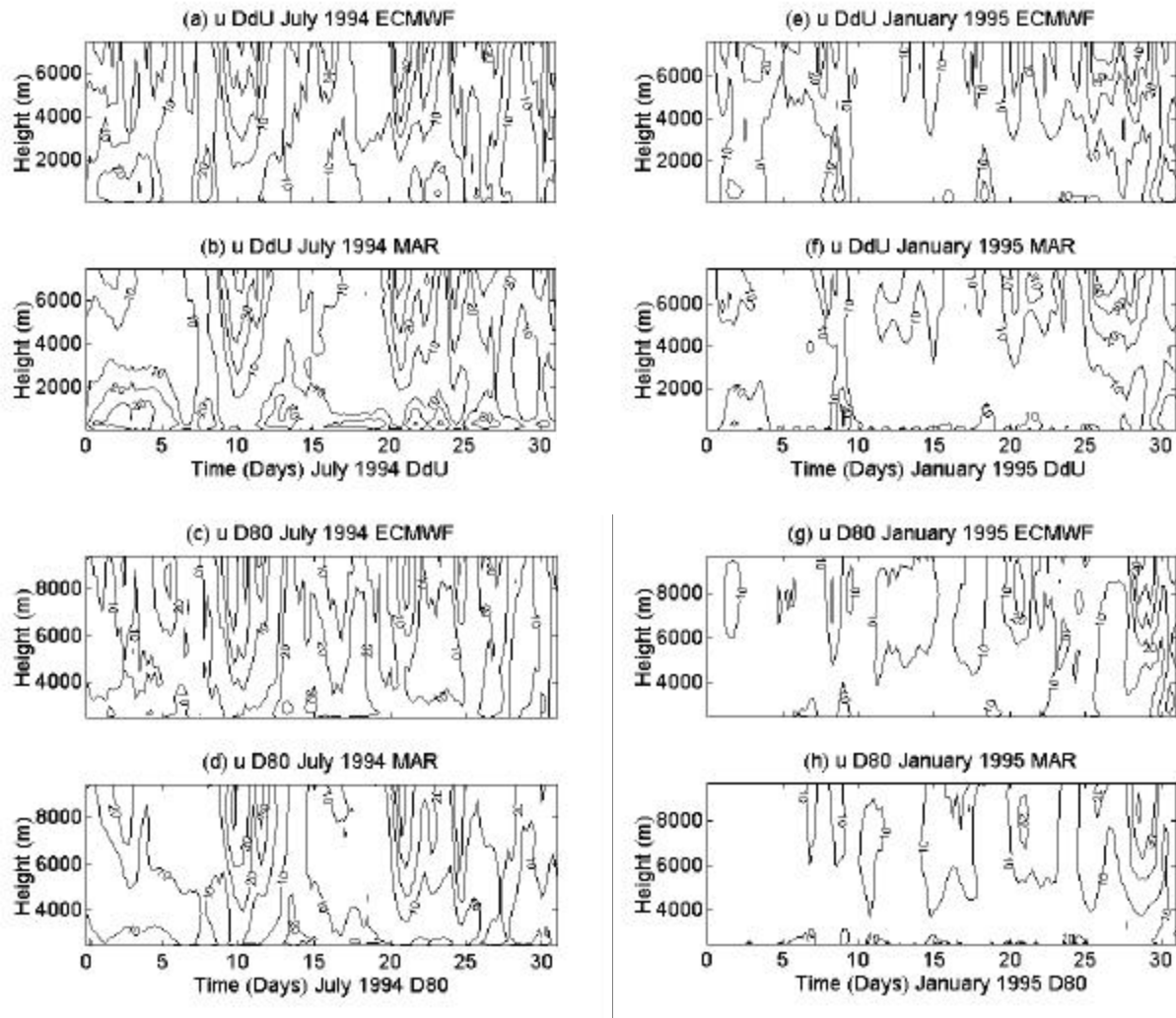


Figure 7. Time height plots of horizontal wind for DdU and D80 for July 1994 and January 1995. (results for first 18 sigma levels are plotted).

Time height plots of MAR simulations for all sites show a good similarity with ECMWF analyses. To see marine intrusion episodes, specific humidity and cloud time-height plots present a good indication. Various episodes of cold air outbreak (Figure 7) and warm air intrusion (Figure 8-9) are well represented by MAR. The magnitude of each episode is either overestimated or underestimated a little by MAR in comparison to ECMWF analyses. In case of a cold air outbreak, MAR magnitudes are overestimated for DdU in July 1994 (Figure 7b), while marine intrusion magnitudes (high humidity episodes) are slightly underestimated for both grid points and for both SOPs (Figure 8). Nevertheless, each episode is clearly identified by MAR. Of notice is the presence of clouds each time an intrusion took place (Figure 9). This is particularly visible in SOP1 (Figures 9a, 9b), where

each small marine air intrusion episode in time and space domain is able to cause cloud formation. In the case of SOP3 (Figures 9c, 9d), episodes of marine air intrusion are not able to cause cloud formation as effectively as during July 1994 episodes.

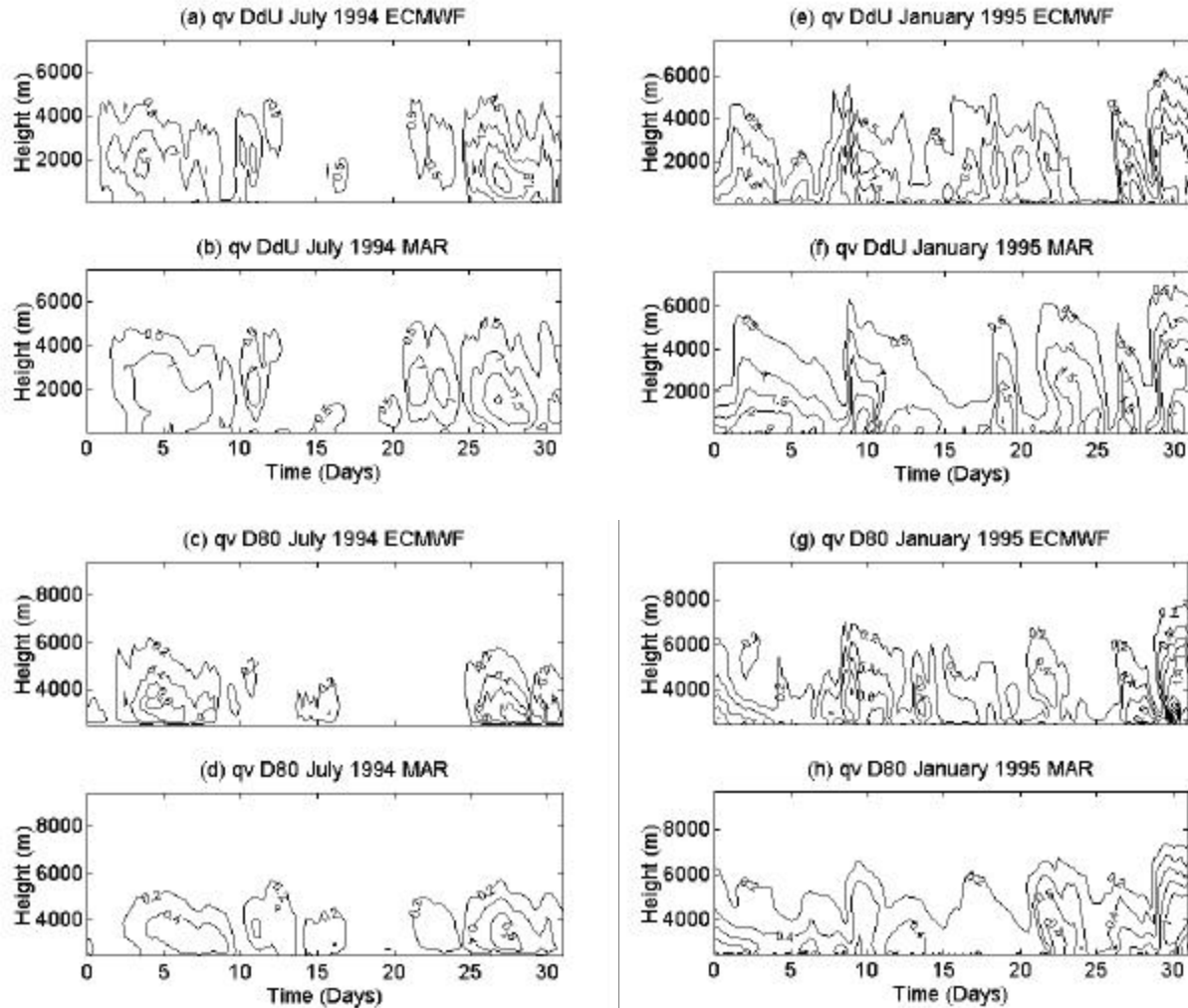


Figure 8. Same as in Figure 7 for specific humidity (g/kg).

In the time series plots (Figures 6-9) we notice certain distinct locations in time, where cold air outbreak and warm air intrusion episodes took place. From time-height plots it is clear that the warming shown by time series of temperature in July 1994 in Figure 6, is due to the combined influence of the vertical mixing provided by strong winds, warm marine air intrusions and the subsequent heating provided by clouds. For instance the first and last week of July 1994 show distinct episodes of marine air intrusion. Similarly, there are some events of marine air intrusions in SOP3; around 3, 10 and 30 January 1995. In the

following section we will focus on two warming/intrusion episodes which occurred in the first and the last week of July 1994, and, three episodes of SOP3. We will see later that synoptic situations in both episodes of SOP1 are totally different.

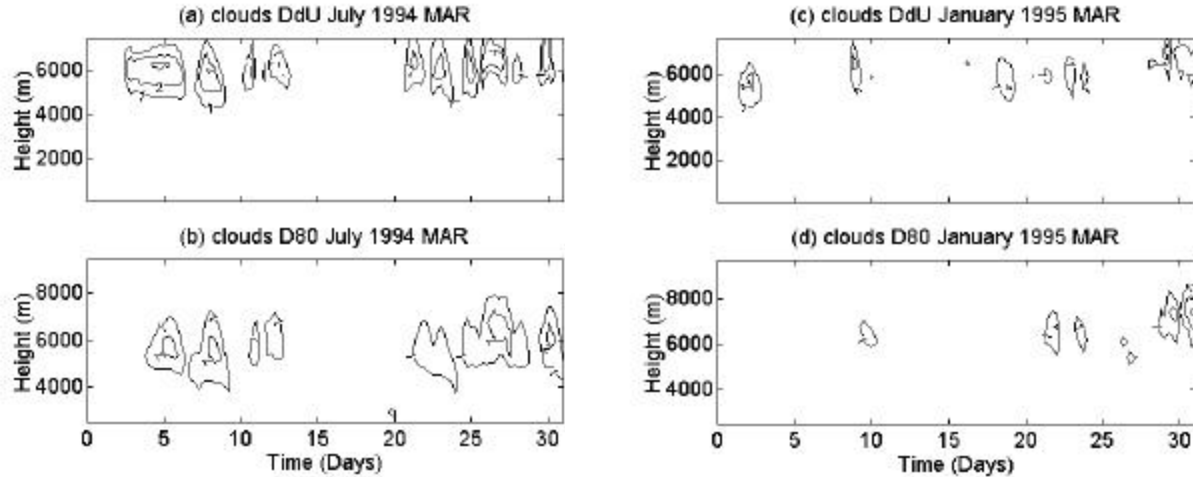


Figure 9. Time height plots of MAR simulated clouds for DdU and D80 for July 1994 and January 1995, respectively. (results for first 18 sigma levels are plotted).

1.3.3. Marine Intrusion Episodes

1.3.3.1. First week of SOP1

Figure 10 shows the composite of MSLP fields and cloud optical depth (OD, g/m^3) simulated by MAR for 2, 4 and 5 July 1994, respectively. Wind vectors are plotted at the first sigma level, i.e., 10 m above the surface. Results are plotted over the model domain. The scale for the optical depth is kept similar for all plots to allow comparison between episodes and seasons.

On 2 July 1994, a low pressure trough influenced the coast. Surface winds increased on 2 July 1994 due to the presence of this small depression near the DdU coast. Strong winds were observed for almost three days. This small depression merged with the main depression after 3 July 1994 and together they helped in the persistence of strong winds.

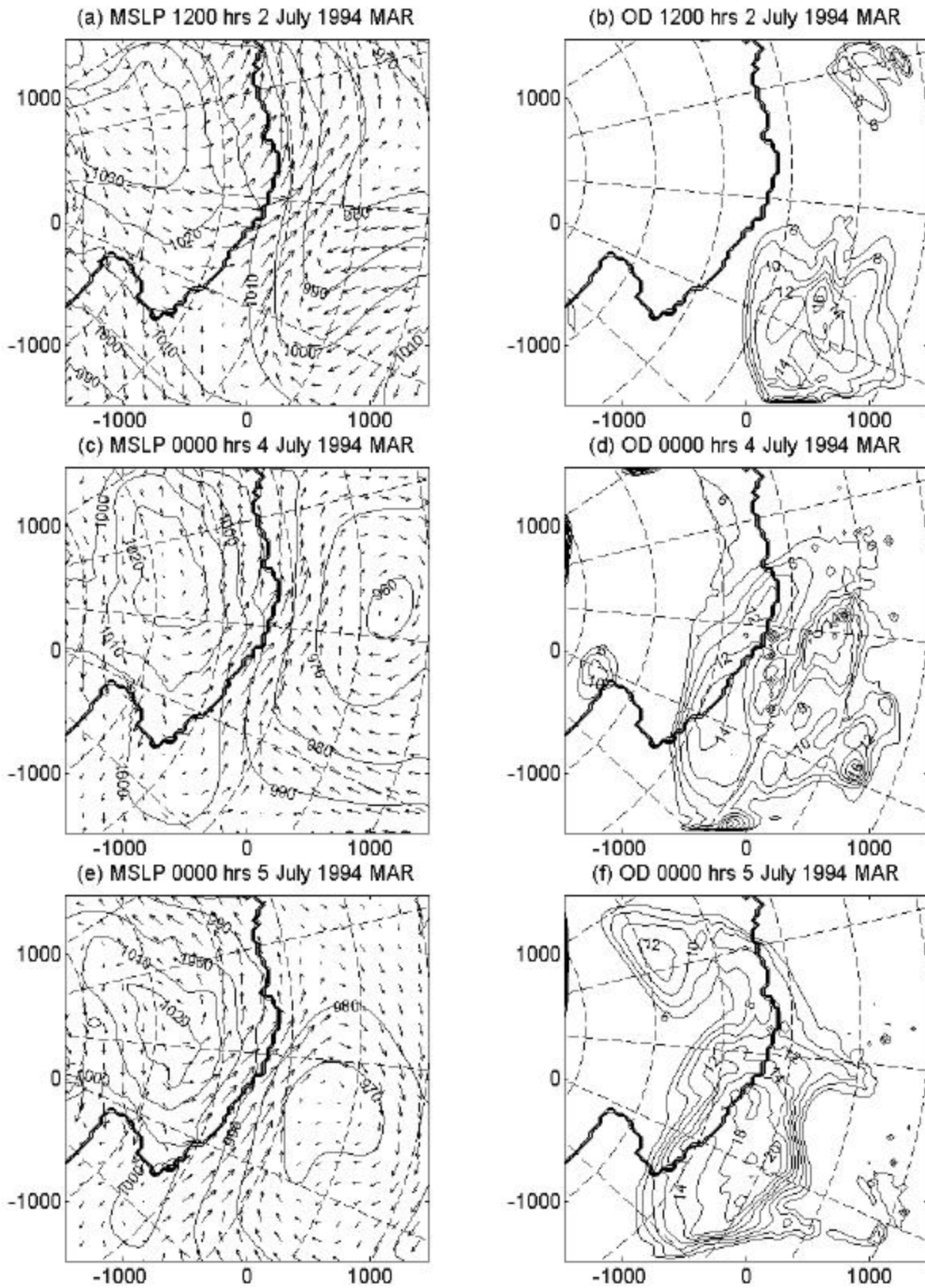


Figure 10. MSLP charts and cloud optical depth simulated by MAR for 2, 4 and 5 July 1994.

The system moved past the DdU site after 5 July 1994. This indicates the influence of cyclones in strengthening the already existing downslope winds by increasing the pressure

gradient between the continent and the coast. During this episode (Figures 7a-7d), first the cold air outbreak took place and then the warm air penetrated. From time height plots (Figures 7a-7d and Figures 8a-8d), we notice that initially the wind was high and the moisture penetration took place above the boundary layer. At the same time a cloud appeared above DdU around 2 July (Figure 10b), which slowly penetrated inland and a little later appeared over D80 (Figures 9a, 9b and 10d) and, finally, on 5 July clouds appeared over DC (Figure 10f). Figures 11a, 11b presents the composite infra-red satellite

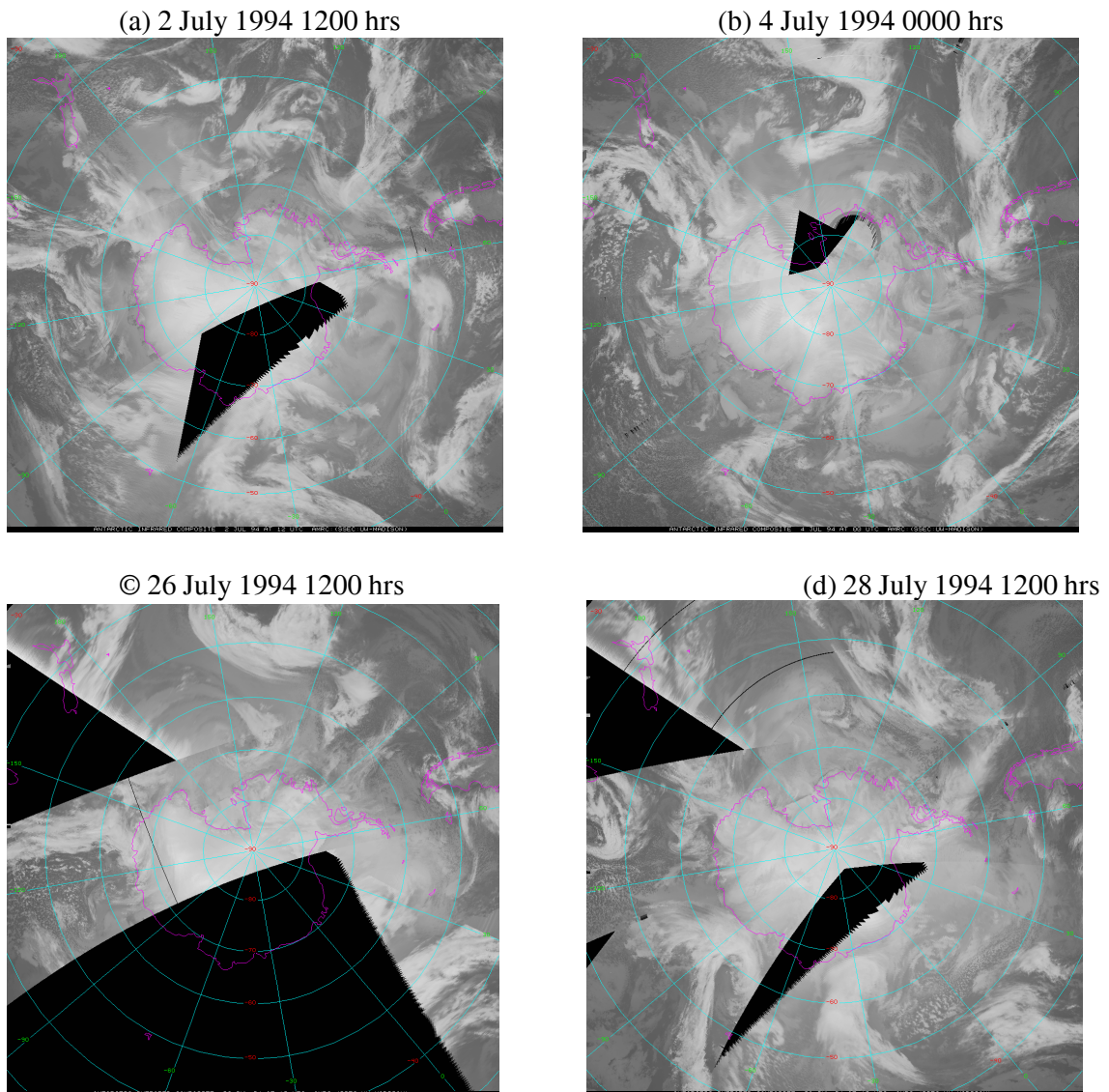


Figure 11. Composite infra-red satellite images for two episodes of July 1994. (Courtesy of the University of Wisconsin-Madison.)

images for 2 and 4 July 1994 on which clouds can be seen advected by the depression. The clouds predicted by MAR in Figures 10b and 10d are similar to those in satellite images. Due to the vertical mixing provided by strong winds, between cold boundary layer air and the warm free atmospheric air, warming took place near the surface. Warming is in part also due to warm air advection and clouds. Presence of clouds increased the long wave radiation back to the surface, resulting in an increase in surface temperature. With the combined effect, the surface temperature rose noticeably, inversions were destroyed and, finally, winds ceased on 5 July 1994. Cessation of winds are also due to the building up of pressure over the Adelie land coast, after the passage of the depression to the east of it.

1.3.3.2. Last week of SOP1

Around 26 July, the wind speed was high over the whole depth of the troposphere (Figures 7a-7d). Figure 12 shows the composite of MSLP fields and the cloud optical depth simulated by MAR for 26 and 27 July 1994, respectively. During this episode the unusual feature which added to the influence of the depression and the high pressure system over the interior, is the presence of an anticyclone to the northeast of Adelie land (Figures 12a and 12c). This high pressure system remained stationary for some time and provided a blocking to the usual eastward motion of the depression to the west of DdU. Due to this blocking anticyclone, the movement of the cyclone was reduced, it intensified and started to penetrate inland. Pressure charts show a high pressure ridge that builds up significantly diagonally over the center of the domain, extending from the NE of the domain, from the high pressure over the ocean, onto the SE into the interior of the continent. Looking into the pressure chart for 27 July 1994, the wind is moving from the high over the ocean situated towards the northeast of DdU to the low situated over the northwest of it, and is continuing into the continent. The penetration of warm marine air into the interior along the ridge caused thick clouds to form during 26 – 28 July 1994. The optical thickness plot for 26 and 27 July 1994 (Figures 12b and 12d) show two maxima around 120E in the interior on the continent (latitude and longitude over the domain are presented in Figure 1). These maxima correspond approximately to two small systems which penetrated into the interior of the continent around that time [see DMSP images of cyclonic vortices over around Casey station at approximately the same time, Figure 7a, 7b of Pook and Cowled, 1997].

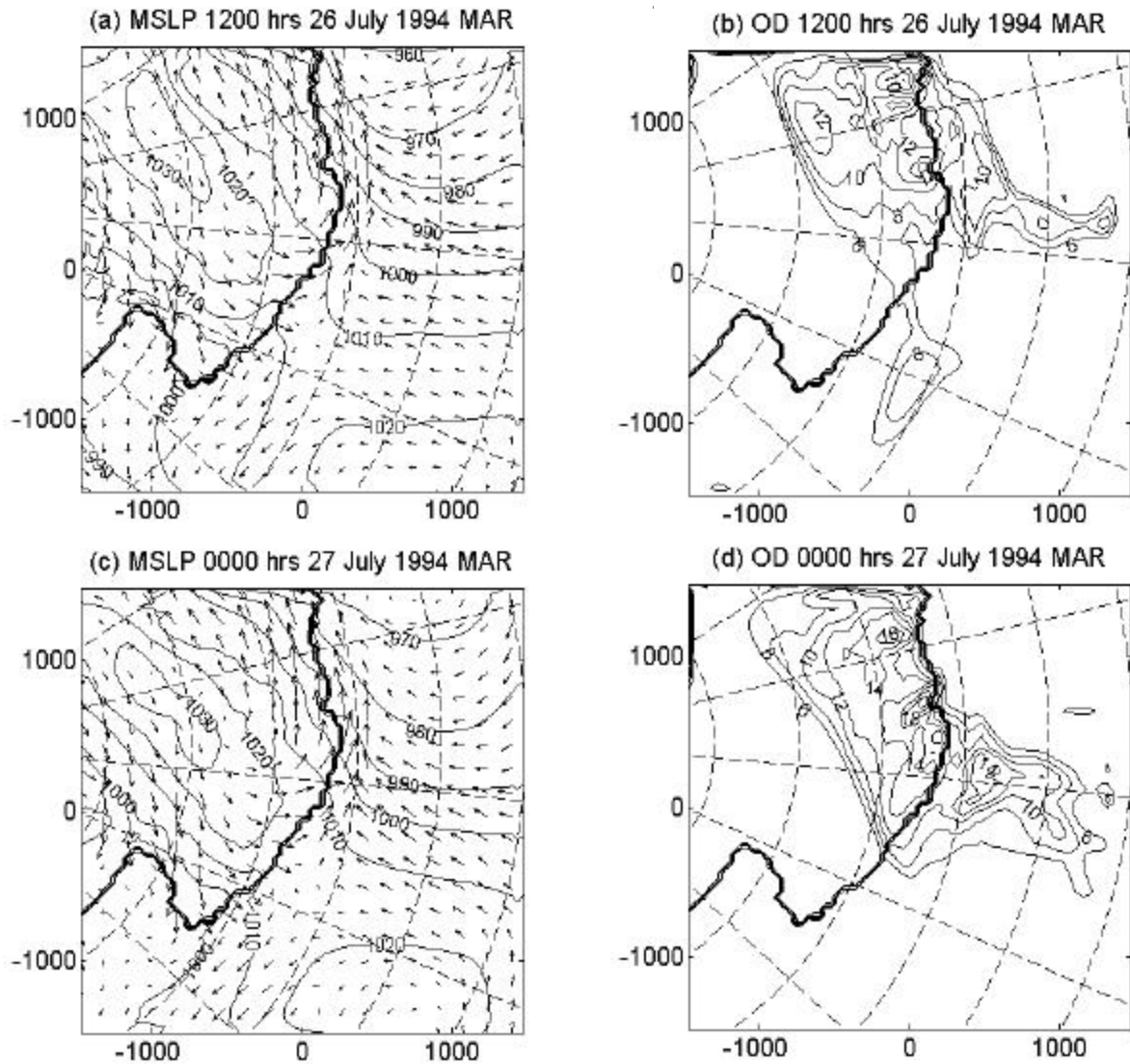


Figure 12. MSLP charts and cloud optical depth simulated by MAR for 26 and 27 July 1994.

Clouds simulated by MAR (Figures 12b and 12d) match very well with DMSP images shown by Pook and Cowled [1999] and composite infra-red images created from NOAA AVHRR passes (Figures 11c and 11d). The clouds represented by the satellite images and MAR simulated cloud optical depth plots are along the high pressure ridge. We see that the marine intrusion and cloud formation for this episode have been due to an entirely different synoptic situation than for the previous episode. It is important to notice that during this episode, in spite of the presence of a blocking high, off the coast towards the east, winds were high and were influenced by the presence of the depression on to the west of Adelie Land.

1.3.3.3. Episodes of SOP3

Figure 13 shows MSLP charts and cloud optical depth simulated by MAR for 3, 10 and 30 January 1995. The high humidity episode visible on the time-height plots (Figure 8) around 3 January 1995 is able to generate clouds only over DdU and not over the interior (Figures 9c and 9d). The marine air could not penetrate far into the interior to have widespread clouds (Figure 13b). The episode around 10 January 1995 could only have a thin speck of cloud over the interior isolated from coastal clouds (Figure 13d). However, if we study the pressure chart for 10 January (Figure 13c), the synoptic situation is similar to the one for the second episode of July 1994 (around 26 July 1994, Figure 12a). On 10 January, the high in the interior is relatively weak and the center of the high-pressure over the ocean to the east of Adelie Land is not inside the domain. However, in this situation also wind speeds are high for the whole depth of the troposphere (Figures 7e-7h) and the marine air intrusion was maximum as compared to all episodes of July 1994 and January 1995 (Figures 8e-8f).

The last episode of January 1995 (30-31 January) resulted in thick widespread clouds. During this episode the winds are high for the whole depth of the troposphere (Figures 7e-7h), particularly in the upper levels. The warm air penetration is significant over a relatively greater depth for all three grid points (Figures 8e-8h). Clouds are thin over DdU and significant over the interior and over the ocean (Figure 13f). The synoptic situation, once again, shows three systems (Figures 13h), one low to the west and one high to the east of the Adelie Land coast and one high in the interior of the continent. The penetration of marine air and the clouds took place due to the presence of the high pressure ridge similar to the one that occurred during the 26-27 July 1994 episode (Figure 12). Winds remained high in spite of the presence of the blocking high over the ocean to the east of DdU, forcing the low pressure center to the west to slow down and intensify. The clouds simulated by MAR are similar to the ones shown by the composite infra-red satellite images (Figure 14) for all the three cases in January 1995.

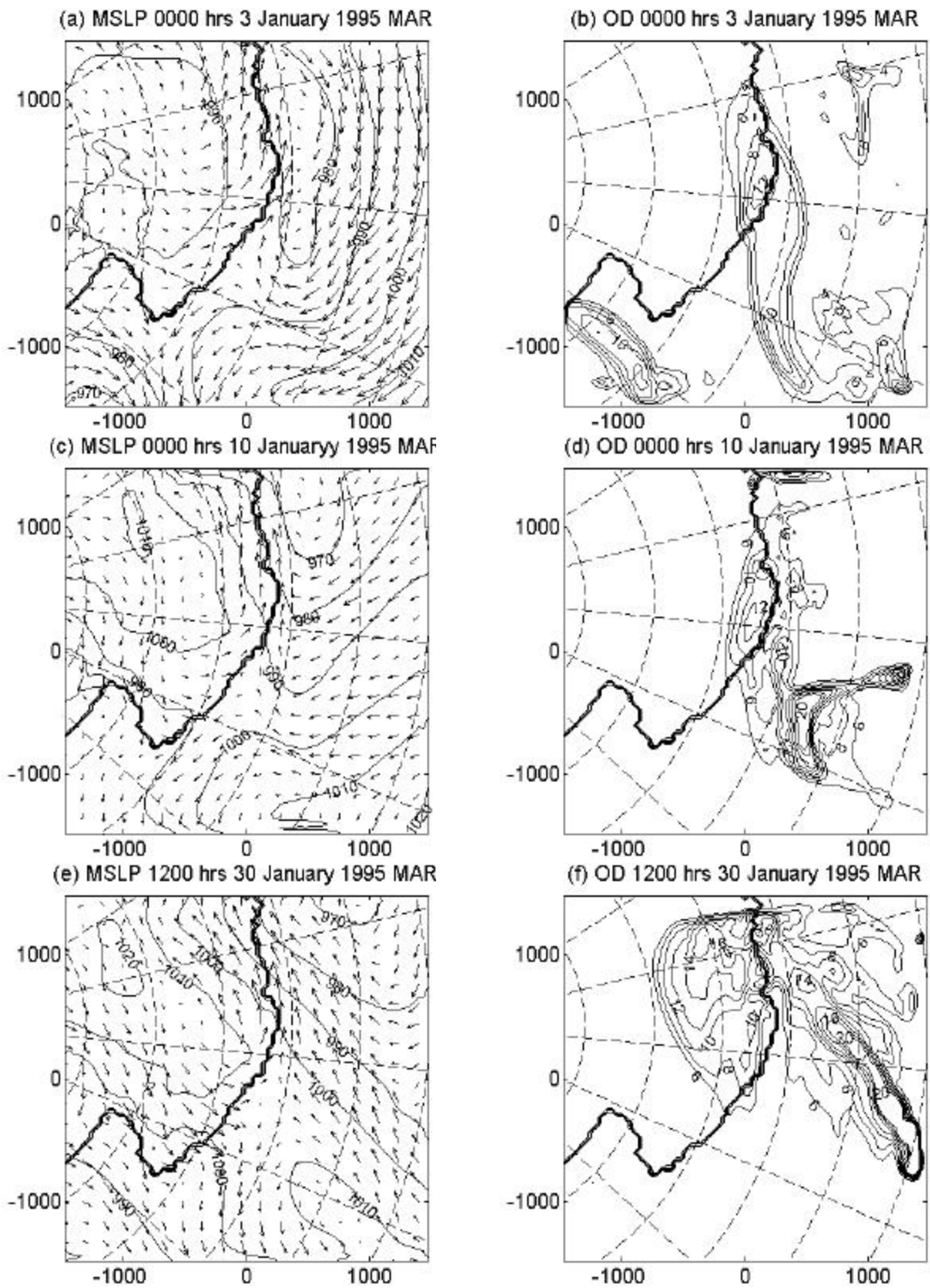


Figure 13. Same as in Figure 12 for 3, 10 and 30 January 1995.

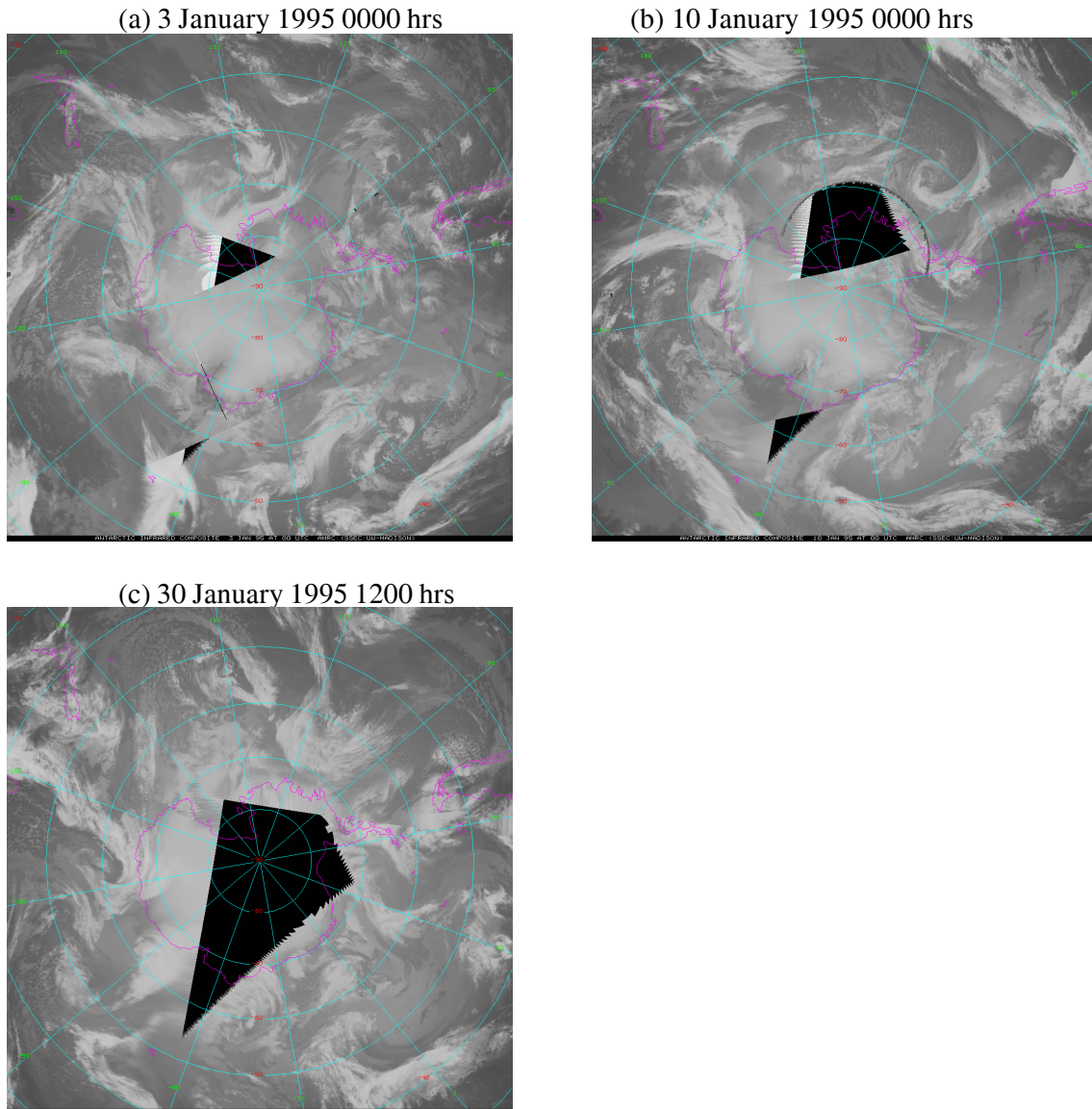


Figure 14. Composite infra-red satellite images for three episodes of January 1995. (Courtesy of the University of Wisconsin -Madison.)

1.4. Discussion and Conclusions

In this study we presented the mechanisms behind marine air intrusions into the interior using observations and model simulations. The regional model MAR is initialized from ECMWF fields. Simulated parameters are in good agreement with ECMWF fields in the whole domain except for a small coastal stretch around Ross Ice Shelf. The comparison with observations for Enigma Lake and Cape Philips AWS sites in this region, indicates

that the MAR simulations are relatively closer to observations than ECMWF analyses along this stretch.

Our results indicated clouds being greater and far deeper into the interior in July 1994 than in January 1995. Widespread clouds were observed due to the passage of a series of depressions. Satellite images and the cloud optical depth simulated by MAR indicate the advection of clouds due to intense depressions, and, also along the high pressure ridges. Although we used only a selected short data set representing winter and summer seasons in Antarctica, we found clouds to be relatively thicker and widespread into the interior in July 1994 than in January 1995 (Figures 8-9). This is envisaged as due to abnormally increased cyclonic activity in July 1994 in spite of this being a winter month. Intense and well organized depressions helped in pulling the moist air from the ocean to over the sea-ice and into the interior of the continent. In normal days the warm air travelling over the ice will cool before arriving near the continent and cannot be expected to be warm to rise against steep ice slopes. Also, the fact that the blocking high-pressure holds the depression in one place for a longer period, therefore, the air above the sea ice is expected to be warm so that the presence of sea-ice becomes less important. Relatively lower air temperatures in July 1994 episodes caused vigorous cooling of the moist marine air and resulted in thick and widespread clouds inland in July 1994 than in January 1995, although the moisture flux was similar during both periods (Figure 8). Widespread clouds far inland were, in particular, observed in July 1994 each time the intrusion took place. Due to lower atmospheric temperatures each passing cyclone could cause clouds in July 1994 (Figure 9). In January 1995, the intensity of depressions were similar to the depressions in July 1994 but the clouds were not observed far inland, except for the last episode of January 1995. This is due to the fact that the central pressure of the semipermanant anticyclone over the continent has been higher in July 1994 than in January 1995, except in the last week when the clouds were widespread into the interior. High-pressure ridges helped in the formation of widespread clouds, particularly in the last week of July 1994 and January 1995.

Presence of depressions well into the vicinity of the Antarctic coast in winter months and their penetration inland have also been reported by Alvarez and Lieske [1960], Neal [1972], Phillipot [1968] and King and Turner [1997]. Neal [1972] using the data for the period November 1969 and June 1970 carried out a similar study. He was looking for

weather systems in the interior of the continent. He found no developments at all over the continent in November 1969, whereas several cyclogenesis events were found near the South Pole and over Coats Land in June 1970. Phillpot [1968] studied three years of observations from Vostok station. He found evidence of 42 depressions having been in the vicinity of the station and detected these systems by precipitation falling and relatively high surface temperatures. Of the depressions, 75% were found in winter months of June to October, suggesting significant cyclonic activity over the continent at that time of the year. King and Turner [1997] reported a rare movement of the depression (a major low), during the period 24-26 May 1988, which tracked southwards from the Weddell sea, over Marie Byrd land and onto the Ross Ice Shelf. Alvarez and Lieske [1960] found one event of inland penetration in May 1957 that brought precipitation to the South pole and caused the surface temperature to rise by 40 degrees over four days as the oceanic air reached the interior. Astapenko [1964] examined the occurrence of depressions over the interior and found that a significant number tracked from the Ross Sea to the Weddell Sea, affecting stations such as Amundsen-Scott. He observed these events in all seasons. Stone [1993] using the radiometersonde and meteorological measurements found the winter season clouds at South Pole associated with large-scale synoptic disturbances that reached the South Pole.

Figure 15 shows MAR simulated cumulative snow for July 1994 and January 1995. In July 1994 the snow accumulation has been larger than in January 1995. However, in both cases the area of maximum snow accumulation has been along the coastal periphery around 120E longitude. Precipitation is observed to be higher in the region of greater cyclonic activity or where depression becomes slow moving. As already discussed, the large specific humidity and clouds in last weeks of July 1994 and January 1995 are due to the presence of a high or blocking anticyclone offshore in the eastern side which provided

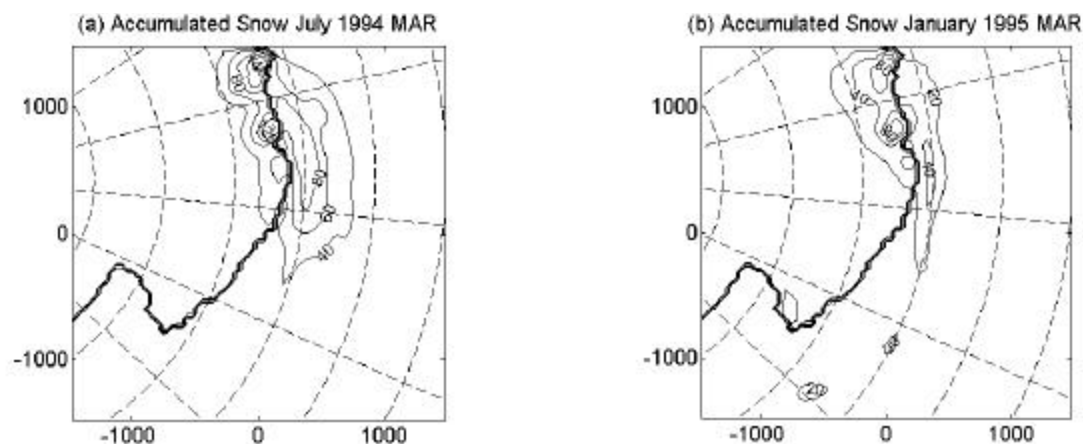


Figure 15. MAR simulated accumulated snow for July 1994 and January 1995.

a blocking to the cyclone on the western side of the Adelie Land coast. Due to this blocking anticyclone, the depression became slow moving, intensified and started to penetrate inland. Pook and Cowled [1999] demonstrated that vortices originating over the Southern Ocean can penetrate the high plateau of east Antarctica and move well inland before decaying. They reported that the development of an intense blocking anticyclone in the Tasman Sea sector appeared to have been critical for the penetration of the depression inland. According to Lejenas [1984], the Pacific-ocean to the east of Australia, between Australia and New Zealand, is the preferred region for blocking anticyclones. His study was based on 500 hPa charts and revealed two annual maxima, one 19% in April and another 20% during June-August. He also reported that the majority of blocks have a mean eastward velocity, although the longer they last the more of them move westward. When a blocking high breaks down or moves away, there is a marked tendency for another high to form and intensify at the same location [Taljaard, 1972]. Trenberth and Mo [1985] also reported using 1000 and 500 hPa charts that the primary location for blocking anticyclones is the New Zealand sector and that the blocking high is accompanied by a cut off low.

Increased near surface temperatures in July 1994 during various episodes can be summed up as due to warm marine air intrusion, increased longwave radiation due to the presence of clouds and the vertical mixing provided by strong winds. These features owe their presence to intense offshore cyclonic activity. This heating is similar to what is reported by Carroll [1983] and Stone and Kahl [1991] for winter warming. Alvarez and Lieske [1960] described a warm advection situation during which the surface temperature at the South Pole rose by nearly 40 degrees in four days during May 1957. Sinclair [1981] reported the abnormally high temperatures at the South Pole, McMurdo and Vostok associated with the warm air intrusion episode. Schwerdtfeger [1968] reported the surface warming to be due to the longwave heating from clouds formed during upper-level intrusion of moist air. Such intrusions are frequently laden with cloud condensation nuclei reaching the interior, producing a variety of cloud types [Ohtake, 1978]. Bodhaine et al. (1986) observed the enhancement of sea-salt aerosols at the South Pole associated with rapid transport of moist air from coastal regions, during surface warming events. According to Hogan et al., [1982], heat, water vapour and aerosols are transported poleward at preferred levels in the troposphere when the position of the polar high-pressure ridge shifts

from a northeasterly to a more northerly orientation. All these studies, including the present one, indicate a surface warming which is due to large-scale circulation patterns.

Strong wind events observed in association with transient eddies are in agreement with Murphy and Simmonds [1993], and Murphy [2000]. Stone and Kahl [1991] also reported that transient weather disturbances are characterized by increased cloud cover, surface warming, a shift in wind direction, increased wind speed and a weakening of inversions at South Pole. Our results also show winds to be higher with the approach of the depression from the west towards the site. This is similar to earlier studies by Streten [1963, 1968], Loewe [1974], Murphy and Simmonds [1993], Murphy [2000] and Naithani et al., [2000]. However, other studies carried out at Adelie Land winds reported winds to be higher on the western side of the depression, i.e., when the pressure is building up after the passage of the depression [Ball, 1960; Parish et al., 1993; Parish and Bromwich, 1998].

The cessation of strong winds during various episodes is in part due to the exhaustion of cold air mass at the point of origin, but mostly due to the building up of pressure along the Adelie Land coast, after the passage of the depression. Also, the warming produced by the combined effect of clouds, high winds and warm air advections, which subsequently destroyed inversions, contributed to abrupt wind cessation.

To conclude, this study confirms conclusions of previous investigations, that cyclones are responsible for much of the moisture transport and cloud formation in the Antarctic continent. The amount of precipitation being maximum in July 1994 is as expected and observed [King and Turner, 1997; Kobayashi, 1985]. The influence of warm air intrusions in increasing the surface temperature was more pronounced in July 1994, while in January 1995 similar intrusions could not effectively increase the surface temperatures. In this study, we also aimed to test the capability of MAR to simulate marine air intrusions and to test its viability as a nested version to study the Antarctic climate. Results have been very optimistic. The nested version of the model is able to simulate correctly synoptic and climatological features of the Antarctic continent and the surrounding ocean viz., the circumpolar trough, development of the ridge, surface layer, upper tropospheric features, and clouds. Comparisons with DMSP images (Figures 7a and 7b of Pook and Cowled [1997]) and composite infrared images created from NOAA AVHRR passes have been very good. MAR simulations are in fairly good agreement with observations and ECMWF

analyses, except for a small stretch along the coast of Victoria Land, where MAR simulations are closer to observations than the ECMWF analyses.

Acknowledgments

This work is part of the European Commission Project for Ice Coring in Antarctica (EPICA). One of the authors (JN) is thankful to the Belgian program of the Scientific Research on the Antarctic (Services of the Prime Minister-Federal Office for Scientific, Technical and Cultural Affairs), for giving the opportunity to work in this project. This author is also thankful to Prof. Furlan, Director TRIL, ICTP, Trieste, Italy and IFA, Roma, Italy for granting the leave to join the present contract at UCL. The analyses to force the model boundaries were obtained from ECMWF archives and the meteorological data has been downloaded from the web sites of the Wisconsin University and British Antarctic Survey. Composite infrared satellite images were provided by the University of Wisconsin-Madison. Data for DdU site has been the courtesy of Dr. Paul Pettre. AWS data for Enigma Lake and Cape Philips were obtained from the Italian National Antarctic Research Programme PNRA, Meteorological Observatory. The help provided by Olivier Brasseur, Alexis Dutrieux, Filip Lefebvre and Phillippe Marbaix during the course of the work is thankfully acknowledged. Thanks are also due to Raoul De Guchteneere, the computer administrator. We are thankful to the helpful comments and suggestions provided by three unknown reviewers.

References

Alvarez, J.A. and B.J. Lieske, The Little America blizzard of May 1957, *Proceedings of the Symposium on Antarctic Meteorology, Melbourne, Australia*, Australian Bureau of Meteorology, Melbourne, pp. 115-127, 1960.

Astapenko, P.D., Atmospheric processes in the high latitudes of the Southern Hemisphere. Section II of the IGY Programme (Meteorology) No.3. Israel Program for Scientific Translations, Jerusalem, Oldbourne Press, London, 286 pp, 1964.

Ball, F.K., The theory of strong katabatic winds, *Aust. J. Phys.*, 9, 373-386, 1960.

Bodhaine, B.A., J.J. Deluisi and J.H. Harris, Aerosol measurements at the South Pole, *Tellus*, 38B, 223-235, 1986.

Brasseur, O., Development and application of a physical approach to estimate wind gusts, *Mon. Wea. Rev.*, 129, 5-25, 2001.

Bromwich, W.D., Snowfall in the high southern latitudes, *Rev. Geophys.*, 26, 149-168, 1988.

Carroll, J.J., Studies of atmospheric energy transfer at the South Pole, *Ant. J. U.S.*, 18(5), 248-249, 1983.

Connolley, W.M., and King, J.C., Atmospheric water vapour transport to Antarctica inferred from radiosonde data, *Quart. J. Roy. Met. Soc.*, 119, 325-342, 1993.

Davies, H.C., Limitations of some common lateral boundary schemes used in Regional NWP models, *Mon. Wea. Rev.*, 111, 1002-1012, 1983.

ECMWF, European Center for Medium-Range Weather Forecasts data services, Shinfield Park, RG2 9AX, United Kingdom.

Gallée, H., and G. Schayes, Development of three-dimensional meso- γ primitive equation model : katabatic winds simulation in the area of Terra Nova Bay, Antarctica, *Mon. Weather Rev.*, 122, 671-685, 1994.

Gallée, H., Simulation of the mesoscale activity in Ross sea, Antarctica, *Mon. Weather Rev.*, 123, 2051-2069, 1995.

Gallée, H., Mesoscale atmospheric circulations over the southwestern Ross sea sector, Antarctica, *J. Applied Meteorol.*, 35, 1129-1141, 1996.

Gallée, H., P. Pettre, and G. Schayes, Sudden cessation of katabatic winds in Adelie land, Antarctica, *J. Applied Meteorol.*, 35, 1142-1151, 1996.

Giorgi, F., M.R ; Marinucci and G.T. Bates, Development of a second generation regional climatic model (RegCM2), Part I, Boundary layer and radiative transfer processes, *Mon. Weather Rev.*, 121, 2794-2813, 1993a.

Giorgi, F., M.R ; Marinucci, G.T. Bates and G. de Canio, Development of a second generation regional climatic model (RegCM2), Part II, Convective processes and assimilation of lateral boundary conditions, *Mon. Weather Rev.*, 121, 2814-2832, 1993b.

Hines, K.M., D.H. Bromwich and T.R. Parish, A mesoscale modeling study of the atmospheric circulation of high southern latitudes, *Mon. Weather Rev.*, 123, 1146-1165, 1995.

Hogan, A., S. Bamard, J. Samson, and W. Winters, The transport of heat, water vapour and particulate material to the south polar plateau, *J. Geo. Res.*, 87(C6), 4287-4292, 1982.

Kessler E.: 1969, On the distribution and continuity of water substance in atmospheric circulation; Meteorological Monography, vol.10, No.~32, American meteorological society.

King, J.C., and Turner, J., *Antarctic Meteorology and Climatology*, pp 409, Cambridge Atmospheric and Space Science Series, Cambridge University Press, 1997.

Kobayashi, D., Annual precipitation estimated by blowing snow observations at Mizuho station, East Antarctica, 1980. In: *Proceedings of Seventh Symposium of Polar Meteorology and Glaciology*, Ed. S. Kawaguchi, National Institute of Polar Research, Tokyo, pp. 117-22.

Lejenas, H., Characteristics of southern hemisphere blocking as determined from a time series of observational data, *Quart. J. Royal. Met. Soc.*, 110, 967-979, 1984.

Lin Y.-L., R.D. Farley and H.D. Orville: 1983. Bulk parameterization of the snow field in a cloud model. *J. Appl. Meteorol.*, 22, 1065--1091.

- Loewe, F., 1974: Considerations concerning the winds of Adelie Land. *Z. Gletscher. Glazialgeol.*, **10**, 189-197.
- Murphy, B.F. and I. Simmonds, An analysis of strong wind events in a GCM near Casey in the Antarctic, *Mon. Wea. Rev.*, 121, 522-534, 1993.
- Murphy, B.F., Severe weather forecasting at east Antarctica coastal stations, Preprint volume of the Antarctic Weather Forecasting Workshop, 17-19 May, Eds. E.N. Cassano and L.R. Everett, 26-31, 2000.
- Naithani, J., G. Mastrantonio, S. Argentini and P. Pettre, Influence of cyclonic perturbations on surface winds around Dumont d'Urville, East Antarctica using wavelet transform, *J. Geo. Res.* (in press), 2000.
- Neal, A.B., Cyclones and anticyclones in November 1969 and June 1970, *Aust. Met. Mag.*, 20, 217-230, 1972.
- Neff, W.D., An observational and numerical study of the atmospheric boundary layer overlying the east Antarctic ice sheet, NOAA Tech. Memo., ERL WPL-67, 272 pp., NOAA/ERL Wave Propagation Lab., Boulder Colorado, 1981.
- Ohtake, T., Atmospheric ice crystals at the south pole in summer, *Ant. J. U.S.*, 13(4), 174-175, 1978.
- Parish, T.P., and K.T. Waight, The forcing of Antarctic katabatic winds. *Mon. Weather Rev.*, 115, 2214-2226, 1987.
- Parish, T.R., and Bromwich, D.W., A case study of Antarctic wind interaction with large-scale forcing, *Mon. Wea. Rev.*, 126, 199-209, 1998.
- Parish, T.P., P. Pettré, and G. Wendler, The influence of large-scale forcing on the katabatic wind regime at Adelie Land, Antarctica. *Meteorol. Atmos. Phys.*, **51**, 165-176, 1993.

Phillipot, H.R., the derivation of 500 hPa height from automatic weather station surface observations in the Antarctic continental interior, *Aust. meteor. Mag.*, 39, 79-86, 1991.

Pook, M., and Cowled, L., On the detection of weather systems over Antarctic interior in the FROST analyses, *Weather and Forecasting*, 14, 920-929, 1999.

Ramanathan, V., R.D. Cess, E.F., Harrison, P. Minnis, B.R., Barkstrom, E. Ahmad and D. Hartman, Cloud-radiation forcing and climate ; Results from earth radiation budget experiment, *Science*, 243, 57-63, 1989.

Schwerdtfeger, W., New data on the winter radiation balance at the south pole, *Ant. J. U.S.*, 3(5), 193-194, 1968

Schwerdtfeger, W., *Weather and climate of the Antarctic*, Elsevier, New York, 1984.

Sinclair, M.R., Record high temperatures in the Antarctic-A synoptic case study, *Mon. Wea. Rev.*, 109, 2234-2242, 1981.

Stone, R.S., Properties of austral winter clouds derived from radiometric profiles at the south pole, *J. Geo. Res.*, 98, 12,961-71, 1993.

Stone, R.S., E.G. Dutton, J.J. Deluisi, Surface radiation and temperature variation associated with cloudiness at the south pole, 1989 Review, *Ant. J. U.S.*, 24(5), 230-232, 1989.

Stone, R.S., and J.D. Kahl, Variation in boundary layer properties associated with clouds and transient weather disturbances at the South Pole during winter, *J. Geophy. Res.*, 96, 5137-5144, 1991.

Streten, N.A., Some observations of Antarctic katabatic winds. *Australian Meteorol. Mag.* 18, 1-20, 1963.

Streten, N.A., Some characteristics of strong wind periods in coastal East Antarctica. *J Appl. Meteorol.*, 7, 46-52, 1968.

Taljaard, J.J., Synoptic meteorology of the southern hemisphere, *Meteorology of the Southern Hemisphere*, Meteorol Monogr. No. 35, Amer. Met. Soc., 139-211, 1972.

Trenberth, K.E. and K.C. Mo, Blocking in the southern hemisphere, *Mon. Wea. Rev.*, 113, 9-21, 1985.

Turner, J., T.A., Lachlan-Cope, J.P. Thomas and S. Colwell, The synoptic origin of precipitation over the Antarctic Peninsula, *Antarctic Science*, 7, 327-337, 1995.

van Loon, H., The half yearly oscillations in middle and high latitudes and the coreless winter. *J. Atmos. Sci.*, 24, 472-486, 1967.

Walsh, K. and J.L. McGregor, Simulation of Antarctic climate using a limited area model, *J. Geophys. Res.*, 101, D14, 19,093-19,108, 1996.

Webster, P.J., and G.L. Stephens, Cloud -radiation interaction and the climate problem, in *The Climate Change*, edited by J. Houghton, 63-78, Cambridge University Press, New York, 1984.

Chapter 2

STRONG WIND EVENTS

Strong wind events over Dumont d'Urville (DdU), an east Antarctic coastal station, and Dome C, an interior station, have been studied to determine the role of large scale disturbances on them. Strong wind events for the years 1993-1999 have been studied using the MSLP fields of the ECMWF analyses. It has been found that these events are associated with the approach of a depression from the west towards the DdU coast. The wind increases in response to the approaching depression and decays once the depression moves past the DdU coast. The response of wind to the approaching depression is not the same for all the events and depends upon the strength of the anticyclone over the continent, the high pressure ridge or a blocking anticyclone over the northeast of the Adelie land coast and the downslope pressure gradient. The presence of the blocking high to the east of DdU renders the approaching depression to the west slow-moving, which intensifies in the process. These intensifying slow-moving blocked depressions start to penetrate inland if the central high of the anticyclone over the plateau happens to be shallow. The winds at Dome C increase to as high as 17 m/sec in response to these penetrating depressions. It is concluded that the strong surface winds in the coastal East Antarctic station, DdU, are governed by the katabatic and the synoptically forced winds operating together.

2.1. Introduction

Surface winds have been most extensively studied over the Antarctic coastal sites. Since the pioneering works of Ball [1956; 1960], katabatic winds are regarded as the dominant component of the surface wind regime, particularly of the east Antarctic coast. In 1963 Streten [1963] reported that katabatic winds at Mawson cannot persist for more than 24 hours on their own. For them to be of longer duration they require a synoptic support. In 1974 Loewe [1974] also said about the influence of cyclones in initiating strong coastal winds. In most of the research articles dedicated to katabatic winds, surface wind regime is regarded as dominated by the katabatic component and no clearly defined significance of the possible contribution of the synoptic component has been mentioned [Ball, 1960; Mather and Miller, 1967a,b; Parish, 1982, 1984; Parish and Waight, 1987; Parish and Bromwich, 1987, 1991, 1998; Parish et al., 1993a, 1994]. It is hypothesised that in the area of confluence, katabatic winds persist unabated for days together owing to the confluence of winds from over a wider area [Parish, 1981, Parish and Wendler, 1991; Parish and Bromwich, 1987, 1991, 1998; Bromwich et al., 1994]. Parish [1981] has proposed that the confluence of drainage streamlines in the interior of the continent upwind from Cape Denison provides an enhanced supply of negatively buoyant air necessary for supporting the intense katabatic wind regime. Parish and Wendler [1991] concluded that the confluence of cold, negatively buoyant air in the interior of the continent provides the large-scale support for the generation and maintenance of strong katabatic winds in coastal Adelie Land. In most of the literature pertaining to studies over Adelie land and in particular to DdU, no considerable importance is mentioned of the possible influence of transient cyclones, which is another most important factor in shaping the weather and climate of the coastal areas, in particular after Antarctic inversions and winds [Streten 1963, 1968, 1990; Loewe, 1974; Murphy and Simmonds, 1993; Murphy 2000; Wendler et al., 1997; Naithani et al., 2001a,b].

It has been reported by Streten [1963] and Loewe [1974] that extremely strong winds in the coastal stations are associated with decreasing station level pressure. However, Ball [1960], Parish et al., [1993b] and Parish and Bromwich [1998] proposed that winds are stronger when the system is to the east of the station, i.e., when the system has already moved past the station and the station level pressure is

building up. Parish and Bromwich [1991, 1998] have argued that the katabatic winds exert a considerable influence on the atmospheric circulation - and hence on synoptic winds. The basic mechanism responsible for the generation and development of downslope winds are the inversions on the Antarctic slopes and the resulting pressure gradient force directed downslope towards the coast. They cause the cold dense air mass on the higher plateau, denser than the air some horizontal distance away at the same elevation towards the coast, to fall down due to its own gravity towards the coast. The speed of this flow, called the katabatic flow, is proportional to the magnitude of the slope and surface friction, while its direction is governed by the fall line and coriolis force. Now incorporating the influence of the transient eddies as they approach the coast and move past the station. The station level pressure decreases with the approach of a depression, this will further increase the existing pressure gradient force between the coast and the point from where the wind originates. In case there was no considerable pressure gradient before, it will be established with the approach of the depression off the coast. The wind should be stronger during this period. As the system moves past the station the pressure starts building up and the pressure gradient becomes less steep, and, the wind should be expected to be low or should cease. The latter, of course, will depend upon several other factors including the availability of cold air mass upslope to be blown past and a high pressure above the continent. The important factor which should be helping in prolonging the flow is the fact that the presence of the cyclone acts to pull the air mass from the interior, plus it converges this excess mass from near the coast and raises it to higher levels. This upward converged flow will diverge at higher elevation and will flow back to the continent's interior and will subsequently subside, and, therefore, helps in the faster replenishment of air mass to feed the gravity flow [Naithani et al., 2001a]. In recent articles [Murphy and Simmonds, 1993; Murphy 2000; Naithani et al., 2001a,b] the relationship between the transient cyclones and katabatic winds has been emphasized, and the effect of the cyclones in initiating and prolonging the flow is reported. However, it has also been observed that there are other factors which affect the flow and its prolongation; the main being the cyclones, their intensity, location and speed.

The flow downslope depends upon the atmospheric conditions at the place of their origin. The katabatic flow at the coast is more a function of inversion strength far

inland from where the winds originate than those near the coast [Murphy and Simmonds, 1993]. Once it starts rolling down it will continue its march unless it encounters instability or heating in a larger part of its descent. Thus, the main factor to cease the flow remains to be the availability of air-mass to fall down [Streten, 1963, 1968], particularly in non-summer months. According to Murray [2000] the high pressure ridge ahead of the cyclone passes allows the boundary layer to become very stable and a large cold air pool to develop. This cold air supply feeds the gravity driven flow that interacts with the large-scale flow at the coast. The low level mixing provided by these winds raises the surface temperature and partially destroys the inversions, which in turn will cease the flow. This is often the case in summer as will be discussed later. The advection of warm marine air inland caused by cyclonic systems also raises the surface temperature. The marine air intrusion takes place above the boundary layer [Schwerdtfeger 1984, p. 139; Naithani et al., 2001b]. The cooling and subsequent condensation of the warm moist air as it climbs the topography help in the formation of clouds, and, often, precipitation in the coastal areas. The presence of clouds, due to increased long wave radiations, raise the surface temperature resulting in the temporary destruction of surface inversions. Cessation of winds can be caused by the combined influence of the vertical mixing provided by strong winds, warm air advection and warming due to clouds [Carroll, 1983; Stone and Kahl, 1991; Naithani et al., 2001b].

The effect of cyclonic circulation which gives rise to polar easterlies is clearly seen in the wind direction in the coastal regions as compared to the interior. In the interior the wind direction is strongly controlled by the local topographic forcing which results in the direction being parallel to the fall line. In the coastal regions, however, wind gets more deflected to the left due to the coriolis force and merges with the coastal polar easterlies forced by the presence of uninterrupted stream of travelling cyclones [King and Turner, 1997]. Schwerdtfeger [1984] notes that the katabatic wind regime acts to reinforce the observed sea level easterly winds, which circumscribe the continent within a band several hundred kilometers wide. This circumpolar zone of convergence also represents the southernmost extent of the sea level trough of low pressure surrounding the Antarctic continent [Parish et al., 1994]. However, Parish et al. [1994] proposed that the Antarctic orography and associated katabatic drainage play a primary role in forcing the pronounced semiannual pressure oscillation and

circumpolar sea level easterly wind regime. They also proposed that the Antarctic katabatic wind regime is a major feature of the mean meridional circulation of the high southern latitudes, and the circumpolar belt of easterly winds is intimately linked to the large-scale mass movement associated with this continental scale circulation. Deep depressions over the ocean when encounter high pressure associated with the semi-permanent anticyclone over the continent bring strong surface winds to the coastal area [King and Turner, 1997, p. 189]. Murphy and Simmonds [1993] demonstrated by means of GCM simulations that the strong wind events around Casey station occur due to the combined influence of the strong pressure gradient due to presence of a depression off shore and the strong katabatic flow working together. Wendler et al., [1997] observed a strong negative correlation between the wind speed and pressure in summer months and a weaker correlation in fall. They reported that the katabatic component has the dominant influence on the wind speed during fall. Recently, Naithani et al. [2001a] used the wavelet transform [WT] analysis to study the influence of cyclones on surface wind regime over Dumont d'Urville (DdU, 67.4S; 140E; 49 m asl). The time scale representation of WT coefficients clearly demonstrated the influence of cyclonic perturbations on surface wind regime over DdU.

This paper aims at finding the extent of the influence of cyclones on strong wind events at DdU and to see if it is the approach of the depression that influences strong winds at DdU or the rear end, i.e., when the depression has moved past the DdU coast. We also aim to find the relative influence of winds and cyclones on each other. In this paper the synoptic situations during the strong wind events at DdU (Figure 2.1) have been studied for some randomly chosen strong wind events from the years 1993-99. Data for Dome C (DC, 75.4S; 123E; 3280m asl) is also discussed. Three hourly synoptic observations near the surface are complemented by the ECMWF analyses mean sea level pressure (MSLP) fields. Three hourly synoptic observations have been downloaded from the British Antarctic Survey [BAS] and the Wisconsin University [WU] web sites. The data is three hourly ten minute averaged values. The data for DC for the year 1999 is ten minute raw data from the Wisconsin University web site. The missing data values are replaced by the previous data values.

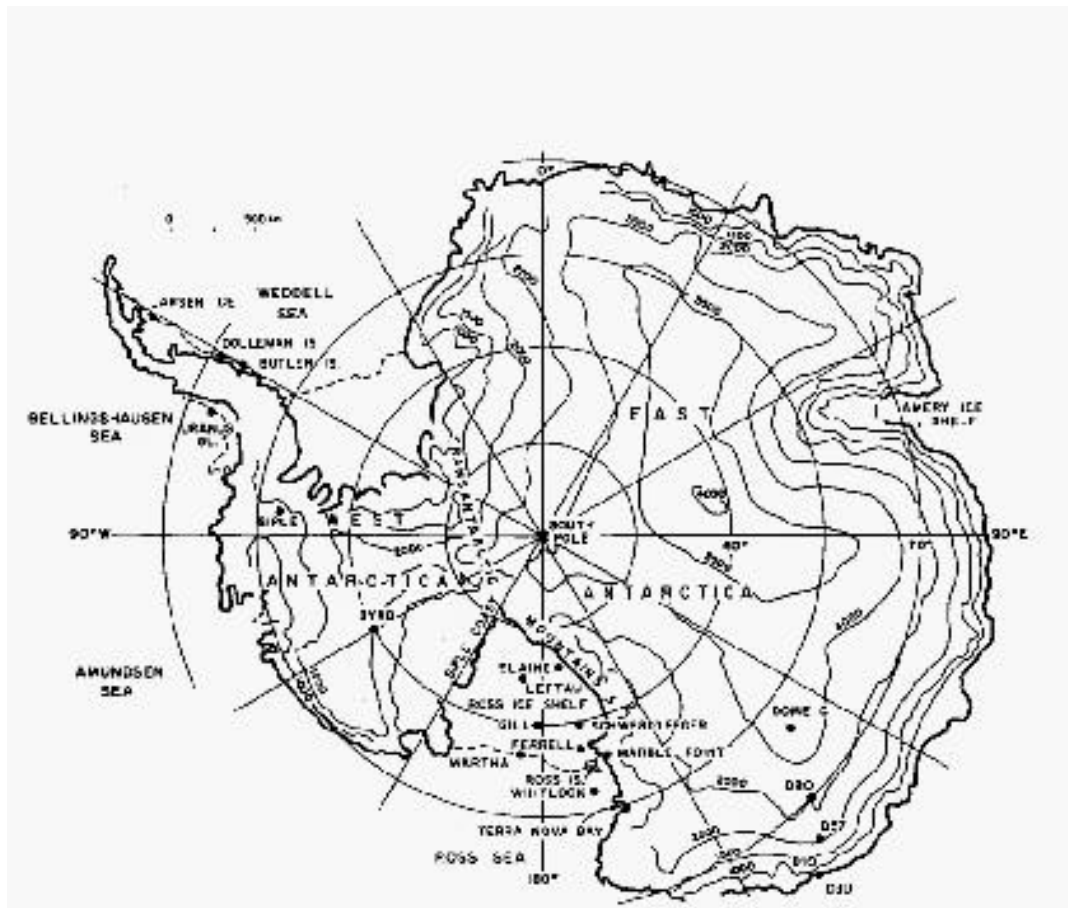


Figure 2.1. The map of Antarctica showing Dumont d'Urville and Dome C.

2.2. Observations

2.2.1. Time series

Figures 2.2-2.5 show the time series of meteorological parameters for DC and DdU for the selected strong wind events. For convenience time series of pressure is plotted together with the time series of temperature and horizontal wind speed. This is to see their correlation with each other in general. It is evident that most of the strong wind events are associated with a decreasing pressure. In most of the cases, an increase of wind speed from 2-5 m/sec to as high as 20-35 m/sec in few hours to a day is observed at DdU. The wind maxima correspond to the pressure minima during most of the episodes. The wind starts increasing the moment the pressure starts falling. In some cases it comes back to normal before the minimum in pressure

is reached. However, if the pressure system becomes stationary due to the presence of a blocking anticyclone to the east of the station or due to some other reason - to be discussed below - the wind may or may not remain high. This suggests that there are other factors which affect the wind flow. In few such cases the wind remain high for the whole duration the pressure remained low, while in some cases winds came down to the initial value much before the pressure starts rising again. In some cases two peaks are observed for a single marked pressure fall. It can also be seen that two successive depressions passing at short intervals of time have their distinct influence on wind. This is the case in almost all the sets of time series chosen.

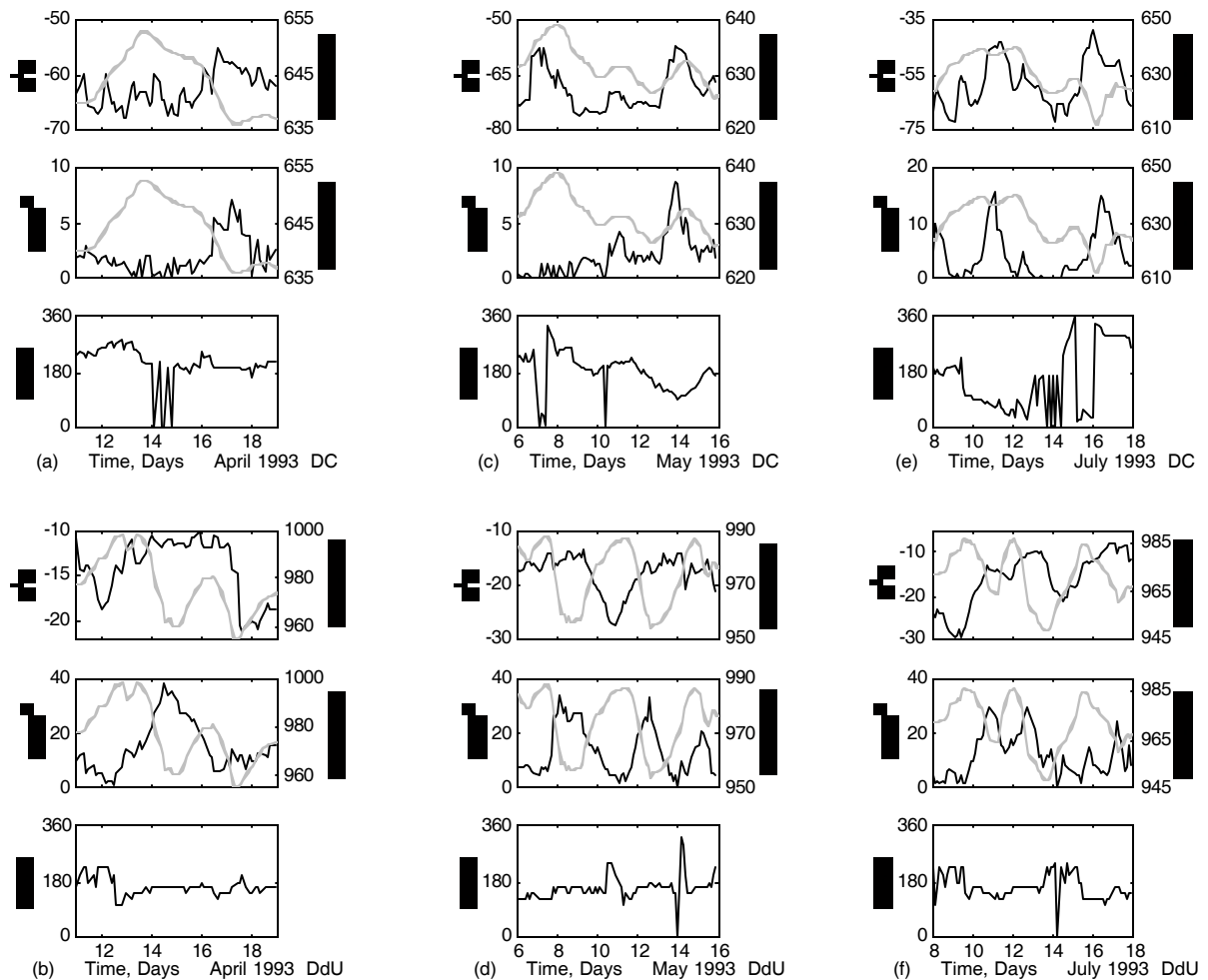


Figure 2.2. Time series of meteorological parameters for Dome C and Dumont d'Urville for strong wind events in April, May and July 1993, respectively.

From Figures 2.2-2.5 it is evidenced that almost each passing depression has some influence on surface wind regime, however, not all the depressions have similar influence. There are events when the decreasing pressure or a passing system is not

accompanied by extreme winds for longer duration. Deep depressions over the ocean when encounter high pressure associated with the semi-permanent anticyclone over the continent are able to have a considerable effect on the duration and intensity of the winds. Some of the depressions are able to influence winds even at DC. However, most of the depressions pass unnoticed for DC, i.e., without affecting the wind or its weather. As can be seen from the time series plots, there are episodes of strong wind events at DC, while at DdU the effect is not much pronounced during these instances. In the following section we will discuss in detail the strong wind events shown in Figures 2.2-2.5 and will discuss the MSLP fields of ECMWF reanalyses/analyses.

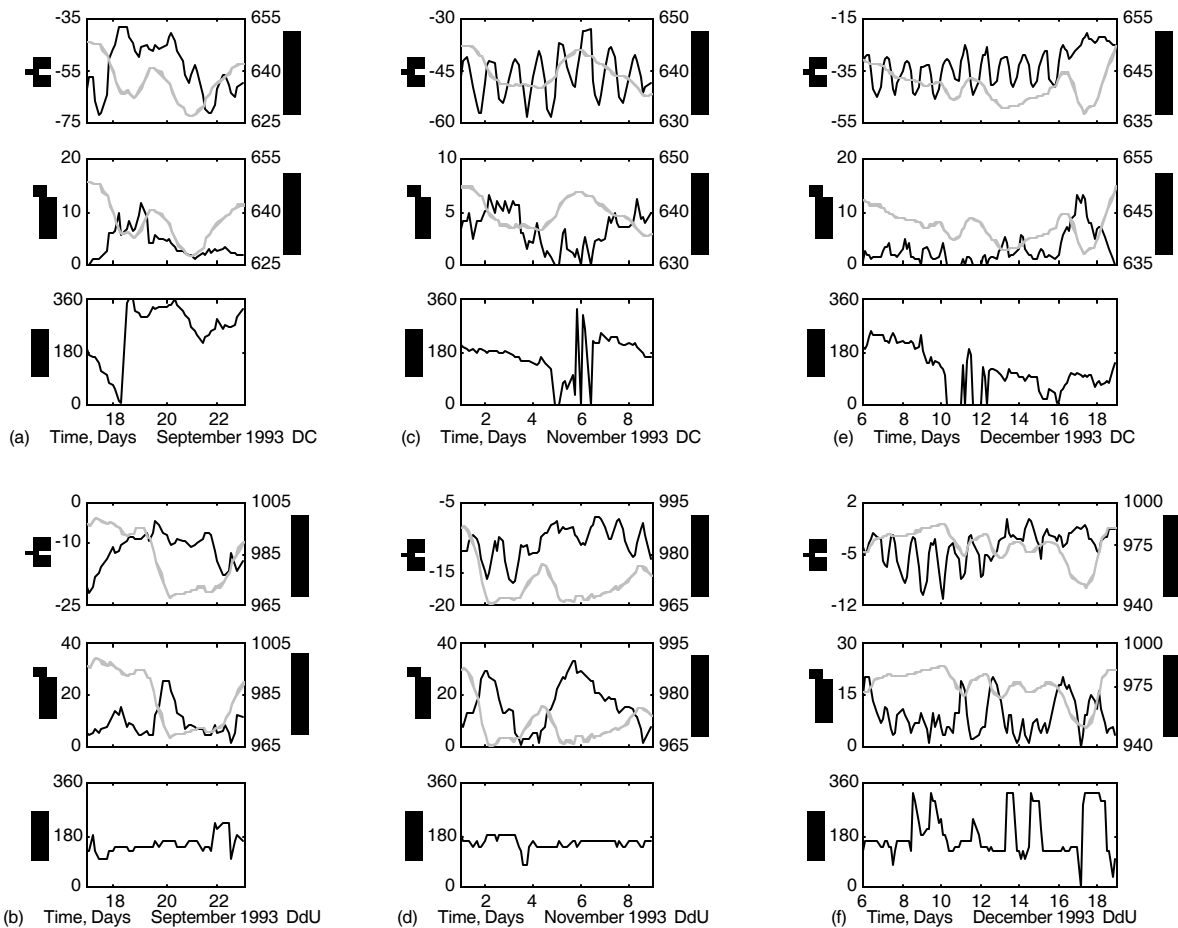


Figure 2.3. Time series of meteorological parameters for Dome C and Dumont d'Urville for strong wind events in September, November and December 1993, respectively.

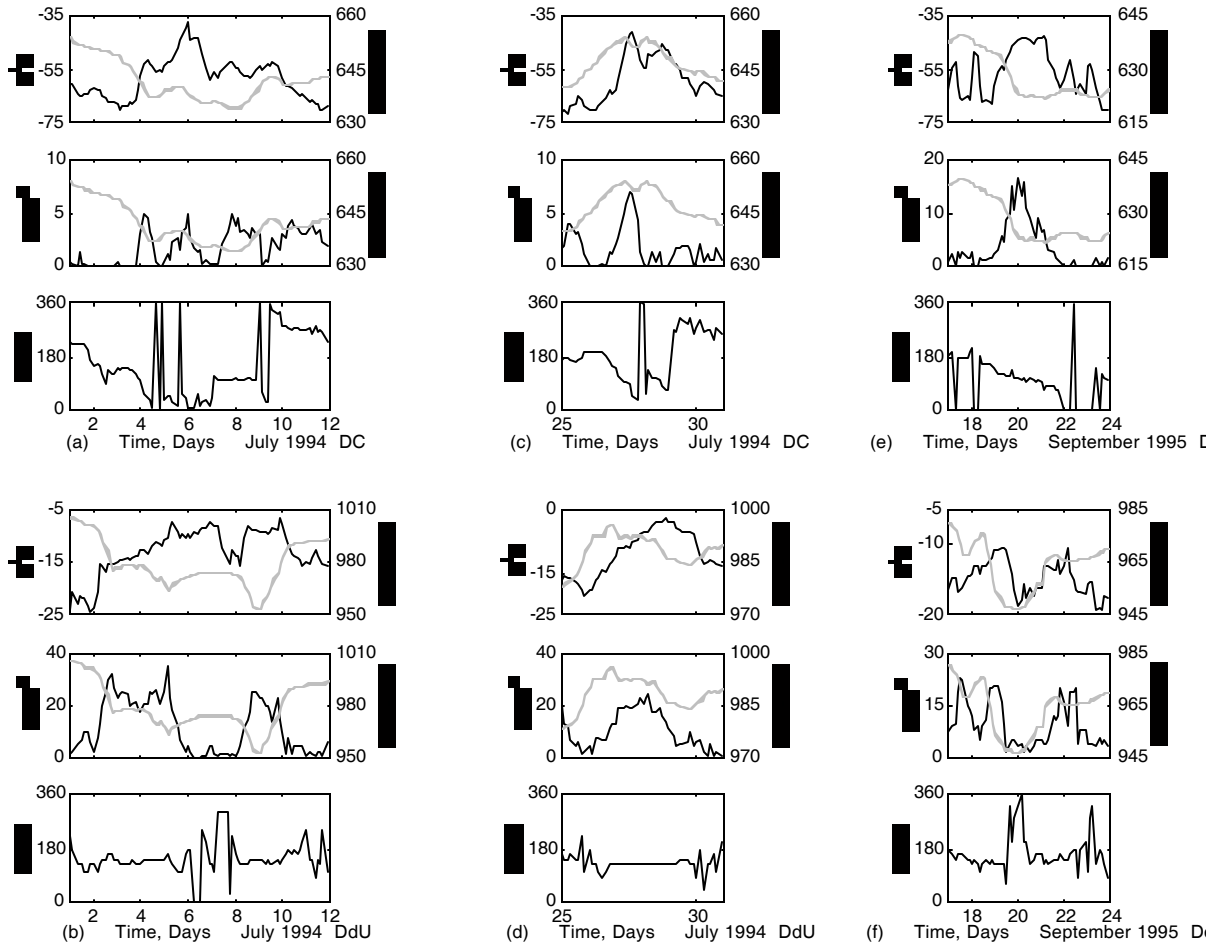


Figure 24. Time series of meteorological parameters for Dome C and Dumont d'Urville for strong wind events in July 1994 and September 1995, respectively.

2.2.2. Synoptic patterns

In the following subsections, the synoptic situation during the various strong wind episodes shown in Figures 2.2-2.5 is discussed.

2.2.2.1. 11-17 April 1993

During this event (Figures 2.2a-2.2b), a low pressure appeared in the vicinity of the Adelie land coast to its west, at 0600 hrs on 13 April centered around 140E and 55S. However, it could not move eastward, due to the presence of an anticyclone to the northeast of the coast. Instead, the system moved southward towards the coast and intensified in the process. It remained stationed at around 62S till 15 April 1993 intensifying continuously, and, thereafter, resumed its usual journey eastward after

the high pressure ridge disappeared. Figure 2.6 shows MSLP fields of ECMWF reanalyses for 1200 hrs on 13 April and 0600 hrs on 14 April 1993. Pressure gradient between the continent and the coast was strengthened during this event. DdU experienced strong winds for the whole duration this low pressure system remained in the vicinity of the station (greater than 20 m/sec with a maxima of around 40 m/sec). The maximum in wind speed is observed approximately at the same time the minimum in pressure is recorded. During this event, pressure at DC decreased and remained stationary for one day and then decreased again in response to another approaching system. The wind at DC, however, did not reflect any significant influence (Figure 2.2a). The latter system had little effect on the winds at DdU, where the winds increased only up to 15 m/sec.

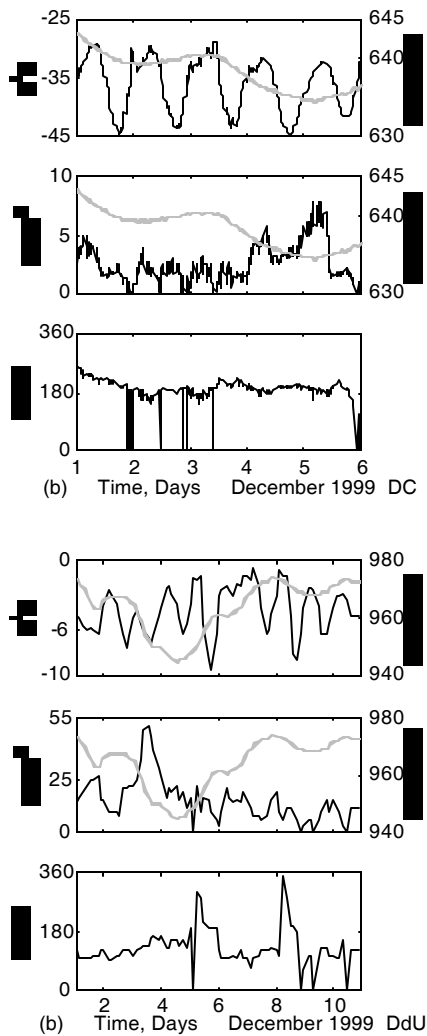


Figure 2.5. Time series of meteorological parameters for Dome C and Dumont d'Urville for strong wind event in December 1999.

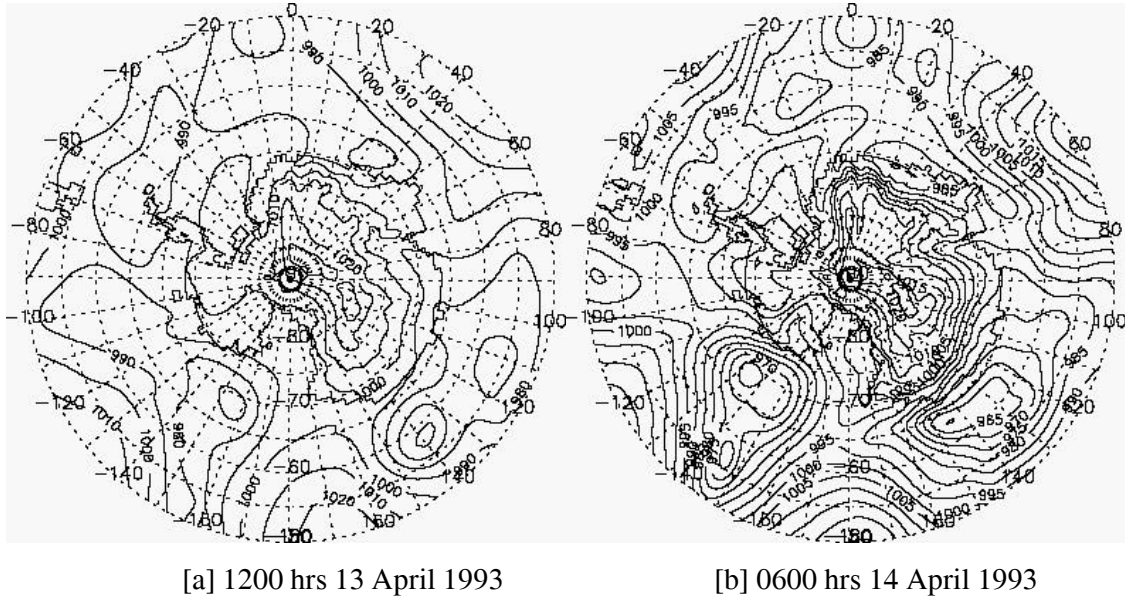


Figure 2.6. ECMWF analyses of MSLP charts for [a] 1200 hrs 13 April and [b] 0600 hrs 14 April 1993, respectively.

2.2.2.2. 6-16 May 1993

Time series of pressure for 6-16 May 1993 (Figures 2.2c-2.2d) shows the passage of two systems, one with its maximum influence in pressure at DdU on 8 May 1993 and another on 12 May 1993. On 6 May 1993, three small vortices integrated to form a larger disturbance. Around 1800 hrs on 6 May, this integrated low pressure system centered at around 53S and 134E started approaching the DdU coast. This system moved past the coast on 7 May 1993 and was closely followed by another system with the same central pressure. This second system became slow-moving due to the presence of a high pressure ridge to the northeast. Figure 2.7a shows the MSLP fields for 1800 hrs 9 May 1993. The pressure at DdU, due to the influence of both these low pressure systems, remained constant for approximately one day before coming back to normal after their passage past its coast. Wind remained high for the whole duration, on account of relatively higher downslope pressure gradient which could sustain stronger winds for longer duration. The wind at DdU during this period remained high, only to come back to its initial magnitude, after the station level pressure started rising again. On 11 May 1993, the pressure started decreasing in response to another low pressure system approaching the Adelie land coast. This system moved past the station around 1800 on 13 May 1993, after which the pressure at DdU started rising once again. During this period the wind showed a

sharp peak at the same time as the minimum in pressure was observed. The decrease in wind strength was rather sharp during this event. The fast decay in wind strength can be accounted for due to the central high pressure over the continent, which shifted further northwest once the depression centre started moving past the DdU coast. This decreased the downslope pressure gradient between the plateau and the coast. Figures 2.7b-2.7c show the MSLP fields for 1200 hrs 11 May and 0600 hrs 12 May 1993, respectively.

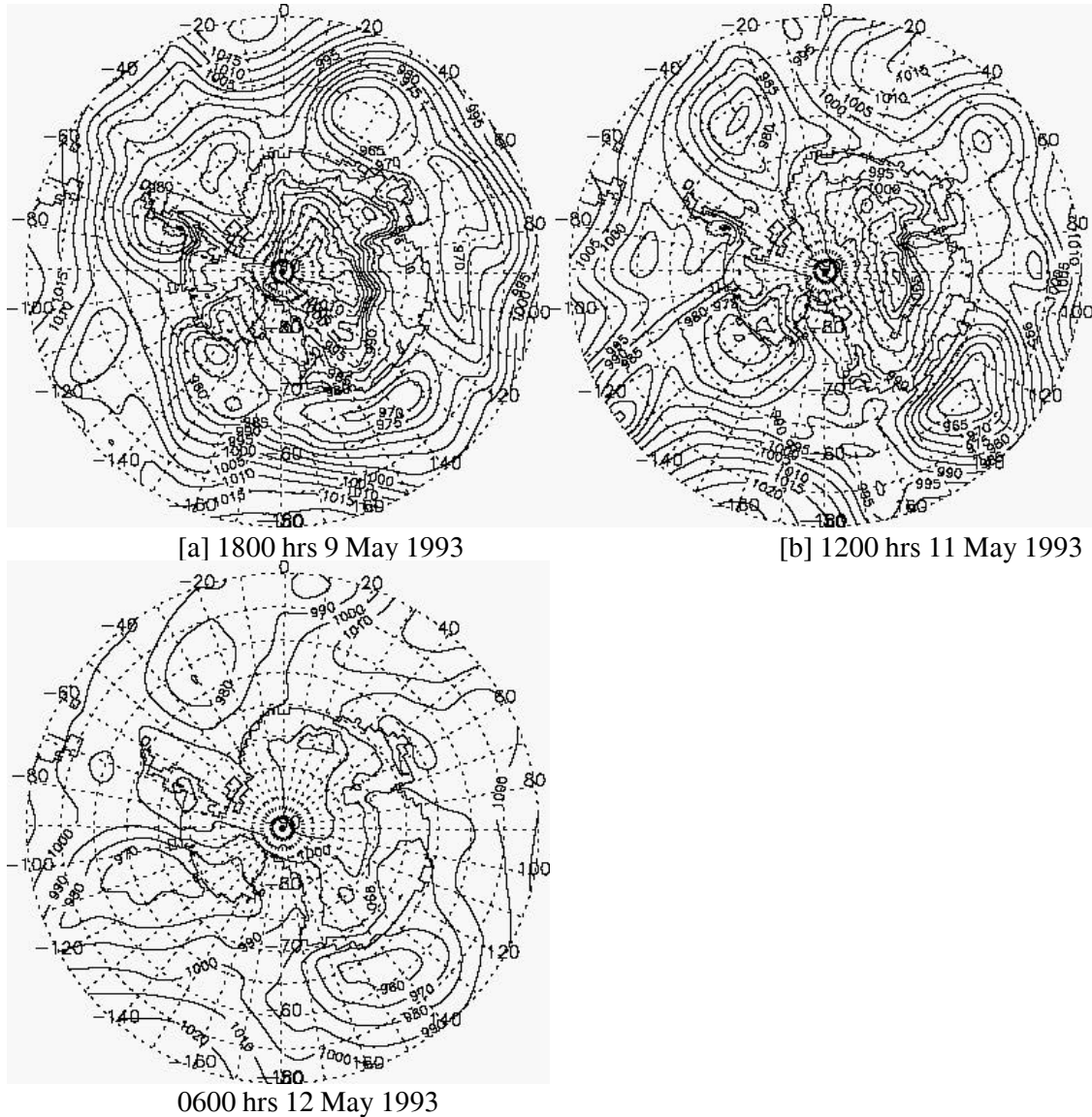


Figure 2.7. ECMWF analyses of MSLP charts for [a] 1800 hrs 9 May, [b] 1200 hrs 11 May and [c] 0600 hrs 12 May 1993, respectively.

From the MSLP charts we see that the pressure gradient between the continent and the coast is strong enough to sustain high winds for the whole duration the low pressure system was in the vicinity of DdU coast. At DC these two events had no effect on the wind. The wind at DC increased and showed a peak after the pressure started building up.

2.2.2.3. 8-18 July 1993

For the first time till now, the lowering of pressure at DC was accompanied by high winds (very high for DC, Figure 2.2e). In fact, all the three lows, have the influence in increasing winds at DC. On 11 July 1993 (Figure 2.8a, MSLP hPa for 0000 hrs 11 July 1993), the low pressure trough had its influence over much of the interior and the anticyclone over the continent had a high central pressure. This influenced strong winds at DC. The influence of the second system is short lived in winds at DC [Figures 2.2f, 2.8b]. At DdU, the first passing system had a good negative correlation with wind, but the wind came down much before the minimum in pressure is reached in response to the second passing system. This second system which became visible at the coast around 1800 hrs on 11 July 1993 intensified as it approached towards the DdU coast. This system moved past the DdU coast on 12 July 1993 and on 13 July 1993 it began to intensify on account of a high pressure ridge to the north of Adelie coast. Figure 2.8b shows the MSLP fields for 1800 hrs 13 July 1993. This system started to penetrate inside the continent on 13 July 1993 from the east of DdU. Its influence started fading on near surface pressure at DdU after 1800 hrs 13 July 1993, when it moved further inland. The system could penetrate far inland as the central high of the anticyclone over the plateau was shallow. While in the previous two episodes, around 14 April 1993 and 9 May 1993, the depression could not penetrate inland, in spite of being blocked in their usual motion eastward by a high pressure ridge to their northeast. This might be due to the central high over the plateau, which was rather high during these episodes.

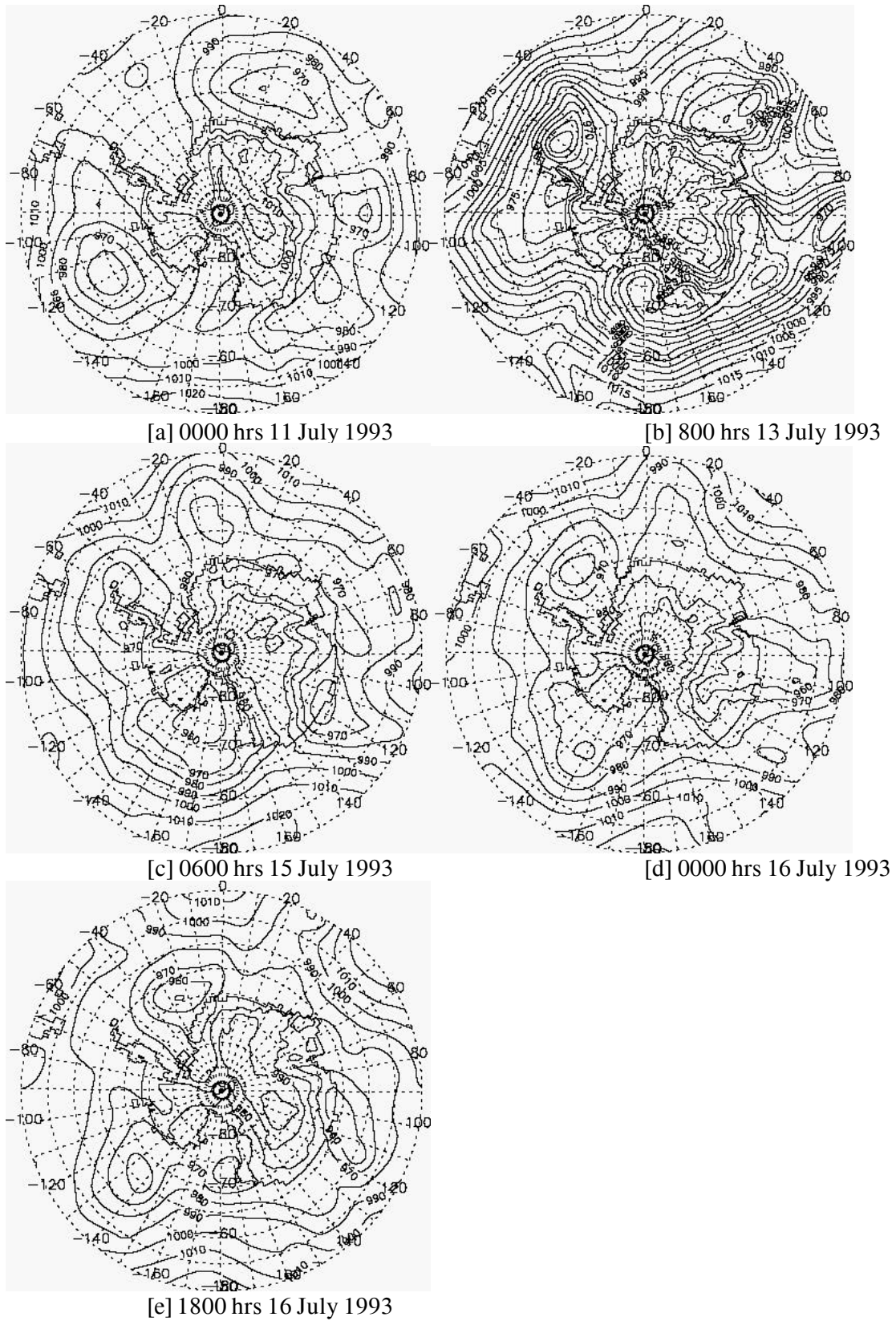


Figure 2.8. ECMWF analyses of MSLP charts for [a] 0000 hrs 11 July, [b] 1800 hrs 13 July, [c] 0600 hrs 15 July, [d] 0000 hrs and [e] 1800 hrs 16 July 1993, respectively.

Winds at DdU showed a response for a short duration, where they increased to up to 30 m/sec suddenly and came down much before the minimum in pressure was reached. This short duration response in wind can be due to the downslope pressure gradient becoming shallow and due to the penetration of the depression inland soon after. During this event the pressure at DC was decreasing in response to this system, however, the wind had not much influence. They showed a small peak of 5 m/sec, which came down much before the minimum in pressure. The central pressure of the anticyclone over the continent was rather low.

On 15 July 1993, a depression started penetrating into the continent from around 120E due to the presence of a high pressure centre to the east near the Adelie land coast. The depression intensified in the process. The centre started enlarging and disintegrated into two small systems, with one centre lying in the interior and the other on the ocean. The one in the interior at around 70S, 100E filled up fast and the other on the ocean at around 58S, 100E continued its march southeastward. The winds at DC remained high (>10 m/sec) for the whole duration the effect of the low pressure system was felt at the station. Figures 2.8c-2.8e show the MSLP fields for 0600 hrs 15 July and 0000 and 1800 hrs 16 July 1993, respectively. The pressure at DdU started falling slowly in response to the pressure system penetrating inland. Later, a shallow low pressure approaching the Adelie land coast from around 58S, 130E on 16 July 1993 had the influence and the pressure at DdU continued to decrease. The fall in pressure was steeper on 16 July 1993. The influence on wind, likewise, was relatively pronounced for this later steep pressure fall period, when it showed a small peak. Initially the slow and gradual pressure decrease could not sustain stronger winds as the central plateau pressure was rather low, moreover, soon much of the interior was under the influence of low pressure system. However, in the beginning on 15 July 1993, winds increased to as high as 19 m/sec with the approach of the depression. The wind came down soon as the system started penetrating the continent and became shallow, and was diffused over much of the interior. Note that the winds increased in spite of relatively lower central plateau pressure, since the depression itself was there to influence winds.

Out of the three events discussed from 8-18 July 1993, the wind at DC increased considerably in response to the first passing depression when the pressure gradient

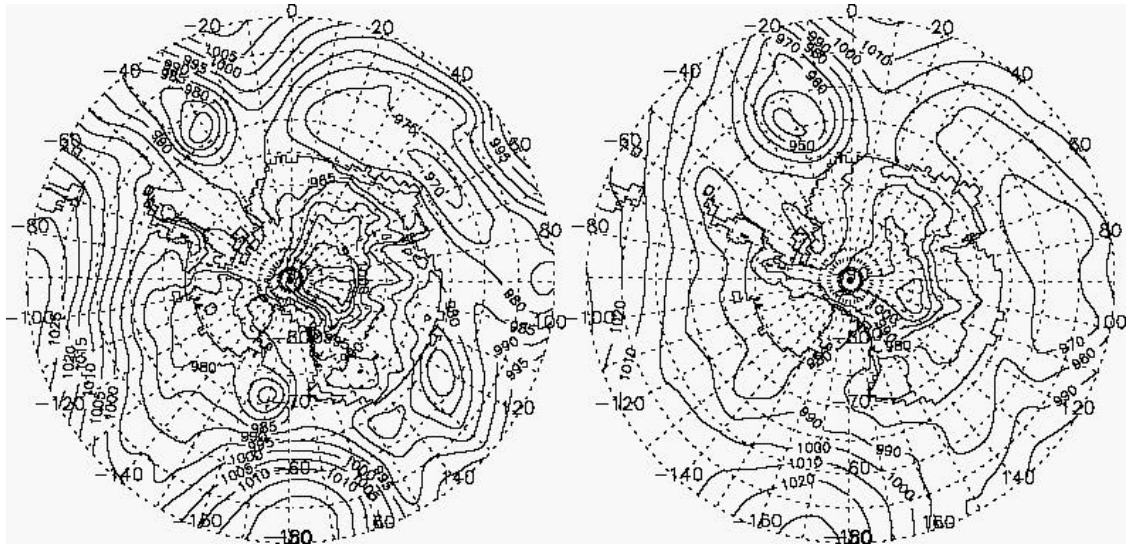
between the plateau and the coast was considerably large, and during the third passing depression whose centre penetrated to as far as DC.

2.2.2.4. 17-22 September 1993

Pressure started falling at DdU on 19 September 1993 (Figure 2.3b) and remained stationary for approximately 3 days and increased thereafter. The surface winds increased in response to the decreasing pressure, but came down even as the pressure remained stationary at a low value for three days. The temperature increased with increasing winds and remained at the high value for the whole duration until the pressure started increasing once again. At DC [Figure 2.3a] the pressure decreased but could not have any influence on surface winds.

Pressure started decreasing on 19 September 1993 with the approach of a depression from the west of DdU coast. At 0000 hrs, 20 September 1993, a small low centre formed to the east of DdU and disappeared soon. Thereafter, much of the east Antarctic coast was influenced by a trough of low pressure. Due to this the station level pressure remained more or less constant (increasing only very slightly!) for almost three days, before rising to the initial value after 22 September 1993 (Figures 2.9a and 2.9b, MSLP fields for 0000 hrs 20 and 21 September 1993, respectively). Wind at DdU started increasing in response to the approaching depression from the west on 19 September 1993 and after around 0600 hrs on 20 September 1993, wind came down. (Here although the pressure at the coast was continuously low the winds were not high. This is envisaged as there was no depression at the coast to influence strong winds from the interior, although the central high over the continent was relatively high.) The wind at DC had no influence, although, the pressure at DC decreased in response to the approaching depression. The decreasing pressure around 17-18 September 1993 at DC was in response to a low pressure which penetrated far into the interior from the west of DdU. This system started penetrating from around 130E on 17 September 1993, even though the central plateau pressure was very high at 1030 hPa. Figure 2.9c shows the MSLP charts for 0000 hrs 18 September 1993. This depression moved westward after it started penetrating inland. The wind at DC also increased in response to the penetration of this system. This system had very small influence on the pressure and wind at DdU, since at this time

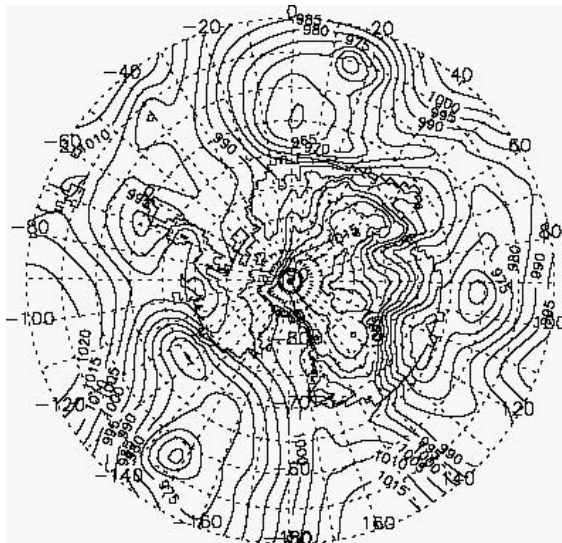
DdU was under the influence of a high pressure ridge. This is the only case where we observed the penetration of depression centre inland in spite of rather high central plateau pressure!



[a] 0000 hrs 20 September 1993

[b] 0000 hrs 21 September

1993



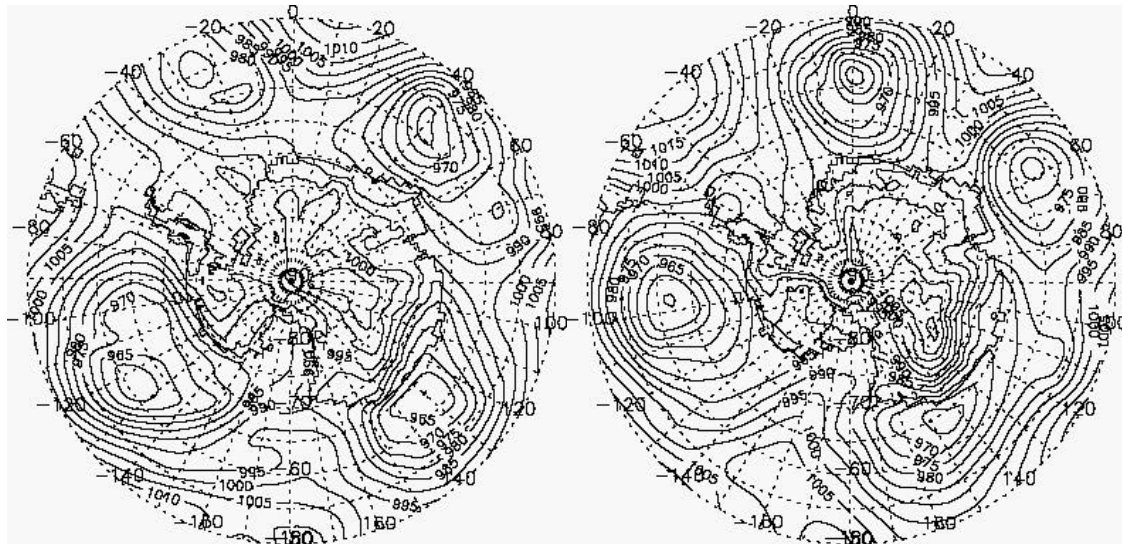
[c] 0000 hrs 18 September 1993

Figure 2.9. ECMWF analyses of MSLP charts for [a] 0000 hrs 20 September and [b] 0000 hrs 21 September and [c] 0000 hrs 18 September 1993, respectively.

2.2.2.5. 1-8 November 1993

This period shows two systems which passed the DdU coast (Figure 2.3d). We will discuss the second system, which had its effect on wind at DdU for approximately 4

days. However, as we can see in the time series, both these systems are clearly visible on the pressure and wind time series for both the sites. The correlation between the pressure and wind time series is negative at both the sites (Figures 2.3c-2.3d). The system started approaching the coast on 4 November. This system intensified as it approached and remained in the vicinity until 0600 hrs, 7 November 1993. This effect can be seen in the more or less stationary pressure around 967 hPa for approximately 2 days (5-6 November 1993, Figure 2.3d) in the time series and a very gradual increase, thereafter, for another two days. Figures 2.10a-2.10b show the MSLP fields for 1800 hrs, 4 November and 0000 hrs, 6 November 1993, respectively. A high pressure ridge to the northeast of the coast did not allow the depression to move further east on its usual track. However, this time the depression did not move inland, in spite of the high pressure ridge to the northeast. This is, once again, envisaged as due to the presence of a comparatively stronger anticyclone over the continent.



[a] 1800 hrs 4 November 1993

[b] 0000 hrs 6 November 1993

Figure 2.10. ECMWF analyses of MSLP charts for [a] 1800 hrs 4 November and [b] 0000 hrs 6 November 1993, respectively.

The wind at DdU started increasing as the pressure started decreasing in response to the approaching system on 3 November 1993, from 5 m/sec to around 35 m/sec on 5 November. Thereafter, it decreased slowly in response to slowly increasing pressure, nevertheless, the wind remained above 20 m/sec and came down to its initial value of 5 m/sec only after the pressure reached its initial value. The central high pressure of the anticyclone over the continent remained high from 3 to 8

November 1993, and, the pressure gradient between the continent and the coast also remained high to sustain stronger winds for a longer duration. The temperature, although depicted a diurnal variation, but remained high. At DC, the response in pressure was delayed and it decreased continuously from 5 November onwards. The wind increased to only upto 7 m/sec at DC as the pressure started decreasing. The continuously strong winds at DdU for approximately four days, can be regarded as supported by the depression. The depression helped in converging and raising the accumulating air mass near the coast, with southerly flow at higher levels and subsequent, subsidence over Antarctica. This, provided a faster replenishment of the air mass at the plateau for the drainage to be stronger and longer lasting.

2.2.2.6. 6-18 December 1993

The time series for this period show (Figures 2.3e-2.3f) diurnal variation in wind due to the diurnal variation in solar radiation, and, hence, temperature, along with the incidences of strong wind events associated with sharp pressure changes, at both the stations. The diurnal cycle in wind which can be considered as due to pure katabatic component, in the larger and small hours of the day, rarely exceeds 5 m/sec at DC and 10 m/sec at DdU. The wind during the steep pressure changes associated with the approach of a depression towards the Adelie land coast, are higher than 20 and 10 m/sec at DdU and DC, respectively. This time series also show a peculiar case at DdU (Figure 2.3f) when the wind showed two distinct peaks for the duration the system had its possible influence at the station level pressure (Figure 2.3f). First peak in the wind was observed when the system was approaching and the pressure was decreasing, and, the second peak when the pressure started increasing in response to the passage of the system past the DdU site. The time series of wind at DC (Figure 2.3e) showed a clear distinct wind peak during the passage of this system, whereby wind increased to higher than 12 m/sec. The temperature at DC increased in response to the increasing winds.

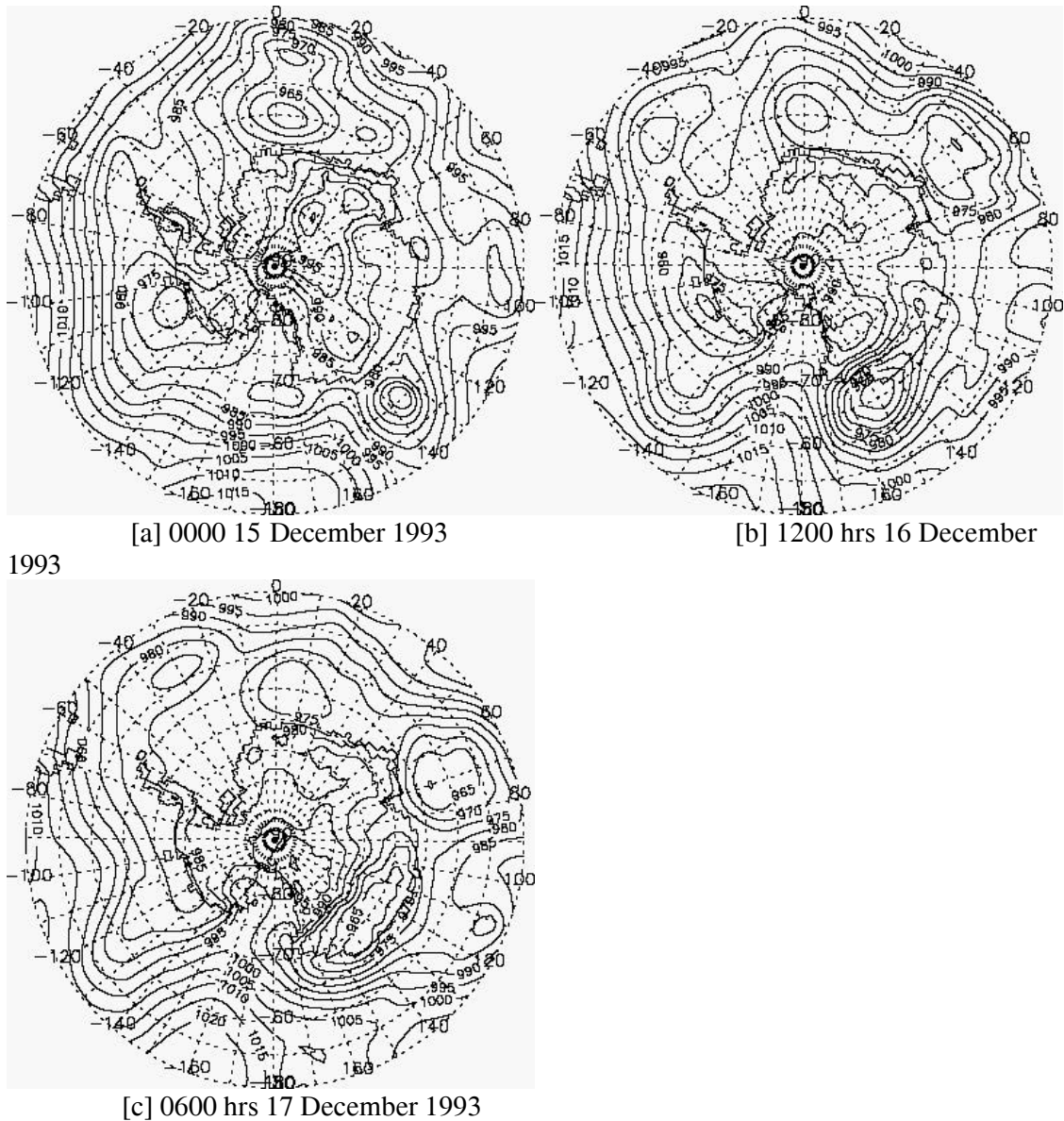


Figure 2.11. ECMWF analyses of MSLP charts for [a] 0000 hrs 15 December, [b] 1200 hrs 16 December and [c] 0600 hrs 17 December 1993, respectively.

A low pressure system slowly approached the coast on 14 December 1993 from northwest and intensified in the process. Once near the Adelie land coast to the east of DdU (centered at 65S and 150E), its movement further east was hampered by a high pressure ridge situated to the east of it. The low pressure system became slow-moving, intensified and started penetrating inland after 1200 hrs, 16 December 1993. At 0600 hrs next day its elongated centre was seen over much of the interior from around 100E to 150E, centered around 70S. Figures 2.11a-2.11c show the MSLP fields for 0000 hrs 15 December, 1200 hrs 16 December and 0600 hrs 17 December

1993, respectively. Winds at DdU increased to around 20 m/sec and were from SE for the time this low pressure system was approaching the DdU coast from the northwest, and came down abruptly once the system started penetrating inland at around 0000 hrs on 17 December 1993. At this point, as the low pressure system started moving further south from DdU, station level pressure started increasing in response. The wind changed direction, became northeasterly and increased to about 15 m/sec. Once the pressure at DdU stabilised to its initial value at around 0600 hrs, 18 December 1993, the wind decreased and became SE once again. When the system was approaching the DdU coast from the west, the central pressure at the plateau was not very high, but it is presumed that the low at the coast was intense enough to influence strong winds. This system could penetrate inland on account of the high pressure ridge to the northeast of Adelie coast and relatively shallow anticyclone over the continent.

Once again, this system could penetrate since the central high pressure of the anticyclone over the plateau was low. Looking into the time series of the station level parameters, pressure in particular, it is difficult to see in which direction the system went! Under normal conditions a depression moves in the eastward direction. The pressure at the station shows a decreasing trend till it approaches the station and an increasing trend afterwards, once it moves past the station. On this particular occasion, the system moved eastward first and then southwestward into the interior, after it moved past DdU. Pressure at DdU started increasing as the centre of the depression moved further inland. The station level pressure recording is similar to what happens when the system moves past the DdU coast in its usual motion eastward. However, the wind direction observed at DdU did throw some light into this event. In any case, this interpretation would be difficult to ascertain without the help of pressure charts.

2.2.2.7. 1-11 July 1994

A trough of low pressure was approaching the Adelie land coast from the northwest on 1 July 1994. On 2 July, a small vortex appeared near the coast, which moved slowly southeast and filled up the next day. The time series of pressure at DdU (Figure 2.4b) showed a minimum, and, a maximum in wind on 2 July 1994. After 3

July, 1993, the main centre of the trough started approaching the coast and once more minimum in pressure and a corresponding maximum in wind were observed at DdU on 4 July 1994. In between these two events, the pressure at DdU decreased very slowly. Figures 2.12a-2.12b show the MSLP fields for 1200 hrs, 2 July and 0600 hrs, 4 July 1994. The central plateau pressure was high during this whole period. The station level pressure at DdU remained almost constant after 5 July 1994 in response to the high pressure ridge to the north of Adelie land coast. Wind during this period remained calm, in spite of the central high pressure over the continent, which was high. This is seen as due to the absence of a depression on the coast to influence strong winds.

After 7 July 1994, the decaying low to the east of DdU integrated with another shallow system to the west of DdU. With the new central low at around 140E and 64S on 8 July 1994, the wind at DdU increased (Figure 2.12c, MSLP at 0600 hrs, 8 July 1994). The wind remained high from SE for the whole duration this low pressure had its influence. Winds at DC increased from near calm to about 5 m/sec during the time the pressure at DC was decreasing (Figure 2.4a). However, the decrease in pressure at DC, for the time series, is not synchronous with those at DdU.

The high pressure ridge after 5 July 1994, preceding the low pressure can be seen as establishing strong surface inversions along the ice slopes and also as helping in building up the pool of cold air mass at the plateau by way of subsidence. This cold air supply can be regarded as providing an intense and longer duration flow during the passage of the depression, apart from the fact that the depression itself can be seen as converging and raising the accumulating air mass near the coast, with southerly flow at higher levels and subsequent, subsidence over Antarctica. Thus, providing faster replenishment of the air mass at the plateau for the drainage to be stronger and persisting. We have seen that the presence of an anticyclone alone over the plateau cannot sustain high winds at DdU, unless a depression is present near the coast to influence strong winds.

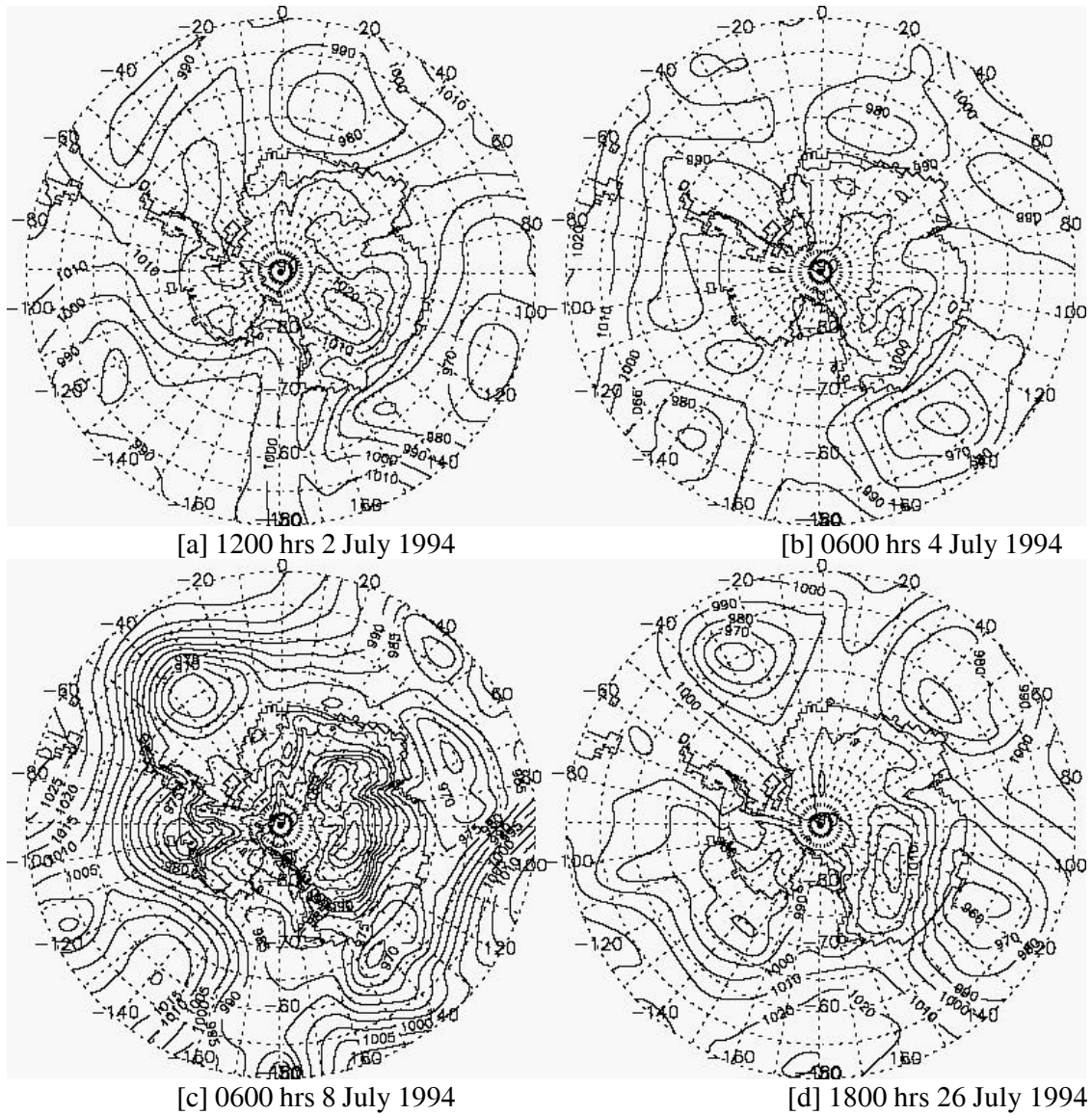


Figure 2.12. ECMWF analyses of MSLP charts for [a] 1200 hrs 2 July, [b] 0600 hrs 4 July, [c] 0600 hrs 8 July and [d] 1800 hrs 26 July 1994, respectively.

2.2.2.8. 25-30 July 1994

The decrease in pressure during this week was not significant and did not indicate the approach of a considerably intense depression in the time series (Figures 2.4c-2.4d), while the wind and the temperature do indicate its presence somewhere. The pressure charts of ECMWF analyses during this period show a depression centred around 60S and 110E on 25 to 27 July 1994, to the west of DdU. This depression was blocked in its usual eastward movement by an anticyclone to the east of DdU.

The depression became slow-moving and intensified in the process. These two counter systems remain stationed for more than three days from 25 to 27 July 1994. The depression to the west of DdU, rendered stationary by the anticyclone, started moving southward on 26 July 1994. The central high at plateau was also relatively high, and, therefore, the depression could not go much further inland and remained intense for longer duration. The pressure at DdU, although was influenced by the depression to the west, decreased very slowly and gradually. The winds at DdU started increasing after 25 July 1994 and came down on 28 July 1994 after the low pressure system filled up. The temperature increased continuously in response to the heating provided by wind generated vertical mixing. Figure 2.12d shows the MSLP fields at 1800 hrs 26 July 1994.

The time series of wind at DC (Figure 2.4c) also show a clear distinct peak in response to the low pressure system with the temperature increasing by more than 20 degrees in one day. Previous studies carried out during this period reported the presence of two small vortices which penetrated inland [Pook and Cowled, 1996], and, the heating during this period to be due to the combined effect of vertical mixing due to strong winds, warm marine air intrusion above the boundary layer and the longwave radiative heating generated by the presence of clouds over much of the interior in the Adelie land sector [Naithani et al., 2001b].

This case indicates that the longer duration strong winds at DdU, although, are not accompanied by the steep fall in pressure, but are associated with the presence of an intense depression to the west of it.

2.2.2.9. 17-22 September 1995

This case represents a profound influence of the depression on winds at DC (Figure 2.4e). The wind at DC increased from around 2 m/sec to 17 m/sec on 20 September 1995. The wind remained high for the whole duration the pressure remained constant at a low value. At DdU (Figure 2.4f), the wind once again came down much in advance to the minimum in pressure. The time series for both stations indicate the presence of a low pressure, which remained constant at a low value for about 24 hours at DdU and more than 24 hours at DC.

On 17 September 1995, a depression started approaching the DdU coast from the west and the pressure at DdU started dropping. Next day the station was under the influence of a high pressure ridge situated at the northeast of DdU coast and the pressure at DdU increased. During this short period, when the pressure was decreasing, the time series of wind at DdU (Figure 2.4f) showed a peak. Later on in the day this low pressure intensified and once again influenced the weather at DdU. The pressure at DdU started falling till 19 September 1995 and remained at a low value for one day until the centre of depression moved past the station and later, there remained only a trough of low pressure. Figures 2.13a, 2.13b show the MSLP fields for 0600 hrs 19 September and 0000 hrs 20 September 1995. During this period the low pressure trough was seen over much of the interior and the central high pressure at the plateau was rather low at around 990 hPa. The wind at DdU increased for a small duration as the pressure started falling and came down once this low centre moved past the station. The pressure continued to remain low for some time on account of the low pressure trough over much of the east Antarctic coast. The wind could not sustain as the downslope pressure gradient diminished. Winds remain high only as long as the depression itself was there to influence it and could not be sustained by the trough.

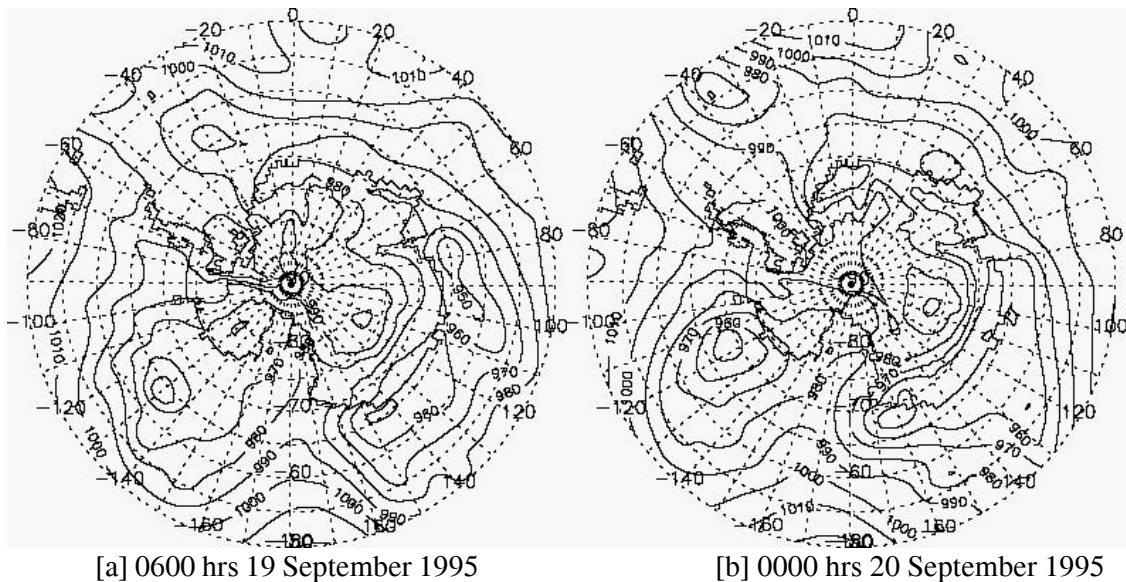


Figure 2.13. ECMWF analyses of MSLP charts for [a] 0600 hrs 19 September and [b] 0000 hrs 20 September 1995, respectively.

At DC the pressure decreased gradually from 17 September 1995. Initially, the decrease was slow. After 19 September 1995 the decrease in pressure was steep and was accompanied by strong winds. During this period the diffused low was seen over much of the interior. The winds increased to about 17 m/sec and remained high for some time, until the pressure remained constant for about one day. After 21 September 1995, the pressure increased slightly and remained more or less constant at a low value for next few days. Around 20 September 1995, the central high pressure at the plateau was low, around 990 hPa.

2.2.2.10. 1-10 December 1999

The time series of winds along with the temperature depict a diurnal variation at both DC and DdU (Figures 2.5a-2.5b). On 2 December 1999 the pressure at DdU started decreasing and the winds increased in response to it and showed the maximum intensity recorded amongst the cases discussed. The wind increased to as high as 51 m/sec at 1200 hrs on 3 December 1999 within few hours. During this event the winds at DC remained unaffected. However, DC showed a marked rise in wind intensity upto 7 m/sec on 5 December 1999 in response to another system whose influence in not much felt at DdU.

Discussions and Conclusion

In this study, we have concentrated on the strong wind episodes observed at DdU and DC during the period (1993-99) to determine the extent of the role of the cyclones on surface winds. The time series of wind and pressure during the strong wind cases indicate that, in most of the cases, strong winds are associated with a decrease in pressure indicating the approach of a cyclone. Due to the general topography and the large elevation, the effect is seen more on the coastal station - DdU, while at DC the effect is usually not present. However, there are instances when the wind increased to above 15 m/sec at DC during the approach of the depression towards the Adelie land coast.

It is observed that the approaching cyclone has greater influence on surface wind regime. They continue to influence the wind until past the station. Almost all strong

wind events at DdU were observed in association with a decreasing pressure and an approaching depression offshore from the west of the station. Intensity and duration of strong wind events also depend very much upon the intensity of the high pressure system over the plateau from where the wind originates, apart from the intensity, position and velocity of the depression. The factors, the presence of the anicyclone over the interior, low over the ocean, its position with respect to the area of study, presence of a blocking anticyclone over the ocean to the northeast of Adelie land coast and maybe some other phenomena, have their combined influence on the intensity and duration of wind.

In summer months, winds along with the temperature show diurnal variation (Figures 2.3e, 2.3f, 2.5a, 2.5b). But mildly high winds (upto 5 m/sec for DC and upto 10-15 m/sec for DdU) are observed only for a short duration in which the inversions exist. This diurnal variation in wind is due to the diurnal variation which exists in its forcing mechanism - inversions. The maxima in wind in pure katabatic wind events during a short period in summer are associated with the minima in the temperature. The wind during these events rarely increase beyond 5-6 m/sec for DC and 10-15 m/sec for DdU. These mildly high winds, which temporarily destroy the inversions by vertical mixing, and, in turn acts to cease themselves. However, much before the wind driven heating could have its influence, the solar heating in the morning starts to increase the near surface temperature and, hence, destroy the inversions, and, therefore, the katabatic winds cease. The cases of longer duration winds with strength greater than 15 m/sec at DdU are associated with a change in pressure, mainly falling with the approach of a depression. The convergence of air mass, the rising motion (within the depression), a return flow and subsequently, subsidence over the continent, takes place rapidly in the presence of a depression offshore [Ekman pumping, Salby 1995; Naithani et al., 2001a]. This is envisaged as helping in maintaining a continuous flow for a longer duration. These strong wind events reach their peak intensity at approximately the same time as the minimum in station level pressure. Whenever a cyclone is approaching, the effect on wind is seen, as the wind is more intense (usually greater than 20 m/sec at DdU and >10 m/sec at DC) and persists for longer duration. This is clearly differentiated/indicated in the December 1993 and December 1999 time series. The diurnal variation in wind has strength not more than 5 m/sec at

DC and 15 m/sec at DdU, while the winds associated with decreasing station level pressure have intensity greater than 10 and 20 m/sec at DC and DdU, respectively.

According to Schwerdtfeger, [1984] due to the presence of a cyclone there will be a reverse flow above the boundary layer. This reverse flow is envisaged to supply the air mass to subside over the continent and helps in the faster replenishment to feed the gravity flow for longer duration [Ekman pumping, Salby 1995; Naithani et al., 2001a]. The high pressure ridge preceding the depression near the coast also helps in the building up of cold air reservoir to feed the gravity flow later for longer duration [Murphy, 2000; Naithani et al., 20001b]. The effect of topography is the dominant force defining the surface wind direction. However, the presence of a cyclone increases the existing pressure gradient between the continent's interior and the coast, which increases the katabatic wind force. Although, the synoptic wind component during the passage of the depression is almost perpendicular to the katabatic flow direction and there will be some cancellation [Murphy and Simmonds, 1993]. However, now the katabatic component is itself strong due to the increased pressure gradient and a large cold air supply. Therefore, the resultant winds as a result of strong katabatic component and strong synoptic component are stronger and flow for a longer duration. In the end we would like to add that the confluence zones provide persistent and extreme force to katabatic winds. Nevertheless, even in these places the effect of cyclones is the same as in many other coastal stations. However, due to the funelling of winds from over a wider area, the wind is generally of gale force and more persistent than in the other coastal sites which do not get the benefit of the confluence.

Out of the strong wind events discussed, few of them showed the effect on the time series at DC. High wind (>15 m/sec) at DC were observed when the depression at the coast had penetrated much into the interior. During these situations, wind at DdU remain low or come down to the initial value in advance of the minimum in pressure, as the downslope pressure gradient becomes shallow during these events. Depressions penetrate inland due to the presence of a high pressure ridge to the northeast of Adelie land coast and a shallow anticyclone over the continent. The depression is unable to penetrate inland, if the anticyclone over the continent

happens to be strong, in spite of the presence of the high pressure ridge to the northeast.

There were other strong wind events during the period 1993 to 1999. However, not all of them could be discussed in the present work, and only a few cases have been discussed. Figure 2.14 shows the time series of horizontal wind and pressure for all the months in the year 1993. The negative correlation between the wind and the pressure in the strong wind cases can be seen. From this figure one can envisage that it is the strong wind which are causing the convergence, and, hence, the cyclonic vorticities to develop near the coast. From the examination of the pressure charts for the same period, however, it is evidenced that, in actuality, it is the low pressure system which initiates strong winds and gets intensified in the process due to the wind drainage. The convergence of wind at the coast (in the absence of a depression) should cause the pressure to become high! However, the depression offshore helps in removing the excess air mass by lifting this air mass higher up with the subsequent return flow at higher levels.

To conclude with, it is observed that the presence of a low is necessary for sustaining strong winds at DdU along with a high over the continent. Although, most of the cases were accompanied by a low over the ocean and a high over the continent. On few occasions, the low over the ocean was able to initiate strong wind at DdU, even though the central high pressure over the plateau was not very high. Nevertheless, it is observed that the presence of a low is necessary for initiating strong wind events at DdU, the coastal Antarctic site. Winds at DdU come down or remain low if there is no depression at the coast, even if the high pressure over the continent continues to be very high. It is observed and envisaged that although the strong wind commences with the approach of the depression towards the Adelie land coast from the west, however, the resulting drainage of wind feeding the cyclones, enhance the baroclinicity. We have tried to explain the strong wind episodes at DdU on the basis of synoptic situations, and to some extent at DC. However, more work is needed to study fully the strong wind events at DC, which are rather rare.

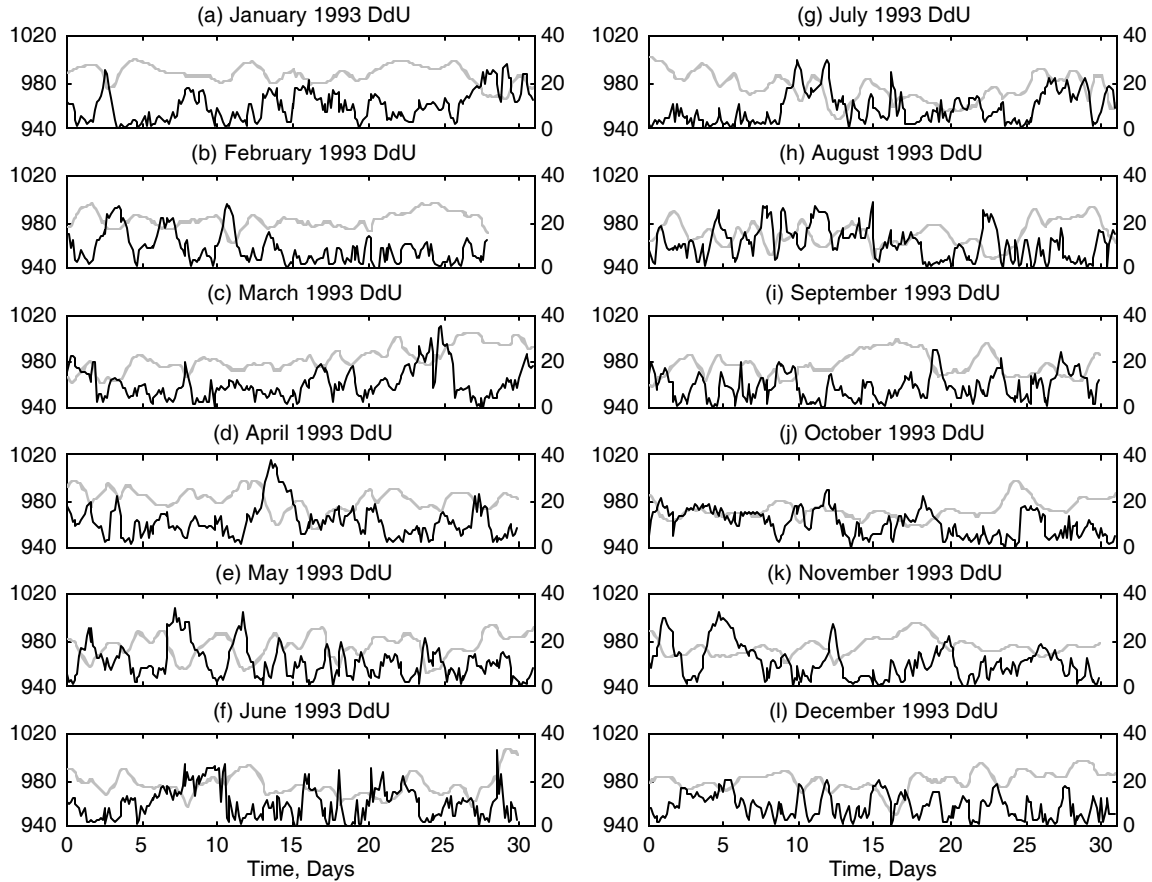


Figure 2.14. Time series of horizontal wind (full) and pressure (dotted) for all the months in the year 1993 for Dumont d'Urville.

Parish and Bromwich, 1998, speculated that the Antarctic continent topography acts as a channel for cold, negatively buoyant air that can feed into the cyclones, enhancing the baroclinicity. They proposed that the orographic forcing and the confluence of cold air over the continent in certain coastal regions provide enhanced support for cyclone formation and development. We propose that the approach of the depression towards the coast from the west triggers the commencement of strong surface winds, these winds in turn feed the cyclones and enhance the baroclinicity. Due to the funnelling of winds from over wider areas in the confluence zones, the enhancement of baroclinicity can be much more than in the rest of the coastal areas. Nevertheless, the fact remains, that it is the approach of the depression which triggers the strong wind events. The preceding high pressure ridge (builds the cold air supply by way of strong inversions) and the depression itself (by way of convergence near the coast, rising motion with a return flow and subsequent subsidence over Antarctica)

help in maintaining the flow for longer duration. We observed the later case being more effective in sustaining intense winds for longer durations.

If katabatic winds are a part of Antarctic weather and climate, cyclones also are a part of it. One cannot talk of Antarctic weather or climate without mentioning the katabatic winds, and, strong winds without mentioning the cyclones. While discussing the weather and climate of Antarctica, particularly the strong surface winds, cyclones cannot be avoided and should be considered an integral part of the Antarctic system. First, they increase temporarily the pressure gradient force and hence, increase the KB wind force. Secondly, they increase the duration of the KB flow by providing a faster way of replenishing the upper air mass in the interior by way of convergence and rising motion at the coast, which moves inland at higher levels and subsequently subsides over the continent.

Acknowledgements

This work is part of the European Commission project for Ice Coring in Antarctica. One of the authors [JN] is thankful to the Belgian Ministry of Science Policy for giving the opportunity to work in this project. Thanks are also due to Dr. Alexis Dutrieux for retrieving the ECMWF analyses from the ECMWF archives. The meteorological data is downloaded from the University of Wisconsin and British Antarctic Survey web sites.

References

- Ball, F.K., The theory of strong katabatic winds, *Aust. J. Phys.*, 9, 373-386, 1956
- Ball, F.K., Winds on the ice slopes of Antarctica, *Antarctic Meteorology, Proceedings of the Symposium held in Melbourne*, February 1959, 9-16, Pergamon Press, New York, 1960.
- BAS, <http://www.nerc-bas.ac.uk/public/icd/metlog/>.
- Bromwich, D.H., Y. Du, and T.R. Parish, Numerical simulation of winter katabatic winds from west Antarctica crossing Siple Coast and the Ross Ice Shelf, *Mon. Wea. Rev.*, 122, 1417-1435, 1994

Carroll, J.J., Structures of atmospheric energy transfer at the South Pole, *Ant. J U.S.*, 18[5], 248-249, 1983.

King, J.C., and Turner, J., *Antarctic Meteorology and Climatology*, pp 409, Cambridge Atmospheric and Space Science Series, Cambridge University Press, 1997.

Loewe, F., Considerations concerning the winds of Adelie land, *Z. Gletscherkd. Glazialgeol.*, 10, 189-197, 1974.

Mather, K.B., and G.S. Miller, Notes on topographic factors affecting the surface wind in Antarctica, with special reference to katabatic winds; and Bibliography, University of Alaska, Fairbanks, 63 pp., Technical Report , Grant no. GA-900, 1967a.

Mather, K.B., and G.S. Miller, The problem of the katabatic winds on the coast of Terre Adelie, *Polar Record*, 13, 425-432, 1967b.

Murphy, B.F., Severe weather forecasting at east Antarctica coastal stations, Preprint volume of the Antarctic Weather Forecasting Workshop, 17-19 May, Eds. E.N. Cassano and L.R. Everett, 26-31, 2000.

Murphy, B.F., and I. Simmonds, An analysis of strong wind events simulated in a GCM near Casey in the Antarctic, *Mon. Weather Rev.*, 121, 522-534, 1993.

Naithani, J., G. Mastrantonio, S. Argentini and P . Pettre, Influence of cyclonic perturbations on surface winds around Dumont d'Urville, East Antarctica using wavelet transform, *J. Geo. Res.* [accepted], 2001a.

Naithani, J., H. Gallée and G. Schayes, Marine air intrusion into the Adelie land sector of East Antarctica - A study using regional climate model [MAR], *J. Geo. Res.* [submitted], 2001b.

Parish, T.R., The katabatic winds of Cape Denison and Port Martin, *Polar Record*, 20, 525-532, 1881.

Parish, T.R., Surface airflow over east Antarctica, *Mon. Weather Rev.*, 110, 84-90, 1982.

Parish, T.R., A numerical study of strong katabatic winds over Antarctica, *Mon. Weather Rev.*, 112, 545-554, 1984.

Parish, T.R., On the role of Antarctic katabatic winds in forcing large-scale tropospheric motions, *J. Atmospheric Science*, 49, 1374-1385, 1992.

Parish, T.R., and D.H. Bromwich, The surface windfield over the Antarctic ice sheet, *Nature*, 328, 51-54, 1987.

Parish, T.R., and D.H. Bromwich, Continental scale simulation of the Antarctic katabatic wind regime, *J. Climate*, 4, 135-146, 1991.

Parish, T.R., and Bromwich, D.W., A case study of Antarctic wind interaction with large-scale forcing, *Mon. Wea. Rev.*, 126, 199-209, 1998.

Parish, T.R., D.H. Bromwich, and Ren-Yow Tzenz, On the role of the Antarctic continent in forcing large-scale circulation in the high southern latitudes, *J. Atmospheric Science*, 51, 3566-3579, 1994.

Parish, T.R. and Gerd Wendler, The katabatic wind regime at Adelie Land, Antarctica, *Int. J. Climatol.*, 11, 97-107, 1991.

Parish, T.P, P. Pettré, and G. Wendler, A numerical study of the diurnal variation of the Adelie Land katabatic wind regime. *J. Geophys. Res.*, 98[D7], 12,933-12,947, 1993a.

Parish, T.P, P. Pettré, and G. Wendler, The influence of large-scale forcing on the katabatic wind regime at Adelie Land, Antarctica. *Meteorol. Atmos. Phys.*, 51, 165-176, 1993b.

Parish, T.R., and K.T. Waight, The forcing of Antarctic katabatic winds, *Mon. Weather rev.*, 115, 2214-2226, 1987.

Pook, M., and Cowled, L., On the detection of weather systems over Antarctic interior in the FROST analyses, *Weather and Forecasting*, 14, 920-929, 1999.

Salby, M.L., *Fundamental of Atmospheric Physics*, International Geophysics Series, vol 61, Academic Press, 627 pp, 1995.

Schwerdtfeger, W., *Weather and climate of the Antarctic*, Elsevier, New York, 1984.
Streten, N.A., Some observations of Antarctic katabatic winds, *Aust. Meteorol. Mag.*, 42, 1-23, 1963.

Streten, Characteristics of strong wind periods in coastal East Antarctica, *J. Applied Meteorol.*, 7, 46-52, 1968.

Streten, A review of the climate of Mawson-A representative strong wind site in east Antarctica, *Antarct. Sci.*, 2, 79-89, 1990.

Wendler, Gred, C. Stearns, G. Weidner and G. Dargaud, On the extraordinary katabatic winds of Adelie Land, *J. Geo. Res.*, 102, 4463-4474, 1997.

WU, <ftp://ice.ssec.wisc.edu/pub/antrdr/>.

BASAL ICE FROM EAST ANTARCTICA (EPICA)

CONTRACT ANTAR IV/DD/E02

R. LORRAIN,
S. SLEEWAEGEN,
R. SOUCHEZ,
J.-L. TISON

Département des Sciences de la Terre et de
l'Environnement
Université Libre de Bruxelles - CP 160/03
Avenue F.D. Roosevelt, 50
B-1050 Brussels
Belgium

TABLE OF CONTENT

ABSTRACT	1
KEY-WORDS	1
1 GOALS AND STRATEGY	2
2 MATERIALS AND METHODS	4
3 STATE-OF-THE-ART	4
4 RESULTS AND DISCUSSIONS	5
4.1 Study of basal ice in the Dry Valleys of South Victoria Land	5
4.1.1 Introduction	5
4.1.2 Site description	7
4.1.3 Ice composition evidence for the formation of basal ice from lake water beneath Sues Glacier	10
4.1.4 Structure and strength of basal ice and substrate of Sues Glacier: evidence for substrate deformation at subfreezing temperatures	14
4.1.4.1 Methods	14
4.1.4.2 Ice movement at the bed	15
4.1.4.3 Shear strength of the ice and substrate	16
4.1.4.4 Discussion	18
4.1.5 Conclusions	19
4.2 Study of ice formed at or near the grounding line in Terra Nova Bay area	20
4.2.1 Introduction	20
4.2.2 Framework of the study	21
4.2.3 Evidence for freezing close to grounding lines in	

Terra Nova Bay	23
4.2.4 Freezing by a double-diffusion mechanism at the grounding line	25
4.2.5 Isotopic evidence of the double-diffusion mechanism	26
4.2.6 Subglacial meltwaters origin and formation of debris-rich ice in the western moraine of HGIS	28
4.2.7 Conclusion	33
4.3. Study of lake ice at the bottom of the Vostok ice core	33
4.3.1 Introduction	33
4.3.2 More than 200 m of lake ice above subglacial Lake Vostok	34
4.3.3 Ice formation in subglacial Lake Vostok	42
4.3.3.1 A rough estimation of Vostok lake salinity	44
4.3.3.2 Water circulation	46
4.3.3.3 Ice formation in the subglacial lake	47
4.3.4 Conclusion	50
5 OVERALL CONCLUSIONS	50
ACKNOWLEDGEMENTS	52
REFERENCES	53

ABSTRACT

Ice composition studies are powerful tools not only to reconstruct past fluctuations of important climatic and environmental parameters but also to study the ice sheet behaviour resulting from interactions between basal ice and the glacier bed. Deep ice drillings in Antarctica are so able, on the one hand, to provide a climatic archive of several hundred thousands years at relatively high resolution based on the properties of glacier ice but also, on the other hand, to give information on past boundary conditions derived from the characteristics of basal ice.

In East Antarctica, radio-echo-soundings have revealed the existence of numerous subglacial lakes, in particular in the Dome C area, site of a deep drilling of the EPICA project. Such lakes are likely to have a considerable influence on ice flow and thus on the age-depth relationship in deep ice. Since ice older than 100.000 years cannot be dated by geochronological methods, the construction of a reliable flow model is required for dating ice at depth.

Within this context, different studies are conducted in areas where the East Antarctic Ice Sheet is interacting with water bodies in order to allow correct interpretation of the basal ice sequence at Dome C. A case study of a cold-based glacier flowing into a lake shows that transient wet-based conditions occur as ice flows into the unfrozen sediments of the lake bottom, creating conditions favorable to the entrainment of sediments and to ice accretion by water freezing. In another case study, a newly discovered freezing mechanism at the grounding line, called double-diffusion freezing, is described and discussed.

The deepest part of the Vostok ice core was also studied during this research program. It consists of lake ice, formed by freezing of water from lake Vostok, an extensive subglacial lake present underneath the drilling site. A study of ice properties of the lake ice allows to reconstruct the mechanisms of its formation and to understand the interactions between the subglacial lake and the ice sheet.

KEY-WORDS

Antarctic glaciology - Basal ice - Grounding line - Lake ice - Stable isotopes - Gases in ice - Dry Valleys - Terra Nova Bay - Vostok.

1 GOALS AND STRATEGY.

In order to be able to understand the behaviour of the East Antarctic Ice Sheet, the interactions between the ice sheet and its substratum must be well known. The study of the composition of basal ice can shed light on the processes acting or having acted at the ice-bedrock interface.

Basal ice can only be reached in three circumstances.

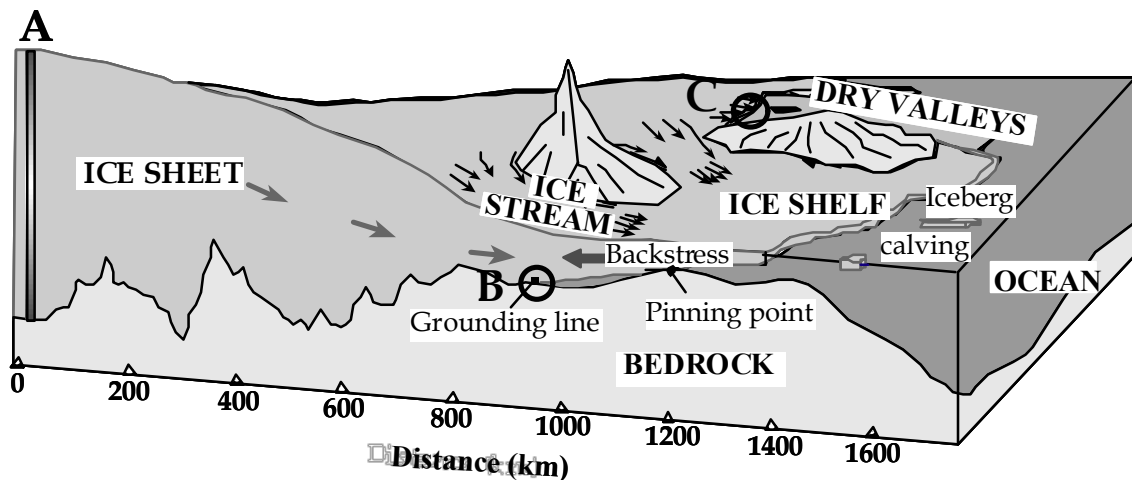


Figure 1 : The research program will focus on the study of basal ice from different sites in Antarctica (see text).

1. A deep drilling reaching the bedrock under the ice sheet is undertaken at one specific place like the deep drilling of the European Program of Ice Coring in Antarctica (EPICA project) at Dome C in the central part of an ice dome in East Antarctica. In such a situation, basal ice can be perforated and sampled like at the location represented by site A in figure 1.

2. Basal ice can leave the ice-rock interface at the grounding line and be included in the ice shelf bordering the ice sheet where a backstress is exerted. This requires that basal melting is not occurring in the contact zone between the ice sheet and the ocean. Such a situation can prevail in areas protected from the influence of high salinity shelf waters (HSSW) which promote melting at the ice-ocean interface. Due to the ablation resulting from the action of katabatic winds at the ice shelf surface, basal ice can ultimately appear at or close to the surface where it can be more easily reached. Such a situation is depicted on site B in figure 1 and presently occurs in Terra Nova Bay near the Italian station of the same name.

3. Due to special environmental circumstances, the ice coming from the central part of the ice sheet does not completely fill the valleys of a marginal mountain range. Some of these valleys are even devoid of an ice cover and are called dry valleys. At the border of the ice sheet or at the margin of its outlet glaciers, basal ice

is outcropping and can be sampled. Site C in figure 1 represents such a situation. The region called the Dry Valleys area in South Victoria Land in the vicinity of the two permanent stations of MacMurdo (USA) and of Scott Base (New Zealand) is such a favorable place.

The strategy set up to gain substantial information within this context is based on the study of the composition of basal ice, mainly the composition in the stable isotopes of oxygen and hydrogen from the ice crystals, the total gas content and gas composition in the principal atmospheric gases (O_2 , N_2 , CO_2) and in methane and also the crystallographic properties. In some circumstances, chemical analyses of major anions and cations are also conducted to derive additional information. Specific techniques are required for the analysis of basal ice, because it is rich in debris and poor in gases. Some of the techniques are already used on a routine basis in our laboratory; others have been developed during the first part of this contract while the efficient use of the helium trap for concentrating gases in the case of an ice sample extremely poor in gas content (less than 0.01 ml / g) is still under development.

Radio-echo-soundings in East Antarctica have revealed the existence in numerous areas of subglacial lakes. The more extensive of these lakes is lake Vostok near the Russian station of the same name which has dimensions comparable to lake Ontario in North America (about 14000 km²). Smaller subglacial lakes are numerous in East Antarctica and present in the immediate vicinity of Dome C. The presence of such lakes is important to consider as far as the interactions of the ice sheet with its substratum are concerned, these interactions playing a major role in ice deformation. A study of basal ice deformation is indeed of paramount importance to be able to develop a flow model for the entire ice sheet in the Dome C area, flow model required to establish an age-depth relationship for the deep ice older than 100000 years which will be reached by the EPICA drilling. Retrieval of reliable palaeoclimatic information from before the last major climatic cycle is thus dependent on the knowledge of basal boundary conditions.

Therefore, the emphasis in this antarctic research contract is put on studying situations where the East Antarctic Ice Sheet is interacting with water bodies in order to be able to interpret correctly the basal ice sequence from Dome C. Furthermore, we have shown that, in Central Greenland, basal ice preserves information revealing genetic processes of the ice sheet, for instance, the incorporation by mixing at the ice sheet base of ice formed at the ground surface, or within the upper part of the ground.

2 MATERIALS AND METHODS

Ice samples are provided, either as ice cores by a drilling operation or as ice blocks using a chainsaw. They are stored in plastic bags and kept at a temperature below -18°C . Moreover, the samples cut for the analyses are retrieved in the cold room of our laboratory after shaving the walls of the cores or re-sawing a slice, 1cm thick, parallel to each side of the chain-sawed blocks. These subsamples are cut with a non contaminating band saw or, if they are rich in mineral particles, with a diamond wire saw (Tison et al., 1994).

The samples are studied for their gas characteristics using methods developed in our laboratory. CO_2 , O_2 and N_2 concentrations are measured by gas chromatography (Varian 3300) using a crushing method to extract the gas (dry extraction) (Souchez et al., 1993). The CH_4 concentrations are also measured by gas chromatography (Chrompack CP 9001) but the gases are extracted using a melting-refreezing method (Blunier et al., 1993). Total gas content is measured by a Toepler pump after a gas extraction by melting-refreezing (Janssens, 1996). The chemical analyses are carried out by atomic absorption spectrophotometry (Varian SpectrAA-300) for the major cations (Na, K, Ca, Mg) and by ion chromatography (Dionex DX-100) for the major anions (Cl, SO_4 , NO_3). The stable isotope measurements are performed at the Nuclear Research Center of Saclay (France) and at the University of Trieste (Italy). HDO and H_2^{18}O concentrations are given in δ units versus VSMOW (Vienna Standard Mean Ocean Water) and expressed in per mil. The results obtained in δD and $\delta^{18}\text{O}$ on mass spectrometers have an accuracy of about 0.1 ‰ in δD and 0.05 ‰ in $\delta^{18}\text{O}$. Only a few millilitres are required to perform both analyses.

3 STATE-OF-THE-ART

Analysis of basal ice from deep ice cores in polar regions dates from the years sixties when two American deep drillings were launched, one at Camp Century in North-West Greenland and the other at Byrd Station in West Antarctica. It became clear from the results of these two ice cores that the composition of ice close to the bed does not reflect past atmospheric conditions contemporaneous with the transformation into ice of the snow accumulations at the ice sheet surface but, instead, is the result of the interactions between the ice sheet and its substratum. Later on, geophysicists of the University of Copenhagen developed flow models taking into account the particularities of this basal ice. Such flow models were

critically needed to obtain an age-depth relationship for deep ice.

A further step occurred in the eighties when we used with scientists from the Centre d'Etudes Nucléaires de Saclay in France a co-isotopic ($\delta^{18}\text{O}$ and δD) approach to the study of basal ice. If such compositions of basal ice are considered together, then phase changes occurring or having occurred at the bottom of an ice sheet can be determined. Such melting and refreezing events are to a large extent responsible for basal sliding which enhances ice flow.

In the nineties, a major european effort, the GRIP project, succeeded to perforate the Greenland Ice Sheet at Summit in its central part and reached bedrock 3030 m below the surface. Results of basal ice studies not only helped to determine basal boundary conditions but also put into light the existence of very old ice formed at the ground surface in the absence of the ice sheet. This ice appeared to have been incorporated and mixed with glacier ice during the subsequent growth of the ice sheet from the eastern mountainous area to the central part of Greenland. Therefore we were able to reconstruct the initial conditions of the ice sheet, an achievement of significant value for model development.

The fact that basal ice was well developed at the base of a great ice dome in Greenland, an unlikely place for its presence due to lack of shear, suggested that Antarctic ice domes could contain information on their early development. As numerous subglacial lakes were recently detected by radio-echo-soundings near Dome C, one of the two sites of the EPICA project, there is now a need for new information about ice sheet interaction with water bodies.

4 RESULTS AND DISCUSSIONS

4.1 Study of basal ice in the Dry Valleys of South Victoria Land

4.1.1 Introduction

Dirty basal ice layers are present at many locations beneath polar glaciers and ice sheets having basal temperatures that are lower than bulk pressure-melting temperature (Holdsworth, 1974; Koerner, 1989; Fitzsimons, 1996; Gow et al., 1997). Entrainment of debris by cold-based glaciers having basal temperatures as low as -17°C can be observed in the Dry Valleys of south Victoria Land. The classical models developed to explain debris incorporation at the glacier base are inappropriate in such cases, since the basal temperature is well below the freezing point.

In the reconstruction of ice sheets and glaciers, geomorphologists tend to associate frozen bed conditions with hiatuses in landform development during which no new landforms are created with the exception of occasional glaciotectionic features (Kleman and Borgström, 1994; Kleman and Borgström, 1996). The underlying assumption of such studies is that glaciers that are frozen to their beds are largely incapable of erosion. However, theoretical studies by Shreve (1984) and Fowler (1986) concluded that sliding is possible at subfreezing temperatures and an empirical study by Boulton (1979) suggested that in some instances dry-based glaciers are capable of bed erosion. Subsequently, a study of the Urumqi Glacier No 1 (basal temperature -5°C) concluded that glacier movement was achieved by deformation of the substrate, movement along discrete shear planes within the frozen substrate or at the ice-substrate interface, and by basal sliding at ice-rock interfaces (Echelmeyer and Zhongxiang, 1987). Despite these theoretical and empirical studies it is still relatively common to encounter studies that reject the possibility of basal sliding and erosion by dry-based glaciers. The apparent divergence in the geomorphological and glaciological literature requires attention if we are to make progress in the reconstruction of the thermal and dynamic conditions of former glaciers from glacial geological evidence.

Among the glaciers flowing down the valley sides of the Dry Valleys of South Victoria Land (Antarctica), those which are not confined to the valley sides but reach the valley floor show thick sequences of debris layers incorporated at their base. Although these glaciers are cold-based (temperature lower than -17°C), those with ice marginal lakes show well preserved stratified sedimentary structures obviously entrained within their basal part. Observations made in a 25 m long tunnel dug at the bed of one of these glaciers (Fitzsimons et al., 1999) confirm that many basal ice structures visible at the ice margin represent extensions of subglacial structures observable 100 m upglacier of the margin.

Recently, Fitzsimons (1996) proposed a model that explained the formation of thrust-block moraines at the margin of such glaciers which flow into lakes maintaining an unfrozen bed (Figure 2). Such lakes are common in the Dry Valleys (Wilson et al., 1974 ; Cartwright and Harris, 1978; Chinn, 1993). This model takes into account the change in position of the 0°C isotherm when a glacier is flowing into a lake. Transient wet-based conditions occur as ice flows onto unfrozen sediments of the lake bottom. Water can be confined near the glacier sole, at the lake margin and basal freezing can occur since glacier ice acts as a cold source. Ice accretion and basal incorporation of sediment layers take place in such conditions. Rising flow vectors characteristic of the ablation zone of the glacier result in the upward movement of the accreted ice and debris.

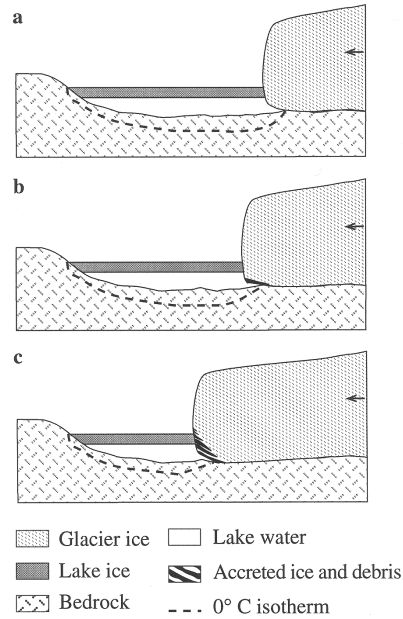


Figure 2 : Depositional model for the formation of thrust-block moraines at the margin of cold-based glaciers that flow into lakes. See text for explanation.

In this context, basal ice from a dry-based glacier was studied: Sues Glacier, in Taylor Valley.

4.1.2. Site description

Suess Glacier is a 5 km long alpine glacier that descends from 1750 m on the Asgard Range and flows across the floor of the Taylor Valley (Figure 3). It rests on unconsolidated sediments that are frozen to a depth of more than 300 m.

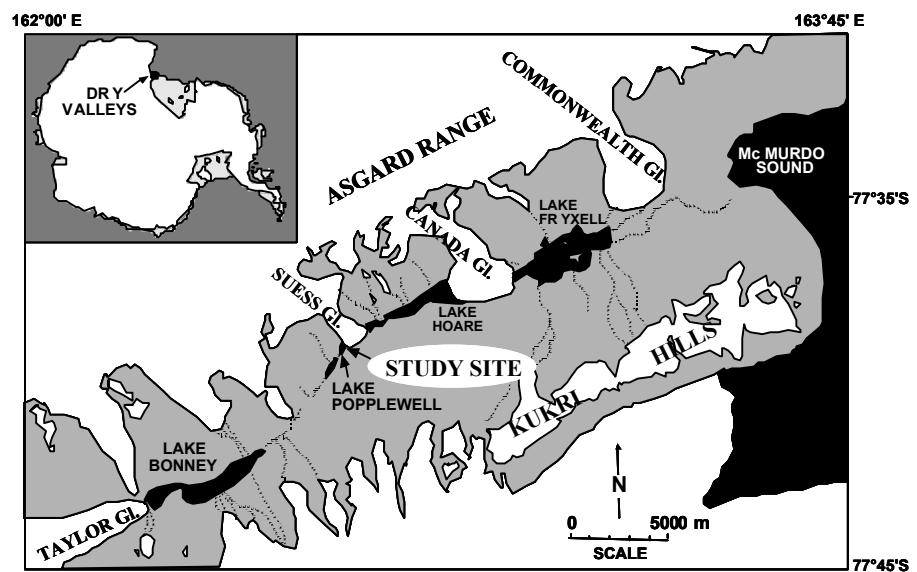


Figure 3 : Location map : the study site is situated where Lake Popplewell and Suess Glacier are the closest to each other.

At the terminus, the right side of the glacier flows up the Taylor Valley and forms a 18-20 m high cliff overlooking an ice and debris apron adjacent to Lake Popplewell. As all the other alpine glaciers of the Dry Valleys, the whole glacier is below the pressure-melting point (Chinn, 1991) and a basal temperature of -17°C has been measured here. The surface of the glacier is debris-free apart from very few boulders coming from the valley sides. The substrate of the glacier (revealed by excavation below the basal ice) consists of frozen planar bedded or crossed-bedded sand and also of massive unstratified sand containing layers of fine gravels.

Direct observation and excavation of the ice and debris apron from its base to its contact with the vertical part of the ice cliff reveals a 3-5 m thick series of ice layers of variable thickness (1 cm to a few decimeters) interbedded with sand and fine gravel beds. Occasionally a thin organic mud layer or an algae layer (a few millimeter thick) is associated with a sand layer. The whole stacked sequence is dipping between 12 and 22 degrees in an up-glacier direction. The particle-size characteristics of the sediment are similar to the ones of the adjacent lacustrine environment (Fitzsimons, 1996).

The ice layers in the apron show different facies which fit the classification scheme developed by Sharp et al. (1994). The main components of the basal ice zone are basal dispersed, basal laminated, basal clear and basal solid facies that are overlain by the amber ice facies, the latter being the only one previously reported in the Dry Valleys at the base of the Meserve Glacier (Holdsworth, 1974). Some blocks of undisturbed lacustrine sediments are included within the sequence especially in the upper part of the apron. The well preserved primary sedimentary structures of these blocks suggest the sediments were frozen during entrainment. This apron is thus very different from the ice cliff above, which consists in bubbly glacier ice devoid of visible particles.

Observation of the basal zone were made thanks to a tunnel excavated in the glacier. At the end of the tunnel, the basal zone is approximately 3.8 m thick and can be divided into five main units (Figure 4) which include clean englacial ice (0-0.3 m), a discoloured ice facies (0.3-1.1 m), a solid layer of frozen sediment (1.1-1.6 m), a basal laminated facies (1.6-4.0 m) and the substrate (Figure 4). The discoloured ice that rests immediately below the clean englacial ice contains dispersed particles and fine aggregates, which give the ice a greenish to amber colour. This ice is the "amber ice" that has been described as an important component of dry-based glaciers throughout the McMurdo Dry Valleys (Holdsworth, 1974). The amber ice is underlain by a broken layer of frozen sand and fine gravel that contains well preserved sedimentary structures. This layer lies about 2 m above the glacier bed. The laminated ice that lies below the main debris band consists of multiple layers that range from near-horizontal, clean bubbly ice to complexly deformed layers of ice with very high debris concentration. Occasional boulders up to 1.2 m in diameter were observed in the laminated ice up to 2 m above the bed. Ice with relatively low debris

concentrations contained abundant ductile structures, whereas structures in the solid layers indicate predominantly brittle deformation. The bulk of the ductile deformation structures are tangential to the bed. Exposures of the substrate in the tunnel showed that the ice-substrate interface was a gently-sloping (c 5°), smooth contact between basal ice and frozen sand. Particle size analysis of the samples from the substrate showed that 75% of samples were polymodal. The most frequently occurring modes were centred on 1.5 mm (very coarse sand), 0.5mm (coarse-medium sand) and 0.2 mm (fine sand).

Both the frozen sediment layer and the basal ice contain numerous cavities. The most widespread type of cavity occurs on the upstream and downstream sides of boulders and sediment blocks where ice flow around the obstacles has resulted in flow separation that have produced cavities up to 1 m long, 0.6 m wide and 300 mm high. Cavities also occur within the sediment band where blocks of frozen sediment have fractured, within relatively clean basal ice and at the ice-substrate interface. Several of the cavities contained gas at pressures slightly higher than atmospheric pressure.

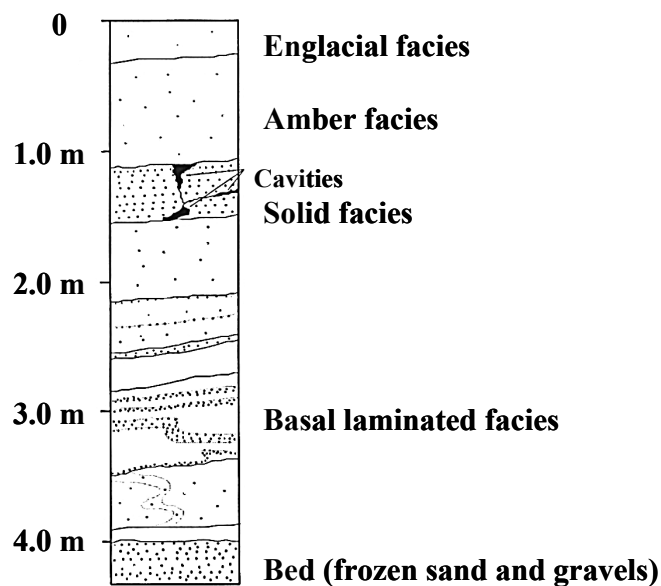


Figure 4 : Description of the basal zone 24m into the tunnel. The ice exposure shows five main units including clean englacial ice (0-0.3 m), a discoloured ice facies (0.3-1.1 m), a solid layer of frozen sediment (1.1-1.6 m), a basal laminated facies (1.6-4.0 m) and the substrate. Layers and structures within the basal zone dip in an upstream direction at angles between 3 and 10°.

Four conclusions can be drawn from observations of the basal zone exposed in the tunnel:

1. Large blocks of sediment have been eroded from the frozen bed of the glacier.

2. Many of the blocks in the basal ice have been entrained without disaggregation.
3. Ice flow has elevated the main sediment layer about 2 m above the bed.
4. The tunnel demonstrates that many of the proglacial structures observed around the margin of the glacier are similar to subglacial structures.

4.1.3 Ice composition evidence for the formation of basal ice from lake water beneath Suess Glacier

An excavation made in the apron permitted sampling of many of the ice beds present in the sequence. All samples were taken with the aid of a chain saw equipped with tungsten carbide teeth. Blocks about 10 cm wide and 30-40 cm high were taken along the vertical sequence, wrapped in polyethylene bags and immediately stored in a freezer installed in the nearby field camp.

Additionally, seven shallow ice cores (1.6 m long) were retrieved from the upper surface of Suess Glacier along a longitudinal profile with a SIPRE type ice auger. Finally, a one meter long ice core was also taken from the ice cover of the adjacent Lake Popplewell.

A subsampling was carried out in the laboratory on the ice for isotopic and gas analyses.

Basal ice clearly differs from glacier ice as far as its isotopic composition is concerned. Displayed on a graph in which $\delta^{18}\text{O}$ is plotted against δD (Figure 5), the twenty five glacier ice samples from the glacier surface are aligned along a straight line with a slope $S = 8.1$. The line has the equation :

$$\delta\text{D} = 8.1 \delta^{18}\text{O} + 9.4 ; r^2 = 0.98 \quad (1)$$

and can be considered as the local Meteoric Water Line as defined by Craig (1961). The world Meteoric Water Line has been recently redefined by Rozanski et al. (1991) as having the equation :

$$\delta\text{D} = 8.17 \delta^{18}\text{O} + 10.35 (r^2 = 0.99 ; n = 206). \quad (2)$$

Such a relationship derived from fresh precipitation is generally true for glacier ice that has not undergone isotopic changes since its formation in the accumulation area.

By contrast, the eighty five ice samples taken from the apron section show a linear relationship with a slope $S = 5.4$. The regression line has the equation :

$$\delta\text{D} = 5.4 \delta^{18}\text{O} - 79 (r^2 = 0.97) \quad (3)$$

This slope is typical for ice due to water freezing as explained by Jouzel and Souchez (1982) and Souchez and Jouzel (1984). These authors have shown theoretically and experimentally that progressive freezing of a water reservoir

induces changes of the isotopic composition of successively formed ice increments. The more negative values correspond to the ice formed when the freezing front draws near to the end of the reservoir. The evolution in δD and $\delta^{18}O$ during freezing defines in a δD - $\delta^{18}O$ diagram a so-called "freezing slope" which constitutes a specific isotopic signature of the ice produced by water freezing. This slope can be calculated by the following equation :

$$S = \frac{\alpha [(\alpha - 1) (1 + \delta_i)]}{\beta [(\beta - 1) (1 + \Delta_i)]} \quad (4)$$

where δ_i is the δD composition of the parent water, Δ_i its $\delta^{18}O$ composition, α and β , the values of the ice-water equilibrium fractionation coefficients for deuterium (taken as 1.0208) and for ^{18}O (taken as 1.003), respectively.

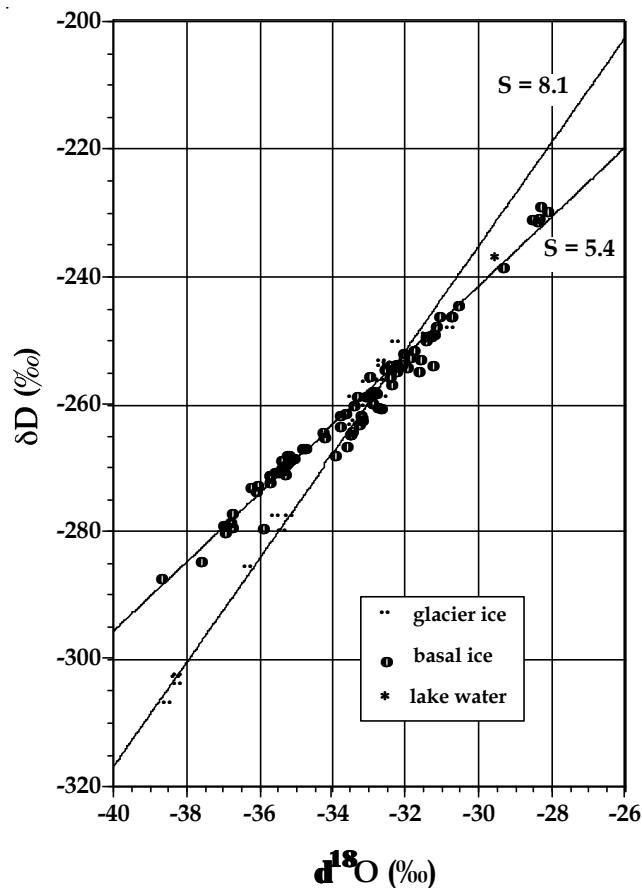


Figure 5 : δD - $\delta^{18}O$ diagram of all samples analysed from the glacier surface (\blacklozenge), from the basal ice (\circ) of Suess Glacier and from lake ice of Lake Popplewell ($*$). S is the value of the slope of the regression line.

If, as suggested by Souchez and Jouzel (1984), the δ -values at the intersection of the two regression lines are taken as the isotopic composition of the parent water

($\delta^{18}\text{O} = -32.74\text{‰}$ and $\delta\text{D} = -255.8\text{‰}$) the slope calculated from equation (4) for a freezing process is 5.4. If water sampled in Lake Popplewell (adjacent to the glacier) is taken as parent water ($\delta^{18}\text{O} = -29.56\text{‰}$ and $\delta\text{D} = -237.5\text{‰}$), the calculated slope is 5.5. These two calculated slopes are in close agreement with the slope of 5.4 obtained from the basal ice samples of the apron of Sues Glacier. Co-isotopic analyses of this ice thus indicate that water freezing plays a major role in the build-up of the basal ice sequence of Sues Glacier.

Results from gas analyses give further arguments. Basal ice indeed clearly differs from surface glacier ice in both gas content and gas composition (Table I).

Table I : Results of gas analyses of ice samples from Sues Glacier and from Lake Popplewell.

Ice type	Sample number	Depth from surface or from the limit between glacier ice and basal ice (cm)	Total gas content ($\text{cm}^3 \text{g}^{-1}$)	[CO ₂] (ppmv)	[O ₂] (%)	[N ₂] (%)	O ₂ /N ₂
Glacier ice	Su G5 b	104-110	0.070	344	21.05	78.90	0.267
Basal ice	Su I 3 bis	-36	0.020	222900	20.00	57.71	0.347
	Su I 3	-83	0.020	56041	21.47	72.92	0.294
	Su I 3/3	-88	0.022	148063	29.01	56.19	0.516
	Su I 16/3a	-303	0.083	6911	21.29	78.02	0.273
	Su I 19 a	-444	0.006	4078	19.61	79.98	0.245
	Su II 3	-28	0.027	51546	21.32	73.52	0.290
	Su II 6 a	-31	0.063	1509	19.18	80.67	0.238
	Su II 6 b	-60	0.064	446	20.40	79.55	0.256
	Su II 14 b	-527	0.021	1177	22.51	77.38	0.291
	Su II 14 a	-535	0.021	11306	30.24	68.63	0.441
Lake ice	Su L Ba	-76	0.007	916	21.88	78.03	0.280

Surface glacier ice has a total gas content close to that typical for polar meteoric ice. This value is about 0.100 cm^3 per gram of ice at standard temperature and pressure conditions. Values between 0.075 and $0.140 \text{ cm}^3\text{g}^{-1}$ have been reported in glacier ice from polar ice cores (Martinerie et al., 1992). Surface ice has a CO₂ concentration slightly higher than the atmospheric one from the pre-industrial period (280 ppmv) and its O₂/N₂ ratio is nearly the atmospheric one (0.268). These characteristics point to the possibility that small quantities of superficial meltwater have penetrated into the firn and have refrozen as a thin layer of ice covering cold snow grains (Stauffer et al., 1985).

By contrast, the basal ice has a strikingly lower total gas content, a very much higher CO₂ concentration and a O₂/N₂ ratio generally higher than atmospheric values. These characteristics indicate that this ice formed, at least partly, from

freezing of liquid water, a process that causes gas rejection and preferential incorporation of CO₂. As compared to the situation in the atmosphere, air dissolved in water at 0°C and atmospheric pressure has a different composition (19300 ppmv CO₂ and O₂/N₂ = 0.56) because of the higher solubility of CO₂ and O₂ compared to N₂ (Stauffer et al., 1985).

In the present case, the CO₂ content reaches much higher values (222900 ppmv). To our knowledge, the highest value of CO₂ content in glaciers ever published was 135000 ppmv which was reported by Souchez et al. (1995 b, c) for basal silty ice from the GRIP core in Central Greenland.

Results of this study show that the O₂/N₂ ratio reaches values as high as 0.516 and are associated with high CO₂ concentrations. This situation is completely different from that described at the base of the GRIP core where high CO₂ concentrations are related to low O₂/N₂ ratios. The latter relationship implies that oxidation of organic matter has produced carbon dioxide since this process is responsible for a lowering of the oxygen content. Our case, on the contrary, precludes this process. Progressive freezing of a water reservoir must be considered.

Results of gas analyses from natural ice formed by water freezing are very scarce in the literature and deal with one or two gases only. However the O₂/N₂ ratio has been studied by Craig et al. (1992) in the water and in the bubbles of lake ice from Lake Hoare situated in the Taylor Valley not far from Suess Glacier (Figure 3). These authors explain that during freezing of lake water, gases become supersaturated in the region immediately below the nearby forming ice until bubbles nucleate and form a gas phase. As freezing proceeds, gas is transferred from solution to the bubbles until finally the bubbles are encapsulated into the ice. In the case of Lake Hoare, the O₂/N₂ ratio measured in such ice bubbles range from 0.48 to 0.51. In the case of the ice cover of Lake Popplewell, sampled in the present study (Table I), this ratio is even lower (0.28). As stated above, the equilibrium value of the O₂/N₂ ratio for air dissolved in water at 0°C and atmospheric pressure is 0.56, but this is not the case in ice formed by water freezing since O₂ and N₂ do not diffuse at the same rate away from the advancing freezing front (at 0°C the O₂ diffusion coefficient in water is 2.08 10⁻⁹m² sec⁻¹ instead of 1.61 10⁻⁹m² sec⁻¹ for N₂). The higher values reached in the ice of Lake Hoare could be explained by the local production of oxygen by photosynthesis which, following Craig et al. (1992), is responsible for 11% of the O₂ input of the lake. Different freezing rates could also play a role since they affect the O₂/N₂ ratio in the boundary layer situated at the ice/water interface. More work is clearly needed to understand all aspects of the gas composition of the basal ice from Suess Glacier but the data cannot be explained without considering freezing of liquid water.

4.1.4 Structure and strength of basal ice and substrate of Suess Glacier: evidence for substrate deformation at subfreezing temperatures

4.1.4.1 Methods

The physical characteristics of the basal ice zone were observed at the foot of the ice cliff and by excavating a 2 m x 1.5 m x 25 m tunnel through the basal zone (Figure 6). The tunnel was excavated over a period of two weeks using chainsaws with tungsten carbide bonded to the cutters. At the end of the right branch of the tunnel a vertical shaft 4.5 m high was cut to expose the entire basal zone. Temperature measurement made at the back of the tunnel using thermocouples and alcohol thermometers showed that the temperature of the base of the glacier was $-17^{\circ}\pm 0.5^{\circ}\text{C}$ during the 6 weeks from early December 1997 to late January 1998.

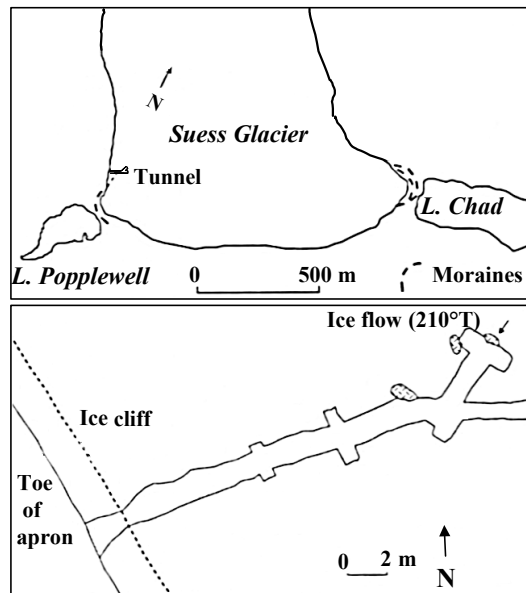


Figure 6 : Location map of Suess Tunnel.

The velocity of the glacier at the bed was measured using linear variable displacement transducers (LVDT's) and precision dial gauges capable of measuring displacements of 0.01 mm. Both the LVDT's and dial gauges were anchored to the substrate using rock bolts and were attached to glacier using wooden pegs drilled and frozen into the ice 5 mm above the bed. Displacements of the LVDT's were recorded using a Campbell data logger and the dial gauges were read every 2 days for 4 weeks and after 348 days. Plumb lines were used to characterise the form of the lower part of the velocity profile of the glacier by fixing a line with a plumb bob to a peg 2 m above a brass target bolted to the substrate. Displacements were measured as the offsets from a vertical line of wooden pegs drilled and frozen into the ice at approximately 200 mm intervals. The displacements were measured using digital callipers capable of recording distances 0.01 mm. Movement of the bed was

monitored at four locations in the tunnel by drilling a 400 mm-long hole and filling the hole with painted wooden dowel segments. The holes were excavated after 348 days and the positions of the dowel segments were measured.

The direct shear tests were conducted in the tunnel at a temperature of $-10^{\circ}\text{C}\pm 2^{\circ}\text{C}$ using a laboratory direct shear device modified for use in the field (Figure 7). Cylindrical samples 59 mm in diameter and 130 mm in length were cored using a dry diamond core bit powered by an electric drill. The samples were frozen into place in the stainless steel plates of the shear box (Figure 7) and a normal load was applied and adjusted using a pneumatic shock absorber, hand pump and a strain gauge. A normal load of 200 Pa was used because this figure equates to the normal load of 20 m of ice which occurred at the site of the experiments. A displacement rate of 0.85 mm hr^{-1} was used for the majority of the tests and most samples were sheared for 3 to 4 hours. Although this displacement rate is two orders of magnitude greater than basal zone velocities reported later in this report it was chosen to facilitate the measurement of a representative number of samples within the limited time of the field season. The shear strength was recorded as the output of a strain gauge that was logged every 61 seconds.

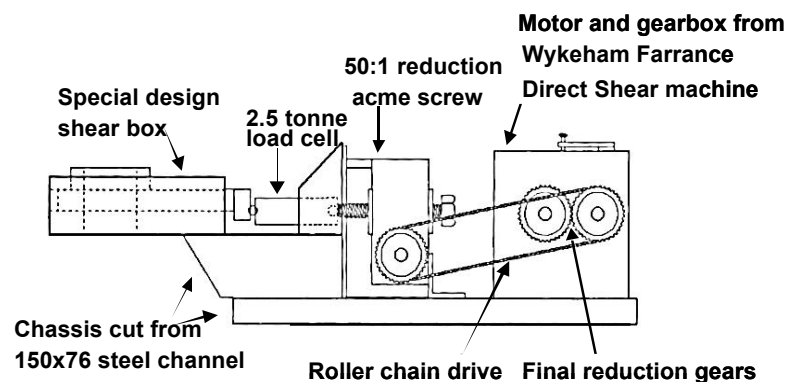


Figure 7 : Diagram of the direct shear device used in this study. The shear box is driven by an electric motor through a reduction screw. The shear strength is measured as the output of the 2.5 tonne load cell between the reduction screw and the shear box.

4.1.4.2 Ice movement at the bed

Plumb lines recorded velocities around 80 mm a^{-1} at 2 m above the bed to 6 mm a^{-1} 50mm above the bed (Figure 8). Three LVDT's and four dial gauges mounted within 10 mm of the bed recorded no movement over a period of four months. Markers placed into four holes drilled into the bed to a depth of 500 mm recorded no displacement within the upper part of the bed after a period of 348 days. The velocity measurements close to the bed show that sliding did not occur at the monitored locations during the four-month measurement period. Unusual patterns in the

velocity profiles such as shown by figure 8 appear to be related to differences in the rheology of basal ice related to debris concentration and to flow separations within the basal zone.

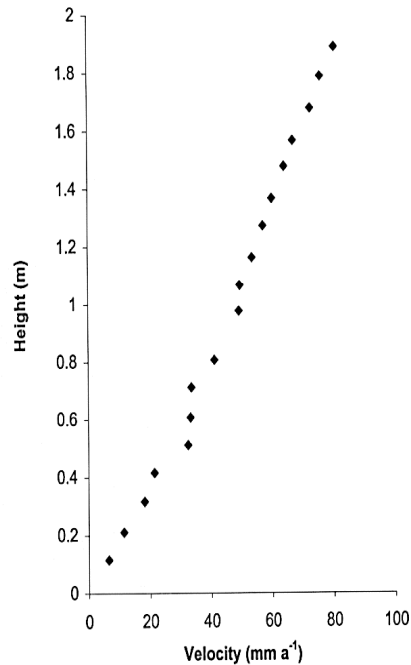


Figure 8 : Velocity profile measured using a plumbline resurveyed after 348 days.

4.1.4.3 Shear strength of the ice and substrate

Results of the direct shear tests are summarised by Table II and representative tests of amber, englacial and basal ice and the substrate are shown by figure 9. Table II shows that the three amber ice samples have the lowest peak strength and least variability. These results are consistent with the work of Holdsworth (1974) and Holdsworth and Bull (1970) who recorded changes in rheology associated with increases in the dissolved solids in the amber ice. The clean englacial ice samples were slightly stronger than the amber ice samples and the stress-strain curves show that the strength of the samples did not decrease much after the peak strength was reached (Figure 9b). Several tests of englacial ice samples produced stress-strain curves that have small steps in which the stress suddenly dropped about 0.06 Mpa (Figure 9d). These steps may be related to the failure of small fracture planes oblique to the shear plane. The average peak strength of the basal ice samples is lower than that of the englacial ice sample. However, Table II shows that there is an overlap in the strength characteristics and Figure 9 shows that the stress-strain curves for some basal ice samples are very similar to the englacial ice samples. Although the debris concentrations in the 19 basal ice samples is highly variable, the standard deviation of the peak strength of these samples is lower than that of the englacial ice samples (Table II). The majority of the tests on the substrate samples

recorded a significant decrease in strength after the peak strength was reached (Figure 9d). In several cases the rapid decline in post-peak strength is related to fracturing along the shear plane. Table I shows that the peak strength of the weakest substrate sample (2.07 MPa) is very similar to the highest peak strength of the basal ice samples (2.04 MPa).

Table II : Peak shear-strength values from direct-shear tests

<i>Material</i>	<i>Number of samples</i>	<i>Peak strength (Mpa)</i>			
		<i>Max.</i>	<i>Min.</i>	<i>Mean</i>	<i>std dev.</i>
Amber ice	3	1.06	0.73	0.9	0.17
Englacial ice	6	1.75	0.79	1.39	0.31
Basal ice	19	2.04	0.94	1.28	0.27
Substrate	8	3.29	2.07	2.53	0.35

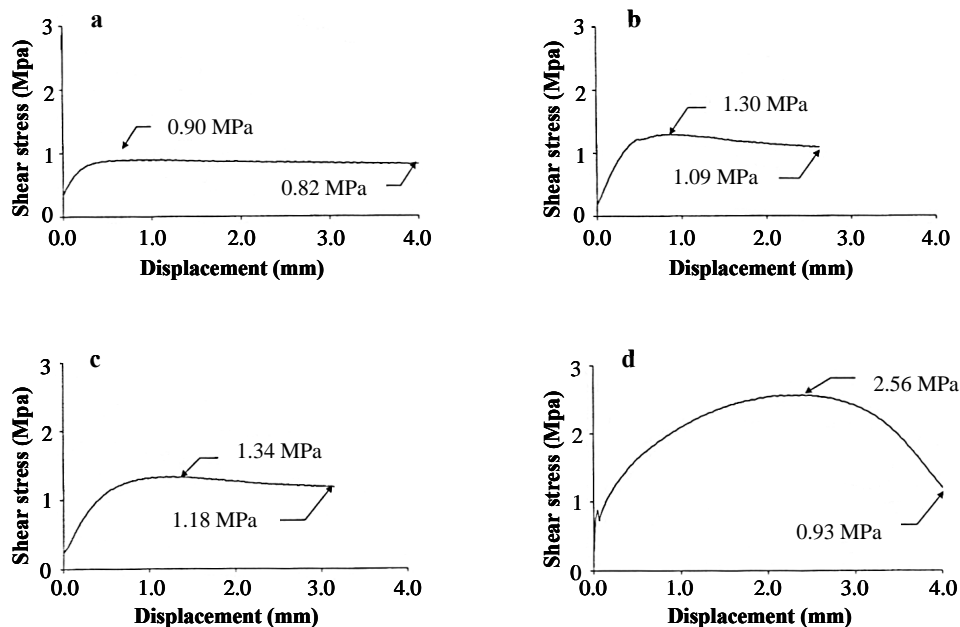


Figure 9 : Representative stress-strain curves: (a) amber ice (b) clean glacier ice, (c) basal ice and (d) the substrate.

Two problems with the direct shear tests need to be considered. Firstly, the direct shear device imposes the orientation and location of the shear plane because the cylindrical sample is placed in a hole drilled in two stainless steel plates. The shear plane is defined by the contact between the two sliding plates and the relationship between the thickness of the bottom plate and the length of the sample. Cutting the samples perpendicular to the structural fabric of the materials and careful alignment of structures and layers with the shear plane provided a partial solution to this difficulty. However, the complex and highly variable structure of the ice meant that in some cases it is likely that the device is shearing across existing structural

elements in the materials that might define layers that have different creep rates. For example, some of the substrate samples contained lenses and layers of segregated ice, which may be significantly weaker than the material in which the ice is confined to the pores. Similarly, the basal ice contains multiple layers of variable thickness and debris concentrations. Given these problems, the shear strength data should be regarded as providing estimates of the bulk strength properties of the samples.

A second problem associated with the direct shear tests is that, in order to test a representative number of samples, a load rate of 0.85 mm hr^{-1} was used. This load rate is considerably greater than the velocities experienced at the base of the glacier (20 mm d^{-1} vs. 0.23 mm d^{-1}). It is possible that the strong peak in the strength of the substrate may be substantially lower if the tests were conducted at more realistic strain rates.

4.1.4.4 Discussion

Taken at face value the direct shear tests suggest that on average the glacier substrate is unlikely to deform at present because the substrate has about twice the strength of the glacier ice. However, the strengths of some of the substrate samples are not significantly greater than some of the glacial ice and basal ice samples (Table II). Relatively small changes in strength might result in the substrate yielding at the same or lower stresses than the basal ice. Research on subglacial sediment deformation provides a useful framework for interpretation of the data presented above. Boulton's (1996) theoretical model emphasises the alteration of shear strength of materials as pore water pressures fluctuate. This analogy is useful because it leads to the question: how can the shear strength of materials be altered in the system described above? On the basis of observations made in the tunnel, it is possible to identify two potential sources of variation:

1. The strength of the substrate might be reduced because of the presence of cavities.
2. The substrate may contain or develop structural weaknesses.

Where cavities have formed adjacent to the substrate or sediment blocks within the basal zone the bottom of the cavities contain accumulations of loose sand and gravel which are the product of sublimation of the ice matrix. Attempts to test the strength of the substrate without pore ice failed because the samples disintegrated when the corer encountered the sediment that did not contain ice. However, the outcome of sublimation is clearly that the strength of the material is dramatically reduced because the cohesion produced by the pore ice is lost. It seems likely that the formation of a cavity can lead to localised weakening of the sediment, fracture and dislodgement.

Two potential forms of structural variation that have been observed in the substrate or in blocks of sediment entrained in the basal ice are thin mud layers, and

segregated ice layers. All the observed layers of mud and ice were less than 5 mm thick and therefore too small to position accurately in the direct shear device. Although this study has not produced any data on the strength characteristics of the mud layers, the data described above shows that the peak shear strength of the ice samples is less than the frozen sand of the substrate samples (Figure 9). As ice content increases above saturation, the shear strength of the material decreases because of the reduction in internal friction as the individual particles are separated by ice (Nickling and Bennett, 1984). It is likely that frozen debris resting between deforming basal ice and a moving ice layer would be entrained.

4.1.5 Conclusions

The stable isotope composition, the total gas content and the gas composition of the basal ice from Suess Glacier indicate that water (most probably lake water) plays a major role in the formation of the stacked sequence of ice and sediment layers accreted at the base. This is consistent with the previously proposed model of debris entrainment by cold-based glaciers that flow into lakes. This model states that transient wet-based conditions occur as ice flows into the unfrozen sediments of the lake bottom, creating conditions favorable to the entrainment of sediments and to ice accretion by water freezing.

Several aspects of this study require further investigation. For instance, occasional organic muds or algae layers are present in the basal ice sequence as well as in the shallow lacustrine environment of the adjacent Lake Popplewell. The potential role of these living organisms in the gas budget of the associated water and ice is of interest for better understanding the gas composition reported here.

Observations of the structure and sedimentology of the basal zone made in the tunnel show that parts of basal zone are derived from the bed. These observations suggest that many features observed at the ice margin are extensions of subglacial structures and that entrainment processes in the Suess Glacier are more complex than previously thought. Measurements of the movement of the lower part of the basal zone suggest that the glacier is not sliding and the bed is not deforming at the monitored locations at present or that the movement is so slight that it is not detectable. Direct shear strength tests of clean ice, debris-laden ice and the bed material show that the average peak strength of the substrate is considerably greater than debris-bearing and clean ice. However, there is almost an overlap in the strength of the samples that were tested. Although we conclude that the substrate is not likely to deform under the present conditions, relatively minor variations in the strength of the substrate would result in bed deformation. Observations of the structure of the basal zone and substrate suggest two possible mechanisms. First, the formation of cavities allows the ice matrix of frozen debris to sublime, which is likely to produce localised variations in strength. Secondly, segregated ice layers and

lenses within the substrate and close to the glacier sole may creep and lead to the deformation and failure of the substrate between two layers of deforming ice. Although the results of this study do not provide a certain interpretation of the bed deformation and entrainment processes, the study suggests that dry-based glaciers are capable of significant erosion in some circumstances.

Triaxial tests with a low strain rate should overcome the problems associated with the direct shear technique and analysis of the composition of basal ice in the tunnel may clarify the origin of the basal ice layers. This is programmed in the future.

Cold-based glaciers can actively entrain basal material. This provides a general mechanism for formation of dirty basal layers, and may in some cases be an important geomorphic process. Sub-freezing entrainment is likely facilitated by interfacial water films, which also allow sliding and abrasion by cold glaciers. The common assumption that cold-based glaciers are “protective rather than erosional” (e.g., Denton et al., 1993, p. 168) is not true in the absolute sense, although is accurate relative to temperate glaciers.

4.2 Study of ice formed at or near the grounding line in Terra Nova Bay area

4.2.1 Introduction

The grounding line is usually defined as a line across the glacier where it goes afloat. However, a grounding line can be considered as the limit between grounded ice and floating ice. Therefore, a grounding line exists if the glacier goes afloat or becomes grounded again. With such an extended definition in mind, the grounding line is in fact a transition zone between a grounded glacier or ice sheet and a floating glacier or ice shelf where the ice loses and makes contact again many times with the subglacial bed before it is eventually floating. Such a transition zone is relevant to consider in a work focusing on possible phase changes. Ice-rafted debris from icebergs derives mostly from subglacial entrainment by glaciers or ice sheets. The ice-substratum interface is indeed a place where particles can be incorporated into the glacier sole. The basal debris can then be carried by glacier flow and reach the ocean if the ice mass begins to float. In order for the debris to be preserved in the basal ice at the front of a floating glacier or of an ice shelf, they must not have been released at the grounding line. If the melting point is reached at the glacier base in the coastal region and if melting prevails at the grounding line, subglacial meltwater loaded with sediments discharges there into the sea. The probability of preservation of basal debris in the frontal zone greatly increases if freezing occurs at or near the grounding line. For the present study, ice from two different locations in the Terra Nova Bay area has been analysed. The study sites are Campbell Glacier tongue and Hells Gate Ice Shelf.

4.2.2 Framework of the study

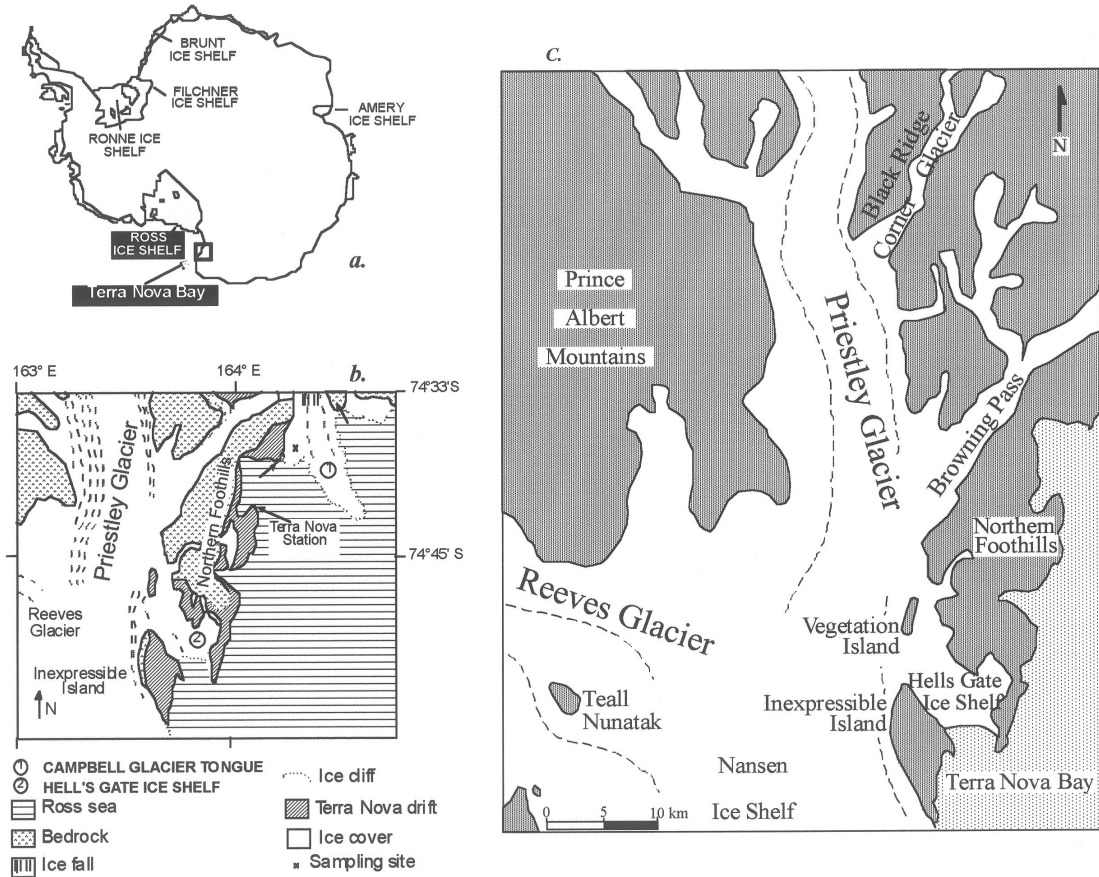


Figure 10 : The sampling sites in Terra Nova Bay area and principal locations cited.

The Terra Nova Bay area is located in northern Victoria Land, along the western margin of the Ross Sea (Figure 10a). It extends from Cape Washington in the North to the Drygalski Ice Tongue in the South. In its southern part, two important outlet glaciers (Figure 10b), Priestley and Reeves glaciers, both originating on the polar plateau in the surroundings of Talos Dome, meet to form the Nansen Ice Shelf (NIS). The small Hells Gate Ice Shelf (HGIS) is separated from the Nansen Ice Shelf by two pinning points: Vegetation Island in its northern part and Inexpressible Island in its southern part (Figure 10c). The ice nourishing this small ice shelf comes from the eastern part of Priestley Glacier and from the adjacent Browning Pass.

The grounding line is thought to be near Black Ridge and recent information from an Italian traverse indicates that a part of the ice coming from Browning Pass is floating (Frezzotti, personal communication). The HGIS is at least partly grounded in the pass between Vegetation Island and Inexpressible Island, as indicated by GPS measurements (Capra et al., 1996). The grounding line of NIS is thought to be situated beneath the highly crevassed area near the point where Teall Nunatak

emerges out of the Reeves glacier.

HGIS is snow-free on the major part of its surface. Due to strong katabatic winds it has a high ablation rate and is losing ice, mostly by sublimation. Since top surface ablation is prevalent, an upward velocity component exists and ice initially at depth is transferred along an inclined plane toward the ice-atmosphere interface downglacier. This is the reason for the appearance at the ice shelf surface of marine ice accreted at the bottom (Baroni et al., 1991 ; Souchez et al., 1991 ; Tison et al., 1993, 1998). HGIS consists of three different sectors separated by ridges of debris cones. Only the western and central sectors will be considered here since they are the only ones nourished by ice from the upglacier drainage basin. These two sectors are separated from each other by a major shear zone including two ridges of debris cones containing rock fragments. Large scale morphological patterns, marine ice outcropping patterns and ice foliation patterns suggest a complex dynamical behavior of converging flow (Tison et al., 1998). An oblique component of the flow into the western sector brings the ice into compression against the central sector.

Campbell Glacier is in the northern part of Terra Nova Bay area and has its accumulation zone in the Transantarctic Mountains; it flows in a NNW-SSE depression carved into the Precambrian and Paleozoic basement rocks (Carmignani et al., 1987). Being deviated by Mount Melbourne which is a Cenozoic volcano, it acquires a more or less north-south direction, and shows a steeper gradient. The presence of small rock outcrops at this level indicates that the base of the glacier is above sea level. Then, Campbell Glacier reaches the sea where it terminates as a protruding glacier tongue (Figure 11).

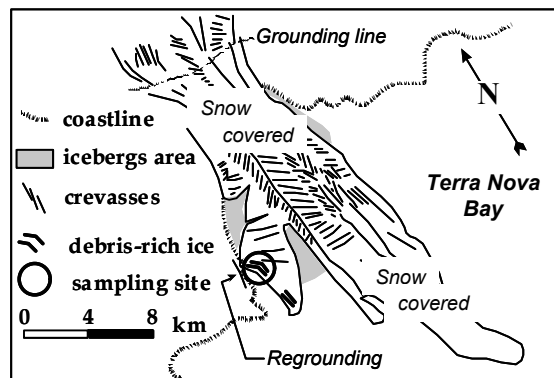


Figure 11 : Detailed sketch of Campbell Glacier Ice Tongue with sampling site.

The grounding line is thought to be located just south of the zone with the steeper gradient (Frezzoti, 1993). Radio-echo-sounding fails to detect it. The reflector is characterized by a weak energy contrast. This could be due to a change in the physical characteristics of the ice, the electromagnetic energy being absorbed because of the conductivity of a lower ice unit. Precise radio-echo-sounding is

moreover difficult to perform in this crevassed area. Although the precise depth of the grounding line is not known, an approximate value can be given. A bathymetric survey in front of the ice tongue (Angrisano, 1989) gives a depth of about 160m for the sea bottom. Overdeepening under the Campbell Glacier Tongue is a possibility but the grounding line depth should be around this value. The sampling site is about 3km downglacier from the presumed position of the grounding line.

By contrast with Hells Gate Ice Shelf, the role of katabatic winds in the Campbell Glacier trough is much reduced. The winds are relatively weak so that the entire glacier is accumulating snow on its surface and, even at the terminus of the floating tongue, a substantial part of the ice cliff is made of ice derived from snow deposited on the tongue.

As a result, there is no upward movement of ice and therefore marine ice, if present at the bottom, is not likely to outcrop at the terminus of the floating tongue. However, the south-western part of the ice tongue near Gondwana Station has impinged on bedrock promontories or protuberances. Consequently, basal ice containing debris layers is visible and can be sampled. At the sampling site (Figure 11), a stacked sequence, a few meters thick, dipping 60 ° towards the center of the glacier tongue shows two distinctive types of ice interbedded with bubbly glacier ice. A first type (type 1) located in the upper part of the basal sequence consists of bands of bubble-free ice with a thickness of the order of a few centimeters. The second type (type 2), located in the lower part of the basal sequence, shows bands of thin clear ice layers and layers of fine debris sometimes appearing folded with a few occasional pebbles. The proportion of bubbly glacier ice layers is much lower in this case. Debris consists mainly of quartz grains with rounded shapes and smooth edges (60%), volcanic glasses with elongated bubbles (30%) and lithic fragments. A few sponge spicules and shell fragments are also present. The heavy minerals mainly consist of pyroxenes (80%) indicating a major volcanic component and a few olivine, garnet and epidote minerals. The SEM (X-ray energy dispersion probe) analysis of the volcanic glass gives a dispersion in a SiO₂ versus alkali diagram similar to that of rocks from the nearby Shield Nunatak complex (Worner et al., 1989), thus suggesting a local origin.

4.2.3 Evidence for freezing close to grounding lines in Terra Nova Bay

Drillings through ice shelves show evidence of accretion of marine ice layers under ice of meteoric origin (Zotikov et al., 1980 ; Oerter et al., 1992). In the upper part of marine shelf ice from the Filchner-Ronne Ice Shelf, Oerter et al. (1992) have shown particle inclusions in conjunction with horizontal layering. The inclusions most probably result from scavenging during marine ice formation. However, the overwhelming absence of debris layers between meteoric ice and marine ice suggests the absence of adfreezing at the grounding line. In general, available

evidence favors melting rather than freezing.

Today, the frontal zone of most of the medium-sized and small ice shelves in Antarctica is well upstream from the maximum extent of the ice during the Last Glacial Maximum. Since glacio-isostatic loading of the crust has resulted in a depression of the coastal zone upstream from the continental slope or since overdeepening by ice flows has occurred, a cavity usually exists between the ice shelf and the ocean floor. This sub-ice cavity is subjected to a specific oceanic circulation (Jacobs et al., 1992). Surface sea water in front of the ice shelf plunges because its density increases by release of sea salts during sea ice formation. This water, at depth (High Salinity Shelf Water - HSSW), is above its pressure melting point since the freezing point of sea water is lower when pressure increases (Lewis and Perkin, 1986). Therefore, this water has at depth sensible heat to transfer to the base of the floating ice. Melting occurs and the less dense water so produced leaves the cavity as Ice Shelf Water (ISW). Hence, melting rather than freezing must prevail today at or near the grounding line. If marine ice forms, it is mainly by accretion of frazil ice crystals generated in the supercooled ISW as it rises towards the surface. The absence of plunging waters is thus a prerequisite for possible freezing at the grounding line.

A detailed investigation of the ice at the level of the HGIS western moraine not only shows debris and clear ice layers but also sponge remains in growth position and serpulid worm tubes. It is difficult to decode the significance of the presence of these serpulid worm tubes since Adelie penguins, which are numerous in the area, are known to build small hillocks of that matter. As shown by photographs from a robotic submarine, sponges are growing near a grounding line (Powell et al., 1996). Sponge remains in growth position can be incorporated into the ice shelf because of anchor ice formation on the sea floor. Dayton et al. (1969) indicate that, in McMurdo Sound, anchor ice develops to about 33 m deep on the sea floor. When it becomes detached, because of inherent buoyancy, it floats to the undersurface of an ice cover, carrying with it portions of the substratum which can weigh at least 25 kg. By this process, sponges can be incorporated into the ice shelf. Because of their location well upstream in the ablation zone of the Hells Gate Ice Shelf, these sponge remains must have been incorporated near the grounding line. The bottom water where the sponges were growing must not have been above the pressure melting point in order for anchor ice to be formed. Therefore, the area where the sponges have grown must have been sheltered somehow from the influence of high salinity shelf waters (HSSW) which would be above their freezing point at depth. Other evidence supporting the possibility of certain areas being sheltered from sub-ice cavity circulation can be inferred from temperature and salinity measurements made in front of the ice shelf (Tison et al., 1997). Oceanic profiles down to 600m depth show a transition between ISW and HSSW below 440m. However, typical high salinity shelf waters were not observed in the profiles. This suggests that plunging of

HSSW only affects a narrow central trough more than 700m deep that exists beneath the ice shelf (Stocchino, 1991). Since maximum ice thickness of about 200m (Tabacco, personal communication) was observed immediately downstream of Vegetation Island, there must be sheltered sea floor areas where anchor ice can develop away from the influence of HSSW.

Bathymetric information available (Stocchino, 1991) in the Campbell Glacier Ice Tongue area also suggests a sheltering effect where the debris-rich ice formed near the grounding line originated (Souchez et al., 1995a).

4.2.4 Freezing by a double-diffusion mechanism at the grounding line

Zotikov (1986) discussed in length the various possible processes controlling the mass balance at the bottom of an ice shelf. Using the Amery Ice Shelf as a case study, this author suggested heat transfer between a water layer of reduced salinity and sea water to explain the abnormally high freezing rates deduced from temperature profiles across the ice shelf. Lambert outlet glacier, at the bottom of which melting takes place because of enhanced ice thicknesses, is seen as a connection between the subglacial basin occupied by the ice sheet center and the sea beneath the Amery Ice Shelf. It provides the source for outflowing waters of reduced salinity under lithostatic load. A rough calculation considering no mixing between the two water layers, salinity differences of about 20‰ and relative flow velocities of about 10 cm s⁻¹, provided freezing rates of about 1 m y⁻¹ in accordance with the observed rates. This mechanism however requires the sea water to be at its local freezing point, which precludes areas under the influence of a sub-ice cavity circulation. On the other hand, the "no-mixing hypothesis" is a rather constraining one, especially giving the fact that there is evidence (MacAyeal, 1984) of efficient tidal mixing near grounding lines. We propose as alternate possibility a double diffusion process within the pores of subglacial sediments, in areas sheltered from the Deep Thermohaline Convection. In such areas, at some distance upstream from the actual decoupling of the glacier from its bed, sea water seeping through the sediments will come into contact with continental meltwaters (Figure 12). Because the freezing point of sea water is lower than that of continental meltwater, heat diffusion will occur. Heat will diffuse through both liquid and solid fractions from upstream to sea water. On the other hand, the salinity of sea water being higher than that of continental meltwater, salts will diffuse from the sea water-saturated sediment into the meltwater-filled subglacial sediment. Salts can diffuse only through liquid unlike heat. Thermal diffusivity is also an order of magnitude higher than salt diffusion. The meltwater-filled sediment loses heat more rapidly than it gains salt and freezing occurs, welding the sediments to the bottom of the ice. Since this mechanism occurs within the subglacial sediments, rapid mixing between continental meltwater and sea water is precluded (Souchez et al., 1998).

If the extended definition of the grounding line is considered, freezing can occur at different places, depending on variable water fluxes. Also, if the ice makes contact with a protuberance of the substratum in this critical area, pressure melting and regelation is likely to take place.

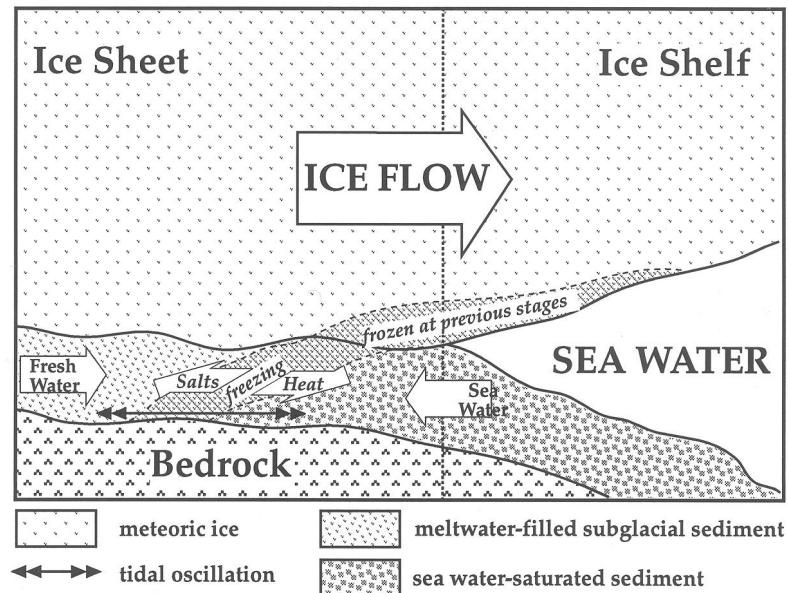


Figure 12 : Sketch of the suggested freezing mechanism by double diffusion at the grounding line.

Such a double-diffusion mechanism leading to freezing at the grounding line will not only explain incorporation of debris into the glacier sole but also preservation of debris-rich ice already present upstream in the basal zone.

Is there evidence that such a process really occurs ? The isotopic composition of debris-rich ice sampled in the region of Terra Nova Bay gives information along these lines.

4.2.5 Isotopic evidence of the double-diffusion mechanism

Samples of bubbly glacier ice which reaches the sea in Terra Nova Bay (Figure 13 - insert), are aligned on a straight line in a δD - $\delta^{18}O$ diagram with equation :

$$\delta D = 7.91 \delta^{18}O + 2.59 \text{ (correlation coefficient : 0.997 ; 55 samples)}$$

The δ -values are more negative than -17‰ in $\delta^{18}O$ and -130‰ in δD . The straight line which can be considered as a local Meteoric Water Line or precipitation line goes close to SMOW. The δ -values of the meltwaters from glacier ice will have the same isotopic composition since there is no fractionation on glacier ice melting.

By contrast, the debris-rich ice layers, thought to have been formed near the grounding line, from the western moraine ridge of Hells Gate Ice Shelf and from the site studied in Campbell Glacier Ice Tongue (Souchez et al, 1995a) have δ -values comprised between -15‰ and -3‰ in $\delta^{18}\text{O}$ and between -120‰ and -30‰ in δD . Detailed sampling locations at HGIS site is shown on figure 15. A thorough description of the samples collected at Campbell Glacier Ice Tongue is given in Souchez et al (1995a). The samples from Hells Gate Ice Shelf are from three shallow (2 meters) ice cores drilled below the surficial dirt layers of two major dirt ice cones located on the western moraine.

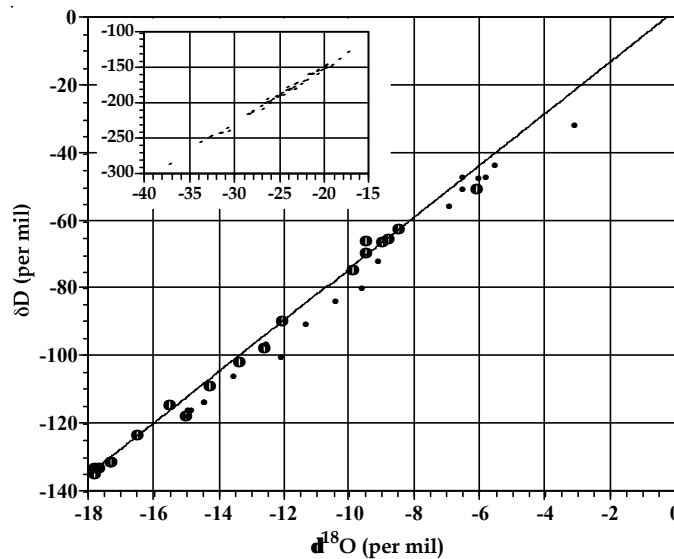


Figure 13 : δD - $\delta^{18}\text{O}$ diagram of the studied basal ice samples from Terra Nova Bay. Black circles = ice samples ; open circles = initial water samples computed from δ -values of ice samples and equilibrium fractionation coefficients. The straight line represents the best fit line for the waters. Insert shows the δD - $\delta^{18}\text{O}$ diagram of glacier ice samples from the area.

The textures of the cores were similar to those described for ice type 2 at Campbell Glacier, showing interlayering of debris layers with bubbly and clear ice layers at centimetric to decimetric scales. The bubbly ice layers show typical meteoric ice values and the clear ice/dirt ice values are in the range of -3.07 to -12.50 ‰ in $\delta^{18}\text{O}$ and -30.03 to -98.90 ‰ in δD . Samples from all cores are well aligned in a δD - $\delta^{18}\text{O}$ diagram on a straight line (Figure 9), the equation of which being:

$$\delta\text{D} = 7.71 \delta^{18}\text{O} - 1.15 \text{ (correlation coefficient : 0.993 ; 18 samples)}$$

Progressive freezing downwards in a water mass or in a subglacial sediment produced, for example, by ice thickness variations cannot explain this last distribution. Indeed, the observed slope is steeper than a freezing slope would be, and the ranges of δ -values are such that near complete freezing of the reservoir

(99%) would be required to understand the most negative δ -values (Souchez and Jouzel, 1984). Ice intrusion of a subglacial sediment by pressure-induced regelation past grains is also precluded since the isotopic signature of such a process would have been different (Iverson and Souchez, 1996). On the other hand, pressure melting and regelation do not significantly modify the isotopic properties of the ice submitted to this process (Souchez et al., 1988).

If glacier ice meltwater within the subglacial sediment enters into contact with sea water at the grounding line, diffusion will occur. Like salts, heavy isotopes of oxygen and hydrogen will diffuse from sea water where they are less impoverished to continental meltwater where they are more depleted. Diffusion coefficients of stable isotopes and of salts in liquid water have the same order of magnitude so that the double-diffusion mechanism described above also leads to isotopic diffusion. Therefore, the isotopic composition of the debris-rich ice layers formed by freezing will be dependent on the magnitude of the diffusion process prior to freezing. Isotopic composition is likely to be a better indicator of the process than the salt content since the different isotopes are within the lattice of the ice formed and only subjected, on very long time scales, to solid state diffusion.

From the isotopic composition of the ice layer formed, it is possible to reconstruct that of the initial water. Freezing at the subglacial site near the grounding line is most probably very slow so that equilibrium fractionation can be considered. Therefore, taking into account the equilibrium fractionation coefficients for deuterium and oxygen 18 and the respective δ -values of the ice, it is possible to compute the isotopic composition of the water which was later partially frozen. The best fit line for the waters (Figure 13) has the following equation :

$$\delta D = 7.63 \delta^{18}O + 1.9 \quad (r = 0.993)$$

This line goes close to points representing δ -values of sea water in the area and δ -values of meltwaters from glacier ice.

Isotopic diffusion within the water-filled subglacial sediment submitted to freezing by a double-diffusion mechanism seems thus to be the process explaining the peculiar distribution in the δD - $\delta^{18}O$ diagram.

4.2.6 Subglacial meltwaters origin and formation of debris-rich ice in the western moraine of HGIS.

Oxygen and hydrogen isotope compositions of the interbedded debris-rich and clear ice layers of the debris cones forming the western medial moraine of HGIS are very different from those of snow and glacier ice. The $\delta^{18}O$ values of the snow collected in various spots of the area (Dini et al., in press) exhibit a good correlation (correlation coefficient $r = 0.898$; 16 samples) with elevation. The equation derived is:

$$\delta^{18}\text{O} = -0.006 E - 17.664$$

with E being the elevation in meters. The intersection of this straight line with 0m elevation indicates that a snow sample is always more negative than -17‰ in $\delta^{18}\text{O}$. This is also true for glacier ice derived from such snowfall, since, in the region, the transformation process implies only a very limited quantity of liquid water. We showed that glacier ice samples from the same area are more negative than -17‰ in $\delta^{18}\text{O}$ and -130‰ in δD ; they are aligned on a straight line in a δD - $\delta^{18}\text{O}$ diagram with equation :

$$\delta\text{D} = 7.91 \delta^{18}\text{O} + 2.59 \text{ (correlation coefficient } r = 0.997; 55 \text{ samples)}$$

which can be considered as a precipitation line (local Meteoric Water Line). Interbedded debris-rich and clear ice layers exhibit by contrast a large range of δ -values between slightly negative values close to standard mean ocean water (SMOW) and -20‰ in $\delta^{18}\text{O}$ or -160‰ in δD . In a δD - $\delta^{18}\text{O}$ diagram, samples from these ice layers are well aligned on another straight line (Figure 14) with equation :

$$\delta\text{D} = 7.78 \delta^{18}\text{O} - 0.16 \text{ (correlation coefficient } r = 0.997; 8 \text{ samples)}$$

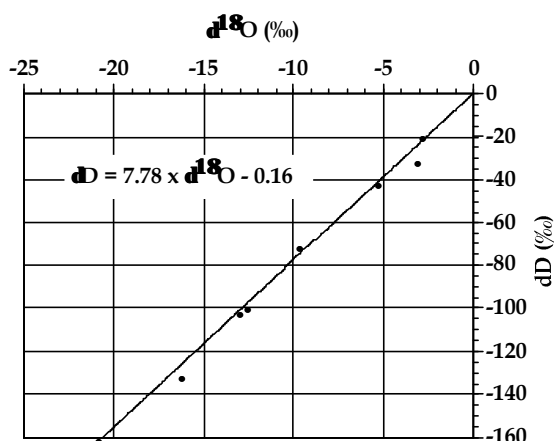


Figure 14 : δD - $\delta^{18}\text{O}$ relationship for interbedded debris-rich and clear ice layers from the western moraine of the Hells Gate Ice Shelf.

This last straight line is however not very different from the previous one on which glacier ice samples are aligned in view of the confidence intervals on the regression lines. This line cannot be considered as a freezing slope which would have a much lower value for the angular coefficient (Jouzel and Souchez, 1982).

The ice forming the interbedded debris-rich and clear ice layers cannot however be of direct glacial origin. Most of the samples have $\delta^{18}\text{O}$ values much less negative than -17‰ , the limiting value for present-day snow or for glacier ice from the Holocene period. For this reason, altitude effects or differences in isotopic composition due to climatic changes cannot explain the distribution. Does the fact

that no freezing slope is displayed on a δD - $\delta^{18}O$ diagram imply that no phase change from liquid water to ice occurred? Freezing is accompanied by an isotopic fractionation. Ice is enriched in heavy isotopes of oxygen and hydrogen compared to water. During freezing of a small finite reservoir, ice initially enriched in heavy isotopes can however become more negative than initial water in the course of the phase change, since residual water becomes more and more depleted in heavy isotopes. Therefore, depending on the sampling resolution, ice due to complete freezing of a limited water reservoir can have the same isotopic composition as the water before the phase change. This is in great contrast with the situation resulting from partial freezing. Another way to understand the absence of significant difference in isotopic composition between ice resulting from water freezing and initial water is by considering the freezing rate. If the freezing rate is high, ice and water will have the same δ -value after a short initial transient (Souchez and Lorrain, 1991). Taking into account that freezing at the base of a glacier is a relatively slow process, occurring most probably close to isotopic equilibrium, such a situation is however less probable.

From the considerations above, the large range in δ -values exhibited by the interbedded debris-rich and clear ice layers cannot result from the distribution of samples along a freezing slope during phase change. It must therefore result from the large differences in isotopic composition of the waters filling the subglacial sediment prior to freezing. Now, the regression line (Figure 14) passes close to the point representing mean sea water in the area (mean δ -values for sea water in front of HGIS are indeed -0.6‰ in $\delta^{18}O$ and -4.0‰ in δD (Souchez et al., 1991)) and the least negative sample of the interbedded debris-rich and clear ice layers is only slightly more negative than local sea water. Such characteristics of the isotopic composition of the interbedded debris-rich and clear ice layers from HGIS are consistent with the double-diffusion freezing mechanism described. If glacier ice meltwater within the subglacial sediment enters into contact with sea water seeping through this sediment at the grounding line (or around a pinning point), diffusion will occur. The isotopic composition of the interbedded debris-rich and clear ice layers thought to be formed by freezing at the grounding line is thus dependent on the magnitude of the diffusion process prior to complete freezing for each increment. The straight line on which the interbedded debris-rich and clear ice layers are aligned in a δD - $\delta^{18}O$ diagram (Figure 14) is thus the consequence of a diffusion process taking place before freezing.

The isotopic composition of the continental meltwater at the origin of the double-diffusion mechanism can be estimated in the following way. The intersection point between the diffusion line equation ($\delta D = 7.78 \delta^{18}O - 0.16$) and the precipitation line on which glacier ice samples are aligned ($\delta D = 7.91 \delta^{18}O + 2.59$) has $\delta D = -164.7\text{‰}$ and $\delta^{18}O = -21.15\text{‰}$. Such δ -values should represent both the composition of the

water and of the ice resulting from freezing of this water if complete freezing occurred for each increment. Indeed, in that case, as discussed above, there is no difference in isotopic composition between ice and water. It should be noted that, if equilibrium fractionation had occurred, reconstruction of the regression line through the parent water for the ice samples would give a $\delta^{18}\text{O}$ value of -0.96‰ for the intersection point with the precipitation line. This is clearly not possible since continental snow or ice never has such a high δ -value and since ice samples with δ -values ranging between -17‰ and -0.96‰ cannot result from freezing of a mixture between sea water and fresh meltwater at -0.96‰ . As indicated above, the δ -values of the intersection point should however be taken with caution in view of the confidence intervals for the regression lines.

Are such δ -values compatible with those existing in basal glacier ice near the pinning point? The determination of the isotopic composition of the ice at the base of HGIS in the central sector close to the pinning point can be appraised in the following way. As a consequence of the upward velocity component indicated above, the contact between glacier ice and marine ice accreted at the bottom of the ice shelf can be traced at the ice shelf surface. The ice just above the contact was previously at depth, presumably close to the base. The possibility that melting occurred at the ice-ocean interface when the glacier becomes afloat and prior to the formation of marine ice at the bottom cannot be excluded. It is however considered as not significant in view of the suggested position of the grounding area and the ice velocity. Moreover, the radiocarbon dates obtained by Baroni (1990) on the biogenic material thought to be incorporated near the southern tip of Vegetation Island suggest that marine ice is formed as soon as the ice going round the island becomes afloat. Furthermore, High Salinity Shelf Water (HSSW) which would be responsible for basal melting is not present at such depths in this location (Tison et al., 1998). Glacier ice previously at the base of HGIS near the grounding area can thus be easily sampled along the line separating, at the ice shelf surface, ice of continental origin from marine ice (black dots in Figure 15). Results of the isotopic analyses indicate $\delta^{18}\text{O}$ values clustering around (-23‰) - (-26‰) with one value reaching -30‰ . Meltwater produced by geothermal and frictional heat at the glacier base has an isotopic composition similar to that of the ice at the glacier-substratum interface since there is no fractionation on ice melting (Moser and Stichler, 1980). Is such water the meltwater required for the double-diffusion freezing mechanism occurring at the grounding line? The similarity of $\delta^{18}\text{O}$ values between that of the intersection point and those of the ice at the base of HGIS in the central sector close to the pinning point is not a decisive argument for the origin of the meltwater. Indeed, the thickness of the ice between Vegetation Island and the Northern Foothills - a place of obliged passage for ice to nourish the central sector of HGIS - is estimated to be of maximum 250 m by radio-echo-sounding (Tison et al., 1998). Taking into account

that the mean surface air temperature in the area is about -18°C , calculations based on the method developed by Hooke (1998) indicate that the pressure-melting point is not reached at the bottom (-9.5°C if horizontal advection is ignored). It is thus unlikely that substantial meltwater could be produced at the ice-bedrock interface by geothermal and frictional heat to sustain the double-diffusion freezing mechanism responsible for the formation of debris-rich ice layers of the western moraine. Is there another possible source of water ?

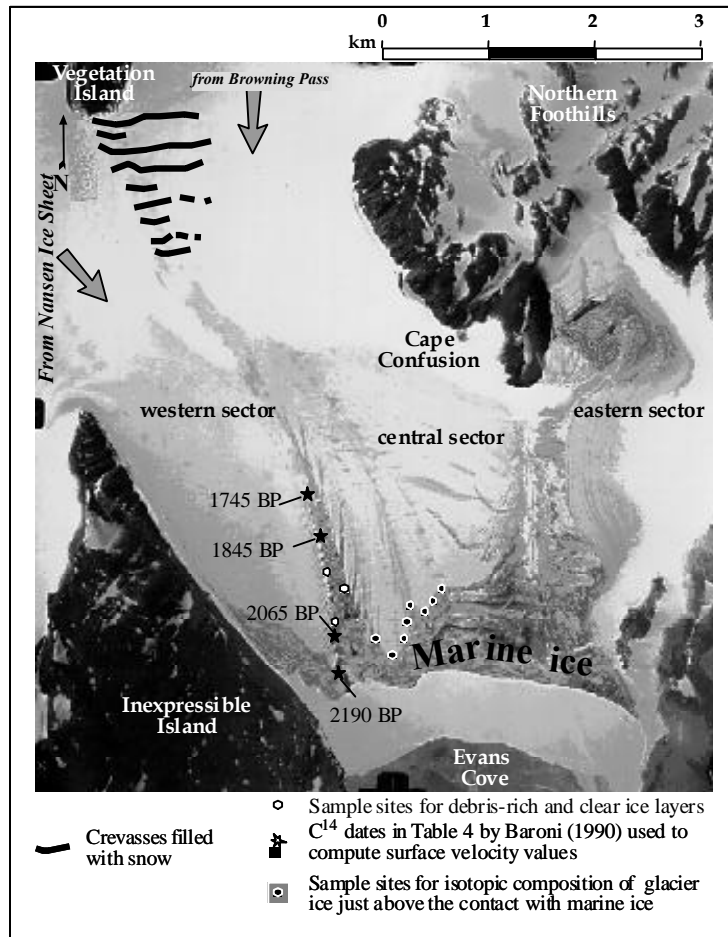


Figure 15 : Sample sites and main features of the Hells Gate Ice Shelf. Based on aerial photograph: Terra Nova Bay - 11.06.1985 - TMA-2851-V.

Meltwater accumulated in marginal lakes may eventually reach the subglacial substrate. A meltwater lake exists near the southern tip of Vegetation Island. A small outlet stream from this lake is disappearing into the ice. At this place the ice is relatively thin, a few tens of meters. The water from this stream has an isotopic composition of about -24‰ in $\delta^{18}\text{O}$. We believe that water from the southern tip of Vegetation Island is the source of the meltwater required for the double-diffusion freezing mechanism. The small thickness of glacier ice and the presence of crevasses near the pinning point are important elements to consider. In certain circumstances they allow meltwater to reach the subglacial substratum. The

suggested mechanism is in accordance with the radiocarbon dates obtained by Baroni (1990), which increase in age in a downglacier direction (Figure 15).

4.2.7 Conclusion

Field observations from the present Interglacial period indicate prevailing melting conditions at the base of the major antarctic ice shelves (Jacobs et al., 1992). Models of the Deep Thermohaline Convection in sub-ice shelf cavities have provided estimates of melt rates and growth rates (marine ice) under various areas of the Fichner-Ronne and Amery ice shelves (Bombosch and Jenkins, 1995 ; Jenkins and Bombosch, 1995 ; Grosfeld et al., 1997 ; Williams et al., 1998). Using a modelled mean bottom melting rate of 0.20 m y^{-1} over 400 km on a downstream direction from the grounding line (Jenkins and Bombosch, 1995) and mean surface velocities of 500 m y^{-1} (Jenkins et al., 1994), the bottom 160 meters of the Ronne Ice Shelf will be lost before marine ice accretion begins. Considering that observed basal debris-rich sequences at the bottom of ice tongues at the grounding lines do not exceed a few tens of meters, it is not surprising to find meteoric/marine ice interfaces devoid of significant sediment loads. During the glacial stages, however, the antarctic ice sheet must have partly or fully re-filled the sub-ice shelf cavities and submarine trenches carved during the previous stages, thereby strongly inhibiting the Deep Thermohaline Convection. Therefore, conditions for freezing by a double diffusion effect, i.e. conditions for preservation of basal debris to the frontal zone in contact with the ocean, would have been more prevalent than today. To what extent this mechanism will allow transport of basal sediments through iceberg drifts off the continental shelves is still conjectural. Recent work in the Prydz Bay area (Domack and Harris, 1998) shows that the grounding line did not make it to the continental shelf edge during the LGM. However, the situation might have been somewhat different in the northern hemisphere or for previous glacial stages in Antarctica. The present work points to the need of including grounding lines adfreezing processes in the general picture developed to fully understand typical events of sediment export to the Deep Sea like the Heinrich events in the North Atlantic. The grounding line is indeed a spot of compelled passage for subglacial debris on their way to the ocean.

4.3 Study of lake ice at the bottom of the Vostok ice core

4.3.1 Introduction

Subglacial lake Vostok in Central Antarctica is 230 km long and 50 km wide and has an area of about $14,000 \text{ km}^2$. The Vostok drilling site (Figure 16) is at the southern end of the lake with a thickness of 3750 m of ice and 600 m of water below.

At its northern end, 200 km away, the ice is 4300 m thick and the lake is shallower. The presence of subglacial lake Vostok is related to the geothermal heat flux, the temperature of the ice at the ice-water interface being that of the melting point.

The Vostok ice core in Central Antarctica has provided the longest record of past changes in climate and atmospheric composition, with four glacial-interglacial cycles displayed down to a depth of 3310 m (zone C ; Figure 17). The ice at that depth is ~ 420 ka (thousand of years before present) old. Isotope studies, which are developed below, show that the Vostok ice core consists of ice refrozen from the Lake Vostok water, from 3539 m below the Antarctic ice sheet surface to its bottom at about 3750 m (Jouzel et al., 1999).

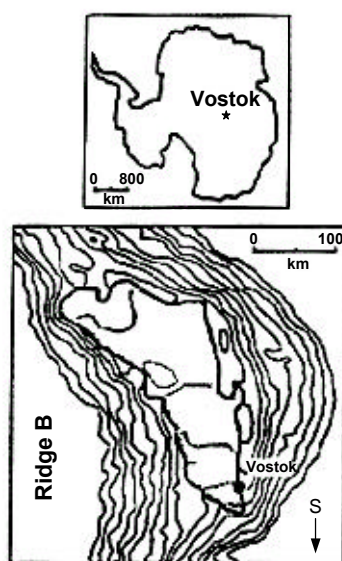


Figure 16 : Localisation of the Vostok ice core. The map of the Vostok lake area is adapted from Kapitsa et al. (1996).

4.3.2 More than 200 m of Lake Ice above Subglacial Lake Vostok

In the basal part of the Vostok ice core, there are two distinct types of ice separated by a very sharp transition which represents the base of a shear zone interpreted as the sole of the moving ice sheet (Lipenkov and Barkov, 1998). This transition zone is zone T, at (Figure 17-18). The ice just above that depth (zone D) is typically ice of glacial origin from the ice sheet although it is disturbed and its climatic record has been modified. The ice below that depth is lake ice as demonstrated underneath.

Several ice properties change at the 3539 m transition. The δD values exhibit a 10 ‰ increase, from about - 452.5 ‰ to 442.5 ‰, and remain stable below 3539 m (Figure 18). The deuterium excess similarly decreases from a value of about 14 ‰ to a near constant value of about 7 ‰. Crystal size increases dramatically, electrical conductivity (ECM) decreases and reaches the detection limit and total gas content changes from a value of about $80 \cdot 10^{-3} \text{ cm}^3/\text{g}$, typical for glacier ice, to a value of

about $6 \cdot 10^{-5} \text{ cm}^3/\text{g}$ in the lake ice. The number of solid inclusions also shows an increase at 3539 m.

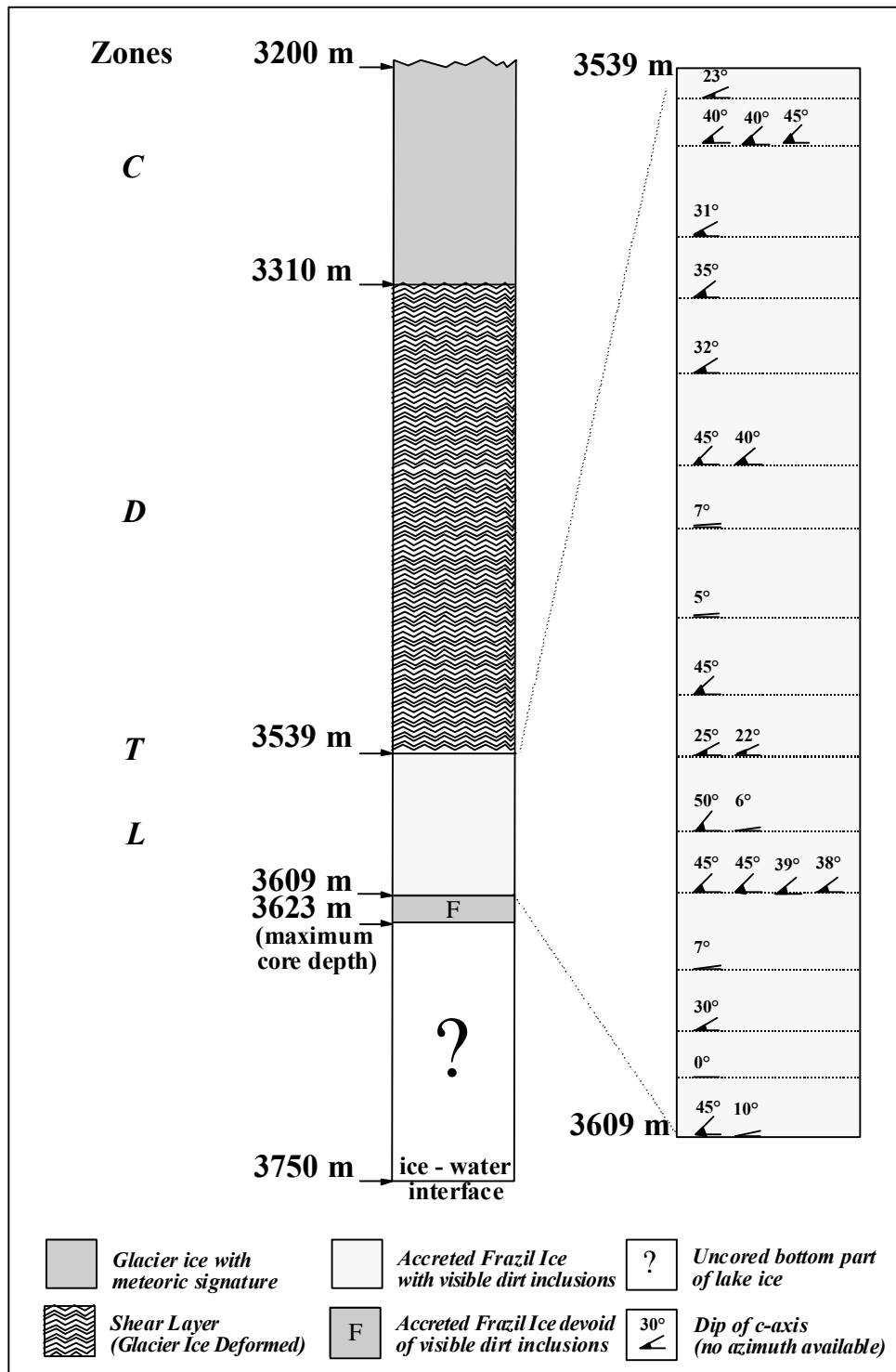


Figure 17 : The different ice types in the Vostok ice core. Dip of each ice crystal measured is indicated by the angle with the horizontal.

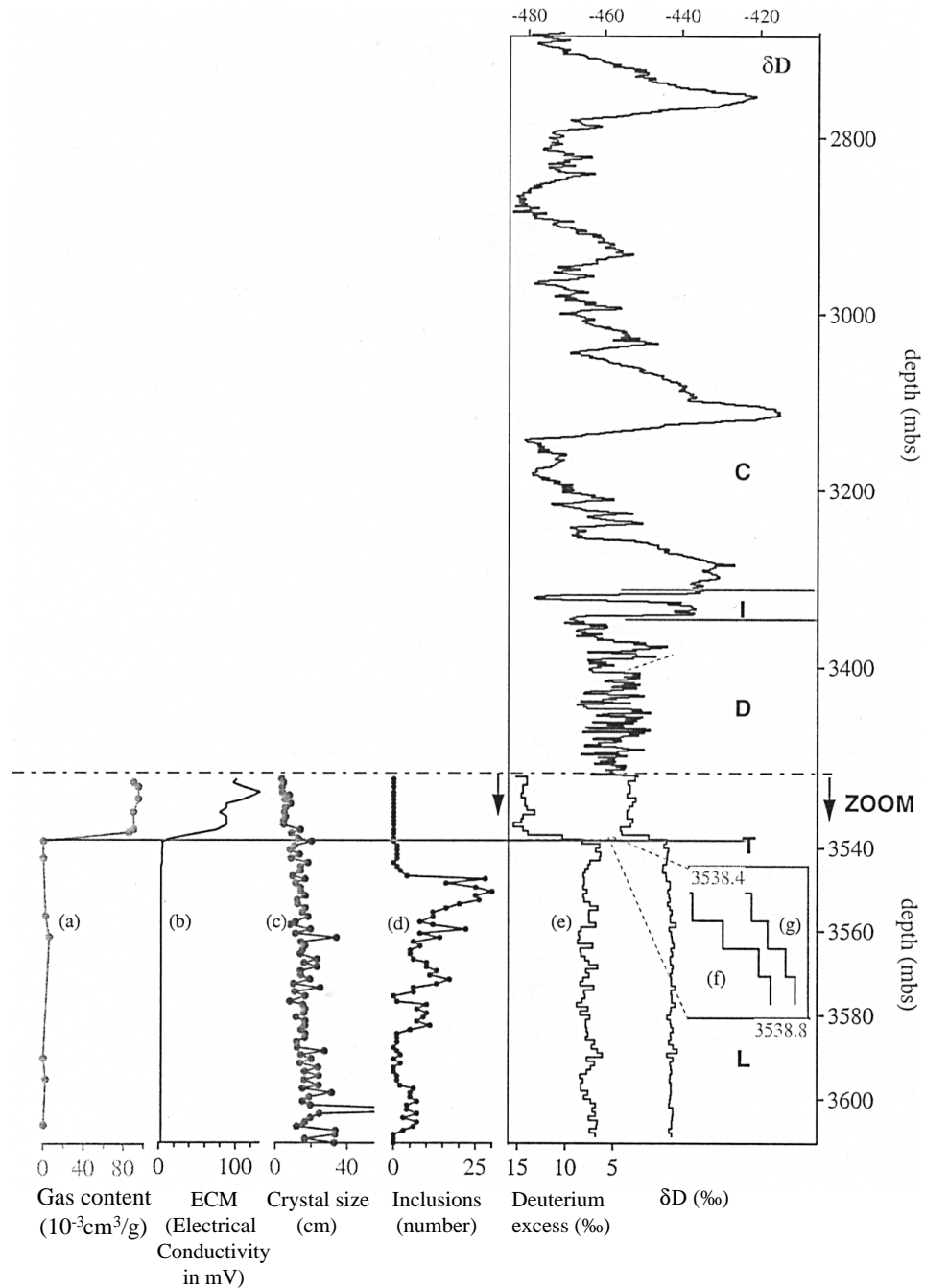


Figure 18: Total gas content (A), ECM (B), crystal size (C), number of visible inclusions per meter (D) and deuterium excess (E) in the Vostok ice core from 3525 to 3611 m. Deuterium excess values are computed from δD and $\delta^{18}\text{O}$ measurements done in Saclay and expressed in per mil with respect to V-SMOW, the Vienna Standard Mean Ocean Water. Crystal mean sizes were determined by counting the number of crystals per meter of the ice core on a longitudinal thin section 4.5 cm wide. The ECM signal (1 millivolt is equivalent to a conductivity of 0.22 micro siemens) represents the mean values on 1m core. The total gas content

measurements (given in mm^3/g at standard temperature and pressure) were made in Grenoble by the barometric method. The deuterium profile is given on the right (F) from 2700 m to 3611 m in order to show the full range of variation of this parameter. The various zones mentioned in the text are indicated along this profile. An enlarged diagram of the δD (F) and deuterium-excess (G) inside and the transition between the glacier and the lake ice (zone T in which 10 cm samples have been analysed) is given in an insert.

The properties of the ice below 3539 m (zone L) suggest that it was formed by freezing of the Vostok lake water. Both, the very low total gas content and the large mean crystal size (> 20 cm, and up to 1 m), are indicative of ice very slowly formed from liquid water. One plausible explanation for low ECM values is the formation of recrystallized ice with associated changes in electrical properties which gives additional support for a lake ice origin. But the strongest evidence for formation from liquid water comes from the isotopic properties of this ice, more specifically from the combined use of deuterium (δD) and oxygen 18 ($\delta^{18}\text{O}$) isotope compositions.

As a result of fractionation processes during the atmospheric water cycle, there is a link between the isotopic composition of precipitated water (δD or $\delta^{18}\text{O}$) and meteorological parameters which allowed reconstructing local temperature change over the last 420 ka (Petit et al., 1999). The deuterium excess profile ($d = \delta\text{D} - 8 * \delta^{18}\text{O}$) provides access to changes in the source region for antarctic precipitation (Vimeux et al., 1999). Major shifts in deuterium and deuterium excess are observed at the 3539 m transition. Within less than 50 cm (Figure 18), deuterium values increase by about 10‰ and deuterium excess values shift from around 14‰, a value typical for glacier ice in this area (Vimeux et al., 1999), to 7 or 8‰. In a $\delta\text{D}/\delta^{18}\text{O}$ diagram (Figure 19), data points from zones I and D fall on the Vostok precipitation line with a slope of 7.93 calculated over the last 420 ka. This slope is quite similar to that of 7.86 obtained for the last 150 ka (Vimeux et al., 1999) and very close from that of the worldwide Meteoric Water Line (slope of 8) defined by Craig (1961). Both δD and $\delta^{18}\text{O}$ have now been measured down to 3611 m. In a $\delta\text{D}/\delta^{18}\text{O}$ diagram, data points from zone I and D are undistinguishable from those of the last 420 ka (zone C), as illustrated from the individual data points from the bottom part of zone D reported on figure 19. In contrast, data from zone L are clustered to the right side of this precipitation line. These isotopic characteristics are a clear fingerprint of the isotopic modifications resulting from a freezing process (Jouzel and Souchez, 1982).

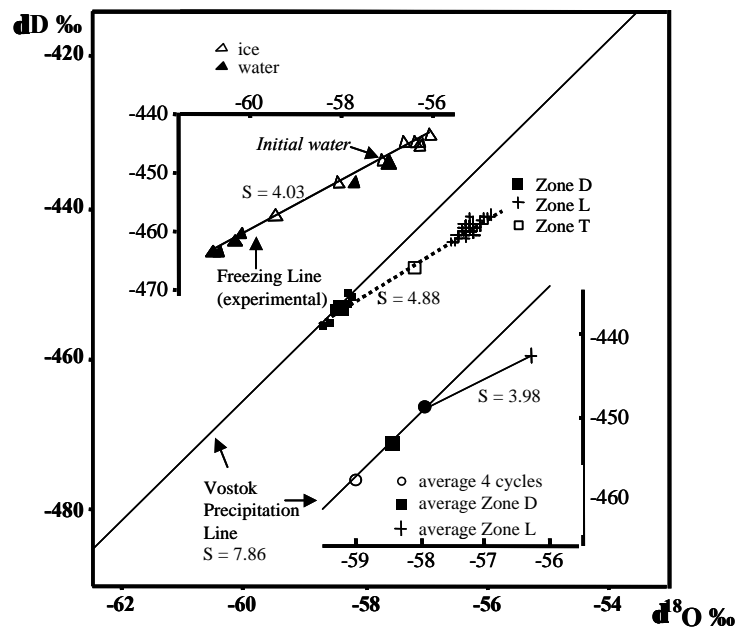


Figure 19 : δD - $\delta^{18}O$ diagram featuring the precipitation line corresponding to the ice samples from the last four climatic cycles (Vimeux et al., 1999; Craig, 1961) and samples from 3520 m to 3611 m. Samples from the bottom part of the disturbed zone D correspond to full squares, from the transition (zone T) to open squares, and from the lake ice (zone L) to crosses. The straight line passing through these ice samples has a slope of 4.88.

Top left. δD - $\delta^{18}O$ diagram of ice (open triangles) and water (black triangles) samples from a progressive freezing experiment of a limited water reservoir with initial water having $\delta D = -408.8\text{‰}$ and $\delta^{18}O = -51.7\text{‰}$ (adapted from Souchez and Jouzel, 1984). The results have been scaled to account for the difference between those isotopic contents of the initial water and those of the Vostok lake water (i.e, see equation in the main text, each experimental value from reference 7 has been multiplied by $(1-0.4493)/(1-0.4088)$ for δD and by $(1-0.0579)/(1-0.0517)$ for $\delta^{18}O$). With the scaling the experimental slope is equal to 4.03 and is very close from the theoretical value (3.98).

Bottom right : δD - $\delta^{18}O$ diagram showing the positions of the mean value for ice from the last four climatic cycles, from the disturbed sequence in the ice deformation zone (Zone D) and from the "lake ice" samples (zone L). The isotopic composition of the lake water (full circle) corresponds to the intersection of the precipitation line and of the line with a slope of 3.98 (theoretical freezing slope) passing through the mean "lake ice" point.

Vostok lake water is believed to originate from the melting of ice formed from snow precipitated on the Central Antarctic Plateau and then transferred at depth in the ice sheet. Based on a steady-state theory, the mean age of the lake water is roughly estimated to 1000 ka. No fractionation occurs upon melting because of the low isotopic diffusion coefficients in ice, which are in the order of $10^{-11} \text{ cm}^2\text{s}^{-1}$. The mean isotopic composition of the water that fed the lake through time (hereafter the lake water) is therefore some weighted average (over time and space) of the isotopic content of precipitation in the Vostok Lake "catchment area", and thus lies on the Vostok precipitation line. By contrast, when part of a water reservoir is allowed to freeze, the ice formed is enriched in deuterium and ^{18}O with respect to the water (Jouzel and Souchez, 1982). Except for very high freezing rates (see below), isotopic equilibrium is reached at the ice water interface, i.e. $(1+\delta_{\text{ice}}) = \alpha^*(1+\delta_{\text{water}})$, where δ stands for either δD or $\delta^{18}\text{O}$ and α for the equilibrium fractionation coefficients ($\alpha_{\text{D}}=1.0208$ and $\alpha^{18}\text{O}=1.0030$). The slope, S , of the line connecting the water and ice data points in the $\delta\text{D}/\delta^{18}\text{O}$ diagram is called the freezing slope :

$$S = ((1-1/\alpha_{\text{D}})/(1-1/\alpha^{18}\text{O})) * (1+\delta\text{D}_{\text{ice}})/(1+\delta^{18}\text{O}_{\text{ice}})$$

$$\text{i.e. } S = 6.81 * (1+\delta\text{D}_{\text{ice}})/(1+\delta^{18}\text{O}_{\text{ice}})$$

S is thus lower if the δ -values of the initial water at the onset of freezing are more negative (Jouzel and Souchez, 1982). For zone L ice, S equals 3.98, i.e. about half the precipitation slope. The lake water isotopic composition corresponds to the intersect of the freezing line passing by the average zone L point and of the precipitation line : $\delta\text{D} = -449.3\text{‰}$, $\delta^{18}\text{O} = -57.9\text{‰}$ (there is no reason to expect a significant change of the $\delta\text{D}/\delta^{18}\text{O}$ relationship for periods prior 420 ka since the central part of the Antarctic ice sheet itself and the surrounding oceans have probably then not been subject to larger changes than during the last 420 ka). The straightforward explanation for the zone L data being on the right side of the precipitation line is thus that this ice was formed by freezing of water from the subglacial lake. The deuterium and ^{18}O enrichment of the lake ice (Figure 19) with respect to lake water (6.6 ‰ in δD and 1.65 ‰ in $\delta^{18}\text{O}$), is however only ~ 60% of what would correspond to isotopic equilibrium (e.g., 11.4 ‰ and 2.8 ‰, respectively). There are several possibilities to explain this behavior none of which, however, affects the value of the freezing slope, and thus the above estimate of the lake water isotopic composition.

The first possibility is a freezing rate effect with high freezing rates producing weaker isotopic enrichments (Souchez et al., 1987). However to be detectable, freezing rates would have to be of the order of mm per hour while a maximum value of 4mm/yr is estimated assuming that the upward heat flux through the ice sheet results only from the released energy from freezing.

Second, in a closed water reservoir, the isotopic enrichment of the ice formed leads to an impoverishment of the residual water (Jouzel and Souchez, 1982). This second process is illustrated by an experiment of progressive freezing (top left of Figure 19) adapted from R. Souchez and J. Jouzel (1984). However (Figure 18) the isotopic composition of the lake ice increases slightly from the transition downwards whereas such a reservoir effect should cause a decrease (Jouzel and Souchez, 1982). At the scale of Lake Vostok there must be a dynamic equilibrium with some melting occurring in certain areas at the separation line while freezing is prevalent elsewhere. The isotopic profile recorded in the lake ice suggests that the subglacial lake is an open system with an efficient circulation of water (equilibrium is practically reached in an open system with a renewal rate larger than the freezing rate).

Third, even if the freezing itself occurs at equilibrium, part of the liquid water may be trapped during ice accretion. Such water pockets will freeze completely afterwards and their bulk isotopic composition is not modified. Therefore, the observed fractionation is less than the true value, depending on how much water is included in water pockets in the ice during the course of freezing (this "mixing" process also leaves the $\delta D/\delta^{18}O$ representative point on the freezing line). The Vostok lake ice contains solid inclusions, suggesting that this ice was formed at or close to the separation line where the ice sheet leaves the substratum and begins to float on the lake. The solid inclusions are millimetric in size and consist of a mineral particle on which dirt is attached. The fact that they are incorporated in the ice supports the idea that water pockets can also be included during freezing and this water trapping provides the best explanation for the limited lake ice isotopic enrichment.

We note that solid inclusions are more numerous in the upper part of the lake ice profile and seem to be absent below 3609 m (Figure 18). Available information (Kapitsa et al., 1996; Siegert and Ridley, 1998) suggests that the ice-lake interface is at a higher level in the Vostok area than elsewhere above the lake, making this area colder since glacial ice above is thinner. In fact, freezing can occur as soon as glacial ice loses contact with bedrock and ice accretion close to the grounding line allows the trapping of dirt particles into the ice (Figure 20). Once the lake becomes deeper, inclusion of particles is no more possible which explains the absence of inclusions in the bottom part of the lake ice. Instead, lake ice isotopic characteristics are exactly the same above and below that 3609 m depth (Figure 18). This supports the idea that processes of formation of the lake ice were unchanged throughout all the depth interval we have analysed (3538.7 to 3611 m).

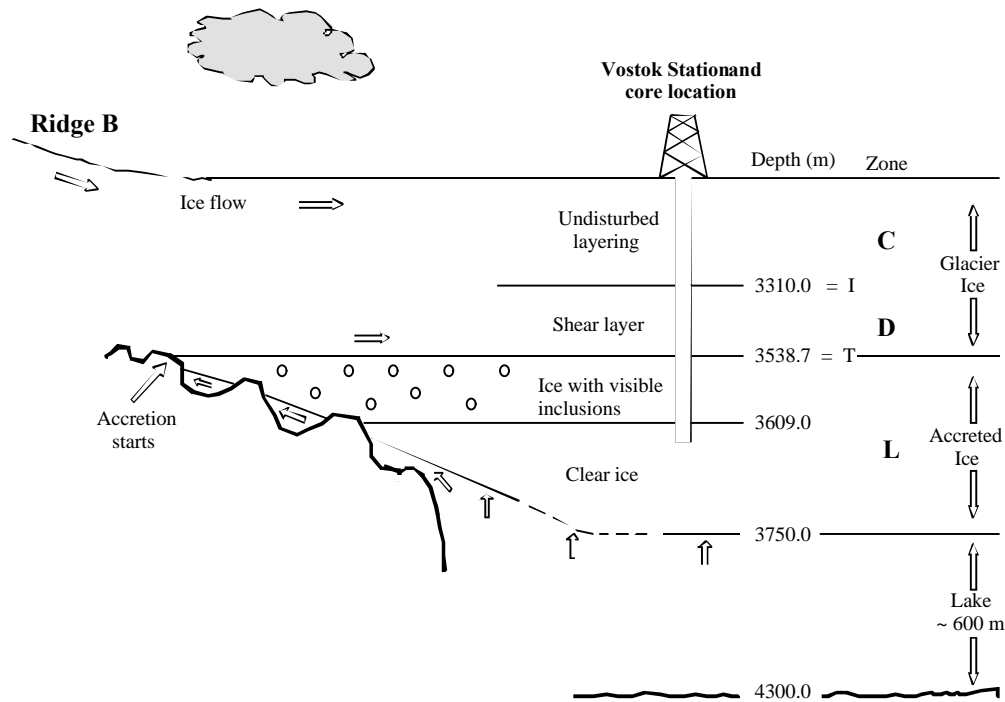


Figure 20 : Sketch of the ice sheet along the stream line passing by the Vostok core site. Ice accretion is thought to begin at the point where the ice sheet overrides the lake and continues throughout. Trapping of particles likely occurs in shallow depth area of the lake.

Interestingly, the lake water isotopic composition differs significantly from that of the overlying glacier ice (zone D) and the point representative of the last four climatic cycles is even isotopically lighter than zone D (bottom right of Figure 19). Zone D should be older than 420 ka and younger than the lake water itself. The decreasing isotopic sequence (lake water, disturbed ice and glacier ice) may result from a warmer average antarctic climate prior to 420 ka. This Antarctic surface cooling ($\sim 2^{\circ}\text{C}$ using the present-day isotope/temperature gradient) could simply reflect the general deterioration of the global climate during the Quaternary which would suggest that lake water is older than 1 million years. Indeed, data suggest warmer global climate (lower continental ice volume) for the period between 2 millions and 1 million years ago than 1 million years. Alternatively, the higher lake isotopic value could be due a different geographical origin between the ice recovered at the Vostok site and the lake water itself. However, the ice accumulated at Vostok during the last 420 ka already comes from a large area (between Ridge B and Vostok). This makes this second possibility less likely than that of a slow cooling trend of Central Antarctica during the Quaternary.

There is no reason to believe that the deeper ice down to the water interface (about 3750 m depth) would not also be refrozen lake water. Therefore a total thickness of about 210 m of lake ice can be reasonably assumed.

4.3.3 Ice formation in subglacial Lake Vostok

The ice ceiling of the lake is tilted, being at 750 m below sea level under 4300 m of ice in the North and at 250 m below sea level under 3750 m of ice in the South near Vostok Station. Therefore a gradient of the pressure-dependent melting point must exist at the base of the tilted ice ceiling (Kapitsa et al., 1996; Siegert et al., 1998). Wüest and Carmack (in press) indicate that, at a glaciostatic pressure of more than 3350 m of ice, the temperature of maximum density of fresh water is lower than the freezing temperature. Therefore, subglacial lake Vostok behaves as an ocean. The gradient of the freezing point along the ice-water interface and the geothermal heat flux are responsible for convection. In such a situation, melting occurs at the "thick-ice" side and freezing at the "thin-ice" side (Siegert et al., 2000). At the scale of the lake, there must be a dynamic equilibrium between melting and freezing.

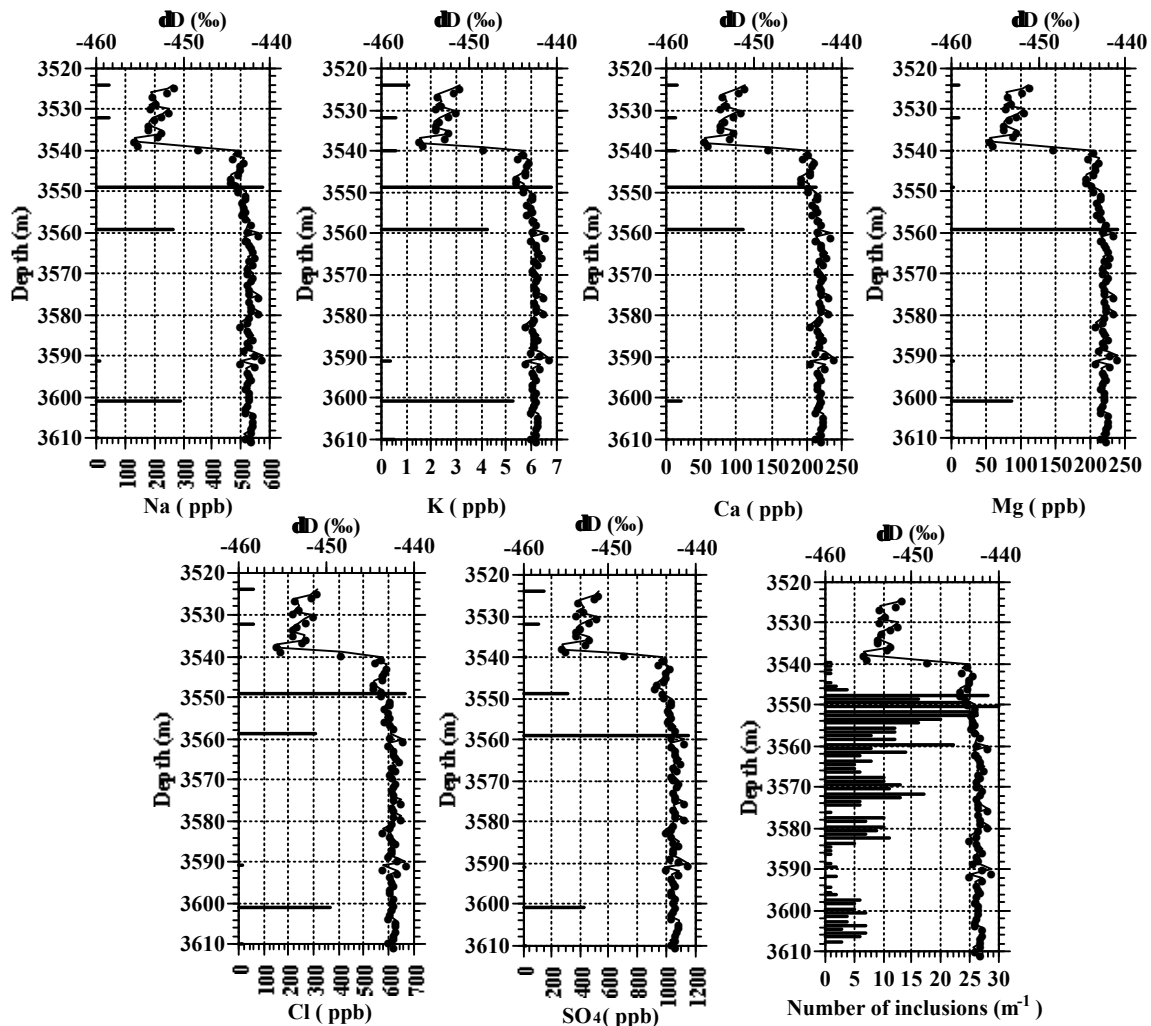


Figure 21 : Concentration in ppb of different chemical compounds in the basal part of the Vostok ice core. The δD vs. depth data are plotted on all graphs as a reference.

Figure 21 gives the concentration in ppb versus depth of different chemical compounds in the basal part of the Vostok ice core. Concentrations are indicated by bars at the depth where sampling occurred. Results indicate three major features :

- a) major elements represented in figure 21 are clearly enriched in lake ice, if compared with glacial ice above ;
- b) lake ice shows very strong variations in concentration of major compounds with, at the level of sampling resolution, peak values at about 3550 m, 3560 m and 3600 m depth respectively ;
- c) the relatively high concentration in major compounds of some lake ice layers compared to glacial ice above is an indication that the waters of lake Vostok are chemically not just pure glacial melt. As suggested by Siegert et al. (2000), impurities are transferred to lake Vostok water upon melting but are not transferred in the same concentrations back to the relatively pure refrozen ice above the lake. This is very important in connection with water circulation in the subglacial lake because, at the melting point, salinity has a major control on water density. However, Gorman and Siegert (1999) showed that radar reflections are present across the northern end of lake Vostok. For VHF radar penetration to be possible in water to 20 m, the water must be fresh but it is difficult from the deduced value of electrical conductivity (between 3 and $5 \cdot 10^{-4}$ mhos m^{-1}) to derive a value of water salinity. The northern end of the lake could also be influenced by meltwater of low salinity as suggested later.

Also indicated in figure 21 is the profile of solid, mineral inclusions within the ice versus depth. These solid inclusions mainly consist of a rock core on which dirt particles are attached ; they reach a few mm thickness in diameter. Solid inclusions are more numerous in the upper part of the lake ice profile and seem to be absent below 3609 m. Ice accretion close to the grounding line allows the trapping of dirt particles into the ice, which is impossible once the lake becomes deeper. Is there some relationship between the dirt concentration profile and the different chemical profiles displayed in figure 21 ? Although the difference in resolution hampers such a comparative study, there seems to be some correlation from visual inspection of the profiles. The microparticles present in the ice could in part be soluble and therefore would affect the chemical results obtained on melted samples but, anyway, they must come principally from the lake waters. It must also be said that at the depth of 3600 m the number of inclusions is about 5 per meter of core. This small number barely affects the chemical results at that level where major chemical elements are in significant higher concentration than in glacier ice above.

4.3.3.1 A rough estimation of Vostok lake salinity

A first approach to estimating Vostok lake salinity is by studying the thermal gradient in the ice. The thermal gradient in the ice at Vostok Station measured at 3600 m depth where the drilling stopped is 0.02 °K per meter. Kapitsa et al. (1996) used detailed radio-echo-soundings to derive the depth of the ice-water interface at the Vostok drilling site : 3750 m deeper than the ice sheet surface, at about 250 m below sea level. This allows calculation of a temperature of - 3.1 °C at the interface by extrapolating linearly the gradient mentioned above.

Now, at a pressure of 337 bars corresponding to the glaciostatic pressure of this column of ice, the pressure melting temperature of pure water is - 2.5 °C, i.e. 0.6 °C higher than the value calculated from the temperature gradient in the ice. Can this difference in temperature be attributed to the salinity of lake Vostok ? In such a case, a difference of 0.6 °C in the pressure melting-freezing temperature is conducive to a value of 12 ‰ in salinity. This is probably too high in view of the results of Gorman and Siegert (1999).

Furthermore, the validity of linear extrapolation of the thermal gradient to the ice-water interface can be questioned in the case where phase changes occur at the interface. During both melting and freezing heat diffuses away from the boundary into the cold ice sheet. The flux is generally higher during melting because the removal of the warmest ice tends to steepen the temperature gradient, whereas during freezing the addition of warm ice to the ice sheet base reduces the gradient (Jenkins and Bombosch, 1995; Paterson, 1994).

Another possible approach to estimate lake Vostok salinity is by studying lake ice chemistry and applying a reasonable distribution coefficient between ice and water so that a deduced lake water salinity can be obtained. Let us take the ice salinity of the sample at 3600 m depth as an example. The ice salinity of this ice layer is about 1 ppm. In order to deduce the water salinity, knowledge of a partitioning coefficient called in the literature the effective distribution coefficient (k_{eff}) is required. The effective distribution coefficient is the ratio between the observed concentration in the ice and the concentration in the liquid far from the interface. k_{eff} is dependent on the freezing rate and on the importance of liquid convection which can homogenise the liquid and suppress chemical gradients near the interface (Ozüm and Kirwan, 1976). Gross et al. (1977) showed experimentally a linear relationship between the concentration of NaCl in the ice and the concentration of NaCl in the water up to a few per mil salinity if the solution is stirred in order to avoid concentration gradients near the interface. This indicates that, in that range of water salinities, the effective distribution coefficient is independent of the concentration. Since concentration gradients near the interface were suppressed in the experiments, such a distribution coefficient is equivalent to the thermodynamic equilibrium coefficient k_{eq} , the ratio of solute concentration in the ice to solute concentration in the liquid at the interface,

which is independent of the freezing rate. Gross et al. (1977) obtained experimentally a value of 0.0028 for k_{eq} .

For higher salinities of the reservoir, the set up of constitutional supercooling induces the development of a dendritic or cellular interface, often described as the "skeletal layer" in the bottom layer of sea ice (Weeks and Ackley, 1986; Eicken, 1998). This results in the incorporation of brines within every single crystal and leads to the development of a typical intra crystalline substructure of brine layers between ice plates (clearly illustrated in horizontal thin sections in Gow et al. (1987), for example). The whole process seriously enhances chemical fractionation and increases k_{eq} values up to 0.12, as has been derived from field measurements on first-year sea ice (Weeks and Ackley, 1986; Nakawo and Sinha, 1981). Theoretical considerations (Weeks and Ackley, 1986; Tillier, 1962) allow one to define a stability criterion for an interface having planar grooves with steep walls (a good proxy for the "skeletal layer"), for water salinities of the order of a few ‰, in natural conditions of convection. This is corroborated by experimental observations of "interface breakdown" for salinities of NaCl solutions between 1 and 3 ‰ (Gross et al., 1977; Nagashiwa and Furukawa, 1997; Weeks and Lofgren, 1967). No intra crystalline substructure is visible in the thin sections from Vostok lake ice, suggesting that the water salinity is such that it did not lead to constitutional supercooling and the development of a skeletal layer at the ice-water interface. Therefore a $k_{eff} = k_{eq}$ value similar to the one obtained by Gross et al. (1977) should apply.

As will be discussed below, we suggest that the lake ice at the base of the Vostok core developed in a way similar to marine ice at the bottom of ice shelves, and not as ice growing by progression of a freezing front at the interface. Marine ice mainly results from the consolidation of loose frazil ice crystals that were formed as individuals in the water column under peculiar oceanic circulation conditions and subsequently accreted under buoyancy at the bottom of ice shelves. Eicken et al. (1994) obtained a value of k_{eff} of about 0.0008 for marine ice at the base of the Ronne Ice Shelf and Tison et al. (1993) a k_{eff} of 0.0009 for orbicular frazil ice at the base of Hells Gate Ice Shelf in Terra Nova Bay. These even lower values of the distribution coefficient result from the fact that marine ice is a complex medium where the mean ice salinity is partly controlled by the proportion of initial individual frazil ice crystals which can be considered, in a first approximation, as devoid of salt impurities.

It thus seems that a reasonable range of k_{eff} values between 0.0008 and 0.0028 would apply for the Vostok case study where the freezing rate is quite low and the lake water not stagnant. This results in lake water salinity prediction between 0.4 ‰ and 1.2 ‰.

A 0.4 ‰ lake water salinity estimate is considered as a minimal rough approximation. Let us noted here that Dry Valleys perennially frozen lakes receiving only meltwaters from direct glacial runoff reach salinities higher than 1 ‰ (Green et

al., 1988). It will however be shown that, for the purposes of this paper, the difference in salinity between glacier ice melt and lake water is much more important to consider than a precise value of lake water salinity. It is moreover quite possible that the salinity of lake Vostok water is higher in the deeper parts of the lake.

The salinity of glacier ice melt is of the order of 0.001 ‰ but, if this water is in contact with the subglacial floor, the salinity can increase to 0.1 ‰, depending on the particle/water ratio. This latter value has been obtained by several chemical studies of subglacial waters in different environments (Raiswell, 1984; Reynolds and Johnson, 1972; Eyles et al., 1982).

4.3.3.2 Water circulation

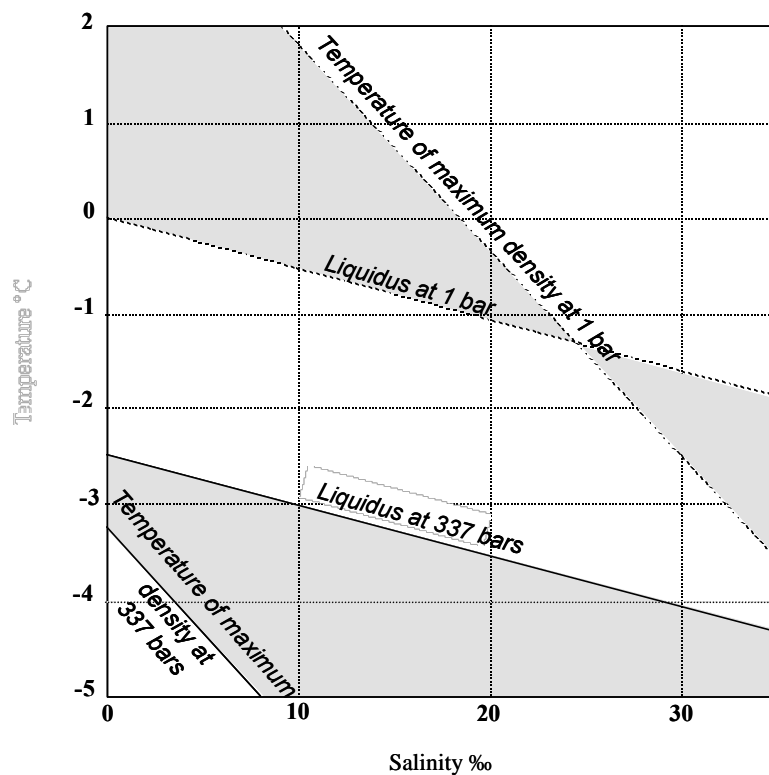


Figure 22 :Temperature of maximum density of water and freezing temperature versus salinity at a pressure of 337 bars. Values were computed from the general state equation of sea water.

Figure 22 gives, at a pressure of 337 bars corresponding to an ice thickness of 3750 m, the temperature of maximum density of water versus salinity and the freezing temperature versus salinity. It can be clearly seen that, whatever the salinity, the freezing temperature is first reached when water is cooled so that, closer to the freezing point, water has a higher density. The consequence of this fact is an unstable water column for geothermal heating from below since warmer water is less dense. Wüest and Carmack (in press) combine this notion with the fact that a

temperature gradient exists along the ice-water interface to construct a model of water circulation in the lake. In this model, salinity is not considered as a factor. It is true that a 0.4 ‰ salinity will not change the general behaviour of lake waters. However, as indicated below, a difference in salinity could have in lake Vostok far greater consequences than a contrast in temperature. At a pressure of 337 bars, a difference of 0.37 °C in temperature corresponding to the difference in the pressure melting temperature between the northern and the southern part of the lake at the ice-water interface gives a difference in σ_w of about 0.03. σ_w is equal to $1000 (\rho_w - 1)$ where ρ_w is the water density. By contrast, at the same pressure, a difference in salinity of 0.4 ‰, like that between lake water and pure glacial meltwater, gives a difference in σ_w of about 0.32. Even a weak salinity must therefore be taken into account to complete the picture of water circulation in lake Vostok.

Information gained by the study of medium-sized Antarctic ice shelves is worth considering in this context. Today, melting generally occurs at the grounding line. Less dense water at the pressure melting point at depth is produced in this way since glacier ice melt has a much lower salinity than sea water. This less dense water rises along the ice shelf-ocean interface. Since the freezing point is higher when pressure decreases, the rising water becomes supercooled. Frazil ice crystals are generated in the rising plume and, because of their lower density, accrete at the bottom of the ice shelf consolidating as a layer of marine ice. Lewis and Perkin (Lewis and Perkin, 1986) called this process the ice pump mechanism.

The situation in lake Vostok is not however identical to that found beneath ice shelves. Firstly, along the glacier flow line in the southern part of the lake passing through Vostok station the highest point of the lake is close to the grounding line, where the ice sheet leaves contact with its solid substratum and becomes floating on the lake. Along this line, the ice-water interface does not change very much in altitude between the grounding line and the place where the ice sheet makes contact again with its solid substratum at the south-eastern end of the lake. By contrast, along a north-south profile, the ice-water interface is at a much lower altitude in the northern part of the lake than in the surroundings of Vostok station in the south. Secondly, lake Vostok is a closed system whereas an ice shelf is open at one hand to the ocean (Mayer et al., in press).

4.3.3.3 Ice formation in the subglacial lake

The isotopic characteristics of the lake ice present at the bottom of the Vostok ice core were given in Jouzel et al. (1999). It is shown that the deuterium and oxygen 18 enrichment of the lake ice in comparison to the deduced values of lake water (6.6 ‰ in δD and 1.65 ‰ in $\delta^{18}O$) is only about 60 % of the corresponding isotopic equilibrium (11.4 ‰ and 2.8 ‰ respectively). Freezing rate and reservoir effects were

discarded as possible explanation. It was suggested that, if freezing itself occurs at equilibrium, water pockets may be trapped during ice accretion. Such water pockets would freeze completely afterwards, and their bulk isotopic composition would not be modified. Therefore the observed fractionation must be less than the true value, depending on how much water is included in water pockets in the ice during the course of freezing. It is now possible with the developments given above to develop such a process in the light of water circulation in the lake.

Let us consider rising meltwaters from the ice-water interface from the northern part of the lake where melting occurs. The rising plume is the consequence of thermal and also probably salinity effects. Such waters will become supercooled as they rise. The maximum water supercooling would be the difference in melting points between the deeper and the upper parts of the lake at the ice-water interface. Nucleation will however start in the rising water for lower supercooling levels. A reasonable range of supercooling is between 0.01°C and 0.1°C. For such values, growth velocities of frazil ice crystals in fresh water are between 10^{-6} and $5 \cdot 10^{-5} \text{ m s}^{-1}$ (Hobbs, 1974). Now, observed isotopic fractionation between ice and water in open systems can be described by an equation similar to Burton's equation (Burton et al., 1953) :

$$\left(\frac{1000 + d_s}{1000 + d_i} \right) = \frac{a}{a - (a - 1)e^{\frac{-h \cdot v}{D}}}$$

where δ_s and δ_i are the respective δ -values of the ice and of the initial water, α the appropriate equilibrium fractionation coefficient, v the freezing rate, h the boundary layer thickness and D the appropriate diffusion coefficient. This equation can be solved either for deuterium or oxygen 18. Using the supercooling range and the associated growth rates mentioned above with a reasonable boundary layer thickness of 0.1 cm, calculations indicate that the frazil ice crystals will have an isotopic enrichment in δD between 4.56 ‰ and 0 ‰ respectively, compared to the lake water (Table III). A higher supercooling will of course lead to higher growth rate and thus, a fortiori, to no isotopic enrichment in the frazil ice crystals. Now, consolidation of loose frazil ice crystals by freezing the host water is a very slow process, thus at isotopic equilibrium. The isotopic composition of the lake ice, which is not at equilibrium freezing taking into account the lake water isotopic composition (enrichment of 6.6 ‰ instead of 11.4 ‰ in Jouzel et al., 1999), can be understood if the frozen host water represents between 30 and 58 % of the bulk lake ice. Such values are comparable to those obtained in experimental and field studies of frazil ice formation (Andersson and Daly, 1992; White, 1991). The characteristics of the isotopic composition of the lake ice thus strongly support the occurrence of a mechanism similar to marine ice formation under an ice shelf, involving consolidation of loose frazil ice crystals accreted at the ice ceiling of the lake (Souchez et al., 2000).

Table III : Proportion of frozen host water in lake ice deduced from its isotopic composition. Burton's equation is used with boundary layer thickness = 1 mm; $\alpha_{eq}=1.0208$, $D = 1.1 \cdot 10^{-9} \text{ m}^2 \text{ s}^{-1}$, $\alpha D_{\text{bulk lake ice}} = -442.7\text{‰}$, $\alpha D_{\text{water}} = -449.3\text{‰}$, $\alpha D_{\text{frozen host water}} = -437.9 \text{‰}$.

Water supercooling (°C)	Crystal growth rate (m s ⁻¹)	Effective fractionation coefficient (α_{eff})	dD _{frazil}	% frazil	% frozen host water
0.01	10 ⁻⁶	1.0083	-444.74	70	30
0.1	5 · 10 ⁻⁵	1.0000	-449.3	42	58

In addition, Priscu et al. (1999) found at 3590 m, the core depth they studied, a much higher proportion of micas in the particles of micrometric size than in crystalline and metamorphic rocks. This is probably an indication of capture by scavenging during frazil ice accretion, the geometry of mica crystals allowing them to float more easily in the lake waters. Ice crystals are fairly big in the lake ice : > 20 cm to 1 m. It is therefore not possible to compare the azimuths of their c-axes and so unambiguous information on their formation process cannot be obtained. The variability in the dip (Figure 17) does not however favour a single process of freezing front progression in the lake water from the ice-water interface.

An additional mechanism is the possibility of glacial meltwater seeping at grounding line at selected places of the ice-bedrock-water contact, for example upglacier from Vostok station. If seeping glacial meltwater with a salinity of the order of 0.1 ‰ or less enters into contact with lake Vostok water of 0.4 ‰ salinity, a peculiar situation occurs. Let us consider that both waters are at their respective pressure freezing point. At a given pressure, the freezing point temperature is dependent on the salinity of the water, being higher if the salinity is lower. Thus the freezing point of lake water is lower than that of seeping glacial meltwater. Heat diffusion will occur locally from the seeping meltwater to the lake. On the other hand, the salinity of lake water being higher than that of glacial meltwater, salts will diffuse from the lake to the meltwater. Thermal diffusivity is an order of magnitude higher than salt diffusion. The seeping glacial meltwater loses heat more rapidly than it gains salt so that supercooling followed by freezing occurs, incorporating into the ice mineral particles present in this locality. This double-diffusion mechanism is responsible for the presence of aggregates of millimetric sizes into the frazil ice. A small water quantity which freezes is enough for mineral inclusion into the frazil ice. Diffusion coefficients of stable isotopes and of salts in liquid water have the same order of magnitude, so that the double-diffusion mechanism described above also leads to isotopic diffusion. The isotopic composition of the ice formed at the grounding line is thus likely to be a good indicator of the process. This is the background of the study undertaken in Terra Nova Bay (Souchez et al., 1995c). In

the case studied here, there is however no significant difference in isotopic composition between glacial meltwater and lake water.

On the time scale for ice to pass over the width of the lake, changes in lake volume and in position of the lower boundary of the ice sheet due to changes in ice thickness are likely to occur. Therefore there could well be periods where lake ice formation is promoted. There is however yet no information for constraining such a hypothesis. It is probably true that freezing will be favoured if the ice thickness is less. Freezing rates determined by Siegert et al. (2000) from radar data could well be not correct if the frazil ice mechanism is retained. Lake ice once formed is entrained by glacier flow and can be exported outside the lake area where ice makes contact again with its substratum at the downstream end of the lake.

4.3.4. Conclusion

From 3539 m below the Antarctic ice sheet surface to its bottom at about 3750 m, Vostok ice core consists of ice refrozen from Lake Vostok water. Evidence comes from the isotope studies, the total gas content, crystal size and electrical conductivity of the ice. Vostok area is a likely place for water freezing at the lake-ice interface since this interface is there at a higher level than elsewhere above the lake. Isotopic data suggest that subglacial lake Vostok is an open system with an efficient circulation of water and that it was formed during periods that were slightly warmer than those of the last 420 000 years.

Ice formation in subglacial lake Vostok is related to the tilted surface of the ice-water interface. Because the lake behaves as an ocean, water circulation is likely to occur. Supercooling in rising waters along the tilted ice-water interface is considered as the mechanism responsible for lake ice formation. This produces loose frazil ice crystals which will accrete at the ice ceiling with subsequent freezing of the host water.

The isotopic composition of the lake ice corroborates ice formation in two steps : loose frazil ice crystals produced in supercooled plumes followed by slow freezing of the host water in which the ice crystals accrete at the ice ceiling.

5 OVERALL CONCLUSIONS

The presence of numerous subglacial lakes, some of them of great extent like lake Vostok, under the East Antarctic Ice Sheet has certainly important consequences on the ice sheet behaviour. Meltwater at the base implies that the pressure melting point is reached in the bottom part of the basal ice. Liquid water

has the potential to induce glacier sliding which would modify the age-depth relationship of the ice at depth.

The EPICA project has as one of its major objectives to derive palaeoclimatic and palaeoenvironmental information from a deep drilling now conducted at Dome C in the central part of East Antarctica. In order to retrieve such an information, a reliable flow model able to date ice at depth must be constructed. Numerous small subglacial lakes have been detected in the vicinity of the Dome C site by radio-echo-soundings. Therefore a study of the interactions between the ice sheet and subglacial water bodies has to be made to help to fulfill the objectives of the program.

Basal ice composition study is a powerful tool for the investigation of the interactions of the ice sheet with its substratum. Isotopic composition in δD and $\delta^{18}O$, gas content and gas composition, crystallographic and chemical properties of the ice are all affected by phase changes and by the presence of liquid water.

In order to be able to interpret correctly the analyses which will be done on the basal ice from the EPICA ice core at Dome C, some sites where the ice sheet is in contact with water bodies have been and are studied within this research contract.

In two circumstances, basal ice originated in the contact zone between an ice sheet and a water body can be easily studied since outcroppings are present at the ice sheet margin or at its surface.

In the Dry Valleys area of South Victoria Land, glaciers below the pressure melting point at their base are flowing into lakes. It can be shown that transient wet-based conditions occur in such circumstances as ice flows into the unfrozen sediments of the lake bottom, creating conditions favorable to the entrainment of debris and to ice accretion by water freezing.

In Terra Nova Bay, ice formed at the grounding line where a glacier enters into contact with the ocean in areas protected from the influence of high salinity shelf waters. Such ice is now outcropping at the ice shelf surface because of strong ablation due to katabatic winds. An upward velocity component thus exists and ice previously at depth reaches the ice shelf surface. Ice composition studies indicate that freezing at the grounding line occurs by a double-diffusion effect, diffusion of heat being an order of magnitude higher than salt diffusion. Double-diffusion freezing at the grounding line is a newly discovered process. Its implications on a larger scale must still be envisaged.

The ice at the bottom of the Vostok ice core is lake ice. It is formed as a result of water circulation in subglacial lake Vostok. Supercooling as a consequence of rising waters and a possible contrast in water salinity gives rise to frazil ice crystals. Subsequent consolidation of the loose ice crystals developed results in the accretion of ice the ceiling of the lake.

The consequence of the presence of such an extensive subglacial lake and of lake ice formation on the behaviour of the ice sheet must still be considered.

ACKNOWLEDGEMENTS

The "Programma Nazionale di Ricerche in Antartide" (PNRA) is gratefully acknowledged for having supported the field work in Terra Nova Bay. Thanks are also due to Antarctica New Zealand for having supported the field trips in the Dry Valleys area. R. Souchez is also grateful to Drs. J. Jouzel and J.R. Petit for including him within the Vostok ice core project.

This report is a contribution to the Belgian Antarctic Program (OSTC - Science Policy Office).

REFERENCES

- Andersson, A. and Daly, S.F. 1992. Laboratory investigations of trash rack blockage by frazil ice, C.R.R.E.L. Report 92-16, Hanover.
- Angrisano, G. 1989. Carta batimetrica Mare di Ross-Baia Terra Nova. Istituto Idrografico della Marina, Genova.
- Baroni, C. 1990. The Hells Gate and Backstairs Passage Ice Shelves, Victoria Land, Antarctica. *Mem. Soc. Geol. Ital.* 43: 123-144.
- Baroni, C., Stenni, B. and Iacumin, P. 1991. Oxygen isotopic composition of ice samples from the Hells Gate and Backstairs Passage ice shelves (Victoria Land, Antarctica) : Evidence of bottom freezing. *Mem. Soc. Geol. Ital.* 46: 45-48.
- Blunier, T. Chappellaz, J.A., Schwander, J., Barnola, J., Desperets, W.T., Stauffer, B., and Raynaud, D. 1993. Atmospheric methane record from a Greenland ice core over the last 1000 year. *Geophys. Res. Lett.* 20: 2219-2222.
- Bombosch, A. and Jenkins, A. 1995. Modeling the formation and deposition of frazil ice beneath Filchner-Ronne Ice Shelf. *J. Geophys. Res.* 100(C4): 6983-6992.
- Boulton, G.S. 1979. Processes of erosion on different substrata. *J. Glaciol.* 23(89): 15-38.
- Boulton, G.S. 1996. Theory of glacial erosion, transport and deposition as consequence of subglacial sediment deformation. *J. Glaciol.* 42(140): 43-62.
- Burton, J.A., Prim, R.C. and Slichter, W.P. 1953. The distribution of solute in crystal growth from the melt. Part I : Theoretical. *J. Chem. Phys.* 21(1): 1987-1991.
- Capra, A., Radiocioni, F. and Vittuari, L. 1996. Kinematic GPS profiles and navigation in Antarctica. *Int. Arch. Photog. Rem. Sens.* 23 (B1): 31-35.
- Carmignani, I. Ghezzi, C., Gosso, G., Lombardo, B., Meccheri, M., Montrasio, A., Pertusati, P.C., and Salvini, F. 1987. Geological map of the area between David and Mariner Glaciers, Victoria Land -Antarctica. Programma Nazionale Ricerche Antartide, C.N.R.-ENEA.
- Cartwright, K. and Harris, H.J.H. 1978. Origin of water in lakes and ponds in the Dry Valley region, Antarctica (Abstracts). *Dry Valley Drilling Project Bull.* 8(8).
- Chinn, T.J.H. 1991. Polar glacier margin and debris features. *Mem. Soc. Geol. Ital.* 46: 25-44.
- Chinn, T.J.C. 1993. Physical hydrology of the Dry Valleys lakes. In: *Physical and biogeochemical processes in Antarctic lakes.* Green, W.J. and Friedmann, E.I. (Eds). Washington, DC, American Geophysical Union. Antarctic Research Series 59: pp. 1-51.
- Craig, H. 1961. Isotopic variations in meteoric waters. *Science.* 133(3465): 1702-1703.
- Craig, H., Wharton Jr., R.A. and McKay, C.P. 1992. Oxygen supersaturation in ice-covered Antarctic lakes: biologic versus physical contributions. *Science.* 255(5042): 318-321.

- Dayton, P.K., Robilliard, G.A. and DeVries, A.L. 1969. Anchor ice formation in McMurdo Sound, Antarctica, and its biological effects. *Science* 163: 273-274.
- Denton, G.H., Sugden, D.E., Marchant, D.R., Hall, B.L., and Wilch, T.I. 1993. East Antarctic Ice Sheet sensitivity to Pliocene climate change from a Dry Valley perspective. *Geographiska Annaler* 75 A: 155-204.
- Dini, M., Longinelli, A., Orombelli, G. and Smiraglia, C. In press. Isotopic composition of snow samples from northern Victoria Land (Antarctica) and correlations with geographical factors. *Geo. Fis. Din. Quat.*
- Domack, E.W., Harris, P.T. 1998. A new depositional model for ice shelves based upon sediment cores from the Ross Sea and Mac Robertson shelf, Antarctica. *Ann. Glaciol.* 27: 281-284.
- Echelmeyer, K. and Zhongxiang, W. 1987. Direct observation of basal sliding and deformation of basal drift at sub-freezing temperatures. *J. Geol.* 33(113): 83-98.
- Eicken, H., Oerter, H., Miller, H., Graf, W. and Kipfstuhl, J. 1994. Textural characteristics and impurity content of meteoric and marine ice in the Ronne Ice Shelf, Antarctica. *J. Glaciol.* 40(135): 386-398.
- Eicken, H. 1998. Deriving modes and rates of ice growth in the Weddell Sea from microstructural, salinity and stable-isotope data. In: *Antarctic sea ice : physical processes, interactions and variability.* M.O. Jeffries. American Geophysical Union, Washington, D.C.: pp. 89-122.
- Eyles, N., Sasseville, D., Slatt, R. and Rogerson, R. 1982. Geochemical denudation rates and solute transport mechanisms in a maritime temperate glacier basin. *Canadian Journal of Earth Sciences.* 18: 1570-1581.
- Fitzsimons, S.J. 1996. Formation of thrust-block moraines at the margins of dry-based glaciers, south Victoria Land, Antarctica. *Ann. Glaciol.* 22: 68-74.
- Fitzsimons, S.J., McManus, K.J. and Lorrain, R.D. 1999. Structure and strength of basal ice and substrate of a dry-based glacier: evidence for substrate deformation at sub-freezing temperatures. *Annals of Glaciology.* 28: 236-240.
- Fowler, A.C. 1986. Sub-temperature basal sliding. *J. Glaciol.* 32(110): 3-5.
- Frezzotti, M. 1993. Glaciological study in Terra Nova Bay, Antarctica, inferred from remote sensing analysis. *Ann. Glaciol.* 17: 63-71.
- Gorman, M.R. and Siegert, M.J. 1999. Penetration of Antarctic subglacial lakes by VHF electromagnetic pulses : Information on the depth and electrical conductivity of basal water bodies. *J. Geophys. Res.* 104(B12): 29311-29320.
- Gow, A.J., Ackley, S.F., Buck, K.R. and Golden, K.M., 1987. Physical and structural characteristics of Weddell Sea pack ice. 87-14, CRREL Report, 87-14.
- Gow, A.J., Meese, D.A., Alley, R.B., Fitzpatrick, J.J., Anandakrishnan, S., Woods, G.A., and Elder, B.C. 1997. Physical and structural properties of the Greenland Ice Sheet Project 2 ice core: A review. *Journal of Geophysical Research.* 102 C: 26,559-26,576.

- Green, W.J., Angle, M.P. and Chave, K.E. 1988. The geochemistry of Antarctic streams and their role in the evolution of four lakes of the McMurdo Dry Valleys. *Geochim. Cosmochim. Acta.* 52: 1265-1274.
- Grosfeld, K., Gerdes, R. and Determann, J. 1997. Thermohaline circulation and interaction beneath ice shelf cavities and the adjacent open ocean. *J. Geophys. Res.* 102: 15595-15610.
- Gross, G.W., Wong, P.M. and Humes, K. 1977. Concentration dependent solute redistribution at the ice-water phase boundary. III. Spontaneous convection, chloride solutions. *J. Chem. Phys.* 67(11): 5264-5274.
- Hobbs, P.V. 1974. *Ice Physics*. Clarendon Press, Oxford, 837 pp.
- Holdsworth, G., 1974. *Meserve Glacier, Wright Valley, Antarctica, part I. Basal processes*. 37, Institute of Polar Studies, The Ohio State University Research Foundation, Columbus.
- Holdsworth, G. and Bull, C., 1970. The flow law of cold ice: investigations on the Meserve Glacier, Antarctica, International Association of Scientific Hydrology Publication 86. Antarctic Glaciological Exploration (ISAGE), Hanover, New Hampshire, pp. 204-216.
- Hooke, R.I.B. 1998. *Principles of glaciers mechanics*. Prentice Hall, New Jersey, 248 pp.
- Iverson, N. and Souchez, R. 1996. Isotopic signature of debris-rich ice formed by regelation into a subglacial sediment bed. *Geophys. Res. Lett.* 23(10): 1151-1154.
- Jacobs, S.S., Helmer, H.H., Doake, C.S.M., Jenkins, A. and Frolich, R.M. 1992. Melting of ice shelves and the mass balance of Antarctica. *J. Glaciol.* 38(130): 375-387.
- Janssens, L. 1996. *Les propriétés des glaces basales révélatrices des interactions calotte glaciaire-substratum au Groenland*, ULB, Brussels.
- Jenkins, A., Vaughan, D. and Doake, C. 1994. Numerical modelling of Filchner-Ronne Ice Shelf. *FRISP Report*. 8: 36-38.
- Jenkins, A. and Bombosch, A. 1995. Modeling the effects of frazil ice crystals on the dynamics and thermodynamics of Ice Shelf Water plumes. *J. Geophys. Res.* 100(C4): 6967-6981. J
- Jouzel, J. and Souchez, R. 1982. Melting-refreezing at the glacier sole and the isotopic composition of the ice. *J. Glaciol.* 28(98): 35-42.
- Jouzel, J. et al. 1999. More than 200 meters of lake ice above subglacial lake Vostok, Antarctica. *Science*. 286(10 December): 2138-2141.
- Kapitsa, A., Ridley, J., Robin, G.d.Q., Siegert, M. and Zotikov, V. 1996. A large deep fresh water lake beneath the ice of Central East Antarctica. *Nature*. 381: 684-686.
- Kleman, J. and Borgström, I. 1994. Glacial land forms indicative of a partly frozen bed. *J. Glaciol.* 40(135): 255-264.

- Kleman, J. and Borgström, I. 1996. Reconstruction of palaeo-ice sheets: the use of geomorphological data. *Earth Surf. Processes and Landforms*. 21(10): 893-909.
- Koerner, R.M. 1989. Ice core evidence for extensive melting of the Greenland ice sheet in the Last Interglacial. *Science*. 244: 964-968.
- Lewis, E.L. and Perkin, R.G. 1986. Ice pumps and their rates. *J. Geophys. Res.* 91(10): 11.756-11.762.
- MacAyeal, D.R. 1984. Thermohaline circulation below the Ross Ice Shelf : a consequence of tidally induced vertical mixing and basal melting. *J. Geophys. Res.* 89: 597-606.
- Martinerie, P., Raynaud, D., Etheridge, D.M., Barnola, J.M. and Mazaudier, D. 1992. Physical and climatic parameters which influence the air content in polar ice. *Earth Planet Sci. Lett.* 112(1-4): 1-13.
- Mayer, C., Grosfeld, K. and Siegert, M.J. In press. Water circulation and mass exchange within subglacial Lake Vostok. .
- Moser, H. and Stichler, W. 1980. Environmental isotopes in ice and snow. In: *Handbook of Environmental Isotope Geochemistry, the terrestrial environment*, 1A. P. Fritz and J. Fontes. Elsevier, New York: pp. 141-178.
- Nagashiwa, K. and Furukawa, Y. 1997. Solute distribution in front of an Ice/Water interface during directional growth of ice crystals and its relationship to interfacial patterns. *J. Phys. Chem. B*(101): 6174-6176.
- Nakawo, M. and Sinha, N. 1981. Growth rate and salinity profiles of first-year sea ice in the high Arctic. *J. Glaciol.* 27: 315-330.
- Nickling, W.G. and Bennett, L. 1984. The shear strength characteristics of frozen coarse granular debris. *J. Glaciol.* 30(106): 348-357.
- Oerter, H. et al. 1992. Evidence for basal marine ice in the Filchner-Ronne Ice Shelf. *Nature*. 358: 399-401.
- Ozüm, B. and Kirwan, D., 1976. Impurities in ice crystals grown from stirred solutions. In: S.S. International Association of Chemical Engineers (Editor), pp. 1-6.
- Paterson, W.S.B. 1994. *The physics of Glaciers*. Elsevier Science Ltd., Oxford, 480p.
- Petit, J. et al. (18 co-authors) 1999. 420,000 years of climate and atmospheric history revealed by the Vostok Deep Antarctic Ice Core. *Nature*. 399: 429-436.
- Powell, R.D., Dawber, M., McInnes, J.N. and Pyne, A.R. 1996. Observations of the grounding-line area at a floating glacier terminus. *Ann. Glaciol.* 22: 217-223.
- Priscu, J. et al. 1999. Geomicrobiology of subglacial ice above lake Vostok, Antarctica. *Science*. 286(10 December): 2141-2147.
- Raiswell, R. 1984. Chemical models of solute acquisition in glacial melt waters. *J. Glaciol.* 30: 49-57.

- Reynolds, R. and Johnson, N. 1972. Chemical weathering in the temperate glacial environment of the Northern Cascade Mountains. *Geochim. Cosmochim. Acta.* 36(5): 537-554.
- Rozanski, K., Araguas-Araguas, L. and Gonfiantini, R. 1991. Isotopic patterns in modern global precipitation. In: *Climate change in continental isotopic records.* Swart, P.K., Lohmann, K.C., McKenzie, J.A. and Savin, S. (Eds). Washington, DC, American Geophysical Union: 1-36 (Geophysical Monograph 78).
- Sharp, M., Jouzel, J., Hubbard, B. and Lawson, W. 1994. The characters, structure and origin of the basal ice layer in a surge-type glacier. *J. Glaciol.* 30 (106): 327-340.
- Shreve, R.L. 1984. Glacier sliding at subfreezing temperatures. *J. Glaciol.* 30 (106): 341-347.
- Siegert, M. and Ridley, J. 1998. An analysis of the ice sheet surface and subsurface topography above the Vostok station subglacial lake, central East Antarctica. *J. Geophys. Res.* 103(B5): 10195-10207.
- Siegert, M.J., Kwok, R., Mayer, C. and Hubbard, B. 2000. Water exchange between the subglacial Lake Vostok and the overlying ice sheet. *Nature.* 403(10 February 2000): 643-646.
- Souchez, R. and Jouzel, J. 1984. On the isotopic composition in δD and $\delta^{18}O$ of water and ice during freezing. *J. Glaciol.* 30(106): 369-372.
- Souchez, R., Tison, J.-L. and Jouzel, J. 1987. Freezing rate determination by the isotopic composition of the ice. *Geophys. Res. Lett.* 14(6): 599-602.
- Souchez, R., Lorrain, R., Tison, J.-L. and Jouzel, J. 1988. Co-isotopic signature of two mechanisms of basal-ice formation in Arctic outlet glaciers. *Ann. Glaciol.* 10: 163-166.
- Souchez, R. and Lorrain, R. 1991. *Ice composition and glacier dynamics.* Springer-Verlag, Berlin, 207 p.
- Souchez, R., Meneghel, M., Tison, J.-L., Lorrain, R., Ronveaux, D., Baroni, C., Lozej, A., Tabacco, I., and Jouzel, J. 1991. Ice composition evidence of marine ice transfer along the bottom of a small Antarctic ice shelf. *Geophys. Res. Lett.* 18(5): 849-852.
- Souchez, R., Lemmens, M., Tison, J.-L., Lorrain, R. and Janssens, L. 1993. Reconstruction of basal boundary conditions at the Greenland Ice Sheet margin from gas composition in the ice. *Earth Planet. Sci. Lett.* 118: 327-333.
- Souchez, R., Janssens, L., Lemmens, M. and Stauffer, B. 1995a. Very low oxygen concentration in basal ice from Summit, Central Greenland. *Geophys. Res. Lett.* 22(15): 2001-2004.
- Souchez, R., Lemmens, M. and Chappellaz, J. 1995b. Flow-induced mixing in the GRIP basal ice deduced from the CO_2 and CH_4 records. *Geophys. Res. Lett.* 22(1): 41-44.

- Souchez, R. et al. 1995c. Investigating processes of marine ice formation in a floating ice tongue by a high resolution isotopic study. *J. Geophys. Res.* 100(C4): 7019-7025.
- Souchez, R., Khazendar, A., Ronveaux, D. and Tison, J.-L. 1998. Freezing at grounding line in East Antarctica; possible implication of sediment export efficiency. *Ann. Glaciol.* 27: 316-320.
- Souchez, R., Petit, J.R., Tison, J.-L., Jouzel, J., Verbeke, V. 2000. Ice formation in subglacial Lake Vostok, Central Antarctica. *Earth Planet. Sci. Lett.* 181: 529-538.
- Stauffer, B., Neftel, A., Oeschger, H. and Schwander, J. 1985. CO₂ concentration in air extracted from Greenland ice samples. In: *Greenland ice core: geophysics, geochemistry and the environment*. C.e.a. Langway. AGU Geophys.: pp. 85-89.
- Stocchino, C. 1991. Carta batimetrica, Mare di Ross - Baia Terra Nova, 1:50000. Istituto Idrografico della Marina, Genova.
- Tiller, W.A. 1962. Effect of grain boundaries on solute partitioning during progressive solidification. *J. Appl. Phys.* 33(10): 3106-3107.
- Tison, J.-L., Ronveaux, D. and Lorrain, R. 1993. Low salinity frazil ice generation at the base of a small antarctic ice shelf. *Antarctic Science.* 5(3): 309-322.
- Tison, J.-L., Thorsteinsson, T., Lorrain, R. and Kipfstuhl, J. 1994. Origin and development of textures and fabrics in basal ice at Summit, Central Greenland. *Earth Planet. Sci. Lett.* 125(1-4): 421-437.
- Tison, J.-L., Barbante, C., Bondesan, A., Lorrain, R. and Capra, A. 1997. Ice shelf/Ocean interactions at the front of Hells Gate Ice Shelf (Terra Nova Bay, Antarctica). *Terra Antarctica reports.* 1: 29-32.
- Tison, J.-L. et al. 1998. Linking landfast sea ice variability to marine ice accretion at Hells Gate Ice Shelf, Ross Sea. In: *Antarctic sea ice : physical processes, interactions and variability*. M.O. Jeffries. American Geophysical Union, Washington, D.C.: pp. 375-407.
- Vimeux, F., Masson, V., Jouzel, J., Stievenard, M., Petit, J.R. 1999. Glacial-interglacial changes in ocean surface conditions in the Southern Hemisphere. *Nature* 398: 410-413.
- Weeks, W.F. and Lofgren, G. 1967. The effective distribution coefficient during the freezing of NaCl solutions. In: H. Oura (Editor), *Physics of Snow and Ice : International Conference on Low Temperature Science*. Inst. of Low Temp. Sci., Hokkaido, pp. 579-597.
- Weeks, W.F. and Ackley, S.F. 1986. The growth, structure and properties of sea ice. In: *The geophysics of sea ice*. N. Untersteiner. Martinus Nyhoff Publ., Dordrecht (Nato ASI Series B, Physics): pp. 9-164.
- White, K.D. 1991. Determining the intrinsic permeability of frazil ice - Part 1. Laboratory investigations., C.R.R.E.L. Report 91-23.

- Williams, M.J.M., Warner, R.C. and Budd, W.F. 1998. The effect of ocean warming on melting and ocean circulation under the Amery Ice Shelf, East Antarctica. *Ann. Glaciol.* 27: 75-80.
- Wilson, A.T., Holdsworth, R. and Hendy, C.H. 1974. Lake Vanda: source of heating. *Antarctic Journal of the U.S.* 9: 137-138.
- Worner, G., Viereck, L., Hertogen, J. and Niephaus, H. 1989. The Mount Melbourne volcanic field (Victoria Land, Antarctica) II. Geochemistry and magma genesis. *Geol. Jb. E* 38: 395-433.
- Wüest, A. and Carmack, E. submitted. A priori estimates of mixing and circulation in the hard-to-reach water body of lake Vostok. *Ocean modelling*.
- Zotikov, I.A., Zagorodnov, V.S. and Raikovsky, J.V. 1980. Core drilling through the Ross Ice Shelf (Antarctica) confirmed basal freezing. *Science*. 207(4438): 1463-1465.
- Zotikov, I.A. 1986. *The thermophysics of glaciers*. Reidel, Dordrecht, 275 p.

Research Project A4/DD/E03

Dynamics of the Antarctic Ice Cap and Climate Changes (a Contribution to EPICA)

FRANK PATTYN¹, HUGO DECLEIR²

Department of Geography
Vrije Universiteit Brussel
Pleinlaan 2, B-1050 Brussel

¹e-mail: fpattyn@vub.ac.be

²e-mail: hdecleir@vub.ac.be

Contents

ABSTRACT	1
1 INTRODUCTION	2
2 MATERIALS AND METHODS	4
2.1 Development of the ICE2D model	4
2.1.1 Field equations	4
2.1.2 Boundary conditions	8
2.1.3 Additional model elements	9
2.1.4 Numerical solution	11
2.2 Ice dynamics inferred from radar interferometry	13
3 RESULTS	18
3.1 The variability of Antarctic ice-sheet response to the climatic signal . . .	18
3.1.1 Experimental setup	19
3.1.2 The Shirase flowline experiments	20
3.1.3 The Asuka flowline experiments	23
3.1.4 Analysis of time series	23
3.2 High-resolution modelling: focus on the grounding zone	27
3.2.1 The ICE2D- versus the SIA-model	28
3.2.2 Enhanced sliding experiment	31
3.3 Preliminary results of model experiments along a flowline in western Dronning Maud Land	33
3.4 Shirase Glacier dynamics inferred from ERS-SAR interferometry	35
3.4.1 Surface velocity and strain rates	36
3.4.2 Large-scale force budget of Shirase Glacier	37
3.4.3 Large-scale mass budget of Shirase Glacier	44

4 DISCUSSION	46
4.1 The variability of Antarctic ice-sheet response to the climatic signal . . .	46
4.2 High-resolution modelling: focus on the grounding zone	47
4.3 Shirase Glacier dynamics inferred from ERS-SAR interferometry	49
5 CONCLUSIONS	51
Acknowledgments	52
REFERENCES	53
A Coordinate transformation	58
B Finite-difference approximation	60

ABSTRACT

This study addresses the dynamics of the Antarctic ice sheet in Dronning Maud Land where it is drained by outlet glaciers, those flowing through coastal mountain ranges, and those fast-flowing streams draining into the ocean. It further investigates the local variation in ice sheet behaviour as a response to the climatic signal over a period of the last 200 000 years and analyzes the influence of coastal ice dynamics on the interpretation of deep ice cores in the vicinity of the future EPICA DML drilling site. These tasks were accomplished by both satellite remote sensing and numerical modelling.

An interferometric analysis on ERS Synthetic Aperture Radar images revealed the detailed surface velocity field of Shirase Glacier, a major outlet glacier draining a substantial part of the ice sheet in Dronning Maud Land. The refinement of this technique made it possible to analyze the ice flow field, to better understand the glacier dynamics, and to determine its mass budget. It was found from a large-scale force budget that more than 80% of the total velocity is due to basal sliding. Furthermore, in order to balance the mass flux between the grounding line and the calving front, a high sub-ice tongue melt rate of 11.5 m a^{-1} should be accounted for.

Within the framework of EPICA we developed a high-resolution two-dimensional flow-line model, that is capable of simulating the thermo-mechanical ice flow as well as ice-stream and ice-shelf mechanics. The model is numerically solved on an irregular-spaced grid, making it more efficient for high-resolution modelling.

Numerical model experiments were carried out along several flowlines in Dronning Maud Land, one flowline passing through the central part of a coastal mountain range (Sør Rondane), one along a major continental ice stream (Shirase Glacier), and one in the area of a future deep drilling site within the EPICA project. The numerical model experiments were capable of simulating different response patterns of the East Antarctic ice sheet to the climatic signal as observed in the field, i.e., the important thinning rate in Shirase drainage basin contrasting the small glacier variations that – according to glacial-geological evidence – occurred over the last 200 000 years in the nearby Sør Rondane Mountains. Preliminary experiments along the flowline in western Dronning Maud land gave an idea of the basic ice-dynamic features of the drainage area in the vicinity of the future EPICA drilling site and the ice dynamics in the Jutulstraumen area.

KEYWORDS

Ice-sheet modelling, Fast-flowing glaciers, Interferometry, ERS, EPICA

1 INTRODUCTION

EPICA¹ is a long-term (7 years) European project in Antarctica to derive high resolution records of climate and atmospheric composition through several glacial-interglacial cycles. During the second phase of the project a core will be obtained from Dronning Maud Land (DML), in that part of Antarctica which faces the Atlantic Ocean and where more detailed information might be obtained about rapid climate oscillations that have been detected across Greenland throughout the last glaciation. The Dronning Maud Land area is also one of the least explored sectors of Antarctica. Therefore, several reconnaissance surveys were carried out during the first phase² of the EPICA project providing the necessary data for both drillers and modelers.

During the former (third) phase of the Belgian Program on Antarctic Research the Department of Geography of the Vrije Universiteit Brussel (VUB) has developed a flowline model capable of simulating the ice cap behaviour on a regional scale. Ideally, such flow line model has the potential to link the detailed information obtained from ice core drilling with the sedimentation and erosion records near the ice margin (ice free areas, marine glacial deposits), although the latter records are notoriously meager in Antarctica. By doing so the dynamics of the ice cap in response to the climatic signal can be reconstructed and understood. This is necessary, as at present we lack knowledge to explain the seemingly rapid variations of the climate on the one hand and the presumed stable behavior of the ice cap on the other hand. The solution might be found in trying to understand the very different behavior of ice streams, which are rapid flowing ice masses within the relative stagnant ice cap and where the basal mechanisms might resemble more ice shelf conditions than those pertaining to grounded ice.

Where some studies of the physical mechanisms in the boundary regions of the ice cap, such as the relation with mass balance and the shift of ice divides, are preferably treated by means of 3-D modeling, others such as those questions related to grounding line shift and basal sliding can best be tackled by flowline modeling on a very refined scale. Moreover, the two-dimensional flow line model is the only feasible method presently available to simulate outlet glaciers and ice stream evolution in the marginal area of Antarctica. Furthermore, it has the potential to produce a maximum resolution and precision in interpreting deep ice core and borehole data, and provides particle paths, stresses, strain rates, temperature profiles and several other derived parameters. For the purpose of this study, the aforementioned flowline model was im-

¹European Project on Ice Coring in Antarctica

²The first phase of the EPICA project coincided with phase 4 of the Belgian Research Programme on the Antarctic, which is reported here



Figure 1: *Monitoring ice movement by measuring bamboo stakes with differential GPS on Heito Glacier, Antarctica, during the 41st Japanese Antarctic Research Expedition.*

proved in order to reconstruct the glacial history of the ice sheet in Dronning Maud Land in relation to climatic parameters, and to investigate the influence of coastal ice dynamics on the central parts of the ice sheet.

While new data necessary for the glacier dynamics in Dronning Maud Land are and will be obtained by collaboration with different countries involved in EPICA and Dome Fuji, the dynamics of outlet glaciers might be inferred from SAR interferometry. In collaboration with the Centre Spatial de Liège, where an interferometric SAR processor was developed, detailed data on the ice flow field of a major outlet glacier in Dronning Maud Land was obtained, and the role of this glacier in the stability of the Antarctic ice sheet was investigated. In addition we participated in field work during the 41st Japanese Antarctic Research Expedition (1999-2000), assembling data on coastal glacier dynamics (Figure 1). The bulk of these research results is expected to become available in the near future.

2 MATERIALS AND METHODS

2.1 Development of the ICE2D model

The numerical ice sheet model that we developed is a dynamic flowline model that predicts the ice thickness distribution along a fixed flowline in space in response to environmental conditions. This response is obtained by calculating at a given moment the two-dimensional flow regime (velocity, strain-rate and stress fields) and the temperature distribution, determined by the ice sheet geometry and boundary conditions. The main boundary conditions to the ice flow field are the mass balance distribution at the surface, basal motion at the bottom and an edge boundary description (ice shelf, ice tongue or ice free surface). The temperature field is conditioned by the surface temperature at the top and the geothermal heat flux at the bottom. Additional sub-models entering as boundary conditions to the main system are considered as well, such as isostatic adjustment of the underlying bedrock, basal motion (sliding, till deformation, ...) and heat conduction in the bedrock.

Compared to the model we developed previously, major improvements include (i) a new efficient and stable numerical solution to the two-dimensional velocity field, (ii) inclusion of horizontal diffusion in the thermodynamic equation, (iii) a straightforward model for lithospheric deflection, and (iv) the use of an irregular grid in both the horizontal and the vertical direction, which allows to perform experiments at very high resolution in key areas of the ice sheet.

2.1.1 Field equations

Consider a Cartesian coordinate system (x, z) with the x -axis along the flow line, parallel to the geoid and the z -axis vertically pointing upward ($z = 0$ at sea level). The only non-zero velocity components are thus u , w (horizontal and vertical velocity, respectively), while the horizontal transverse velocity $v = 0$. Since the flow-line geometry considers transverse velocity gradients, it follows that $\frac{\partial v}{\partial y} = \frac{u}{\omega} \frac{\partial \omega}{\partial x}$, where ω is the width of the drainage basin taken perpendicular to the flow line. The equations for conservation of mass and linear momentum then become

$$\frac{\partial u}{\partial x} + \frac{u}{\omega} \frac{\partial \omega}{\partial x} + \frac{\partial w}{\partial z} = 0. \quad (1)$$

$$e \frac{\partial \tau_{xx}}{\partial x} + \frac{\partial \tau_{xz}}{\partial z} = 0, \quad (2)$$

Table I: *Constants used in the numerical model.*

Symbol	Constant	Value	Units
β	Dependence of melting on pressure	$9.8 \cdot 10^{-8}$	K Pa^{-1}
ρ	Ice density	910	kg m^{-3}
B_0	Flow-rate factor	2.207	$\text{Pa a}^{1/n}$
C	Flow-rate factor	0.16612	K^K
G	Geothermal heat flux	$4.2 \cdot 10^{-2}$	W m^{-2}
K	Flow-rate exponent	1.17	
L	Specific latent heat of fusion	$3.35 \cdot 10^5$	$\text{J m}^{-1} \text{K}^{-1} \text{a}^{-1}$
Q	Activation energy for creep	$7.88 \cdot 10^4$	J mol^{-1}
R	Universal gas constant	8.31	$\text{J mol}^{-1} \text{K}^{-1}$
T_r	Limit temperature in flow-rate factor	273.39	K
c_p	Thermal conductivity	2009	$\text{J kg}^{-1} \text{K}^{-1}$
g	Gravitational constant	9.81	m s^{-2}
k_i	Thermal conductivity	$6.62 \cdot 10^{-7}$	$\text{K}^{-1} \text{a}^{-1}$
m	Enhancement factor in flow law	1	
n	Exponent in Glen's flow law	3	

$$e^2 \frac{\partial \tau_{xz}}{\partial x} + \frac{\partial \tau_{zz}}{\partial z} = \rho g, \quad (3)$$

where ρ is the ice density, g is the gravitational constant, and τ_{ij} are the stress components. The values for these and all other constants used in this paper, are given in Table I. e is the aspect ratio ($e = \{H\}/\{L\}$, where $\{L\}$ and $\{H\}$ are the characteristic horizontal and vertical extent of the ice mass, respectively). According to the scale analysis by Dahl-Jensen (1989), Eqs. 2 and 3 describe the second-order approximation. Deleting terms in e^2 but retaining terms in e fulfills the first-order approximation. For $e \ll 1$, such as large ice sheets characterized by small surface and bedrock slopes, the *zeroth-order* approximation applies, which is better known as the *shallow-ice approximation*.

Neglecting atmospheric pressure, an expression for τ_{zz} is obtained by integrating Eq. 3 from the surface s to a height z in the ice body

$$\tau_{zz} = -\rho g(s - z) + e^2 \underbrace{\frac{\partial}{\partial x} \int_z^s \tau_{xz} dz}_{R_{zz}}. \quad (4)$$

The second term of the right-hand side of Eq. 4 represents the vertical resistive stress R_{zz} , which is responsible for the so-called bridging effect (Van der Veen and Whillans, 1989). Deviatoric stresses are related to the stress components by $\sigma_{ii} = \tau_{ii} - \frac{1}{3}(\tau_{xx} + \tau_{yy} + \tau_{zz})$ for $i = x, y, z$, and $\sigma_{xz} = \tau_{xz}$. Making use of Eq. 4 and inserting the deviatoric stresses, Eq. 2 becomes

$$e \frac{\partial}{\partial x} (2\sigma_{xx} + \sigma_{yy}) + e^2 \frac{\partial^2}{\partial x^2} \int_z^s \tau_{xz} dz + \frac{\partial \tau_{xz}}{\partial z} = \rho g \frac{\partial s}{\partial x}. \quad (5)$$

The constitutive equation governing the creep of polycrystalline ice and relating the deviatoric stresses to the strain rates, is taken as a Glen-type flow law with exponent $n = 3$ (Paterson, 1994).

$$\sigma_{ij} = 2\mu \dot{\epsilon}_{ij}, \quad \mu = \frac{1}{2} A(T^*)^{-1/n} (\dot{\epsilon} + \dot{\epsilon}_0)^{(1-n)/n}, \quad (6)$$

where $\dot{\epsilon}$ is the second invariant of the strain-rate tensor, defined by $\dot{\epsilon}^2 = \sum_{ij} \frac{1}{2} \dot{\epsilon}_{ij} \dot{\epsilon}_{ij}$ and μ is the effective viscosity. $\dot{\epsilon}_0$ is a small number (10^{-30}) to validate Glen's flow law in cases where $\dot{\epsilon}$ equals zero, and singularity might occur. The use of such a small number does not have an effect on the numerical outcome of the model. The flow-law rate factor $A(T^*)$ is a function of temperature, where T^* is the ice temperature (K) corrected for pressure melting, i.e., $T^* = T + \beta P$, where P is the ice pressure ($P = e\sigma_{xx} + e\sigma_{yy} + e^2 R_{zz} - \rho g(s - z)$). Following Hooke (1981), $A(T^*)$ is set to

$$A(T^*) = m \left(\frac{1}{B_0} \right)^n \exp \left(\frac{-Q}{RT^*} + \frac{3C}{(T_r - T^*)^K} \right). \quad (7)$$

Here Q is the activation energy for ice creep, R is the universal gas constant, and m is an enhancement factor (or tuning parameter). By definition, strain rates are related to velocity gradients by $\dot{\epsilon}_{ij} = \frac{1}{2} \left(\frac{\partial u_i}{\partial x_j} + \frac{\partial u_j}{\partial x_i} \right)$. Applied to the flow-line geometry and making use of the conservation of mass (Eq. 1), one obtains

$$\dot{\epsilon}_{xx} = e \frac{\partial u}{\partial x} \quad (8)$$

$$\dot{\epsilon}_{yy} = e \frac{u}{\omega} \frac{\partial \omega}{\partial x} \quad (9)$$

$$\dot{\epsilon}_{xz} = \frac{1}{2} \left(\frac{\partial u}{\partial z} + e^2 \frac{\partial w}{\partial x} \right) \quad (10)$$

$$\dot{\epsilon}^2 = \dot{\epsilon}_{xx}^2 + \dot{\epsilon}_{yy}^2 + \dot{\epsilon}_{xz} \dot{\epsilon}_{yy} + \dot{\epsilon}_{xz}^2. \quad (11)$$

Combining the flow-law equation (Eq. 6) and the horizontal stress-field equation (Eq. 5), and replacing the strain-rate components by velocity gradients using Eqs. 8 to 11, one obtains

$$4e \frac{\partial}{\partial x} \left(\mu \frac{\partial u}{\partial x} \right) + 2e \frac{\partial}{\partial x} \left(\frac{\mu u}{\omega} \frac{\partial \omega}{\partial x} \right) + \frac{\partial}{\partial z} \left(\mu \frac{\partial u}{\partial z} + e^2 \mu \frac{\partial w}{\partial x} \right) = \rho g \frac{\partial s}{\partial x} - e^2 \frac{\partial^2}{\partial x^2} \int_z^s \tau_{xz} dz \quad (12)$$

where

$$\mu = \frac{1}{2} A (T^*)^{-1/n} \left\{ \left(e \frac{\partial u}{\partial x} \right)^2 + \left(e \frac{u}{\omega} \frac{\partial \omega}{\partial x} \right)^2 + e \frac{u}{\omega} \frac{\partial u}{\partial x} \frac{\partial \omega}{\partial x} + \frac{1}{4} \left(\frac{\partial u}{\partial z} + e^2 \frac{\partial w}{\partial x} \right)^2 \right\}^{(1-n)/2n}. \quad (13)$$

Expanding Eq. 12 and rearranging terms, leads to

$$\begin{aligned} & e \frac{u}{\omega} \left\{ 2 \frac{\partial \mu}{\partial x} \frac{\partial \omega}{\partial x} + 2 \mu \left(\frac{\partial^2 \omega}{\partial x^2} - \frac{1}{\omega} \left(\frac{\partial \omega}{\partial x} \right)^2 \right) \right\} + e \frac{\partial u}{\partial x} \left(4 \frac{\partial \mu}{\partial x} + \frac{2 \mu}{\omega} \frac{\partial \omega}{\partial x} \right) \\ & + \frac{\partial u}{\partial z} \frac{\partial \mu}{\partial z} + 4 e \mu \frac{\partial^2 u}{\partial x^2} + \mu \frac{\partial^2 u}{\partial z^2} = \rho g \frac{\partial s}{\partial x} - e^2 \frac{\partial^2}{\partial x^2} \int_z^s \tau_{xz} dz - e^2 \frac{\partial \mu}{\partial z} \frac{\partial w}{\partial x} - e^2 \mu \frac{\partial^2 w}{\partial z \partial x} \end{aligned} \quad (14)$$

An expression for the vertical velocity w is obtained through vertical integration of the incompressibility condition (Eq. 1) from the base of the glacier to a height z

$$w(z) - w(b) = - \int_b^z \nabla \vec{v}(z) dz = - \int_b^z \left(\frac{\partial u}{\partial x} + \frac{u}{\omega} \frac{\partial \omega}{\partial x} \right) dz. \quad (15)$$

The thermodynamic equation for the ice flow along a flow line is written as

$$\rho c_p \frac{\partial T}{\partial t} = k_i \left(\frac{\partial^2 T}{\partial x^2} + \frac{1}{\omega} \frac{\partial \omega}{\partial x} \frac{\partial T}{\partial x} + \frac{\partial^2 T}{\partial z^2} \right) - \rho c_p \left(u \frac{\partial T}{\partial x} + w \frac{\partial T}{\partial z} \right) + 2 \dot{\epsilon} \tau, \quad (16)$$

where k_i and c_p are the thermal conductivity and the specific heat capacity, respectively, and τ is the effective stress or the second invariant of the stress tensor. The heat transfer is thus a result of horizontal and vertical diffusion, horizontal and vertical advection, and internal friction due to deformational heating.

Starting from the known bedrock topography and surface mass balance distribution, and assuming a constant ice density, the change of ice thickness along the flow line is then predicted as

$$\frac{\partial H}{\partial t} = -\frac{1}{\omega} \frac{\partial(\bar{u}H\omega)}{\partial x} + M_s - M_b, \quad (17)$$

where \bar{u} is the depth averaged horizontal velocity (m a⁻¹), H the ice thickness (m), M_s the surface mass balance (m a⁻¹ ice equivalent), and M_b the melting rate at the base of the glacier (m a⁻¹).

2.1.2 Boundary conditions

Boundary conditions to the ice mass are a symmetric ice divide ($\frac{\partial s}{\partial x} = \frac{\partial H}{\partial x} = 0$), zero ice thickness at the downstream edge of the glacier, a stress-free surface and a basal sliding function at the bottom of the glacier, which is a function of the basal drag $u_b = \mathcal{F}(\tau_b)$. Whenever the ice sheet ends in the ocean, the outer boundary condition becomes an ice shelf, implying $\tau_b = 0$ and $\sigma'_{yy} = 0$. Simplified, this means that $\frac{\partial \bar{u}}{\partial x} = m \overline{A(T^*)} \overline{\sigma'_{xx}}^n$, where $\overline{\sigma'_{xx}}$ at the downstream edge of the ice tongue is determined from hydrostatic equilibrium (Thomas, 1973). The kinematic boundary condition at the lower ice surface reads

$$w(b) = \frac{\partial b}{\partial t} + \vec{v}_b \nabla b + M_b \quad (18)$$

The basal drag is defined as the sum of all basal resistive forces and written as (Van der Veen and Whillans, 1989)

$$\tau_b = \tau_{xz}(b) - (2e\sigma_{xx}(b) + e\sigma_{yy}(b) + e^2 R_{zz}(b)) \frac{\partial b}{\partial x} \quad (19)$$

The stress-free surface implies that $(2e\sigma_{xx}(s) + e\sigma_{yy}(s) + e^2 R_{zz}(s)) \frac{\partial s}{\partial x} - \tau_{xz}(s) = 0$ and where $e^2 R_{zz}(s) = \tau_{xz}(s) \frac{\partial s}{\partial x}$. Written in terms of velocity gradients this results in

$$e \frac{\partial s}{\partial x} \left(4 \frac{\partial u}{\partial x} + \frac{2u}{\omega} \frac{\partial \omega}{\partial x} \right) + \left(\frac{\partial u}{\partial z} + e^2 \frac{\partial w}{\partial x} \right) \left(e^2 \left(\frac{\partial s}{\partial x} \right)^2 - 1 \right) = 0. \quad (20)$$

Boundary conditions to the thermodynamic equation (Eq. 16) follow from the mean annual air temperature at the surface. At the base, the temperature gradient is defined as

$$\frac{\partial T_b}{\partial z} = -\frac{G + \tau_b u_b}{k_i}, \quad (21)$$

where G is the geothermal heat flux. The basal temperature in the ice mass is kept at the pressure melting point whenever it is reached, and the basal melt rate M_b is calculated as

$$M_b = \frac{1}{\rho L} \left(k_i \frac{\partial T_b}{\partial z} + G + u_b \tau_b \right), \quad (22)$$

where L is the specific latent heat of fusion. For the calculation of the heat transfer in the underlying bed, only vertical diffusion is considered in a rock slab of 2000 m thickness. The temperature change in time is written as

$$\frac{\partial T_r}{\partial t} = \frac{k_r}{\rho_r c_r} \frac{\partial^2 T_r}{\partial z^2},$$

where T_r is the rock temperature (K), ρ_r the rock density (3300 kg m^{-3}), and c_r the specific heat capacity ($1000 \text{ J kg}^{-1} \text{ K}^{-1}$). The lower boundary is defined as the geothermal heat flux entering through the base of the considered rock slab.

2.1.3 Additional model elements

In the case of two-dimensional deflections of the lithosphere under a point load with dependence only on x , the deflection equation can be written as (Nunn and Aires, 1988)

$$\frac{\partial^2}{\partial x^2} \left(D_\ell \frac{\partial^2 w_\ell}{\partial x^2} \right) + \rho_r g w_\ell = P, \quad (23)$$

where w_ℓ is the vertical displacement of the bedrock (positively downwards), $D_\ell = 10^{25} \text{ N m}$ is the effective flexural rigidity (taken constant for this type of experiments), $\rho_r g w_\ell$ is the upward buoyancy force exerted on the deflected part of the lithosphere inside the asthenosphere, and P the local load, i.e., $P = \rho_r g H$ for an ice column resting on the bed, and $P = -\rho_s g b$ for a water column (of density $\rho_s = 1028 \text{ kg m}^{-3}$) on top of the bedrock b . The time-dependent response of bedrock to a changing ice load is modeled by a simple relaxation model (Le Muer and Huybrechts, 1996)

$$\frac{\partial b}{\partial t} = -\frac{1}{\Theta} (w_\ell - b), \quad (24)$$

where Θ is the characteristic time scale taken as 3000 a.

Basal motion of the grounded ice sheet can originate from sliding of the ice over its bed and deformation of the bed itself, the latter if the bed consists of sediments saturated with water at a pressure that closely matches the ice overburden pressure. Sliding is thus only expected where the basal ice is at melting point (Paterson, 1994). A general sliding law has the form of (e.g., Budd and Jenssen, 1987)

$$u_b = A_b \tau_b^p N^{-q}, \quad (25)$$

where p and q are positive numbers ranging between 0 and 3, A_b a sliding law parameter, T_0 the absolute temperature (273.15 K). N is the effective normal pressure at the base. For glaciers that terminate in the sea, subglacial water pressure at the grounding line may be calculated from the flotation criterion, so that the effective normal pressure N is proportional to the height of the glacier surface above buoyancy.

$$N = p_i - p_w \equiv \rho g H + \rho_s g b, \quad (26)$$

where p_i and p_w are the ice and water pressure, respectively. In some flow models of the Antarctic ice sheet (Huybrechts, 1992), the effective normal pressure is calculated in the same fashion over the whole model domain and not only at the grounding line. However, the physical restriction is that the bedrock should lie beneath sea level and that the water pressure originates from sea water infiltrating at the grounding line and moving in the upstream direction. A more straightforward treatment of the basal water flow is to consider a water film underneath the ice sheet. According to Weertman and Birchfield (1982), the sliding velocity is dependent on the depth of the water layer δ and the critical particle size δ_c

$$\begin{aligned} u_b &= A_b \tau_b^p \left(1 + 10 \frac{\delta}{\delta_c} \right) & \text{if } \delta < \delta_c \\ &= 10 A_b \tau_b^p \frac{\delta}{\delta_c} & \text{if } \delta \geq \delta_c \end{aligned} \quad (27)$$

and

$$\delta = \left(\frac{12 \mu Q_w}{P_g} \right)^{\frac{1}{3}},$$

where Q_w is the water flux per unit width ($\text{m}^2 \text{s}^{-1}$), calculated through downstream integration of the basal melting rate, μ the viscosity of water ($1.8 \cdot 10^{-3} \text{ Pa s}$), and P_g the pressure gradient (Alley, 1989).

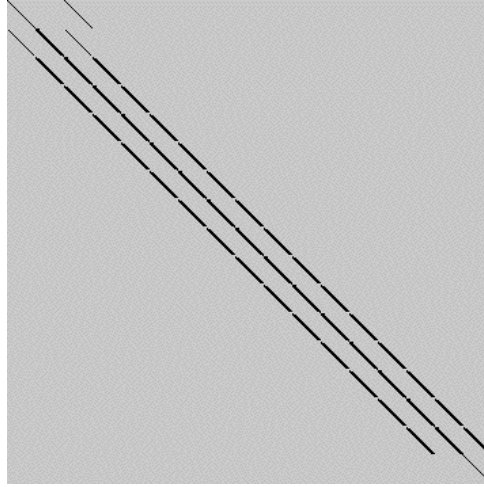


Figure 2: Structure of the coefficient matrix \mathbf{A} for a numerical grid of 17 by 21 nodes, i.e., 357 by 357 elements. Nonzero elements are shown in black.

2.1.4 Numerical solution

For numerical convenience a dimensionless vertical coordinate is introduced to account for ice-thickness variations along the flow line, and which is defined as $\zeta \equiv (s - z)/H$, so that $\zeta = 0$ at the upper surface and $\zeta = 1$ at the base of the ice mass. The coordinate transformation maps $(x, z) \rightarrow (\xi, \zeta)$, where $\xi \equiv x$ is the transformed horizontal coordinate. Details on the transformation of the global velocity term (Eq. 14), the viscosity term (Eq. 13) and the surface boundary condition (Eq. 20) are given in Appendix A. After this transformation, all equations are solved on an irregular spaced grid in ξ and ζ . Central differences are used to compute first- and second-order gradients. At the boundaries, upstream and downstream differences are employed (see Appendix B for more details on the procedure).

The finite difference form of the transformed differential equations for u (Eqs. 65 and 66) is written as a set of linear equations with $u(\xi, \zeta)$ as unknowns. In matrix notation this becomes

$$\mathbf{A}(\mathbf{u}^\ell) \cdot \mathbf{u}^{\ell+1} = \mathbf{b}(\mathbf{u}^\ell), \quad (28)$$

where ℓ is the iteration number. Starting from a zeroth-order estimate of the horizontal velocity field \mathbf{u}^0 , a new estimation \mathbf{u}^1 of the velocity is obtained by solving the set of linear equations. For a numerical grid of $N_\xi = 17$, $N_\zeta = 21$, the matrix \mathbf{A} consists of $(17 \times 21)^2 = 127\,449$ nodes. However, only 2 642 nodes contain nonzero elements, which is 2% of \mathbf{A} (Fig. 2).

A solution to the linear system of Eq. 28 is accomplished using the sparse matrix algorithms of Press et al. (1992), which are based on the conjugate gradient method. Although the coding of sparse matrices is rather complicated, they are far more efficient in terms of computation time compared to point-relaxation algorithms on the full or even parts of the matrix. Because of the non-linear nature of Eq. 65, \mathbf{A} and \mathbf{b} contain three parameters that are still a function of u , i.e., the viscosity term μ , the vertical velocity w , and the vertical resistive stress R_{zz} , which have to be determined in an iterative fashion (the iterative determination of both w and R_{zz} applies only to the *second-order* approximation in e^2). The successive substitution method or Picard iteration was used for this purpose. In order to optimize the rate of convergence a relaxation formula was added based on the unstable manifold correction (Hindmarsh and Payne, 1996). Therefore, Eq. 28 is written as

$$\begin{aligned}\mathbf{A}(\mathbf{u}^\ell) \cdot \mathbf{u}^* &= \mathbf{b}(\mathbf{u}^\ell) \\ \mathbf{u}^{\ell+1} &= \alpha \mathbf{u}^* + (1 - \alpha) \mathbf{u}^\ell\end{aligned}\quad (29)$$

Consider this iterative solution of a non-linear equation which generates a series of approximate solutions $\mathbf{u}^{\ell+1}, \mathbf{u}^\ell, \dots$, being updated by a series of correction vectors $\mathbf{c}^{\ell+1}, \mathbf{c}^\ell, \dots$ such that $\mathbf{u}^{\ell+1} = \mathbf{u}^\ell + \mathbf{c}^\ell$. If $\mathbf{e}^{\ell+1}, \mathbf{e}^\ell, \dots$ is taken as the error in the solution vector $\mathbf{u}^{\ell+1}, \mathbf{u}^\ell, \dots$, then we can state that $(\mathbf{e}^{\ell+1}, \mathbf{e}^\ell, \dots) = \alpha(\mathbf{c}^{\ell+1}, \mathbf{c}^\ell, \dots)$. Assuming that the decay is on a straight line in the correction space we obtain that (Hindmarsh and Payne, 1996)

$$\alpha = \frac{\|\mathbf{c}^{\ell-1}\|}{\|\mathbf{c}^\ell - \mathbf{c}^{\ell-1}\|}$$

where $\mathbf{c}^\ell = \mathbf{u}^* - \mathbf{u}^\ell$, and the modified correction vector becomes $\mathbf{c}_*^\ell \approx \alpha \mathbf{c}^\ell$. The direction θ between successive correction vectors is computed as

$$\theta = \arccos\left(\frac{\mathbf{c}^\ell \cdot \mathbf{c}^{\ell-1}}{\|\mathbf{c}^\ell\| \cdot \|\mathbf{c}^{\ell-1}\|}\right)$$

where the norms refer to the L_2 norm. Whenever this angle is near enough 0 or π , the subspace iteration might become applicable. Using this subspace relaxation algorithm the solution vector properly converges, which is not the case with the Picard iteration method.

The continuity equation (Eq. 17) is reformulated as a diffusion equation for ice thickness H , i.e.,

$$\frac{\partial H}{\partial t} - \frac{\partial}{\partial x} \left(D \frac{\partial H}{\partial x} \right) - \frac{D}{\omega} \frac{\partial \omega}{\partial x} \frac{\partial H}{\partial x} = \frac{\partial}{\partial x} \left(D \frac{\partial b}{\partial x} \right) - \frac{D}{\omega} \frac{\partial \omega}{\partial x} \frac{\partial b}{\partial x} + M_s - M_b, \quad (30)$$

where $D = \frac{\bar{u}H}{\nabla_s}$. Equation 30 results in a tridiagonal system of N_ξ equations, and is solved using the tridiagonal algorithm of Press *et al.* (1992).

The thermodynamic equation (Eq. 67) is solved implicitly in the vertical, giving rise to a tridiagonal system of N_ζ equations and which is solved using the tridiagonal algorithm of Press *et al.* (1992). A two-point upstream difference notation was employed for the horizontal, while central differences were used in the vertical. The horizontal implicit terms are found by iteration of this scheme. Only a few iterations are necessary to obtain a good convergence.

2.2 Ice dynamics inferred from radar interferometry

This research tries to give an insight in the present dynamics of Shirase Glacier, a fast-flowing outlet glacier in Dronning Maud Land (Fig. 3), based on a satellite-derived surface velocity field of the area near the grounding line. During the Tandem phase of the ERS-1 and ERS-2 satellites³, where both satellites were placed in the same orbit to ensure a one day repeat coverage, several Synthetic Aperture Radar (SAR) images covering Shirase Glacier were obtained, from which the surface displacements could be determined using an interferometric technique, called *coherence tracking*.⁴

Interferometric techniques applied to SAR imagery have the potential for surface displacement determination with a centimeter precision. Co-registration of two SAR images of the same region allows one to generate an interferogram, or a plot of phase shifts as a function of position. The phase in the resulting SAR interferogram can be divided into two terms. The first term, the interferometric phase, contains relative optical path variations between the two SAR acquisitions. The second term, the coherence term, contains phase differences due to changes in the response of illuminated scatterers. Optical path variations have different origins: (i) an *orbital phase* depending on the viewing geometry of the SAR image pair, (ii) a *topographic phase* due to the relief of the imaged area, and (iii) a *differential phase* caused by local displacements of the ground surface in consecutively scanned images. The differential phase is a measure of displacement of a ground surface point in the look direction of the spacecraft, within

³ERS = European Remote Sensing Satellite.

⁴The development of the interferometric processor as well as the interferometric processing was carried out by Dr. D. Derauw from the Centre Spatial de Liège, Université de Liège, Belgium.

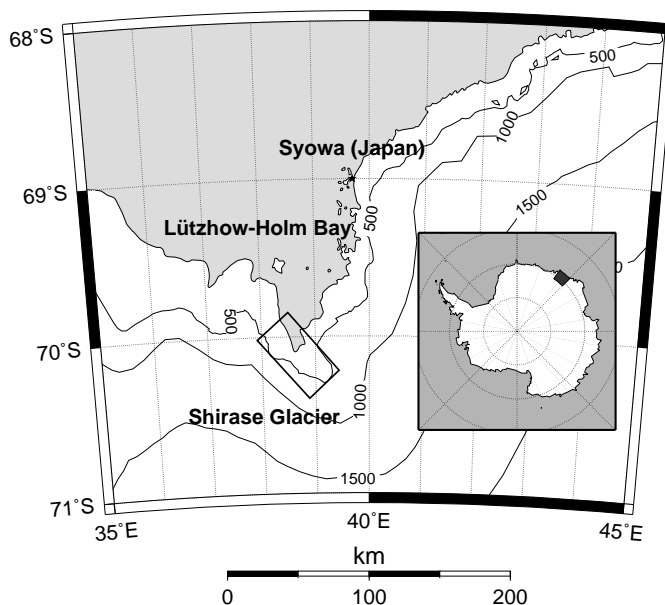


Figure 3: Map of Lützow-Holm Bay, Dronning Maud Land, East Antarctica. The small rectangle corresponds to the Shirase Glacier study area as depicted in Fig. 4A.

the time span between the acquisition of the two images, i.e., $\Delta\phi_d = \frac{4\pi}{\lambda}\Delta z$, where $\lambda = 5.6$ cm is the wavelength of the ERS radar and Δz is the look-direction component of the optical path variation. Half a wavelength of displacement in the look direction produces a phase shift of 360° . If the displacement has a component in the direction of the satellite's motion⁵, it has no influence on the differential phase. The sensitivity to topography depends on the ambiguity of altitude, which is related to the viewing geometry and is typically of the order of a hundred of meters for most interferometric applications using ERS sensors, while sensitivity to displacement (or to any other local optical path variation) depends on the wavelength of the radar.

Retrieving ERS-SAR images from Antarctica is hampered due to the satellite orbital configuration, i.e., only the area north of 78°S can be viewed. Moreover, within the same region only a fraction of the potential imagery is retrieved, i.e., in the vicinity of the operational receiving stations and depending on the logistics available at each station. For the purpose of this study only three suitable ERS-1/2 Tandem pairs were acquired at Syowa Station, Antarctica. Among these three pairs, the pair of June 2 and 3, 1996 has a favorable altitude ambiguity with respect to differential interferometry, making the phase nearly insensitive to topography. When an interferogram is generated from such an image pair, the observed fringes can be directly interpreted as differential fringes. This Tandem pair is therefore used in this analysis (Figure 4A).

⁵The orbit track defines the azimuth axis; the line of sight defines the range axis of SAR images.

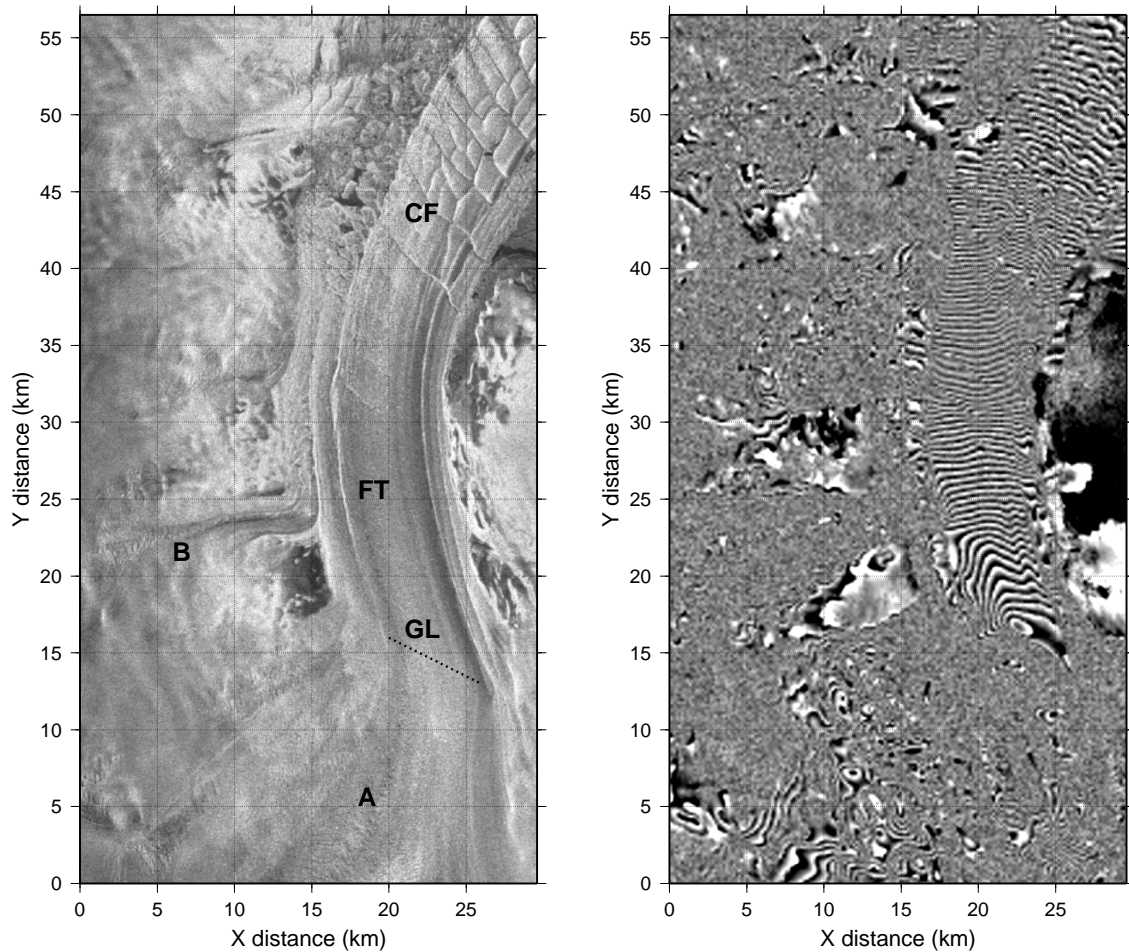


Figure 4: (A) Amplitude image of the ERS-1 scene of Shirase Glacier acquired on June 2, 1996. The main ice flow is from the bottom of the image towards the top. x -axis corresponds to the satellite look direction (slant-range), while the y -axis is along the direction of satellite's motion (azimuth). CF = calving front, FT = floating tongue, GL = grounding line, A = Shirase Glacier main stream, B = secondary stream; (B) Tracked interferogram obtained from the June Tandem pair.

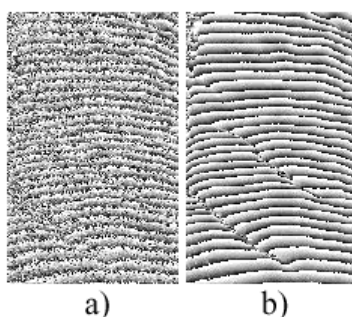


Figure 5: *Sample interferogram obtained on the floating ice tongue of Shirase Glacier. a) after co-registration of the whole scene; b) after local co-registration of several image samples (coherence tracking).*

However, since most glacier movement is mainly along the azimuth direction, proper differential interferometry is of poor use. Horizontal ice displacement was therefore obtained by means of the *coherence tracking* method (Derauw, 1999). This method uses the maximum interferometric coherence as a measure of matching small image kernels (windows) taken from two complex SAR images corresponding to the same part of the ice surface. The technique is comparable to speckle tracking (Gray *et al.*, 1998), but uses the phase information instead of the coherent speckle information in the amplitude images.

As a first step in the process, an interferogram was calculated based on a co-registration of non-moving parts of the scene. A high interferometric coherence was obtained for the slow-moving parts, but on the fast-flowing ice tongue, most of the coherence was apparently lost, hence inducing very noisy interferometric fringes. However, ice in movement should also conserve a good coherence as does ice that is not moving. We therefore made the hypothesis that low coherence levels on the fast-moving ice were due to wrong *local* co-registration. To verify this hypothesis, a small portion of the scenes, taken on the floating tongue of Shirase Glacier and characterized by a high noise level and hence a low interferometric coherence, was co-registered independently from the rest of the scene. A clear fringe pattern was obtained, confirming that coherence losses were only apparent and due to local co-registration errors (Figure 5). Co-registration errors do not induce phase bias but only an increase of phase variance (Just and Bamler, 1994).

Consequently, the co-registration procedure was modified with a complex matching tool. For a small image kernel (master) centered around a particular anchor point in one of the SAR images, a conjugate point was sought for in the other image (slave) by calculating the local interferometric coherence between the master image kernel and a

moving slave kernel of the same size. The maximum local coherence of all searches refers to the corresponding point, which was determined with sub-pixel accuracy. For each anchor point we obtain the relative azimuth and range displacement, the *tracked* coherence and the *tracked* interferometric phase. Based on the latter a so-called *tracked* interferogram is calculated, in which the noise induced by mis-registration is removed (Figure 4B). In order to measure more accurately the coherence and the localization of its local maximum, the SAR scenes were zoomed by a factor 2.5 using a phase-preserving interpolation tool. A mesh of anchor points covering the whole scene with a grid spacing of 3 pixels in azimuth and 15 pixels in range was defined so that displacement measurements were obtained every 24 meter in x and y . The optimal kernel sizes proved to be 25 pixels in azimuth and 5 pixels in range. The *tracked* coherence shows a much higher coherence over the surface of Shirase Glacier compared to the coherence obtained previously. The relative shifts in x - and y -direction – obtained with sub-pixel accuracy – are then easily translated to surface velocities.

The *tracked* interferogram (Figure 4B), corrected for the local registration errors, gives – after unwrapping – the displacement in the range direction with a very high accuracy, i.e., only dependent on the wavelength of the radar. The error in *unwrapped* velocity is given by

$$\sigma'_u = \frac{\lambda}{4\pi \sin \alpha} \frac{\sigma_\phi}{\gamma} \quad (31)$$

where $\alpha = 23^\circ$ is the incidence angle and λ is the wavelength of the radar. $\sigma_\phi = \frac{1}{\sqrt{2N}} \frac{\sqrt{1-\gamma^2}}{\gamma}$ is the error estimate in phase (Just and Bamler, 1994; Rodriguez and Martin, 1992), where γ is the coherence and N the interferometric multi-looking factor, i.e., the number of full-resolution samples used for the coherence estimation. For the present case, taking into account the kernel size and the zoom factor, $N = 50$. For an average coherence $\gamma = 0.7$, Equation 31 gives an error of $\sigma'_u \approx 1.16 \times 10^{-3} \text{ m day}^{-1} \approx 0.425 \text{ m a}^{-1}$. However, the velocities obtained by *coherence tracking* are somewhat less accurate. We can evaluate the accuracy of the *tracked* velocity in two ways: (i) by direct comparison with the *unwrapped* velocity, and (ii) by analyzing the error for the non-moving parts in the scene. A linear regression between the *unwrapped* velocity field and the velocities obtained from *coherence tracking* results in an error estimate on the *tracked* velocities of $\sigma_u \approx 69 \text{ m a}^{-1}$. Errors for the non-moving parts are determined as $\sigma_u \approx 74 \text{ m a}^{-1}$ and $\sigma_v \approx 57 \text{ m a}^{-1}$, which are of the same order of magnitude.

3 RESULTS

3.1 The variability of Antarctic ice-sheet response to the climatic signal

The East Antarctic ice sheet appears as a stable and dominant feature on earth at least for the last few million years. Three-dimensional model experiments (Huybrechts, 1993) demonstrated that a large temperature rise is necessary (more than 15 K) to reduce the ice sheet significantly. The reason why the East Antarctic ice sheet is able to resist a much larger warming than its West Antarctic counterpart is partly due to the presence of several mountain systems, enabling the ice sheet to retreat at a higher, hence colder, elevation if a significant warming would occur (Huybrechts, 1993). The three major mountain systems are the Transantarctic Mountains, the Gamburtsev subglacial mountains in the central part of the East Antarctic craton and a semi-continuous belt of coastal mountains in Dronning Maud Land stretching from Heimefrontfjella in the west (15°W) to the Yamato Mountains in the east (35°E). These mountain systems are separated by large subglacial depressions, such as the Pensacola, Wilkes and Aurora subglacial basins between the Transantarctic and Gamburtsev Mountains, and Lambert Glacier between Gamburtsev subglacial mountains and Enderby Land. Within the Dronning Maud Land coastal mountain chain some transverse gaps are noticed, such as Jutulstraumen in the west and Shirase Glacier in the east, which together with Lambert Glacier form the most prominent outlet glaciers of East Antarctica.

The alternation of marginal mountain glacier systems and fast-flowing outlet glaciers imply a local differentiation in ice-sheet behaviour as a reaction to a changing climate, which is confirmed by observations. Stake measurements in Shirase Drainage Basin, Dronning Maud Land (Mae and Naruse, 1978; Nishio *et al.*, 1989) show at present an important thinning of the ice sheet at a rate of more than one meter per year. However, in the nearby Sør Rondane Mountains, Moriwaki *et al.* (1992) found that the maximum ice surface attained over the last 100,000 year was only a few meters higher than the present surface, whereby the authors concluded that only minor glacier fluctuations occurred over this period (in the order of a few meters to a few tens of meters). The first observation points to a dynamical ice sheet, while the second observation – made in a neighboring area 500 km to the west – corroborates the idea of a very stable ice sheet.

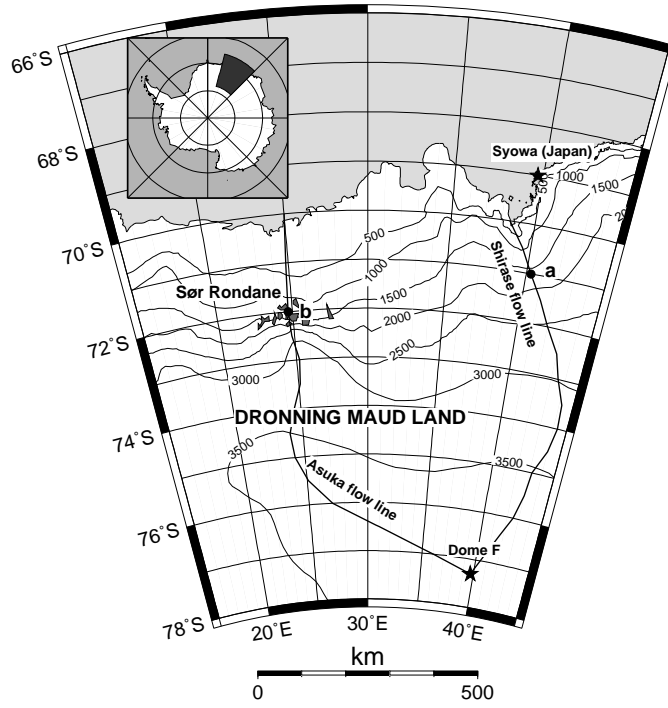


Figure 6: Situation map of Dronning Maud Land displaying the Shirase flow line from Dome Fuji to Shirase glacier and the Asuka flow line through the Sør Rondane Mountains.

3.1.1 Experimental setup

Numerical modelling experiments were carried out along two flowlines in Dronning Maud Land (Fig. 6), i.e., a flowline along a major outlet glacier (Shirase Drainage Basin: Shirase flowline, Fig. 7), and one flowline through the central part of a coastal mountain range (Sør Rondane Mountains: Asuka flowline, Fig. 8). Both start at the Dome Fuji ice divide and reach beyond the edge of the continental platform in the Southern Ocean. Each model experiment is a twofold process. First, a steady-state ice sheet at 200 000 BP is established starting from an ice-free bedrock topography isostatically adjusted to the removal of the present ice load, under climatic conditions taken as the mean of the last 200 ka, i.e., a background temperature of -5.2 K compared to present. Second, the model is run forward in time, forced by the Vostok signal (Jouzel *et al.*, 1993). Changes in surface temperature also affect accumulation rates, according to Lorius *et al.* (1985):

$$M_s(t) = M_s(0) \exp \left[22.47 \left(\frac{T_0}{T_f(0)} - \frac{T_0}{T_f(t)} \right) \right] \left[\frac{T_f(0)}{T_f(t)} \right]^2, \quad (32)$$

where M_s is the surface accumulation rate (m a^{-1}), $T_0 = 273.15 \text{ K}$, $T_f(t) = 0.67 T_s(t) + 88.9$ the temperature above the inversion layer and $T_s(t)$ the surface temperature. This

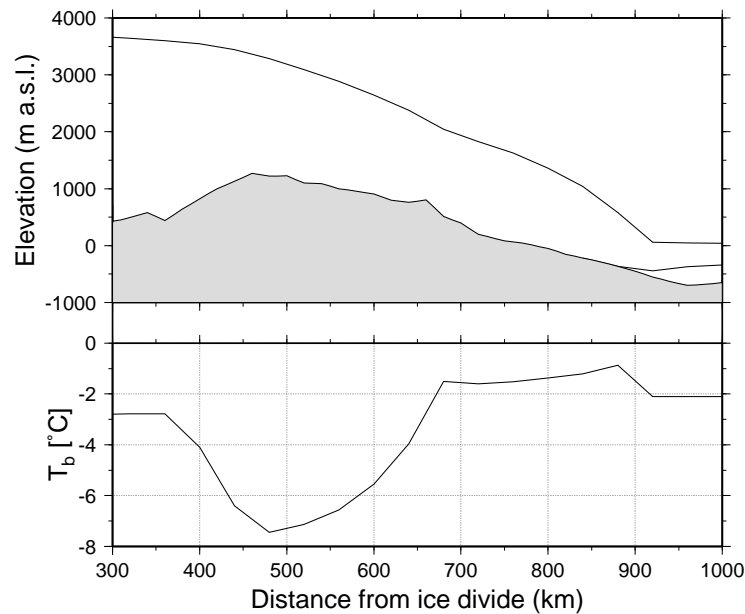


Figure 7: *Present modeled longitudinal profile of the Shirase flowline after 200 ka of forward integration. Lower panel displays the corresponding basal temperature profile.*

means that changes in surface accumulation rate exactly follow changes in background temperature. Thus, for each gridpoint along the flowline a local time series according to Eq. 32 and a local ice-sheet response time series according to Eq. 17 of vertical ice-surface changes over the last 200 000 years is obtained.

3.1.2 The Shirase flowline experiments

Previous modelling experiments of Shirase Glacier (Pattyn and Decler, 1995) showed that the large observed thinning rate could not be explained as a reaction to the climate signal alone. Another mechanism should account for this. A sensitivity analysis of the effect of basal motion on fast-flowing outlet glaciers (Pattyn, 1996) revealed different patterns of cyclic behaviour in glaciers depending on the basal boundary conditions. In this study similar experiments are repeated, this time applied to the Shirase flowline. Basal motion was treated by considering a water film underneath the ice sheet (Eq. 27, with $A_b = 2.0 \cdot 10^{-11} \text{ Pa}^{-2} \text{ m}^{-1} \text{ a}^{-1}$), as radio-echo sounding measurements (Nishio and Uratsuka, 1991) demonstrated that subglacial water is omnipresent in the downstream area of the Shirase drainage basin. Two model experiments were carried out, both over a period of 200 000 year forced by the Vostok signal: the first model run (TYPE I) based on the sliding law of Eq. 27; the second (TYPE II) based on a sliding law which is independent of the presence of subglacial water and widely used in numerical ice-

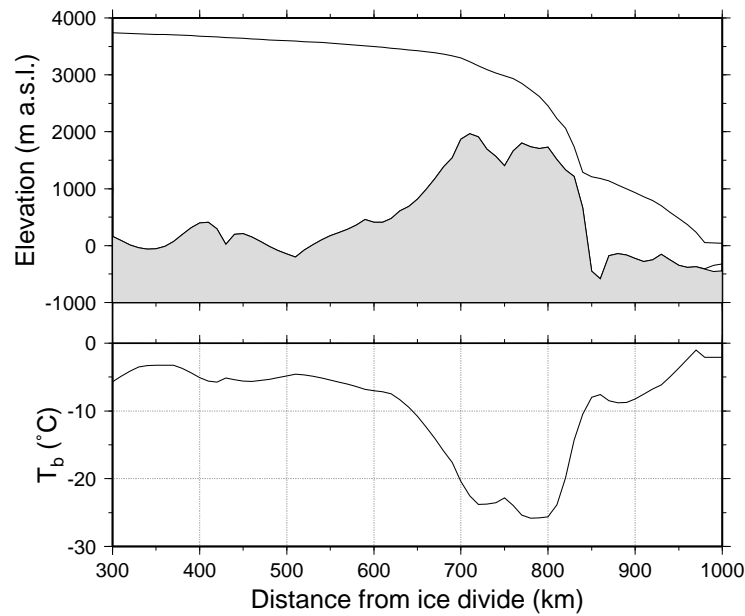


Figure 8: *Present modeled longitudinal profile of the Asuka flowline after 200 ka of forward integration. Lower panel displays the corresponding basal temperature profile.*

sheet modelling, using Eq. 25 and 26 (Fig. 9). According to the TYPE I experiment, high frequency oscillations occur during the coldest phase of the glacial periods and during the warmest phase of the interglacials. They are due to the interaction of the ice-sheet temperature field and the conditions at the base: basal motion causes the ice sheet to move more rapidly, hence increasing horizontal and vertical advection rates. Cold ice is thus advected towards the bottom, hence reducing the total surface subjected to melting. Basal velocities decrease, stabilizing the ice-sheet motion. The whole process gives rise to a cyclic behaviour; the slower ice sheet will tend to grow, advection rates decrease, bottom melting increases, hence resulting in large basal velocities. The periodicity of these cycles is approximately 3000 to 4000 years. High frequency oscillations are only observed in the downstream area of Shirase Glacier, and disappear gradually towards the inland plateau.

The TYPE I experiments show that there is no need for a massive drainage in the coastal area of Shirase Glacier to explain the large thinning rate observed in the field, the high frequency of the oscillations account for this, while the ice sheet remains stable. Any runaway of ice is counteracted by the thermo-mechanical process described above. A marine instability is unlikely to occur since most of the bedrock lies above sea level.

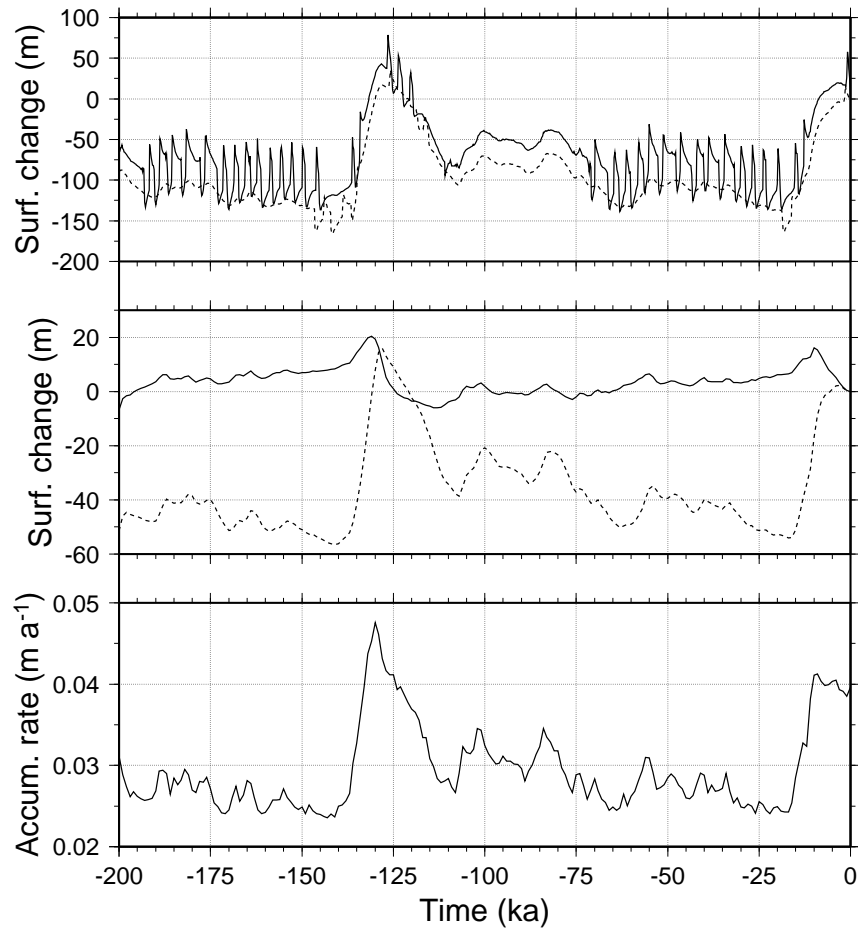


Figure 9: Time series of TYPE I (solid line) and II (dotted line) experiments along the Shirase flowline at gridpoint a (upper panel); time series of T-COUPLING (solid line) and ISOTHERM (dotted line) experiments along the Asuka flowline at gridpoint b (middle panel); time series of surface accumulation rate at gridpoint b (lower panel). See Fig. 6 for situation of points a and b along both flowlines.

3.1.3 The Asuka flowline experiments

Pattyn and Declair (1998) carried out a large number of model experiments each with different settings of boundary conditions. The results were then compared with glacial-geological evidence and field measurements such as ice velocities and ice thickness. Experiments in agreement with these observations could be divided in two major groups or scenarios. The first scenario (T-COUPLING) is the so-called standard model experiment, i.e., with full thermo-mechanical coupling (ice stiffness depends on local ice temperature), while for the second scenario (ISOTHERM) a constant flow parameter for the whole ice sheet is used, i.e., independent of the ice-temperature distribution (constant ice stiffness). Although the response time series of both scenarios are similar along the flowline, a marked discrepancy is observed in the mountain area (Fig. 9). One interpretation (T-COUPLING) is that only minor glacier variations have occurred during the last 200 ka, as was concluded by Moriwaki *et al.* (1992) based on glacial-geological evidence, and the present glacier surface is close to its minimum, while the other interpretation (ISOTHERM) is that glacier variations are of the order of 60 m, but that the present glacier surface is close to its maximum elevation of the last 200 ka. Outside the Sør Rondane (not shown), on the polar plateau, as well as in the coastal area, both scenarios are in accord and ice-sheet surface variations are of the order of 60-80 m. The main difference between the inland area and the coast is that near the ice divide the ice sheet seems at present close to its maximum position, while in the coastal area deglaciation is completed and the ice-sheet surface seems close to its minimum.

3.1.4 Analysis of time series

The model ice sheet reacts to the climatic signal according to Eq. 17, where the rate of change of the ice sheet $\frac{\partial H}{\partial t}$ is a function of changes in the surface mass balance (through $M_s(x, t)$) and a function of changes in ice temperature (that influence the velocity field and hence the flux-divergence term in Eq. 17). The complexity and non-linear nature of this relation make that $H(x, t)$ will differ from the climatic record that enters the model as $M_s(x, t)$ and $T_s(x, t)$. One way to investigate the response of the ice sheet to changes in climate is by comparing the time series of $H(x, t)$ and $M_s(x, t)$ in both time and spectral domain.

Lag correlation analysis

The reaction time of the ice sheet to the climatic signal can be expressed by the time lag. The correlation between the forcing time series (surface accumulation rate at

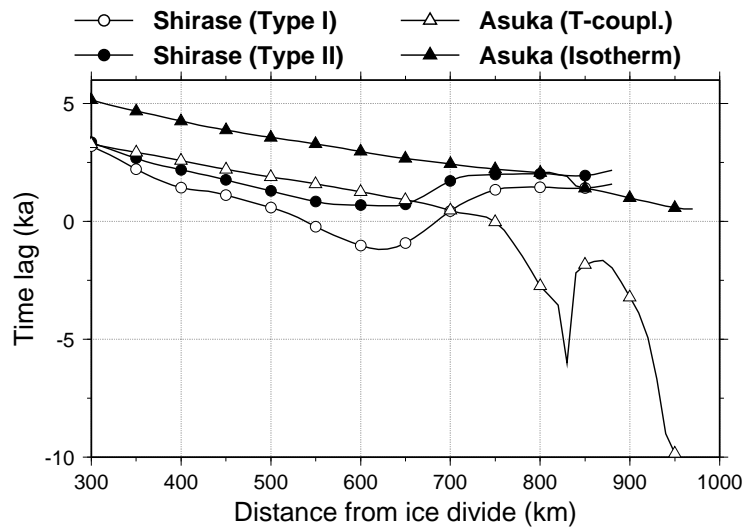


Figure 10: Time lag between the input and response time series at each gridpoint along the flowline for the four experiments, i.e., TYPE I (open circle) and TYPE II (filled circle) along the Shirase flowline; T-COUPPING (open triangle) and ISOTHERM (filled triangle) along the Asuka flowline.

a given gridpoint $M_s(x, t)$) and the response time series (ice-surface variations at that gridpoint $H(x, t)$) was calculated for different lags using the fast Fourier transform (Press et al., 1992). The lag corresponding to the maximum correlation then gives the time lag between both time series (Fig. 10). For all model experiments, the time lag is positive for the interior ice sheet and gradually decreases towards the coast, meaning that a maximum ice-surface elevation is reached some time (2-5 ka) after the maximum of the accumulation rate signal. However, the T-COUPPING experiment shows a large negative time lag clearly associated with the presence of the mountain range. The ISOTHERM experiment does not show this discrepancy, hence the negative time lag is probably due to differences in ice stiffness along the flowline as basal temperatures are low in the mountain area and increase rapidly northward of the ice fall (Fig. 8). A slight negative time lag is also observed for the TYPE I experiment along the Shirase flowline. Although a damming mountain range is not present in this area, a subglacial continuation of the mountain chain can be observed between 400 and 600 km from the ice divide, associated with a similar pattern in the basal temperature profile (Fig. 7).

Range analysis

The amplitude of the response time series, i.e., the range of vertical surface variations at each gridpoint, is taken as the difference between the maximum and the minimum of the series (Fig. 11). Generally, the range of ice-surface variations along the Shirase flowline is higher (150-200 m) than for the Asuka experiments (40-100 m). Since ice

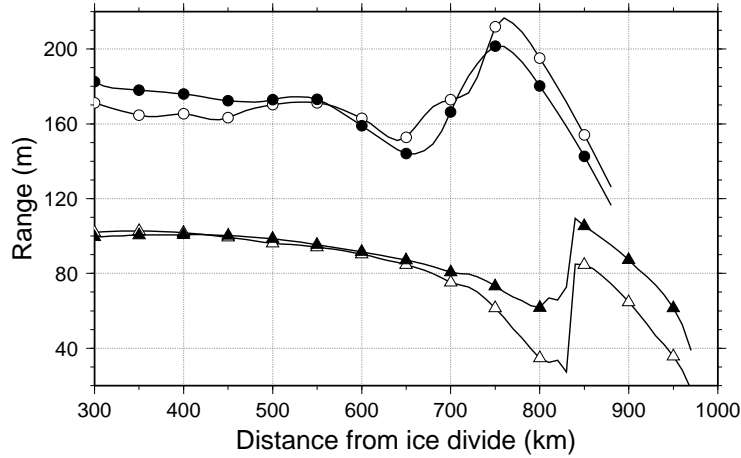


Figure 11: *Range (difference between maximum and minimum) of the vertical ice-surface variations at each gridpoint along the flowline for the four experiments. Same legend as Fig. 10.*

thickness in the inland part are comparable for both flowlines, the difference might be due to a lower accumulation rate in the Asuka drainage basin. Furthermore, ice motion is much faster in the Shirase drainage basin. Again, all four curves in Fig. 11 display a marked jump associated with the presence of the (subglacial) mountain range. The smallest amplitude is encountered in the mountain area for the T-COUPPING experiment, which corresponds to the time series of Fig. 9.

Fractal analysis

Long-term climatic series are considered to be self-affine fractals (Fluegelman and Snow, 1989), characterized by a fractal dimension lying between 1.0 and 1.5. The aim of this study is to use a fractal analysis – or an analysis of variance on different time scales – to interpret the difference in response patterns along the two flowlines. A common technique is the rescaled range analysis (RSA; Feder, 1988) that was applied to the time series of local imbalance $\chi(t) = \frac{\partial H}{\partial t}$. The rescaled range R/S then is the ratio of the range R , i.e., the difference between the maximum and minimum of cumulated values of χ at time t over a time span τ , and the standard deviation S estimated from the observed values $\chi(t)$

$$\begin{aligned}
 R(\tau) &= \max_{1 \geq t \geq \tau} X(t, \tau) - \min_{1 \geq t \geq \tau} X(t, \tau), \\
 S(\tau) &= \left(\frac{1}{\tau} \sum_{u=1}^{\tau} (\chi(u) - \langle \chi \rangle_{\tau})^2 \right)^{\frac{1}{2}}, \quad \text{where}
 \end{aligned}
 \tag{33}$$

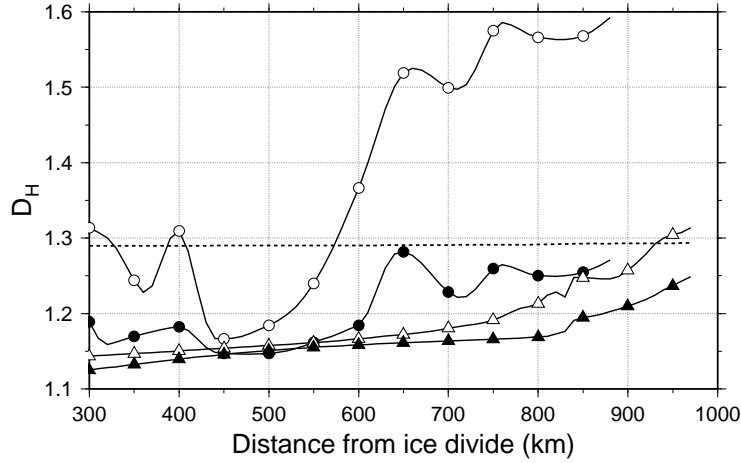


Figure 12: *Fractal dimension determined by rescaled range analysis of the variation of local imbalance at each gridpoint along the flowline for the four experiments. The dotted line shows the fractal dimension of the input signal ($\frac{\partial M_s}{\partial t}$) which is constant along the flowline. Same legend as Fig. 10.*

$$X(t, \tau) = \sum_{u=1}^t (\chi(u) - \langle \chi \rangle_\tau),$$

$$\langle \chi \rangle_\tau = \frac{1}{\tau} \sum_{t=1}^{\tau} \chi(t).$$

The rescaled range is shown to have a power law dependence on time span τ (Feder, 1988)

$$R/S \sim \tau^H, \quad (34)$$

where H is the Hurst exponent, related to the fractal dimension by $D_H = 2 - H$. For each response time series along the flowline, D_H was determined from a linear least squares fit of $\log(R/S)$ versus $\log(\tau)$ (Fig. 12). For the Asuka flowline experiments D_H lies between 1.1 and 1.3, gradually increasing towards the coast. The D_H of the ISOTHERM experiment is lower over the whole flowline. A much higher fractal dimension is observed for the TYPE I experiment associated with the occurrence of the high frequency oscillations, which is not shown in the TYPE II experiment. The sharp vertical jump in this D_H curve around 600 km from the ice divide (Fig. 12) marks the limit of the influence area of these oscillations.

The variance on different time spans of the response signal increases towards the coast, but is hardly influenced by the presence of subglacial mountains, nor the contrast

in stiffer / softer ice. Different response patterns in terms of high frequency oscillations account for a high fractal dimension. With exception of the TYPE I experiment, the fractal dimension of the response series is lower than the D_H of the input signal (taken as $\chi(t) = \frac{\partial M_s}{\partial t}$). This means that the response signals are smoother and that small scale climatic variations have less effect on the ice-sheet response.

3.2 High-resolution modelling: focus on the grounding zone

While ten years ago the ice-sheet modelling community employed computer models at a higher spatial resolution compared to the data availability, at present the reverse is true. Satellite altimetry data and dense airborne and overland radio-echo sounding missions filled up many of the ‘white spaces’, especially on the Antarctic continent. Improved data sets on Antarctic surface elevation, ice thickness and ice velocity now allow for detailed modelling of the ice-sheet dynamics. However, an increase in spatial model resolution puts higher demands on computation time and also requires an analysis of the internal ice dynamics, especially with regard to the *shallow-ice approximation* that forms the basis of most present-day Antarctic ice-sheet models.

Moreover, when the ice-sheet margin terminates in the sea in the form of a floating ice shelf, a transition zone can be defined where the ice-sheet dynamics gradually evolve towards ice-shelf dynamics. Studies on this grounding zone have revealed that for small basal motion the width of the transition zone is of the same order of magnitude as the ice thickness, and a full derivation of the Stokes balance equations is not necessary (Herterich, 1987; Van der Veen, 1987). However, when basal motion dominates the internal ice dynamics, not only shearing but longitudinal stretching is involved as well.

This study aims at investigating the steady-state behaviour of the Antarctic ice sheet in Dronning Maud Land at different spatial resolutions, i.e., at grid spacings ranging from 40 km down to 5 km, and compares the results of the ICE2D-model with a similar model based on the *shallow-ice approximation* (SIA). The horizontal velocity in the grounded ice sheet according to the SIA is determined as (e.g. Huybrechts and Oerlemans, 1988)

$$u(z) - u_b = -2(\rho g)^n \left| \frac{\partial s}{\partial x} \right|^{n-1} \frac{\partial s}{\partial x} \int_h^z A(T^*) (s-z)^n dz. \quad (35)$$

Note that for the SIA-model, the basal shear stress (τ_b) equals the driving stress $\tau_d = -\rho g H \frac{\partial s}{\partial x}$.

The primary input for the model is the present bedrock and ice surface profile sampled along the central flowline of Shirase drainage basin from the ice divide (Dome Fuji) to

the edge of the continental shelf (Fig. 6). Data were sampled from different oversnow traverses (Kamiyama *et al.*, 1994). Ice thickness in the stream region was compiled after Mae and Yoshida (1987). Data were originally sampled at a 2 km resolution. In order to obtain reference datasets at different (higher) resolutions, these data were filtered using a Savitzky–Golay smoothing filter (Press *et al.*, 1992) and resampled at the appropriate resolutions (5, 10, 20 and 40 km grid size). ω , the width of the drainage basin, is determined from the size of the drainage area. Present surface accumulation and temperature data along the flowline were taken from Takahashi and Watanabe (1995) and Satow and Kikuchi (1995), respectively.

3.2.1 The ICE2D- versus the SIA-model

The ICE2D- and the SIA-model were run forward in time until a steady state was achieved after about 200 000 years, with $m = 0.5$ and $m' = 0.5$ in order to adjust the height-to-width ratio of the ice sheet and the ice tongue. Both models use the same tuning parameters. By applying these tuning parameters it was possible to obtain ice-sheet surface profiles that are in general agreement with the present observed surface profile of Shirase drainage basin (Fig. 13). However, both model profiles show a higher elevation in the divide region probably due to the presence of a subglacial mountain situated at about 150 km from Dome Fuji, which is probably a nunatak so that the main ice flow is most likely at the sides of this topographic feature. The difference in ice thickness between both models is 2 to 5%, with a maximum near the grounding line. At first glance, there is no indication that the increase in horizontal resolution influences to a large extent the ice-sheet surface profile. A closer look at the grounding line reveals the major differences between the employed resolutions (Fig. 14). Surface gradients at the grounding line increase with increasing resolution, but decrease at 5 km grid size. The reverse is true for mass fluxes ($\bar{u}H$) at the grounding line (Fig. 14). Two factors play a role for this: (i) at a low resolution, surface gradients are calculated over larger areas, hence overseeing the inflection point at the interface between the ice sheet and the ice shelf; (ii) the increase in mass fluxes with resolution implies a flattening of the surface, as can be observed in the field on ice streams, and which is apparent at a 5 km grid size. One can observe a maximum difference of about 10% in mass fluxes between both models.

Figs. 15 and 16 display the major velocity and stress components at the grounding line as a function of resolution for the ICE2D- and the SIA-model, respectively. Both basal and surface velocity at the grounding line increase with increasing resolution (Fig. 15). Moreover, the sliding velocity takes a larger part in the total ice velocity with increas-

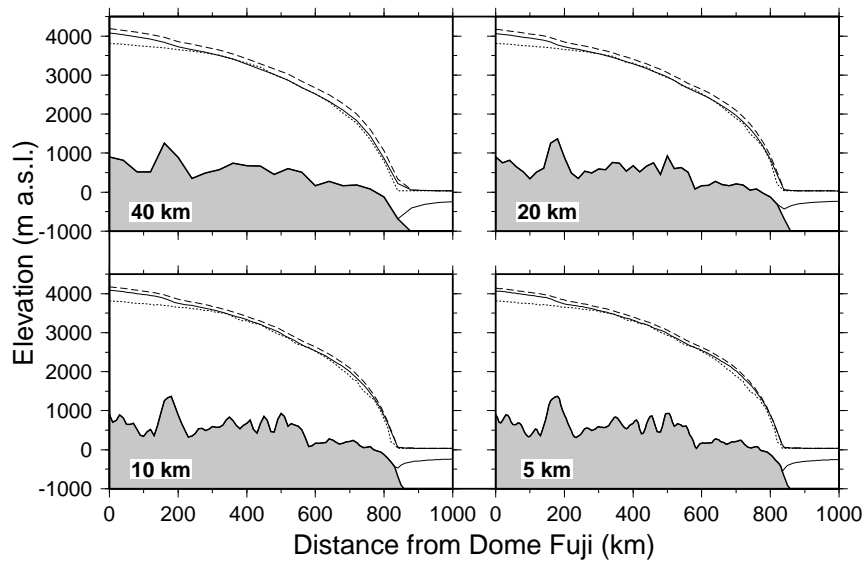


Figure 13: *Steady-state solutions of the Shirase flowline for different horizontal grid spacings (40, 20, 10 and 5 km). - - - present observed surface profile; — ICE2D-model result; — — SIA-model result.*

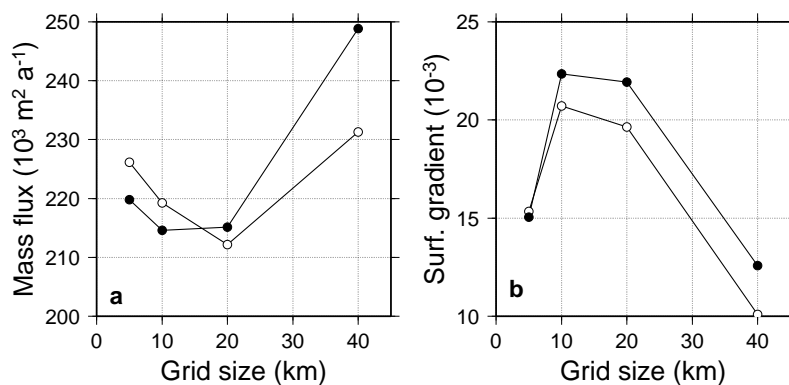


Figure 14: *Mass flux (left panel) and the absolute value of the surface gradients (right panel) at the grounding line for different resolutions according to the ICE2D-model (○) and the SIA-model (●).*

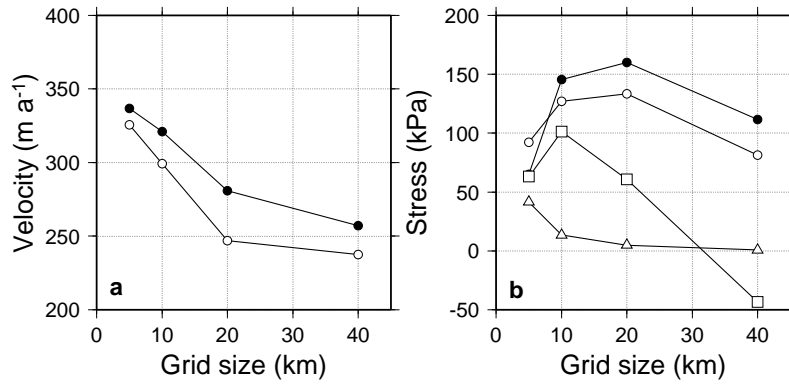


Figure 15: *Velocity and stress field at the grounding line for different resolutions according to the ICE2D-model. Left panel: basal (\circ) and surface (\bullet) horizontal velocities. Right panel: driving stress τ_d (\circ), basal shear stress τ_b (\bullet), basal σ'_{xx} (Δ) and surface σ'_{xx} (\square).*

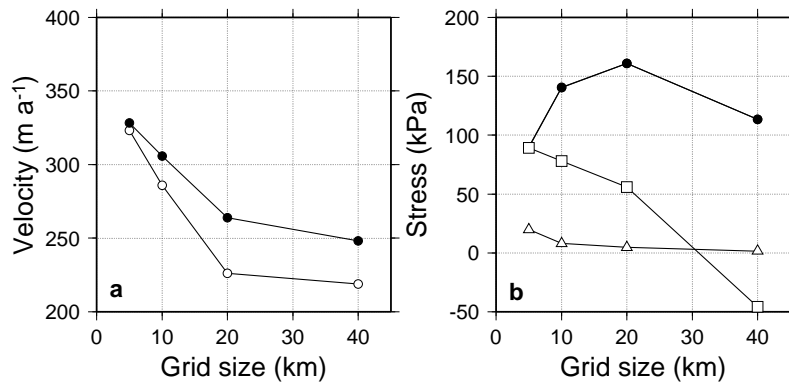


Figure 16: *Velocity and stress field at the grounding line for different resolutions according to the SIA-model. Same legend as Fig. 15. Note overlapping τ_d and τ_b curves.*

ing resolution, although the sliding parameter A_b remains the same for all experiments. Basal shear and driving stress attain a maximum at a grid size of 20 km and then decrease at higher resolutions. Basal shear stress is higher than the driving stress, except at a grid size of 5 km where τ_b is 40 kPa lower than τ_d . The longitudinal stress deviator σ'_{xx} increases with increasing resolution (except for the highest resolution experiment). The same picture appears more or less in Fig. 16 for the SIA experiments, albeit that both basal and surface velocities are somewhat lower than for the ICE2D experiments. An explanation needs to be sought in the difference in basal boundary conditions applied to both models, which is confirmed by the fact that the basal shear stress in the SIA-model equals the driving stress for different resolutions.

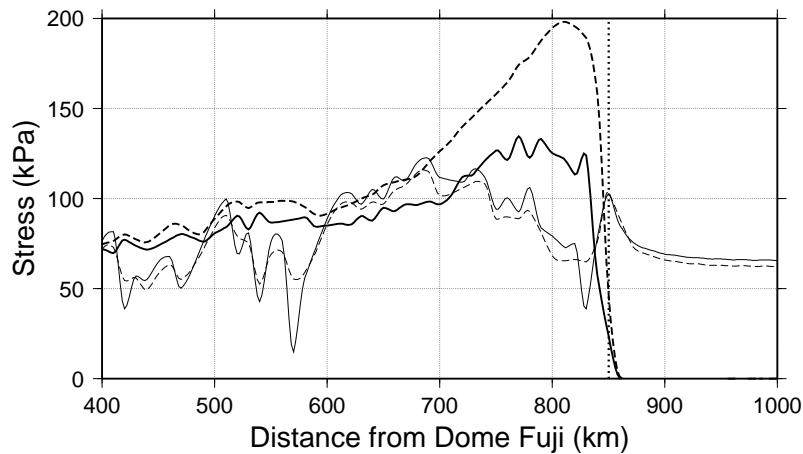


Figure 17: *Basal shear stress (thick lines) and surface longitudinal stress deviator (thin lines) for the enhanced sliding experiment (—) and the standard experiment (- - -). The vertical dotted line shows the position of the grounding line.*

3.2.2 Enhanced sliding experiment

For the 10 km grid data set an enhanced sliding experiment is carried out by setting the parameter A_b in Eq. 25 three times higher than in the reference experiment in order to examine the transition zone under more realistic circumstances. Besides the fact that basal sliding takes up a larger part in the total velocity near the grounding line – which leads to a significant increase in horizontal velocity – the basal shear stress is reduced over the whole flowline and significantly lower in the area between 700 km and the grounding line (Fig. 17). The basal shear stress reaches its maximum at approximately 80 km upstream of the grounding line and is as low as 120 kPa, compared to 200 kPa in the moderate sliding case. It is noteworthy to mention that surface longitudinal stresses are hardly altered compared to the standard experiment.

A complete overview of the stress fields in the downstream area of Shirase drainage basin is given in Fig. 18 according to the enhanced sliding experiment. The grounding line is situated at 850 km from Dome Fuji. The maximum surface gradient occurs at 50 km upstream from this point from where the surface becomes concave in the downstream direction. The maximum basal shear stress does not coincide with the maximum surface slope, but is attained upstream from this point. The maximum value of the longitudinal stress deviator σ'_{xx} is reached at the grounding line. The longitudinal stress deviator is higher than the shear stress everywhere in this downstream region. High values of σ'_{xx} do not occur at the surface but at a height halfway up the ice sheet, due to the thermo-mechanical coupling of the velocity field to the temperature field: since most shear deformation is situated near the base of the ice sheet, one

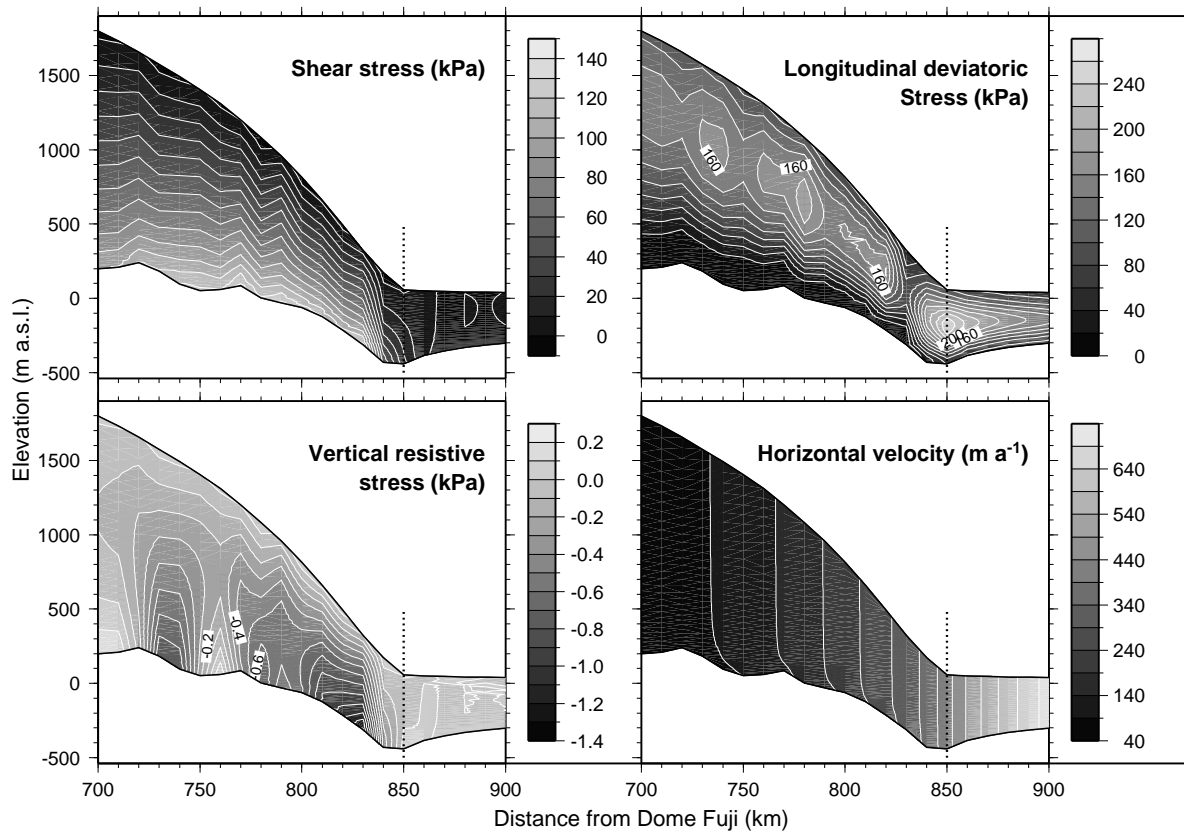


Figure 18: *Basal shear stress, longitudinal stress deviator, vertical resistive stress and horizontal velocity in the downstream area of Shirase drainage basin according to the enhanced sliding experiment. The vertical dotted line shows the position of the grounding line.*

can assume that in the upper 80% of an ice column $\sigma_{xz} \ll \sigma'_{xx}$, so that the flow law in this area reduces to $\frac{\partial u}{\partial x} \approx A(T^*)\sigma'_{xx}{}^n$. Due to the temperature dependence $A(T^*)$ varies a few orders of magnitude with depth in the downstream area of an ice mass and is lowest there where the ice is coldest, i.e., where advection of cold ice occurs. Hence, σ'_{xx} reaches a maximum value where $A(T^*)$ reaches a minimum. The variation of the longitudinal stress deviator σ'_{xx} with depth is much larger than what previous studies show. This led some authors to assume that σ'_{xx} could be replaced by its vertical mean (e.g. Van der Veen, 1987). The main reason for this significant variation is due to the thermo-mechanical coupling. Experiments with a constant value for $A(T^*)$ show that σ'_{xx} is more or less constant in the vertical but increases near the surface where it reaches a maximum.

Vertical resistive stresses become important upstream of the grounding line, though they are still 2 orders of magnitude smaller than both the longitudinal stress deviator and shear stress. Compared to the SIA-model, ice thicknesses computed with the ICE2D-model are approximately 7% smaller in the downstream area, and horizontal velocities are 7% higher. However, differences in driving stress are of the order of 20%.

3.3 Preliminary results of model experiments along a flowline in western Dronning Maud Land

Flowline modeling along two flowlines in eastern Dronning Maud Land (Fig 19), i.e. one from Dome Fuji to Shirase Glacier and one from Dome Fuji through the Sør Rondane Mountains, demonstrated that the inland ice sheet in eastern Dronning Maud Land is highly influenced by the coastal ice sheet dynamics and the presence of the subglacial mountain system present in the whole Dronning Maud Land area (see section 3.1). The purpose of this study is to examine the response of the ice sheet to the climatic signal in western Dronning Maud Land and to investigate the influence of coastal ice sheet dynamics, i.e. fast outlet glaciers such as Jutulstraumen, on the inland ice sheet. Both analyses are important for the interpretation of deep ice cores in Dronning Maud Land and for linking the climatic information to glacial-geological proxy records in order to reconstruct the glacial history of the ice sheet. The analysis remains however preliminary, as during the first EPICA phase ground truth was collected.

The ice-sheet model is numerically solved on a fixed grid in space and time, i.e. a flowline starting from the ice divide (Dome Fuji) to the edge of the continental shelf, which forms the maximum possible lateral extension of the ice sheet, with a horizontal

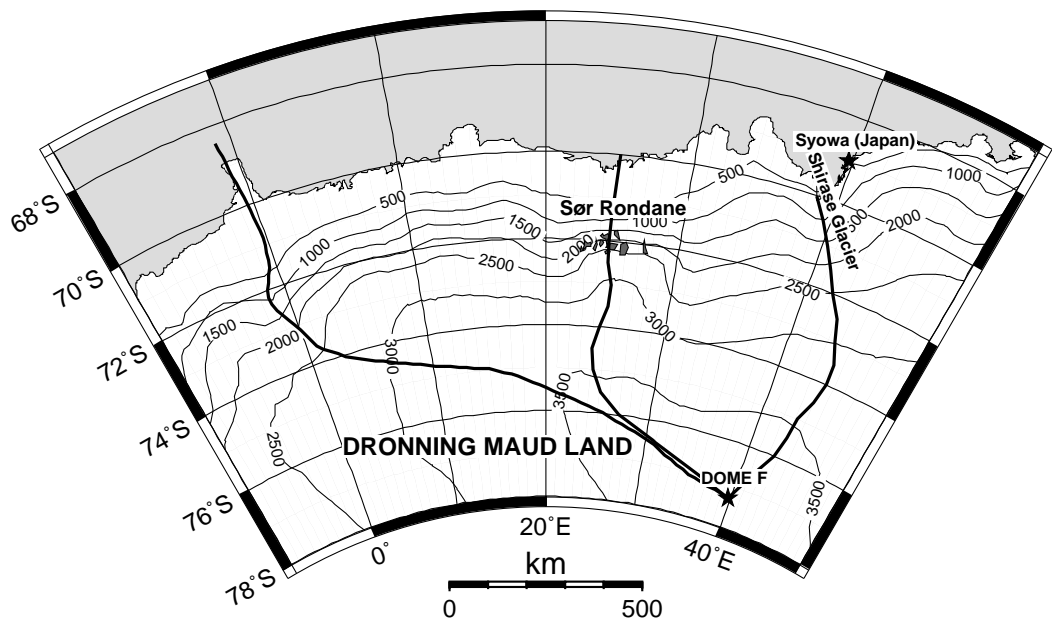


Figure 19: *Situation map of flowlines in Dronning Maud Land.*

grid-size spacing of 20 km, 20 layers in the vertical, and a time step of 10 years. The primary inputs for the model are bedrock and ice surface profiles along a flowline (Fig. 19). Data were sampled from a database compiled from dense airborne radio-echo sounding carried out in western Dronning Maud Land during the EPICA project.⁶ Present surface-temperature and mass-balance distribution were parameterized from data of oversnow traverses in Dronning Maud Land and from Satow and Kikuchi (1995) based on measurements in eastern Dronning Maud Land. In the future, data from EPICA traverses will become available and will be included as well.

The present experiments were designed to test the model setup and determine the tuning parameters in the model more accurately. Using the data on present surface temperature and accumulation rate, the model was run forward in time until a steady state was achieved. Fig. 20 displays the steady-state longitudinal deviatoric stress and shear stress, respectively. Characteristic for the western Dronning Maud Land flowline are the irregular subglacial topography, which influences to a large extent the stress field in the glacier. An irregular pattern of longitudinal pushes and pulls can therefore be observed along the flowline, which seem important close to the ice sheet surface. In the downstream area (Jutulstraumen), very high shear and longitudinal deviatoric stresses are observed, which is in accord with the observations and calculations of Høydal (1996). Also the horizontal velocities in the stream area are of the order of

⁶These data were supplied by Dr. U. Nixdorf and Dr. D. Steinhage at the Alfred Wegener Institute (AWI), Germany.

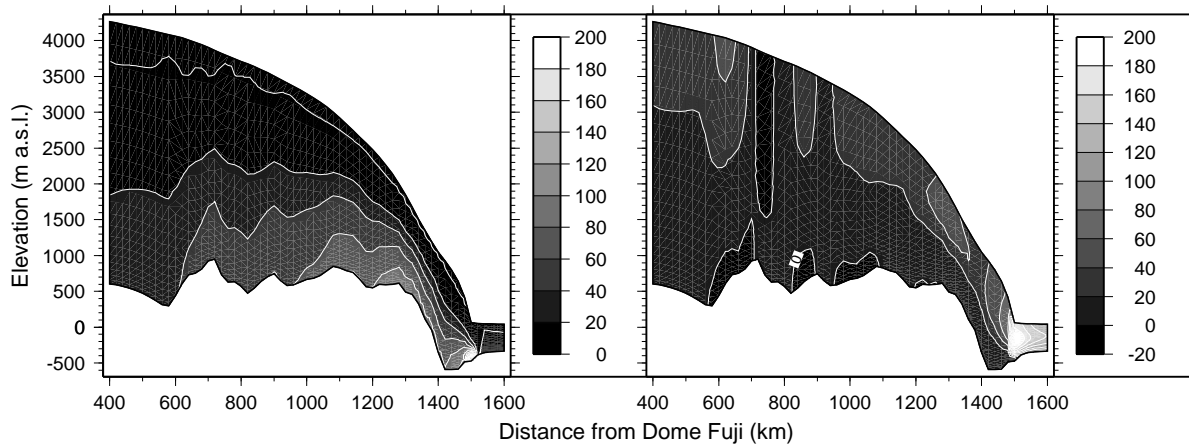


Figure 20: *Steady-state shear-stress distribution (left panel) and steady-state longitudinal deviatoric stress distribution (right panel) along the western Dronning Maud Land flowline.*

magnitude of the observed ones.

3.4 Shirase Glacier dynamics inferred from ERS-SAR interferometry

The Antarctic ice sheet is primarily drained by large outlet glaciers, which play a decisive role in the dynamic behaviour of the ice sheet. Shirase Glacier is such a glacier, situated along the coast of eastern Dronning Maud Land (Figure 3). Characterized by a surface velocity of up to $2,700 \text{ m a}^{-1}$ at the calving front, Shirase Glacier is one of the fastest outlet glaciers draining the Antarctic ice sheet, although its total mass output is less impressive, i.e., 12.5 Gt a^{-1} estimated at the calving front (Fujii, 1981). Shirase Glacier lies in a narrow trough $< 10 \text{ km}$ in width, and which reaches depths of $> 1500 \text{ m}$ near the present calving front (Moriwaki and Yoshida, 1983). In the grounded area the ice flow is convergent; 90 % of the ice from the Shirase drainage basin is drained by this glacier (Fujii, 1981), thus forming a “bottleneck” for ice flowing from the inland ice sheet. Shirase Glacier does not calve directly into sea but ends in a 40 km long floating ice tongue, which is confined by the surrounding slow-moving ice sheet and by a few nunataks.

Not much is known on the dynamics of Shirase Glacier, as difficult access hampers field work activities in the downstream area of the drainage basin. The only adjacent area that has been thoroughly investigated is situated near Mizuho plateau, roughly 200 km upstream of the grounding line. Subsequent field measurements revealed that

the ice sheet in this area is thinning rapidly at a rate of 0.5 to 1.0 m a⁻¹ (Mae and Naruse, 1978; Nishio et al., 1989; Toh and Shibuya, 1992). The possible cause for this thinning seems not due to a decrease of the accumulation rate due to a change in climate, but is believed to result from important basal sliding (Mae, 1979). Besides Mizuho plateau, the calving front of Shirase Glacier has been the subject of a number of investigations, mainly through analysis of aerial photographs (Nakawo et al., 1978; Fujii, 1981).

The position of the calving front of Shirase Glacier is depicted in Figure 4A. In this area the floating ice tongue disintegrates into a conglomerate of several large icebergs, which are clearly visible in this satellite image. These icebergs stick together in the fast ice that covers the entrance of Lützow-Holm Bay, thus forming a continuation of the tongue. At regular intervals (few years to tens of years), these icebergs are cleared from the area as the fast ice breaks up in Lützow-Holm Bay. This repeated change is also visible from an analysis of 1963 Declassified Intelligence Photography (DISP), Landsat data and RADARSAT-1 image mosaics (Kim et al., 2001). In 1962 this iceberg conglomerate was at its furthest extent, then retreated about 60 km in the mid-1970's to a position that nearly matched the 2000 position. Between 1997 and 2000 a retreat of about 12 km could be observed (K. C. Jezek, personal communication). It should be stressed, however, that such retreat is not a retreat of the grounding line of the glacier, nor of its calving front, but a removal of icebergs that have already calved off.

This study will focus on the ice-dynamical behaviour of Shirase Glacier. Based on the surface displacements obtained from the *coherence tracking*, a large-scale force budget was applied to estimate the major forces balancing the driving stress. Finally, the present dynamical state of Shirase Glacier is estimated by analyzing its mass budget.

3.4.1 Surface velocity and strain rates

The displacements obtained from the interferometric analysis were recalculated on a regular grid of 200 by 200 m. Since these velocities still contain high-frequency noise associated with the substantial errors of ± 70 m a⁻¹, velocity and strain-rate estimates were evaluated within a larger image window of 6 by 6 km. Smaller window sizes (from 1 to 6 km) were used as well, but did not hamper the analysis from the viewpoint of 'overseeing' ice dynamics, such as smoothing out stress or strain gradients, especially near the grounding line. Using such large windows has the advantage that all high-frequency noise is removed. Velocities are then taken as the mean of all velocity estimates within the window. Strain rates at each grid point are considered constant

within the window, and are determined from a linear regression analysis of all u and v values in each window with respect to the x and y direction (Figures 21A and B). Since the major ice motion is in the y direction, the major strain components are the surface longitudinal strain rate $\dot{\epsilon}_{yy}$, the surface transverse strain rate $\dot{\epsilon}_{xx}$, and the surface lateral shear-strain rate $\dot{\epsilon}_{xy}$, defined as

$$\dot{\epsilon}_{yy} = \frac{\overline{\Delta v}}{\Delta y} \quad (36)$$

$$\dot{\epsilon}_{xx} = \frac{\overline{\Delta u}}{\Delta x} \quad (37)$$

$$\dot{\epsilon}_{xy} = \frac{1}{2} \left(\frac{\overline{\Delta v}}{\Delta x} + \frac{\overline{\Delta u}}{\Delta y} \right) \quad (38)$$

As shown in Figure 21A, velocities in the floating ice tongue (zone FT in Figure 4A) are almost constant over the whole length of the tongue (2,200–2,500 m a⁻¹), i.e., no significant acceleration along the central flowline is observed. This is in sharp contrast with the grounded area, upstream of the grounding line (zone A in Figure 4A), where the ice speeds up rapidly from about 1,000 m a⁻¹ to 2,000 m a⁻¹ over a horizontal distance of less than 10 km (Figure 21A), hence giving rise to a large longitudinal strain rate $\dot{\epsilon}_{yy}$ of the order of 0.1 a⁻¹. Previous estimates of the velocity field on Shirase Glacier were based on aerial photographs of 1962, 1969, 1975 and 1977 of the floating part of Shirase Glacier; Fujii (1981) calculated calving front velocities of 2,500–2,700 m a⁻¹. However, the ERS velocities are slightly lower than the photogrammetric ones, probably due to the shorter time span over which the ERS images were evaluated.

A map of the surface lateral shear strain rates $\dot{\epsilon}_{xy}$ on Shirase Glacier is given in Figure 21B. High values are associated with the sides of the glacier, especially at both sides of the floating ice tongue. However, even in the grounded part of the glacier (the grounding line is denoted by GL in Figure 4A) this channel effect can be noticed, as the high values of $\dot{\epsilon}_{xy}$ occurring at the western margin of the glacier continue upstream towards the south (Figure 21B). It can also be seen that the calving front (CV in Figure 4A) coincides with the area where the lateral shearing ends.

3.4.2 Large-scale force budget of Shirase Glacier

The calculation of the force budget is based on a similar analysis by Rolstad *et al.* (2000), i.e., by assessing the relative importance of the forces controlling the ice flow in a large imaginary box in the glacier. We adapted these force-balance calculations to

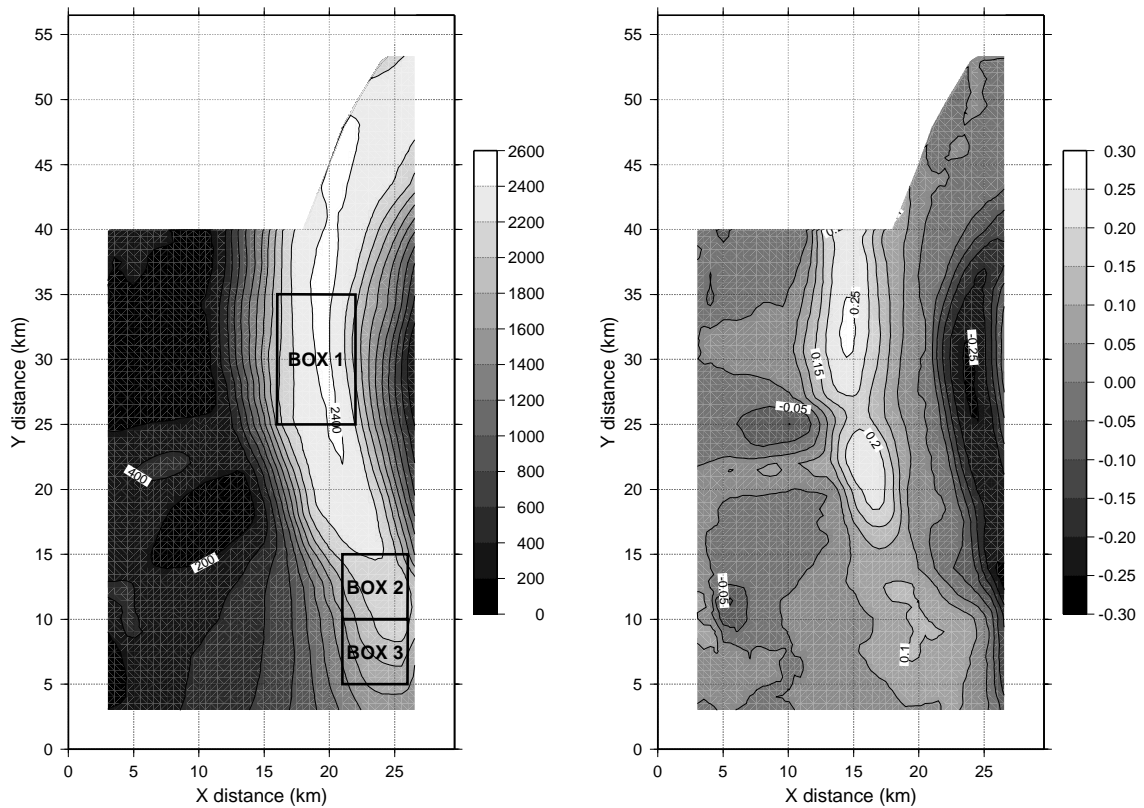


Figure 21: (A) Shirase Glacier surface velocity field (m a^{-1}). Large-scale force budget calculations are carried out for the three depicted boxes; (B) Surface shear-strain rate $\dot{\epsilon}_{xy}$ (a^{-1}).

three dimensions by integrating numerically over the ice thickness, so as to assess an estimate of the horizontal shear stress and the basal velocity in each box. Hence, each box consists of a number of planes parallel to the surface. Three boxes of dimensions $W \times L$ (L is taken parallel to the glacier motion) were selected on the glacier surface. Box 1 is situated on the floating ice tongue, Box 2 is centered on the grounding line and Box 3 is taken on the inland ice slope where the ice is grounded (Figure 21A). Only the force balance in the main direction of the ice flow is considered, i.e., parallel to the y axis. For a Cartesian coordinate system the force balance yields (Van der Veen and Whillans, 1989)

$$\frac{\partial R_{xy}}{\partial x} + \frac{\partial R_{yy}}{\partial y} - \rho g \nabla_s + \frac{\partial R_{yz}}{\partial z} = 0 \quad (39)$$

where ∇_s is the surface gradient, R_{yz} is the horizontal shear stress, R_{xy} the lateral shear stress, and R_{yy} the longitudinal resistive stress in the direction of the flow. To obtain the force budget and an estimate of the basal drag, Equation 39 has to be integrated from the surface of the glacier to the base, yielding

$$\frac{\partial}{\partial x} \int_b^s R_{xy} dz + \frac{\partial}{\partial y} \int_b^s R_{yy} dz + \tau_d - \tau_b = 0 \quad (40)$$

where $\tau_d = -\rho g H \nabla_s$ is the driving stress, and τ_b the basal drag, or the sum of all resistance to the flow at the base. Stresses are related to strain rates by means of a constitutive equation, in this case Glen's flow law for the flow of polycrystalline ice, with $n = 3$.

$$R_{xy} = B \dot{\epsilon}_e^{\frac{1-n}{n}} \dot{\epsilon}_{xy} \quad (41)$$

$$R_{yz} = B \dot{\epsilon}_e^{\frac{1-n}{n}} \dot{\epsilon}_{yz} \quad (42)$$

$$R_{yy} = B \dot{\epsilon}_e^{\frac{1-n}{n}} (2\dot{\epsilon}_{yy} + \dot{\epsilon}_{xx}) \quad (43)$$

where $\dot{\epsilon}_e$ is the effective strain rate, or the second invariant of the strain-rate tensor, defined by $\dot{\epsilon}_e^2 = \sum_{ij} \frac{1}{2} \dot{\epsilon}_{ij} \dot{\epsilon}_{ij}$, for $i, j = x, y, z$. Conservation of mass implies that $\dot{\epsilon}_{xx} + \dot{\epsilon}_{yy} + \dot{\epsilon}_{zz} = 0$, so that the effective strain rate might be written as

$$\dot{\epsilon}_e = (\dot{\epsilon}_{xx}^2 + \dot{\epsilon}_{yy}^2 + \dot{\epsilon}_{xx} \dot{\epsilon}_{yy} + \dot{\epsilon}_{xy}^2 + \dot{\epsilon}_{yz}^2)^{\frac{1}{2}} \quad (44)$$

The stiffness parameter B is related to temperature through an Arrhenius-type relation (Hooke, 1981).

$$B = B_0 \exp \left(\frac{Q}{nRT} - \frac{3C}{n(T_r - T)^k} \right) \quad (45)$$

where $B_0 = 2.207 \text{ Pa a}^{1/n}$, $C = 0.16612 \text{ K}^k$, $T_r = 273.39 \text{ K}$, $k = 1.17$, $R = 8.31 \text{ J mol}^{-1} \text{ K}^{-1}$ is the gas constant, and $Q = 7.88 \times 10^4 \text{ J mol}^{-1}$ is the activation energy for creep. The major simplification we will make is that all *measured*⁷ strain rates are kept constant with depth and are equal to their surface value (Høydal, 1996). Their associated stresses will vary with depth, as the flow-law parameter B changes with temperature and the effective strain rate is a function of the depth-varying horizontal shear-strain rate $\dot{\epsilon}_{yz}$ as well.

Equation 39 is integrated numerically from the surface of the glacier to a height z , starting from the surface stress field, and using 50 equidistant layers in the vertical. A stress-free surface implies that $R_{yz}(s) = R_{yy}(s) \nabla s$. Values of R_{xy} and R_{yy} are calculated for the sides of the box, based on the mean values of the strain rates at these sides. The horizontal shear stress at a height z in the ice box is then given by

$$\begin{aligned} R_{yz}(z) = R_{yz}(s) &+ \rho g \frac{s_{\text{up}} - s_{\text{down}}}{L} \int_z^s dz + \int_z^s \frac{R_{xy_{\text{east}}} - R_{xy_{\text{west}}}}{W} dz \\ &+ \int_z^s \frac{R_{yy_{\text{up}}} - R_{yy_{\text{down}}}}{L} dz \end{aligned} \quad (46)$$

where subscripts 'up' and 'down' refer to the upstream and downstream side of the box, respectively, and subscripts 'east' and 'west' refer to the western (left) and eastern (right) sides of the boxes, respectively. At each level the effective strain rate is calculated, according to Equation 44, while the horizontal shear-strain rate is obtained from Equation 42. Assuming no vertical shear, the horizontal shear-strain rate is related to the velocity field by $\dot{\epsilon}_{yz} = \frac{1}{2} \frac{\partial v}{\partial z}$, from which the velocity at each level can be calculated. To determine the flow-rate factor B a linear temperature profile was considered, based on the mean surface temperature of the box, using data from Satow and Kikuchi (1995), and a temperature at the base kept at pressure melting point. High

⁷By *measured* we mean the strain rates determined directly from the surface velocity field, i.e., $\dot{\epsilon}_{xx}$, $\dot{\epsilon}_{yy}$, and $\dot{\epsilon}_{xy}$.

Table II: *Measurements and averaged strain rates at the sides of the boxes. Ice thickness is taken from Wada and Mae (1981) and Mae and Yoshida (1987); surface elevation from Bamber and Bindschadler (1997). Uncertainties, determined from error propagation, are given between brackets.*

		Box 1	Box 2	Box 3
L	(km)	10 (0)	5 (0)	5 (0)
W	(km)	7 (0)	5 (0)	5 (0)
\bar{H}	(m)	525 (50)	900 (100)	800 (100)
\bar{s}_{up}	(m)	90 (1)	368 (5)	591 (5)
\bar{s}_{down}	(m)	60 (1)	171 (5)	368 (5)
$\bar{\dot{\epsilon}}_{xy\text{east}}$	(10^{-3} a^{-1})	-137 (4)	-196 (4)	-91 (4)
$\bar{\dot{\epsilon}}_{xy\text{west}}$	(10^{-3} a^{-1})	191 (4)	54 (4)	93 (4)
$\bar{\dot{\epsilon}}_{yy\text{up}}$	(10^{-3} a^{-1})	19 (6)	22 (9)	44 (9)
$\bar{\dot{\epsilon}}_{yy\text{down}}$	(10^{-3} a^{-1})	6 (6)	44 (9)	79 (9)
$\bar{\dot{\epsilon}}_{xx\text{up}}$	(10^{-3} a^{-1})	9 (1)	-6 (1)	8 (1)
$\bar{\dot{\epsilon}}_{xx\text{down}}$	(10^{-3} a^{-1})	-47 (1)	7 (1)	-45 (1)

basal temperatures are very likely, as radio-echo soundings in this area have demonstrated that a water layer should be present in the downstream area of the grounded part of Shirase Glacier (Nishio and Uratsuka, 1991). Once the integration reaches the base, the stress balance is obtained by integrating the stresses at depth over the whole ice column, leading to

$$\tau_{dy} = \tau_{by} - \underbrace{\frac{H\bar{R}_{xy\text{east}} - H\bar{R}_{xy\text{west}}}{W}}_{\bar{\tau}_{\text{lat}}} - \underbrace{\frac{H\bar{R}_{yy\text{up}} - H\bar{R}_{yy\text{down}}}{L}}_{\bar{\tau}_{\text{lon}}} \quad (47)$$

The calculated strain rates and their associated stresses for the four sides of the boxes are given in Tables II and III. Errors are determined from the theory of error propagation. For instance, the error in lateral shearing (Equation 41) is

$$\sigma_{R_{xy}} = \left\{ \left(\frac{\partial R_{xy}}{\partial \dot{\epsilon}_{xy}} \right)^2 \sigma_{\dot{\epsilon}_{xy}}^2 + \left(\frac{\partial R_{xy}}{\partial \dot{\epsilon}_e} \right)^2 \sigma_{\dot{\epsilon}_e}^2 + \left(\frac{\partial R_{xy}}{\partial B} \right)^2 \sigma_B^2 \right\}^{\frac{1}{2}}$$

Table III: *Calculated stresses and force-balance components based on measurements and calculations given in Table II. Uncertainties, determined from error propagation, are given between brackets. u_d and u_b are the deformational and the basal velocity, respectively.*

		Box 1	Box 2	Box 3
\bar{B}	(kPa a ⁻¹)	254 (51)	300 (54)	316 (56)
$\bar{R}_{xy_{\text{east}}}$	(kPa)	-132 (26)	-169 (31)	-115 (22)
$\bar{R}_{xy_{\text{west}}}$	(kPa)	148 (29)	72 (16)	126 (24)
$\bar{R}_{yy_{\text{up}}}$	(kPa)	86 (29)	49 (25)	162 (47)
$\bar{R}_{yy_{\text{down}}}$	(kPa)	-57 (24)	149 (46)	181 (48)
$\bar{\tau}_{dy}$	(kPa)	14.1 (1.4)	316 (37)	318 (41)
$\bar{\tau}_{\text{lat}}$	(kPa)	-21.0 (3.0)	-43.3 (6.3)	-38.5 (5.3)
$\bar{\tau}_{\text{lon}}$	(kPa)	7.5 (2.0)	-18.0 (9.5)	-3.1 (10)
$\bar{\tau}_{by}$	(kPa)	0.5 (3.8)	255 (38)	277 (43)
$u_d/(u_d + u_b)$	(%)	0.0	14.9	21.8

$$= \left\{ \left(B \dot{\epsilon}_e^{\frac{1-n}{n}} \right)^2 \sigma_{\dot{\epsilon}_{xy}}^2 + \left(\frac{1-n}{n} B \dot{\epsilon}_{xy} \dot{\epsilon}_e^{\frac{1-2n}{n}} \right)^2 \sigma_{\dot{\epsilon}_e}^2 + \left(\dot{\epsilon}_e^{\frac{1-n}{n}} \dot{\epsilon}_{xy} \right)^2 \sigma_B^2 \right\}^{\frac{1}{2}} \quad (48)$$

Similar expressions are found for all other calculated variables. Despite the large errors associated with the uncertainties in input parameters, such as glacier geometry and velocity, the propagated errors in the force-budget calculations are acceptable (Table III). In the floating tongue (Box 1), the basal drag should be zero by definition, which is confirmed by the numerical calculations. Lateral drag is more important than the driving stress, but the longitudinal stress gradient cannot be neglected in balancing – together with the driving stress – the lateral drag as well. The impact of horizontal shear is negligible, as the basal velocity equals the surface value. This means that the effective strain rate remains constant with depth (Figure 22A) and that the stress components R_{xy} and R_{xx} vary linearly with depth due to the assumed linear temperature profile (Figure 22B).

Near the grounding line (Box 2), driving stresses are large (> 300 kPa), due to steep surface gradients and a relatively important ice thickness. The basal drag is reduced by lateral drag and – to a somewhat lesser extent – the longitudinal stress gradient. The grounding line area is the only area where $\bar{\tau}_{\text{lon}}$ has a role to play, due to the

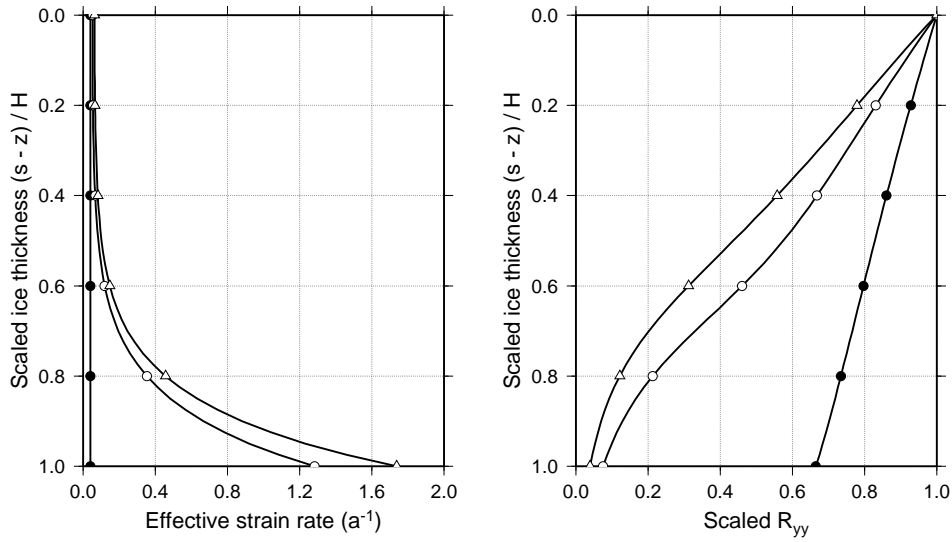


Figure 22: (A) Effective strain rate $\dot{\epsilon}_e$ as a function of depth for Box 1 (\bullet), Box 2 (\circ), and Box 3 (\triangle); (B) Scaled longitudinal resistive stress $R_{yy_{up}}$ as a function of depth for Box 1 (\bullet), Box 2 (\circ), and Box 3 (\triangle). The variation of the scaled R_{xy} with depth is similar to this graph, and therefore not shown.

change of grounded ice flow to shelf flow. In the grounded part ice acceleration $\dot{\epsilon}_{yy}$ is important, while in the floating ice tongue $\dot{\epsilon}_{yy}$ is reduced due to important shearing at the margins. Consequently, the effect of $\bar{\tau}_{lon}$ is negligible upstream of the grounding line (Box 3). Hence, the main difference in the force balance between Box 2 and Box 3 is the difference in importance in the longitudinal stress gradient $\bar{\tau}_{lon}$, since the lateral drag $\bar{\tau}_{lat}$ is in both areas of the same importance in reducing the basal drag. Horizontal shear is the most important stress component in the force budget of Box 2 and 3. Shear-strain rates exceed 1.5 a^{-1} , which is far more important than surface lateral shear and normal strain rates (Figure 22A). Consequently, the depth variation of the other resistive stresses R_{xy} and R_{yy} is non-linear and depends not only on temperature variations but on the impact of high horizontal shear-strain rates as well. Although horizontal shear is dominant in this area, the impact of the deformation velocity u_d in the total velocity field is very low, i.e., 15% and 22% for Box 2 and Box 3, respectively, which means that more than 80% of the vertical mean horizontal velocity is due to basal sliding.

In short, the above force-budget calculations demonstrate that, despite the high surface and basal velocities, Shirase Glacier is distinguished from an ice stream by the relative importance of driving stress and basal drag, even though basal drag is to some extent reduced by the impact of lateral drag – due to the convergent flow upstream of the

grounding line – and the longitudinal stress gradient. The latter is only of importance in a small zone centered around the grounding line.

3.4.3 Large-scale mass budget of Shirase Glacier

To determine the mass budget of Shirase Glacier, we compare the ice flux at the grounding line with balance-flux calculations of the Antarctic ice sheet and with the calving flux. Based on an update of the Giovinetto and Bentley (1985) dataset of the surface mass balance, and the refined surface-elevation dataset of Bamber and Bind-schadler (1997), Huybrechts *et al.* (2000) calculated balance fluxes of the Antarctic ice sheet on a 20 km grid. The balance flux at a certain position in the ice sheet equals the total amount of accumulated ice (the surface integral of the surface mass balance) that is drained in the direction of the flow towards that position. Huybrechts *et al.* (2000) find a total balance flux at the grounding line of Shirase Glacier (this represents both the discharge through main stream A and B in Figure 4A) of $0.68 \text{ km}^2 \text{ a}^{-1}$ of ice, which corresponds to a total mass flux of 12.4 Gt a^{-1} at the grounding line. On the other hand, Fujii (1981) calculated mass fluxes at the calving front of Shirase Glacier. He estimated a mass flux of 10.3 and 2.2 Gt a^{-1} for stream A and B, respectively, leading to a total mass flux of 12.5 Gt a^{-1} . Comparing this figure with the balance fluxes of Huybrechts *et al.* (2000) leads to the conclusion that the Shirase Glacier drainage basin seems in steady state.

However, from the present study the mass flux at the grounding line can be determined as well, albeit limited to stream A. For an vertical mean velocity of $2,035 \text{ m a}^{-1}$ (a value determined from the force budget integration), a mean ice thickness of 900 m and a cross-sectional width of 8.3 km, we obtain a mass flux 13.8 Gt a^{-1} at the grounding line. Since approximately 82% of the total ice discharge in Shirase Glacier is through stream A (Fujii, 1981), the balance fluxes of Huybrechts *et al.* (2000) account for a mass flux of 10.2 Gt a^{-1} , which, compared to our calculated mass flux of 13.8 Gt a^{-1} , leads to a mass deficit of 3.6 Gt a^{-1} . Similarly, the balance between the grounding line and the calving front leads to a mass surplus of 3.5 Gt a^{-1} . This might indicate that upstream of the grounding line the ice sheet is out of balance, and that underneath the floating tongue an important amount of basal melting should be accounted for. The largest uncertainty in our grounding line flux calculation is the ice thickness. However, we expect that 900 m is probably an underestimation of the ice thickness in this area. According to the surface elevation data and considering hydrostatic equilibrium at the grounding line, the ice might be more than 1 km thick, which would lead to an even higher mass flux at the grounding line.

So, in order to balance the ice fluxes in the floating tongue between the grounding line and the calving front, i.e., over a surface of approximately 300 km^2 , the mass loss should be around 3.5 Gt a^{-1} , corresponding to a mean basal melt rate of 11.5 m a^{-1} w.e. It is possible that such high basal melt rates might occur near the grounding line. As Shirase Glacier is lying in a subglacial trench it is assumed that Circumpolar Deep Water (CDW) is transported along these glacial troughs in Lützow-Holm Bay, which results in a significant amount of heat supply into the water (Ohshima *et al.*, 1991). Evidence for such high basal melt rates are also found elsewhere from oceanographic observations (e.g. beneath Pine Island Glacier, West Antarctica; Jenkins *et al.*, 1997). The inland imbalance, due to the difference between the balance flux and the calculated grounding-line flux, spread out over the whole drainage basin would lead to a thinning rate of 2 cm a^{-1} . This value is much lower than the $0.5\text{--}1.0 \text{ m a}^{-1}$ suggested by other authors (e.g. Mae and Naruse, 1978; Nishio *et al.*, 1989; Toh and Shibuya, 1992). Even if we limit the thinning to the area of Mizuho Plateau, i.e., the area below the 2400 m contour, the thinning rate would be around 8.5 cm a^{-1} , still an order of magnitude lower than suggested by field evidence.

4 DISCUSSION

4.1 The variability of Antarctic ice-sheet response to the climatic signal

Numerical ice-sheet model experiments were capable of simulating different response patterns of the East Antarctic ice sheet to the climatic signal as observed in the field, i.e. the large thinning rate in Shirase drainage basin and the small glacier variations that – according to glacial-geological evidence – occurred over the last 200 ka in the nearby Sør Rondane Mountains, Dronning Maud Land. Whether the high frequency oscillations, as a result of the interaction between the ice-sheet thermodynamics and basal sliding, are a dynamic process that really occurs in Shirase drainage basin has never been proven due to the lack of field evidence. However, similar mechanisms are capable of explaining the dynamics of the Siple Coast ice streams, i.e. a switching between fast and slow ice-stream flow (Payne, 1998).

All of the above described time series analyses, i.e. lag correlation, range and fractal analysis, demonstrate that the presence of a coastal mountain range influences to a large extent the response of the ice sheet to the climatic signal, not only in places where the ice is clearly dammed (Sør Rondane for instance), but also where a subglacial continuation of this mountain chain is visible (Shirase Glacier). In the first case (Asuka flowline) the damming effect is observed by the marked concavity in the ice-surface topography forming an ice fall (Fig. 8, upper panel) and the reduced surface velocities at the bottom of the ice fall (compressed flow), while in the latter case (Shirase flowline) none of these are observed. The lag correlation analysis in particular reveals something more: in the case of the Asuka flowline experiments, the time lagged response of the ice sheet is positive along the whole flowline when an isotherm ice sheet is considered (ISOTHERM). However, a marked differentiation is observed when full thermo-mechanical coupling is considered (T-COUPLING). Since most of the ice deformation is concentrated in the lower (basal) layers of the ice sheet, basal temperature controls to a large extent the flow characteristics of the ice sheet. For both flowlines, cold basal temperatures are found in the presence of subglacial mountains (Figs. 7 and 8, lower panel), where a small ice thickness and a high surface elevation imply a faster advection of cold ice towards the base of the ice sheet.

While both lag-correlation and range analysis clearly show an aberrant ice-sheet behavior related to the presence of subglacial mountains, the fractal analysis only accounts for the effect of coastal high frequency oscillations caused by basal sliding. The fractal dimension of the ice-sheet response is lower than the dimension of the input signal, but increases towards the coast, hence the ice-sheet response is smoother in

Table IV: *Relative magnitude of $\overline{\sigma'_{xx}}$: τ_d : D at several distances upstream from the grounding line for the reference and the enhanced sliding experiment. See text for more details.*

km	reference	sliding
0	20:2:1	10:1:1
5	15:5:1	
10	10:5:1	25:3:1
20	5:5:1	10:5:1
50	2:5:1	10:10:1

the interior than in the coastal area.

4.2 High-resolution modelling: focus on the grounding zone

Can we capture grounding-line ice dynamics with the model, and if so at what resolution does the calculation of the total stress field become important? An estimate of the relative importance of all stresses near the grounding line can be obtained by integrating Eq. 5 over the vertical so that it takes the form $\sigma_{xz}(b) = \tau_d + D$, where D includes the effect of the longitudinal stress gradient and the vertical resistive stress (Van der Veen, 1985). The relative magnitude of the stress components $\overline{\sigma'_{xx}}$: τ_d : D is listed in Table IV for both the standard and the enhanced sliding experiment and emphasizes the importance of all stress components over a horizontal distance of several times the ice thickness upstream from the grounding line. This distance is at least 20 km for the standard experiment and more than 50 km for the enhanced sliding experiment. So, at least at a grid size of 5 km for moderate sliding and at a grid size of 10 km for pronounced sliding the total stress field should be taken into account. The transition zone can be defined as the area where the flow deviates from the ice-sheet and the ice-shelf flow. Upstream, this zone extends to the point where the velocity and its gradient start to increase. Downstream, this zone ends where the gradients decrease (Herterich, 1987). For the standard experiment, this zone extends approximately 50 km upstream from the grounding line and is smoothed out to a larger extent in the enhanced sliding experiment.

Compared to satellite observations on Shirase Glacier the velocities obtained with the model in the ice-stream area – even for the enhanced sliding case – are much lower than those observed at present, which are of the order of 1500–2000 m a⁻¹. Using the

above described model parameters it is possible to simulate the present surface profile and observed velocities of most of the ice sheet in the Shirase drainage area, with exception of the downstream area. Furthermore, the tuning parameter m is considered low compared to other modelling studies of the Antarctic ice sheet (e.g. Huybrechts, 1992), and is supposed to be of the order of 5.0 - 10.0. Applying those values to Shirase drainage basin results in a steady state ice sheet which is not in accordance with the present observations, not even the stream area. This may imply that (i) the ice properties in this area differ from other areas of the East-Antarctic ice sheet, that (ii) the model is not capable of simulating the complex flow pattern in this area – even though the divergence - convergence of the ice flow is taken into account, or that (iii) the present ice sheet in Shirase drainage basin is not at all in steady state. The last explanation is plausible, as field observations in the downstream area of Shirase drainage basin report considerable thinning rates of the ice sheet surface, up to 1 m a^{-1} . A possible mechanism that explains a large thinning rate is given by Pattyn (1996) which also gives rise to high velocities in the stream area. The relatively low value of m' is explained by the fact that Shirase Glacier experiences a considerable lateral drag in the stream area.

Nevertheless, the purpose of these experiments is to evaluate the impact of model resolution on ice dynamics near the grounding line and to validate the importance of all stress components at higher model resolutions, for which a detailed topographic dataset is necessary. The analysis demonstrates that at a low resolution (i.e. grid size of 20 to 40 km) the grounding zone is smaller than the grid size. At higher resolutions, the force balance demonstrates that the size of the grounding zone is larger than the grid size, and hence all stress components should be considered. From the geometry of the ice sheet it is apparent that at higher resolutions (5 km grid size) the surface profile near the grounding line flattens (concavity) which demonstrates the transition between the ice-sheet and the ice-shelf flow.

The major difference between the ICE2D- and the SIA-model – upstream of the grounding zone – can be addressed to the use of the basal shear stress in the basal sliding law. In the ICE2D-model the basal shear stress deviates up to 20% from the driving stress in the upstream area, which influences the basal sliding considerable. Finally, the experiments demonstrate that σ'_{xx} varies considerably with depth in the downstream area due to the thermo-mechanical coupling of the ice flow. Future experiments will focus on the transient state of ice sheets and ice streams with the ICE2D-model, as the response of the grounding-line dynamics to changing environmental conditions might be different at high resolutions compared to the SIA-model.

4.3 Shirase Glacier dynamics inferred from ERS-SAR interferometry

We were capable of inferring the surface velocity field of Shirase Glacier, a fast-flowing East-Antarctic outlet glacier, from ERS Synthetic Aperture Radar (SAR) images, obtained from the ESA Tandem Mission. This velocity field was determined with a *coherence tracking* algorithm, since conventional interferometric SAR analysis was not capable of producing a high-resolution velocity field. The *coherence tracking* technique tries to match small image kernels of two complex SAR images by maximization of the local coherence. This technique differs from speckle tracking by using the phase information instead of the coherent speckle information in the amplitude images, and by producing a *tracked* interferogram as well as a *tracked* coherence image.

Surface strain rates were calculated based on these velocity estimates. A large-scale vertically-integrated force budget then allowed for the determination of the major stress components (basal drag, lateral drag and the longitudinal stress gradient opposing the driving stress) in the floating ice tongue, near the grounding line and on the inland slope. Results showed that for the whole glacier system, lateral drag is an important factor in reducing the basal drag. Longitudinal stress gradients, however, have a limited effect and are confined to a small area of a few kilometers in length near the grounding line, even though longitudinal stresses are dominant over the whole grounding zone and inland slope region. Such a situation is in contrast with the ice-dynamic conditions in the transition zone between an ice sheet and an ice shelf, where not only longitudinal stress gradients have a limited effect, but where longitudinal stress, lateral shear and basal sliding are unimportant as well (Mayer and Huybrechts, 1999). Although Shirase Glacier is characterized by high basal velocities (more than 80% of the total velocity is due to basal sliding), this glacier can be clearly distinguished from an ice stream by a large driving stress and basal drag in the grounded part of the transition zone.

A comparison is made with a balance-flux distribution of the Antarctic ice sheet (Huybrechts *et al.*, 2000) and calving fluxes determined by Fujii (1981). This confirms a thinning of the ice sheet in the downstream area, albeit less important than previous studies by Mae and Naruse (1978), Nishio *et al.* (1989), and Toh and Shibuya (1992) suggest, and might indicate that the ice sheet in this area has reached a more stable condition. An analysis of ERS altimeter data for the period 1992–1996 (Wingham *et al.*, 1998) also suggests a moderate thinning in Shirase drainage basin. However, large data gaps in the downstream area, which are due to tape-recorder limitations, prevented a more accurate assessment of the imbalance in this region. Pattyn (1999) tried to elucidate the origin of the presumed thinning in the downstream area of the Shirase drainage basin using a thermo-mechanical numerical ice-sheet model. Re-

sults showed that an imbalance could result from a cyclic behaviour of local growing and shrinking of the ice sheet due to an interaction between the ice-sheet temperature field and its basal conditions, and suggest that an increase in imbalance (thinning) is due to an increase in basal velocity. As the present force budget calculations show that more than 80% of the horizontal velocity is due to basal sliding, an important thinning might not be excluded.

Finally, in order to balance the mass flux between the grounding line and the calving front, an important basal melting rate beneath the floating tongue of 11.5 m a^{-1} should be accounted for. However, we lack at present direct evidence confirming such high melting rates underneath the ice tongue. Future field research in this downstream area of Shirase Glacier should shed a light on this.

5 CONCLUSIONS

The East-Antarctic ice sheet is primarily drained by large outlet glaciers which play a decisive role in the dynamic behaviour of the ice sheet with changing climate. Monitoring of these outlet glaciers is one of the prime objectives of the glaciological community. The knowledge of the ice dynamics of these glaciers is necessary for interpreting ice cores, especially when they are not drilled at a major ice divide, but within their drainage area, as is the case with the future EPICA–DML drilling site. However, a significant amount of information – both glacial-geologic and ice dynamic – stems from those parts of the ice sheet which reacts differently to the climatic signal (such as the outlet glaciers, the local glaciers and the ice sheet in mountain areas). Unraveling the complex behaviour is the keystone for understanding the dynamics of the ice cap in response to the climatic signal.

In view of these needs we developed a high-resolution second-order numerical ice-sheet model with full thermo-mechanical coupling, and capable of simulating the ice-sheet response to the climatic signal. Numerical model experiments were carried out along several flowlines in Dronning Maud Land, one flowline passing through the central part of a coastal mountain range (Sør Rondane), one along a major outlet glacier (Shirase Glacier), and one in the area of a future deep drilling site within the EPICA project. These model experiments revealed different response patterns of the East Antarctic ice sheet to the climatic signal, strongly related to subglacial conditions, such as the presence of subglacial mountain ranges. A similar differentiation in ice-sheet response is also observed in the field, such as the *dynamic* ice sheet in the downstream part of the Shirase drainage basin and the *stable* ice sheet in the nearby Sør Rondane Mountains. Experiments along a flowline in western Dronning Maud land gave an idea of the basic ice-dynamical features of the drainage area in the vicinity of the future EPICA–DML drilling site and the ice-stream dynamics in the Jutulstraumen area.

A more profound study on the ice-dynamical behaviour near the grounding line of fast-flowing outlet glaciers showed the importance of longitudinal stresses at the ice-sheet/ice-shelf interface at different grid sizes, and the importance of basal drag vs driving stress in basal sliding laws. When sliding becomes dominant, this transition zone considerably widens. Furthermore, the longitudinal stress deviator is found to vary considerably with depth due to the thermo-mechanical coupling.

Finally, interferometric processing of ERS Synthetic Aperture Radar images led to the determination of the surface velocity field of Shirase Glacier. A large-scale vertically-integrated force budget calculation then allowed for the determination of the major

stress components in the floating ice tongue, near the grounding line and on the inland slope. In the grounded part, more than 80% of the total velocity seems due to basal sliding. A comparison with a balance-flux distribution of the Antarctic ice sheet (Huybrechts *et al.*, 2000) suggests a thinning of the ice sheet in the downstream area of the Shirase Glacier drainage basin as well as a high sub-ice tongue melting rate.

Acknowledgments

This report forms a contribution to the Belgian Research Programme on the Antarctic (Federal Office for Scientific, Technical and Cultural Affairs), contract A4/DD/E03. The interferometric processing was carried out by Dr. D. Derauw from the Centre Spatial de Liège (CSL), Université de Liège (ESA–ERS project ESA.AOT.B03). Part of the research was carried out at the National Institute of Polar Research (NIPR), Tokyo, Japan and in part supported by the Japan Society for the Promotion of Science (JSPS) The authors are indebted to Dr. J. Bamber for supplying the surface elevation data set, Dr. P. Huybrechts for supplying the balance flux data, Dr. U. Nixdorf and Dr. D. Steinhage at AWI for providing basal topographic data along the EPICA transect, and Prof. Y. Fujii and Prof. R. Naruse for helpful discussions on the dynamical behaviour of the ice sheet in Shirase drainage basin.

REFERENCES

- Alley, R.B. 1989. Water-pressure coupling of sliding and bed deformation: I. water system. *J. Glaciol.*, 35(119): 108–118.
- Bamber, J.L. and Bindschadler, R.A. 1997. An improved elevation data set for climate and ice sheet modelling: Validation with satellite imagery. *Ann. Glaciol.*, 25: 439–444.
- Budd, W.F. and Jenssen, D. 1987. Numerical modelling of the large-scale basal water flux under the West Antarctic ice sheet. In Van der Veen, C.J. and Oerlemans, J. (Eds.), *Dynamics of the West Antarctic Ice Sheet*. Dordrecht, Kluwer Academic Publishers, 293–320.
- Dahl-Jensen, D. 1989. Steady thermomechanical flow along two-dimensional flow lines in large grounded ice sheets. *J. Geophys. Res.*, 94(B8): 12,355–10,362.
- Derauw, D. 1999. Phasimétrie par Radar à Synthèse d'Ouverture: Théorie et Applications. PhD. Thesis, Université de Liège.
- Feder, J. 1988. *Fractals*. Plenum Press (New York).
- Fluegelman, R. H. and Snow, R. S. 1989. Fractal analysis of long-range paleoclimatic data: Oxygen isotope record of Pacific Core V28-239. *Pure and Applied Geophysics (PAGEOPH)*, 131(1/2): 307–313.
- Fujii, Y. 1981. Aerophotographic interpretation of surface features and estimation of ice discharge at the outlet of the Shirase Drainage Basin, Antarctica. *Nankyoku Shiryô (Antarct. Rec.)*, 72: 1–15.
- Giovinetto, M.B. and Bentley, C.R. 1985. Surface balance in ice drainage systems of Antarctica. *Antarct. J. U.S.*, 20(4): 6–13.
- Gray, L., Mattar, K., and Vachon, P. 1998. InSAR results from the RADARSAT Antarctic mapping mission: Estimation of glacier motion using a simple registration procedure. In *Int. Geoscience and Remote Sensing Symp. IGARSS'98*, 6-10 July 1998, Seattle, Washington, USA, 1638–1640.
- Herterich, K. 1987. On the flow within the transition zone between ice sheet and ice shelf. In Van der Veen, C.J. and Oerlemans, J. (Eds.), *Dynamics of the West Antarctic ice sheet*. Dordrecht, Kluwer Academic Publishers, 185–202.
- Hindmarsh, R.C.A. and Payne, A.J. 1996. Time-step limits for stable solutions of the ice-sheet equation. *Ann. Glaciol.*, 23: 74–85.

- Hooke, R.LeB. 1981. Flow law for polycrystalline ice in glaciers: Comparison of theoretical predictions, laboratory data, and field measurements. *Rev. Geophys.*, 19(4): 664–672.
- Høydal, Ø.A. 1996. A force-balance study of ice flow and basal conditions of Jutulstraumen, Antarctica. *J. Glaciol.*, 42(142): 413–425.
- Huybrechts, P. and Oerlemans, J. 1988. Evolution of the East Antarctic ice sheet: a numerical study of thermo-mechanical response patterns with changing climate. *Ann. Glaciol.*, 11: 52–59.
- Huybrechts, P., Steinhage, D., Wilhelms, F., and Bamber, J. 2000. Balance velocities and measured properties of the Antarctic ice sheet from a new compilation of gridded data for modelling. *Ann. Glaciol.*, 30: 52–60.
- Huybrechts, P. 1992. The Antarctic ice sheet and environmental change: a three-dimensional modelling study. *Ber. Polarforsch.*, 99: 1–241.
- Huybrechts, P. 1993. Glaciological modelling of the Late Cenozoic East Antarctic ice sheet: Stability or dynamism? *Geografiska Annaler*, 75A(4): 221–238.
- Jenkins, A., Vaughan, D.G., Jacobs, S.S., Hellmer, H.H., and Keys, J.R. 1997. Glaciological and oceanographic evidence of high melt rates beneath Pine Island Glacier, West Antarctica. *J. Glaciol.*, 43(143): 114–121.
- Jouzel, J., Barkov, N.I., Barnola, J.M., Bender, M., Chappellaz, J., Genthon, C., Kotlyakov, V.M., Lipenkov, V., Lorius, C., Petit, J.R., Raynaud, D., Raisbeck, G., Ritz, C., Sowers, T., Stievenard, M., Yiou, F., and Yiou, P. 1993. Extending the Vostok ice-core record of palaeoclimate to the penultimate glacial period. *Nature*, 364(6436): 407–411.
- Just, D. and Bamler, R. 1994. Phase statistics of interferograms with application to synthetic aperture radar. *Applied Optics*, 33: 4361–4368.
- Kamiyama, K., Furukawa, T., Maeno, H., Kishi, T., and Kanao, M. 1994. Glaciological data collected by the 33rd Japanese Antarctic Research Expedition in 1992. *JARE Data Reports*, 194: 1–67.
- Kim, K.T., Jezek, K.C., and Sohn, H.G. 2001. Ice shelf advance and retreat rates along the coast of Queen Maud Land, Antarctica. *J. Geophys. Res.*, 106(C4): 7097–7106.

- Le Muer, E. and Huybrechts, P. 1996. A comparison of different ways of dealing with isostasy: Examples from modelling the Antarctic ice sheet during the last glacial cycle. *Ann. Glaciol.*, 23: 309–317.
- Lliboutry, L. A. 1987. *Very Slow Flows of Solids*. Dordrecht, Martinus Nijhoff Publ.
- Lorius, C., Jouzel, J., Ritz, C., Merlivat, L., Barkov, N.I., Korotkevich, Y.S., and Kotlyakov, V.M. 1985. A 150,000-year climatic record from Antarctic ice. *Nature*, 316(6029): 591–596.
- Mae, S. and Naruse, R. 1978. Possible causes of ice sheet thinning in the Mizuho Plateau. *Nature*, 273: 291–292.
- Mae, S. and Yoshida, M. 1987. Airborne radio echo-sounding in Shirase Glacier Drainage Basin, Antarctica. *Ann. Glaciol.*, 9: 160–165.
- Mae, S. 1979. The basal sliding of a thinning ice sheet, Mizuho Plateau, East Antarctica. *J. Glaciol.*, 24(90): 53–61.
- Mayer, C. and Huybrechts, P. 1999. Ice-dynamic conditions across the grounding zone, Ekströmsisen, East Antarctica. *J. Glaciol.*, 45(150): 384–393.
- Moriwaki, K. and Yoshida, Y. 1983. Submarine topography of Lützow–Holm Bay, Antarctica. *Mem. Natl Inst. Polar Res., Spec. Issue*, 28: 247–258.
- Moriwaki, K., Hirakawa, K., Hayashi, M., and Iwata, S. 1992. Late Cenozoic history in the Sør Rondane Mountains, East Antarctica. In Yoshida, Y., Kaminuma, K., and Shirashi, K. (Eds.), *Recent Progress in Antarctic Earth Science*. Tokyo, Terra Sci. Publ., 661–667.
- Nakawo, M., Ageta, Y., and Yoshimura, A. 1978. Discharge of ice across the Sôya Coast. *Mem. Natl Inst. Polar Res., Spec. Issue*, 7: 235–244.
- Nishio, F. and Uratsuka, S. 1991. Subglacial water layer and grounding line derived from backscattering coefficients of radio echo sounding in the Shirase Glacier and Roi Baudouin Ice Shelf, East Antarctica. *Proc. NIPR Symp. Polar Meteorol. Glaciol.*, 4: 93–102.
- Nishio, F., Mae, S., Ohmae, H., Takahashi, S., Nakawo, M., and Kawada, K. 1989. Dynamical behavior of the ice sheet in Mizuho Plateau, East Antarctica. *Proc. NIPR Symp. Polar Meteorol. Glaciol.*, 2: 97–104.
- Nunn, J.A. and Aires, J.R. 1988. Gravity anomalies and flexure of the lithosphere at the Middle Amazon Basin, Brazil. *J. Geophys. Res.*, 93(B1): 415–428.

- Ohshima, K.I., Ono, N., and Takizawa, T. 1991. A note on water exchange under fast ice in Lützow-Holm Bay, Antarctica. *Proc. NIPR Symp. Polar Meteorol. Glaciol.*, 4: 74–80.
- Paterson, W.S.B. 1994. *The Physics of Glaciers*. Oxford, Pergamon Press, 3rd edition.
- Pattyn, F. and Declerq, H. 1995. Numerical simulation of Shirase Glacier, East Queen Maud Land, Antarctica. *Proc. NIPR Symp. Polar. Meteorol. Glaciol.*, 9: 87–109.
- Pattyn, F. and Declerq, H. 1998. Ice dynamics near Antarctic coastal mountain ranges: Implications for interpreting the glacial-geological evidence. *Ann. Glaciol.*, 27: 327–332.
- Pattyn, F. 1996. Numerical modelling of a fast-flowing outlet glacier: Experiments with different basal conditions. *Ann. Glaciol.*, 23: 237–246.
- Pattyn, F. 1999. The variability of Antarctic ice-sheet response to the climatic signal. *Ann. Glaciol.*, 29: 273–278.
- Payne, A.J. 1998. Dynamics of the Siple Coast ice streams, West Antarctica: results from a thermomechanical ice sheet model. *Geophys. Res. Letters*, 25(16): 3173–3176.
- Press, W.H., Teukolsky, S.A., Vetterling, W.T., and Flannery, B.P. 1992. *Numerical Recipes in C: The Art of Scientific Computing*. Cambridge University Press (Cambridge), 2nd edition.
- Rodriguez, E. and Martin, J.M. 1992. Theory and design of interferometric synthetic aperture radar. *IEE Proceedings – F*, 139(2): 147–159.
- Rolstad, C., Whillans, I.M., Hagen, J.O., and Isaksson, E. 2000. Large-scale force budget of an outlet glacier: Jutulstraumen, Dronning Maud Land, Antarctica. *Ann. Glaciol.*, 30: 35–41.
- Satow, K. and Kikuchi, T. 1995. The 10 m snow temperature in the ice sheet. In Higashi, A. (Ed.), *Antarctica, East Queen Maud Land, Enderby Land; Glaciological Folio*. Tokyo, Natl Inst. Polar. Res.
- Takahashi, S. and Watanabe, O. 1995. Snow accumulation (surface mass balance). In Higashi, A. (Ed.), *Antarctica, East Queen Maud Land, Enderby Land; Glaciological Folio*. Tokyo, Natl Inst. Polar. Res.
- Thomas, R.H. 1973. The creep of ice shelves: Theory. *J. Glaciol.*, 12(64): 45–53.

- Toh, H. and Shibuya, K. 1992. Thinning rate of ice sheet on Mizuho Plateau, East Antarctica, determined by GPS differential positioning. In Yoshida, Y., Kaminuma, K., and Shirashi, K. (Eds.), *Recent Progress in Antarctic Earth Science*. Tokyo, Terra Sci. Publ., 579–583.
- Van der Veen, C.J. and Whillans, I.M. 1989. Force budget: I. theory and numerical methods. *J. Glaciol.*, 35(119): 53–60.
- Van der Veen, C.J. 1985. Response of a marine ice sheet to changes at the grounding line. *Quat. Res.*, 24: 257–267.
- Van der Veen, C.J. 1987. Longitudinal stresses and basal sliding: a comparative study. In Van der Veen, C.J. and Oerlemans, J. (Eds.), *Dynamics of the West Antarctic Ice Sheet*. Dordrecht, Kluwer Academic Publishers, 223–248.
- Wada, M. and Mae, S. 1981. Airborne radio echo sounding on the Shirase Glacier and its drainage basin, East Antarctica. *Antarctic Record*, 72: 16–25.
- Weertman, J. and Birchfield, G.E. 1982. Subglacial water flow under ice streams and West Antarctic ice sheet stability. *Ann. Glaciol.*, 3: 316–320.
- Wingham, D.J., Ridout, A.J., Scharroo, R., Arthern, R.J., and Shum, C.K. 1998. Antarctic elevation change from 1992 to 1996. *Science*, 282: 456–458.

A Coordinate transformation

Due to the coordinate transformation $(x, z) \rightarrow (\xi, \zeta)$, whereby $\zeta \equiv (s - z)/H$ and $\xi \equiv x$ the function derivatives transform to (Lliboutry, 1987)

$$\frac{\partial f}{\partial x} \equiv \frac{\partial f}{\partial \xi} \frac{\partial \xi}{\partial x} + \frac{\partial f}{\partial \zeta} \frac{\partial \zeta}{\partial x} \quad (49)$$

$$\frac{\partial f}{\partial z} \equiv \frac{\partial f}{\partial \zeta} \frac{\partial \zeta}{\partial z} + \frac{\partial f}{\partial \xi} \frac{\partial \xi}{\partial z}, \quad (50)$$

where $\frac{\partial \xi}{\partial x} = 1$, $\frac{\partial \xi}{\partial z} = 0$, $\frac{\partial \zeta}{\partial x} = a$, $\frac{\partial \zeta}{\partial z} = -\frac{1}{H}$. The function-derivatives can thus be rewritten as

$$\frac{\partial f}{\partial x} \equiv \frac{\partial f}{\partial \xi} + a \frac{\partial f}{\partial \zeta} \quad (51)$$

$$\frac{\partial^2 f}{\partial x^2} \equiv \frac{\partial^2 f}{\partial \xi^2} + b \frac{\partial f}{\partial \zeta} + a^2 \frac{\partial^2 f}{\partial \zeta^2} + 2a \frac{\partial^2 f}{\partial \xi \partial \zeta} \quad (52)$$

$$\frac{\partial f}{\partial z} \equiv -\frac{1}{H} \frac{\partial f}{\partial \zeta} \quad (53)$$

$$\frac{\partial^2 f}{\partial z^2} \equiv \frac{1}{H^2} \frac{\partial^2 f}{\partial \zeta^2} \quad (54)$$

$$\frac{\partial^2 f}{\partial x \partial z} \equiv \frac{1}{H} \left(\frac{1}{H} \frac{\partial H}{\partial \xi} \frac{\partial f}{\partial \zeta} - \frac{\partial^2 f}{\partial \xi \partial \zeta} - a \frac{\partial^2 f}{\partial \zeta^2} \right), \quad (55)$$

where

$$a = \frac{1}{H} \left(\frac{\partial s}{\partial \xi} - \zeta \frac{\partial H}{\partial \xi} \right) \quad (56)$$

$$b = \frac{\partial a}{\partial \xi} + a \frac{\partial a}{\partial \zeta} = \frac{1}{H} \left(\frac{\partial^2 s}{\partial \xi^2} - \zeta \frac{\partial^2 H}{\partial \xi^2} - 3a \frac{\partial H}{\partial \xi} \right), \quad (57)$$

so that the incompressibility condition (Eq. 1) becomes

$$\frac{\partial w}{\partial \zeta} = H \left(\frac{\partial u}{\partial \xi} + a \frac{\partial u}{\partial \zeta} + \frac{u}{\omega} \frac{\partial \omega}{\partial \xi} \right). \quad (58)$$

Eq. 14 thence becomes after coordinate transformation, by making use of Eqs. 51 to 57

$$\begin{aligned}
& e \frac{2u}{\omega} \left\{ \frac{\partial \omega}{\partial \xi} \left(\frac{\partial \mu}{\partial \xi} + a \frac{\partial \mu}{\partial \zeta} - \frac{\mu}{\omega} \frac{\partial \omega}{\partial \xi} \right) + \mu \frac{\partial^2 \omega}{\partial \xi^2} \right\} + \\
\frac{\partial u}{\partial \zeta} & \left\{ 4ea \left(\frac{\partial \mu}{\partial \xi} + a \frac{\partial \mu}{\partial \zeta} \right) + \frac{1}{H^2} \frac{\partial \mu}{\partial \zeta} + e\mu \left(4b + \frac{a}{\omega} \frac{\partial \omega}{\partial \xi} \right) \right\} + \frac{\partial^2 u}{\partial \zeta^2} \mu \left(4ea^2 + \frac{1}{H^2} \right) \\
& e \frac{\partial u}{\partial \xi} \left\{ 4 \left(\frac{\partial \mu}{\partial \xi} + a \frac{\partial \mu}{\partial \zeta} \right) + \frac{2\mu}{\omega} \frac{\partial \omega}{\partial \xi} \right\} + 4e\mu \frac{\partial^2 u}{\partial \xi^2} + 8ea\mu \frac{\partial^2 u}{\partial \xi \partial \zeta} = \\
\rho g \frac{\partial s}{\partial \xi} & + \frac{e^2}{H} \left\{ \frac{\partial \mu}{\partial \zeta} \left(\frac{\partial w}{\partial \xi} + a \frac{\partial w}{\partial \zeta} \right) - \mu \left(\frac{1}{H} \frac{\partial H}{\partial \xi} \frac{\partial w}{\partial \zeta} - \frac{\partial^2 w}{\partial \xi \partial \zeta} - a \frac{\partial^2 w}{\partial \zeta^2} \right) \right\} - \\
& e^2 \left(\frac{\partial R_{zz}}{\partial \xi} + a \frac{\partial R_{zz}}{\partial \zeta} \right), \quad (59)
\end{aligned}$$

where

$$R_{zz} = H \frac{\partial \phi}{\partial \xi} + \phi \frac{\partial H}{\partial \xi} + 2aH\mu \dot{\epsilon}_{xz} \quad (60)$$

$$\phi = 2 \int_0^{\zeta} \mu \dot{\epsilon}_{xz} d\zeta. \quad (61)$$

The strain-rates are then re-written as

$$\dot{\epsilon}_{xx} = e \left(\frac{\partial u}{\partial \xi} + a \frac{\partial u}{\partial \zeta} \right) \quad (62)$$

$$\dot{\epsilon}_{yy} = e \frac{u}{\omega} \frac{\partial \omega}{\partial \xi} \quad (63)$$

$$\dot{\epsilon}_{xz} = \frac{1}{2} \left(e^2 a H (\dot{\epsilon}_{xx} + \dot{\epsilon}_{yy}) - \frac{1}{H} \frac{\partial u}{\partial \zeta} + e^2 \frac{\partial w}{\partial \xi} \right). \quad (64)$$

Eq. 59 can be decomposed further by replacing the terms involving $\frac{\partial w}{\partial \zeta}$ with the incompressibility condition of Eq. 58. Rearranging terms then leads to

$$\begin{aligned}
& \frac{u}{\omega} \left\{ \frac{\partial \omega}{\partial \xi} \left[2e \frac{\partial \mu}{\partial \xi} + \left(a \frac{\partial \mu}{\partial \zeta} - \frac{\mu}{\omega} \frac{\partial \omega}{\partial \xi} \right) (2e - e^2) \right] + \mu \frac{\partial^2 \omega}{\partial \xi^2} (2e - e^2) \right\} + \\
\frac{\partial u}{\partial \zeta} & \left\{ 4ea \frac{\partial \mu}{\partial \xi} + \frac{\partial \mu}{\partial \zeta} \left[\frac{1}{H^2} + a^2 (4e - e^2) \right] + \mu b (4e - e^2) + \frac{a\mu}{\omega} \frac{\partial \omega}{\partial \xi} (2e - e^2) \right\} + \\
\frac{\partial u}{\partial \xi} & \left\{ 4e \frac{\partial \mu}{\partial \xi} + a \frac{\partial \mu}{\partial \zeta} (4e - e^2) + \frac{\mu}{\omega} \frac{\partial \omega}{\partial \xi} (2e - e^2) \right\} + \mu \frac{\partial^2 u}{\partial \xi^2} (4e - e^2) + \\
& \mu \frac{\partial^2 u}{\partial \zeta^2} \left\{ \frac{1}{H^2} + a^2 (4e - e^2) \right\} + 2a\mu \frac{\partial^2 u}{\partial \xi \partial \zeta} (4e - e^2) = \\
\rho g \frac{\partial s}{\partial \xi} & + \frac{e^2}{H} \frac{\partial \mu}{\partial \zeta} \frac{\partial w}{\partial \xi} - e^2 \left(\frac{\partial R_{zz}}{\partial \xi} + a \frac{\partial R_{zz}}{\partial \zeta} \right). \quad (65)
\end{aligned}$$

Similarly, the upper boundary condition (Eq. 20) is then transformed to

$$\begin{aligned} \frac{u}{\omega} \frac{\partial \omega}{\partial \xi} \left(2e \frac{\partial s}{\partial \xi} + e^2 acH \right) + \frac{\partial u}{\partial \xi} \left(4e \frac{\partial s}{\partial \xi} + e^2 acH \right) + \\ \frac{\partial u}{\partial \zeta} \left(4ea \frac{\partial s}{\partial \xi} + c \left(e^2 a^2 H - \frac{1}{H} \right) \right) = e^2 c \frac{\partial w}{\partial \xi}, \end{aligned} \quad (66)$$

where $c = e^2 \left(\frac{\partial s}{\partial x} \right)^2 - 1$. The thermodynamic equation (Eq. 16) after transformation becomes

$$\begin{aligned} \frac{\partial T}{\partial t} + \frac{\partial T}{\partial \zeta} \left(\frac{\partial s}{\partial t} - \zeta \frac{\partial H}{\partial t} + ua - \frac{w}{H} - \frac{k}{\rho c_p} \left(b + \frac{a}{\omega} \frac{\partial \omega}{\partial \xi} \right) \right) - \\ \frac{\partial^2 T}{\partial \zeta^2} \left(a^2 + \frac{1}{H^2} \right) \frac{k}{\rho c_p} + \frac{\partial T}{\partial \xi} \left(u - \frac{k}{\rho c_p \omega} \frac{\partial \omega}{\partial \xi} \right) - \frac{\partial^2 T}{\partial \xi^2} \frac{k}{\rho c_p} - \frac{\partial^2 T}{\partial \xi \partial \zeta} \frac{2ka}{\rho c_p} = \frac{2}{\rho c_p} \dot{\epsilon} \tau. \end{aligned} \quad (67)$$

B Finite-difference approximation

Eqs. 65 to 67 are solved on an irregular grid in ξ and ζ . First- and second-order central differences approximations on an irregular grid are governed by

$$\begin{aligned} \frac{\partial f}{\partial \zeta} \Big|_{i,k} &\approx f_{i,k-1} \frac{\zeta_k - \zeta_{k+1}}{(\zeta_k - \zeta_{k-1})(\zeta_{k+1} - \zeta_{k-1})} + f_{i,k} \frac{\zeta_{k+1} - 2\zeta_k + \zeta_{k-1}}{(\zeta_k - \zeta_{k-1})(\zeta_{k+1} - \zeta_k)} + \\ &\quad f_{i,k+1} \frac{\zeta_k - \zeta_{k-1}}{(\zeta_{k+1} - \zeta_k)(\zeta_{k+1} - \zeta_{k-1})} \\ \frac{\partial^2 f}{\partial \zeta^2} \Big|_{i,k} &\approx f_{i,k-1} \frac{2}{(\zeta_k - \zeta_{k-1})(\zeta_{k+1} - \zeta_{k-1})} + f_{i,k} \frac{-2}{(\zeta_{k+1} - \zeta_k)(\zeta_k - \zeta_{k-1})} + \\ &\quad f_{i,k+1} \frac{2}{(\zeta_{k+1} - \zeta_k)(\zeta_{k+1} - \zeta_{k-1})}. \end{aligned} \quad (68)$$

The horizontal gradients $\frac{\partial f}{\partial \xi}$ and $\frac{\partial^2 f}{\partial \xi^2}$ are obtained from Eq. 68 by substituting ζ_k by ξ_i . An expression for $\frac{\partial^2 f}{\partial \xi \partial \zeta}$ is obtained by combining the finite-difference approximation of $\frac{\partial f}{\partial \xi}$ and $\frac{\partial f}{\partial \zeta}$. At the surface boundaries $i = N_\xi$ and $k = N_\zeta$, first- and second order gradients are computed using upstream differences:

$$\begin{aligned} \frac{\partial f}{\partial \zeta} \Big|_{i,k} &\approx f_{i,k-2} \frac{\zeta_k - \zeta_{k-1}}{(\zeta_{k-1} - \zeta_{k-2})(\zeta_k - \zeta_{k-2})} + f_{i,k-1} \frac{\zeta_{k-2} - \zeta_k}{(\zeta_k - \zeta_{k-1})(\zeta_{k-1} - \zeta_{k-2})} + \\ &\quad f_{i,k} \frac{2\zeta_k - \zeta_{k-1} - \zeta_{k-2}}{(\zeta_k - \zeta_{k-1})(\zeta_k - \zeta_{k-2})}. \end{aligned} \quad (69)$$

At the surface boundaries $i = 1$ and $k = 1$, downstream differences are formulated by replacing $(k - 1) \rightarrow (k + 1)$ and $(k - 2) \rightarrow (k + 2)$ in Eq. 69. With exception of the surface boundaries, central differences are used everywhere.

Research contract A4/DD/G01

ANTARCTIC SHELF-SLOPE DYNAMICS
AN INNOVATIVE GEOPHYSICAL APPROACH



M. De Batist - J.P. Henriët
Renard Centre of Marine Geology
Universiteit Gent

CONTENTS

ABSTRACT	1
GOALS, STRATEGY AND ACHIEVEMENTS	2
CHAPTER 1: Late-Glacial mass-wasting processes on the Trinity Peninsula Margin, Antarctic Peninsula	4
1. The Trinity Peninsula margin in Central Bransfield Basin	4
1.1. Geological setting and physiography	4
1.2. Seismic stratigraphy of the Central Bransfield Basin	5
2. Data and methods	6
3. Description of the data	7
3.1. The Gebra Slide	7
3.2. Seismic stratigraphy in the Gebra Slide area	13
4. Evidence for a multi-phase instability event	14
5. Age of the Gebra Slide	15
6. Possible trigger mechanisms	17
CHAPTER 2: A sub-glacial sedimentary system along the northern Antarctic Peninsula from sea-floor and sub-sea-floor evidence	20
1. Study area and data set	20
2. Sea-floor morphology	21
2.1. Inner continental shelf	21
2.2. Outer continental shelf and shelf edge	23
2.3. Continental slope and base of slope	24
2.4. Internal structure	25
3. Model of the sedimentary system	27
CHAPTER 3: Development of a new deep-tow reflection seismic acquisition system	29
1. Introduction	29
2. Description	29
2.1. The winch	32
2.2. The cable	33
2.3. The streamers	34
2.4. Transmission via optic fibres	35
3. Testing and sea trials	37
3.1. Celtic Sea (1996)	38

3.1.1. The "Touch-and-go" configuration	38
3.1.2. The "Jumbo" configuration	40
3.2. Antarctica ANTXVII/2 (2000)	43
3.2.1. Technical information	43
3.2.2. Results	45
3.3. Belgica 00/16 (2000)	47
3.4. SO-150 HYDGAS expedition (2000)	50
3.4.1. Re-design of the system	50
3.4.2. Results	51
4. Recent developments	56
OVERALL CONCLUSIONS	56
ACKNOWLEDGEMENTS	57
REFERENCES	58

ABSTRACT

We investigated a large sub-marine slide – the Gebra Slide – on the continental margin of Trinity Peninsula, Central Bransfield Basin, Antarctic Peninsula. The slide scar is clearly expressed in the bathymetry, over an area of 230 km². The associated debris-flow deposit extends over a total surface of about 280 km². The total volume of sediment involved in the mass movement is about 20 km³. The Gebra slide took place in two phases. Indirect dating, using seismic-stratigraphic criteria, suggests that both phases occurred at the transition between the last glacial period that affected the area and the present-day interglacial (between 13500 and 6500 yrs. B.P.). Large slope failures like this may be an important factor controlling slope-to-basin sediment transport in periods other than glacial maxima.

Integration of swath-bathymetry data and high-resolution seismic reflection profiles on the scale of the whole Trinity Peninsula margin has also allowed us to portray with unprecedented detail the sub-glacial sedimentary system of the Last Glacial Maximum in this part of the Antarctic Peninsula. The studied sedimentary system over extends 250 km, from about 1000 m above sea level to about 2000 m water depth. We propose a model for sub-glacial sedimentary systems during glacial periods that consists of (1) an upper ice-catchment or erosional zone on the innermost continental shelf, extending onshore; (2) a transitional erosional-depositional zone on the inner shelf with drumlins on the sea floor; (3) a depositional outer-shelf zone with mega-scale glacial lineations or "bundle structures"; and (4) a debris apron on the continental slope and base of slope formed under floating ice shelves but with debris delivery linked to grounding lines along the shelf break. The data clearly outline the dramatic shift of ice cover and depositional conditions off the northern Antarctic Peninsula between the LGM and the present day.

We also developed a new multi-functional deep-tow reflection seismic acquisition system for collecting good-quality high-resolution seismic data in Antarctic waters. The system is characterised by a modular design, including a surface seismic source, an umbilical cable, a winch with slip-ring units, a MC or SC streamer sub- or deep-tow streamer, a streamer-depth monitor and a deep-water digital acquisition system. The system can be operated in various different configurations: e.g. the sub-tow profiling mode, the full deep-tow profiling mode, the "Jumbo" profiling mode using two receivers, and the "touch-and-go mode including stationary measurements on the sea floor. The system has been successfully deployed in the Antarctic and in the northeastern Pacific. The system remains under continuous development and new applications are currently being implemented and tested.

GOALS, STRATEGY AND ACHIEVEMENTS

The project was conceived with three main project goals in mind:

1. Analysing the various depositional and erosional processes controlling Antarctic shelf-to-slope sediment transport.
2. Further unravelling the glacial record contained in Antarctica's margin sediments, and using this record to contribute to a reconstruction of the glacial history of Antarctica.
3. Developing an innovative geophysical methodology for obtaining good-quality, high-resolution seismic records of Antarctic margin deposits.

In order to achieve the above-defined project goals and to fulfil the project tasks, the following research strategies and methodological approaches were adopted:

1. To acquire, process and interpret new grids of reflection seismic profiles and multi-beam bathymetry data from the shelf and slope domains along various parts of the Antarctic continental margin, especially in areas with well-developed trough-mouth fan systems, and/or affected by large-scale gravitational instabilities.
2. To remain actively involved in the Weddell Sea ODP drilling proposal, either by following-up the course of the proposal within the ODP system, or by participating to the actual drilling leg or to new site surveys (depending on externally imposed planning strategies and selection procedures).
3. To design a new concept of a deep-tow reflection seismic system, to analyse the potential of new sources and receivers, to develop a prototype of the new system, and to use it to acquire high-resolution reflection seismic data in Antarctic waters.

During the project, the following results have been obtained for each of the above-defined project goals:

1. *Analysis of the depositional and erosional processes controlling Antarctic shelf-to-slope sediment transport.*

Research has focussed on the Trinity Peninsula margin of central Bransfield Basin, along the Antarctic Peninsula. New grids of high-resolution reflection seismic profiles and multi-beam bathymetry data have been acquired during the GEBRAP-96 expedition (December 1996 – January 1997) and the MAGIA-99 expedition (January-February 1999) onboard of B.I.O. Hesperides. These data have been fully processed and interpreted during the project.

This data interpretation has allowed us to produce the first comprehensive description of a recent, large-scale sub-marine landslide on an Antarctic

continental margin, and to interpret its origin, cause and possible link to glacial-interglacial cyclicality. These results were obtained in the framework of an M.Sc. thesis [Stumpfe, 1998] and are part of an ongoing IWT-supported Ph.D.-study [Imbo, in preparation]. They have been submitted for publication [Imbo et al., submitted] and are here presented in **Chapter 1**.

Integration of bathymetry and seismic data has also allowed us to develop a novel “source-to-sink” depositional/erosional sedimentation model for sub-glacial sedimentary systems associated with ice streams, based on new insights in sub-ice-stream shelf morphologies. This model was submitted and accepted for publication [Canals et al., in press] and is here presented in **Chapter 2**.

2. *Unravelling the glacial record contained in Antarctica’s margin sediments.*

The main focus here has been on the follow-up of the Weddell Sea ODP drilling proposal, which included numerous re-writes and re-submissions, as well as the acquisition of additional site-survey data. In 1999, the proposal was then finally ranked as “fully ready to drill”, but due to reasons beyond our control (ie. the ship schedule of the Joides Resolution) this leg could until present not be planned.

Nevertheless, particular efforts have been made to acquire additional site-survey data in the Weddell Sea, using RCMG’s newly developed deep-tow system. Results of these activities will be included in **Chapter 3**, which reports on the R&D results with regard to the development of a new deep-tow seismic acquisition system.

3. *Development of a new deep-tow reflection seismic acquisition system.*

A lot of effort was put in the development of a new deep-tow reflection seismic acquisition system, adapted for work in Antarctic waters. Throughout the project, the system has gone through several stages of conceptual design, prototypes have been extensively field-tested, and successful deployments have been made in the Antarctic (during the ANTXVII/2 expedition on board of R/V Polarstern in the Weddell Sea) and in the northeastern Pacific (during the SO-150 HYDGAS expedition on board of the R/V Sonne). Part of the work have been done in the framework of licentiate or M.Sc. theses [Monte, 1998; Gelfort, 1998], and an overview of the system and of the results of the field tests is presented in **Chapter 3** of this report.

CHAPTER 1

LATE-GLACIAL MASS-WASTING PROCESSES ON THE TRINITY PENINSULA MARGIN, ANTARCTIC PENINSULA

Imbo, Y., De Batist, M., Canals, M., Prieto, M.J. & Baraza, J.

1. THE TRINITY PENINSULA MARGIN IN CENTRAL BRANSFIELD BASIN

1.1. Geological setting and physiography

The Bransfield Basin is a narrow, ENE-WSW elongated basin at the northern tip of the Antarctic Peninsula (Fig. 1). It is bounded by the South Shetland Islands to the north and by Trinity Peninsula to the south. To the west the basin is limited by the prolongation of the Hero Fracture Zone, and to the east by that of the Shackleton Fracture Zone.

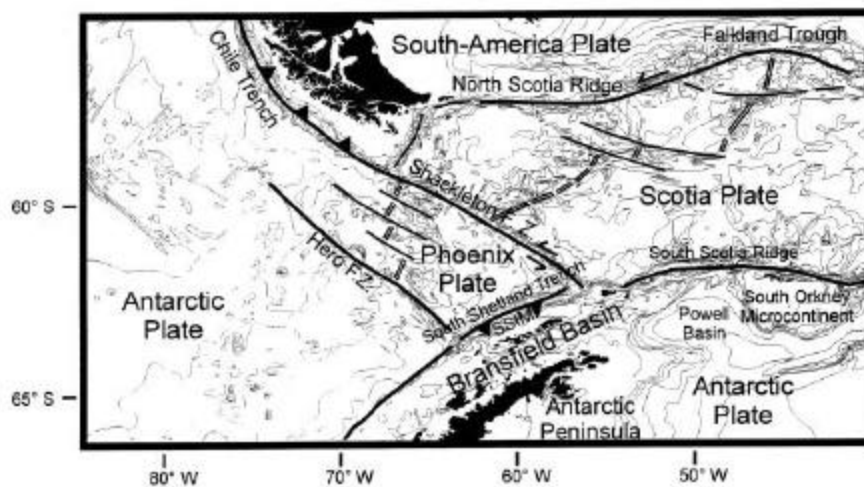


Fig. 1: Plate-tectonic setting of Bransfield Basin at the northern tip of the Antarctic Peninsula.

Structurally and morphologically, Bransfield Basin is divided into three sub-basins: the Western, Central and Eastern Bransfield Basin, which are separated by the highs of Deception Island and Bridgeman Islands respectively. Here, we will focus on the Central Bransfield Basin. The Central Bransfield Basin is about 230 km long and 125 km wide. It is an asymmetric basin, limited by a steep, rectilinear South Shetland margin in the north and a gentle, undulating Trinity Peninsula margin in the south [Gracia et al., 1996].

The Trinity Peninsula margin has a total width of 80 km and includes a continental shelf, an upper-slope terrace, a lower slope and a continental rise that extends down to the basin floor (Fig. 2) (see also Chapter 2). The continental shelf is up to 250 m

deep and incised by four large glacial troughs [Szeliga, 1990]. The troughs merge into the upper-slope terrace, which varies in depth from about 900 m in the SW to only 500 m in the NE, facing the Antarctic Sound [Szeliga, 1990]. The terrace edge forms a sinuous slope break characterized by three basinward-convex lobes that are the basinward prolongation of the main glacial troughs (Fig. 2). The upper slope is a steep (up to 20°) and essentially continuous feature locally incised by gullies [Ercilla et al., 1998]. A 20-32 km wide, gently sloping continental rise separates the lower slope from the flat basin floor [Gracia et al., 1997]. The basin floor progressively deepens and widens towards the NE. In a discontinuous line from Deception Island to Bridgeman Island six large volcanic edifices rise above the sedimented sea floor, where they depict an incipient sea-floor spreading ridge [Gracia et al., 1996]. From SW to NE, four bathymetric levels can be distinguished, separated from each other by NW-SE morphological steps [Gracia et al., 1996; 1997]. The largest and the deepest of these levels constitutes the King George Basin, 20 km wide and 50 km long, with a maximum depth of 1950 m (Fig. 2).

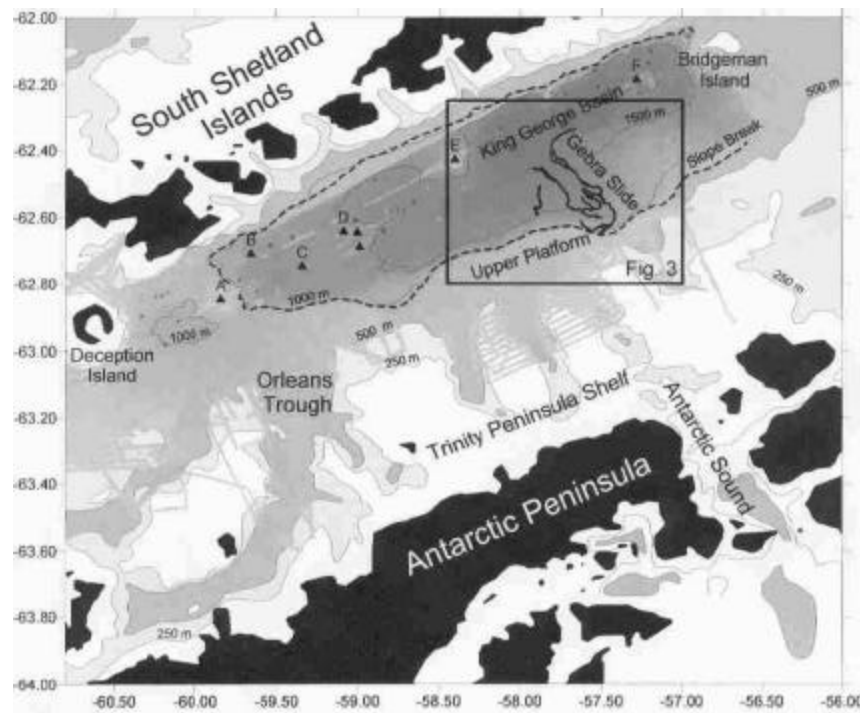


Fig. 2: Bathymetric contour map of the Central Bransfield Basin, based on multi-beam bathymetry data of the GEBRA-93, GEBRAP-96 and MAGIA-99 expeditions and published contours by Szeliga [1990]. Labels A to F represent volcanic edifices on the basin floor [after Gracia et al., 1996].

1.2. Seismic stratigraphy of the Central Bransfield Basin

Two regional sedimentary sequences overlying the basement have been identified

during previous seismic-stratigraphic studies [Gambôa and Maldonado, 1990; Jeffers and Anderson, 1990; Henriët et al., 1992; Prieto et al., 1998; 1999]. A folded and faulted lower sequence reflects extensive tectonic activity during the opening and the persisting extension of the Bransfield Basin since 4-1.3 Ma; it is hence often referred to as the “rift sequence”. The overlying “drift sequence” is characterized by only minor tectonic influences and by the presence of regional internal erosion surfaces, which find their origin in the cyclic, climatically driven advances and retreats of a grounded ice sheet. Based on these regional discontinuities, Prieto et al. [1999] distinguished 8 seismic-stratigraphic units (U1-U8), the extension of which is essentially controlled by the position of the ice sheet relative to the slope break throughout the glacial-interglacial cycles. During glacial periods, when the ice sheets reach their maximum extension far beyond the slope break, slope units (U1, U3, U5 and U7) are deposited on the Trinity Peninsula and South Shetland Islands continental margins. During “interglacial” periods, when the grounding line of the ice sheets has retreated far up the shelf, sedimentation is restricted to hemipelagic deposition over the whole basin and to deposition of turbidites at the base of the continental slope and on the basin floor. During these periods, the basin-fill units (U2, U4, U6 and U8) are deposited, primarily in the deeper parts of the basin.

2. DATA AND METHODS

The seismic data used in this study have been acquired in 1999 during the MAGIA-99 expedition on board of R/V Hesperides. This data set comprises a total of 22 high-resolution single-channel seismic profiles, with a combined length of 490 km (Fig. 3). It covers an area of 1015 km² centred on the Gebra Slide and located between 57°10' and 58°10' W and 62°20' and 62°45' S. All of the seismic data were shot with a sleeve-gun array of 4 x 0.65 l as seismic source, and a 3-channel SIG streamer of 150 m length as receiver. The data were recorded digitally with an ELICS DELPH-2 acquisition system. Post-acquisition data processing included band-pass filtering (40-150 Hz), spiking deconvolution and scaling and was conducted on a Landmark ProMax processing system. The data have a theoretical vertical resolution of 8 ms (approx. 6 m) and a penetration ranging from 200 ms TWT on the shelf to 900 ms TWT in the deeper basin.

We also included a number of seismic lines that were acquired across the deep King George Basin during the previous GEBRA-93 expedition (GEBRA-93 Lines #5 and #11) (Fig. 3). For these data, the seismic source was a 2.9 l Bolt 1500C air gun, and the reflected signals were detected with a 3-channel SIG-120 streamer. Also these data were recorded digitally with an ELICS DELPH-2 system, and data processing

(band-pass filtering, deconvolution and scaling) was carried out both on the DELPH-2 system itself and on the SSL Phoenix Vector processing system.

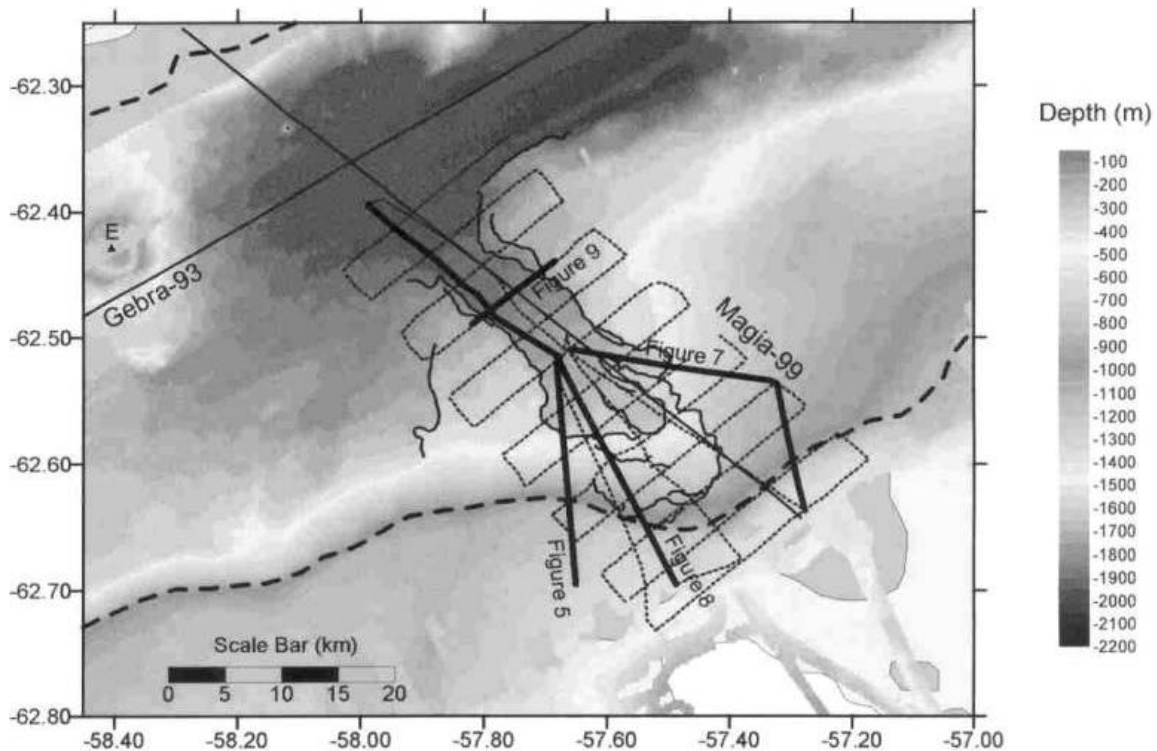


Fig. 3: Zoom of the bathymetric contour map for the Gebra Slide area, with indication of the GEBRA-93 and MAGIA-99 seismic lines used in this study.

The multi-beam bathymetry data were acquired during three successive expeditions in Bransfield Basin (GEBRA-93, GEBRAP-96, MAGIA-99), using the combined SIMRAD EM-12S/EM-1000 multi-beam system on board of R/V Hesperides. Data processing of the individual data sets was done with the Mermaid and Neptune software packages. The three data sets were merged and data extraction was performed using an Irap GST option, so that each extracted point represents the mean value of all depth points in a grid of 75 by 75 m. In this way, the bathymetry data used in this study are a synthesis of all currently available (Spanish) multi-beam bathymetric data in the Bransfield Basin.

3. DESCRIPTION OF THE DATA

3.1. The Gebra Slide

The multi-beam bathymetry data from the Central Bransfield Basin clearly reveal the presence of a major morphological anomaly on the lower, gentle slope of the

northeastern part of the Trinity Peninsula margin, situated between 1500 m and 1950 m of water depth and at about 57°40' W and 62°30' S (Fig. 4) [Canals et al., 1994; Gracia et al., 1996]. The shape, position and overall aspect of the anomaly – on bathymetry data as well as on seismic profiles – suggest that it represents a large slide scar, very similar to sub-marine slide scars observed on other glacial continental margins, such as the Storegga Slide [Bugge et al., 1987], the Trænadjupet Slide [Laberg et al., 2000] and the Andøya Slide [Laberg et al., 2000].

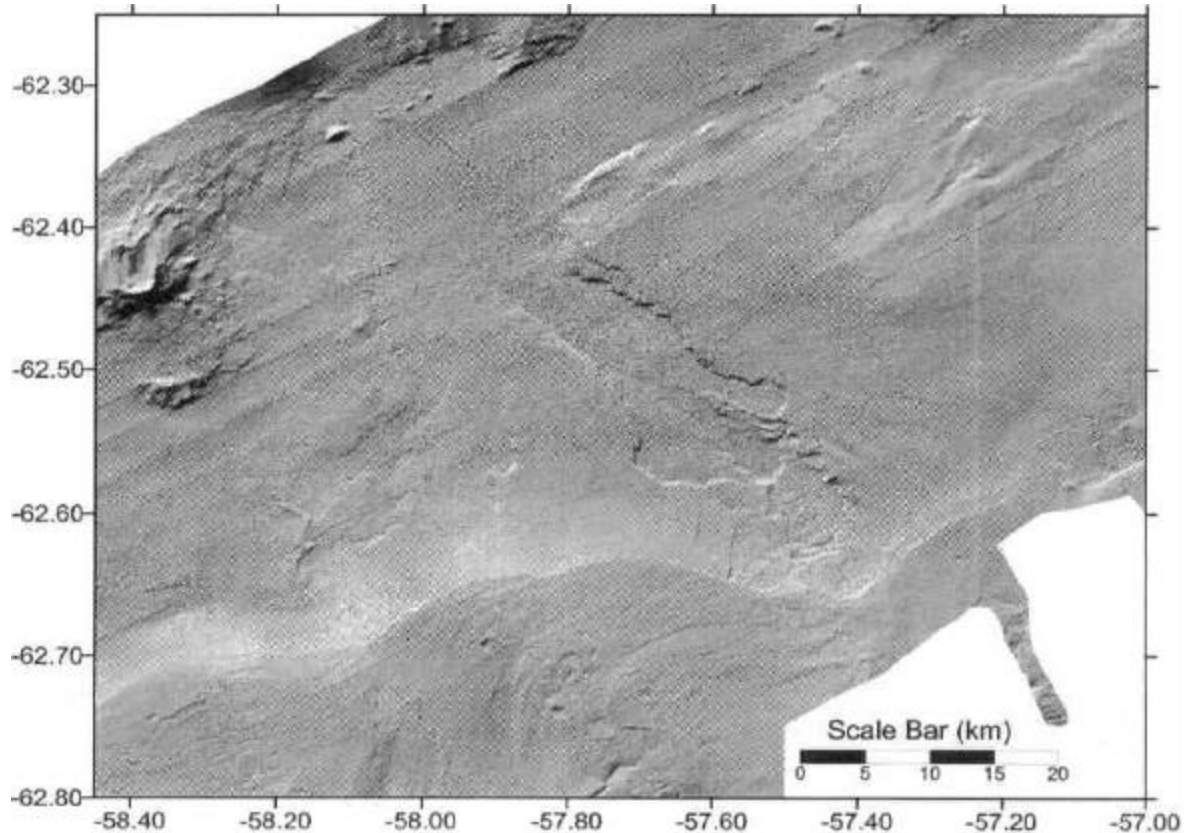


Fig. 4: Shaded-relief image of the bathymetry in the Gebra Slide area.

The Gebra Slide scar has a cauliflower-like shape with well-exposed scarps. It is about 30 km in length and 4.5 to 6.2 km wide. It has a distinct Ushape in cross section: the floor of the slide scar is flat, while the sidewalls are extremely steep with a mean gradient of 17° and a maximum incision of 230 ms TWT (about 175 m). The scar cuts into seismic-stratigraphic slope units U7, U5 and U3 (Figs. 5, 6). The head of the slide scar is formed by an amphitheatre-shaped scarp with an elevation of 130 ms TWT (about 100 m) (Fig. 5). It occurs at a constant depth of about 1500 m, and has a gradient of 16°. The entire slide scar area, bounded by these clearly defined head- and sidewalls, amounts to about 160 km².

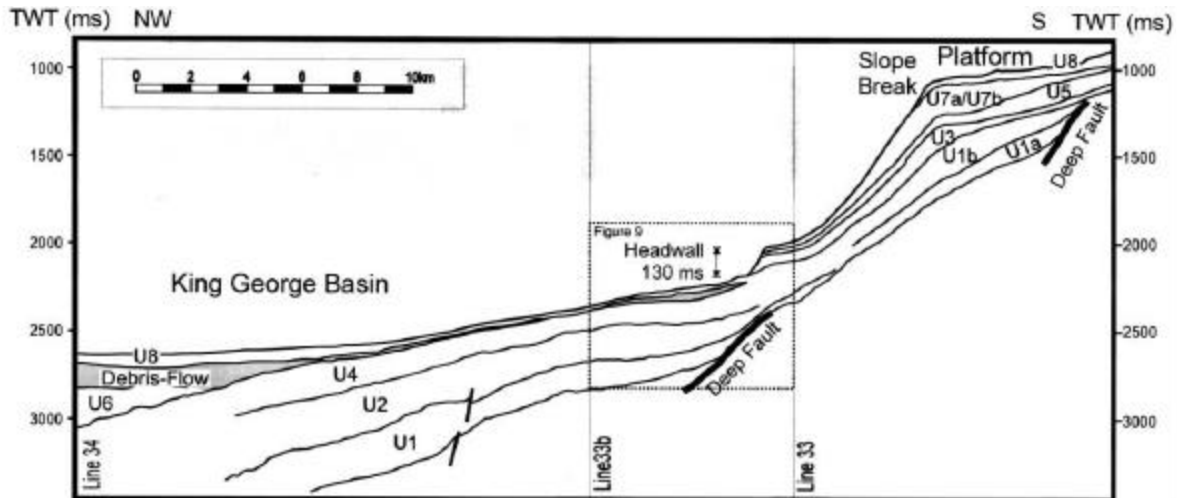


Fig. 5: Typical cross-section through Trinity Peninsula margin illustrative of the stratigraphic and structural architecture of the margin. The cross-section is based on MAGIA-99 profiles 33, 33b and 34 (for location see Fig. 3).

Further upslope from this slide scar, a second scarp is visible in water depths of 1000 to 1500 m (Fig. 4). This secondary, less well-developed scarp gradually disappears upslope towards the southwest, where it approaches but not completely reaches the slope break. The slide-scar area bounded by this secondary headwall is about 70 km², which brings the total surface affected by the Gebra Slide to 230 km².

The Gebra Slide is located at the transition between two distinct morphostructural segments of the Trinity Peninsula margin (Prieto et al., in prep.), and in between two of the basinward-convex lobes that mark the upper-slope platform edge (Fig. 4) [Prieto et al., 1999; Canals et al., in press]. To the northeast of the Gebra Slide the lower margin consists of a gentle, uniform slope with a mean gradient of about 2° and underlain by an up to 600 m thick sedimentary sequence. In the upper part of this sequence, the strata are characterized by a discontinuous wavy pattern, which resembles creep folds [Mulder and Cochonat, 1996] and may announce further failure of the Trinity Peninsula margin (Fig. 7). Southwest of the Gebra Slide, the margin changes to a slope with a steeper, exponential curvature, with a maximum gradient of about 20° (Fig. 8). Here, mass-wasting is apparent on the seismic data from a number of slid blocks on the lower slope, and on the bathymetry data from several 10-15 km long gullies incised in the slope strata. These gullies have a U shaped cross-section, and reach widths of up to 2 km and depths of up to 40 m.

At the downslope end of the Gebra Slide scar, the basin floor of the King George Basin is completely smooth and flat at a depth of 1950 m; there is no sign in the

bathymetry data of any depositional mound related to the Gebra mass-wasting event (Fig. 4). The seismic data, however, reveal the presence of a large, well-defined sedimentary unit – up to about 100 m (135 ms TWT) thick – embedded in the basin-fill unit U6, and completely covered by another 100 m of the youngest basin-fill unit U8 (Fig. 5). Its seismic facies is characterized by a reflection-free to chaotic, irregular, low-amplitude pattern, and a high-amplitude reflector often marks its base (Fig. 9).

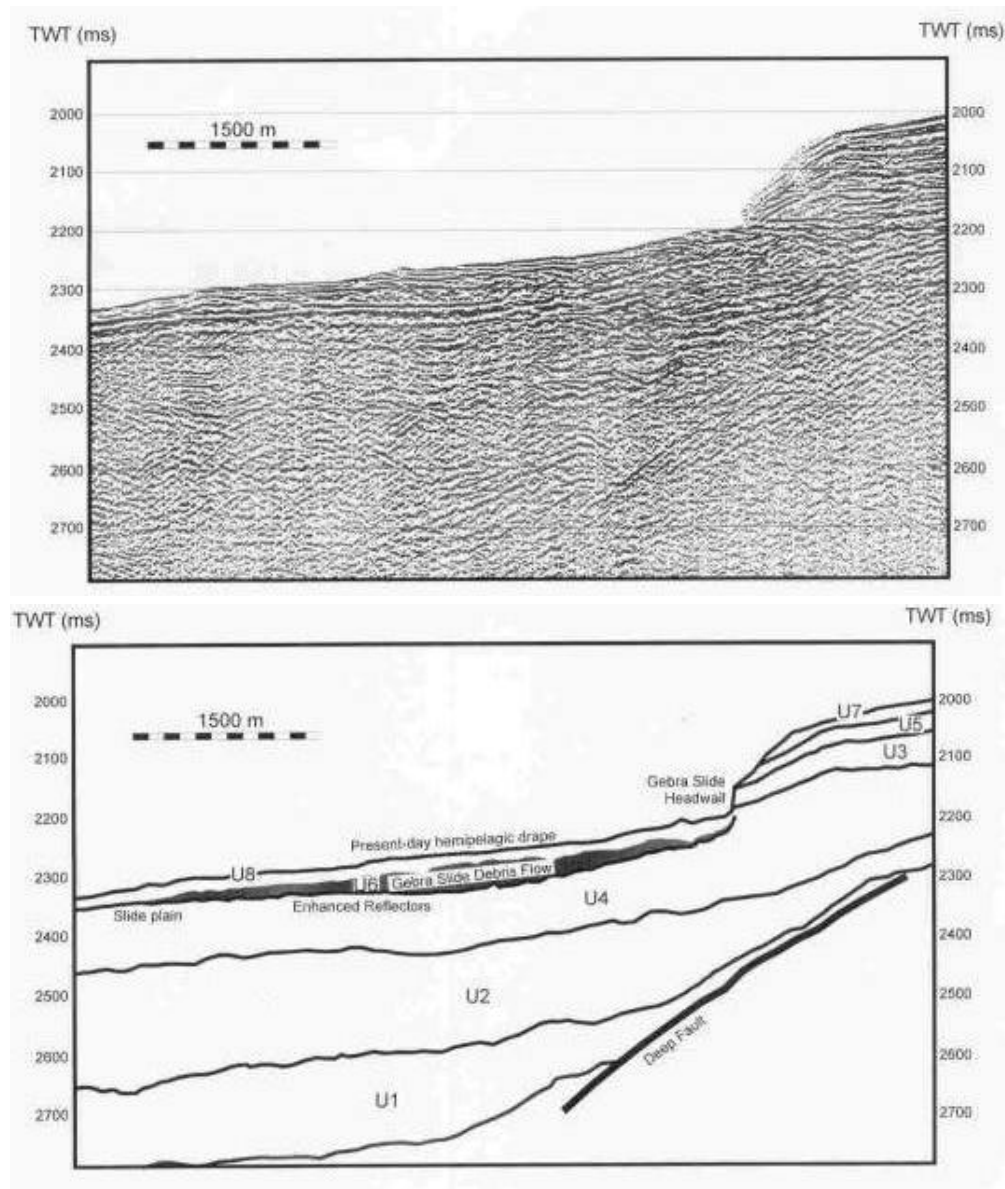


Fig. 6: Detail of MAGIA-99 profile 33b, with interpretation. For location see Fig. 3.

This facies is typical for debris-flow deposits and clearly contrasts with the horizontal-stratified, high-amplitude facies with continuous reflectors characteristic of units U8 and U6. This mostly transparent facies unit fills in the western part of the King

George Basin and pinches out against the lower slopes of volcanic edifices F in the east and D in the west, against the foot of the South Shetland Islands margin in the north and against the foot of the Trinity Peninsula margin in the south, at about 2500 ms TWT water depth near the downslope limit of the Gebra Slide scar (Fig. 10). It covers a total surface of about 280 km². Upslope from there, transverse seismic profiles MAGIA-99 #34 and MAGIA-99 #36 reveal a second small isolated lens of the debris-flow deposit, characterized by its typical chaotic seismic facies, within the confines of the main slide scar, near the main scarp at a depth of 1500 m (Fig. 10).

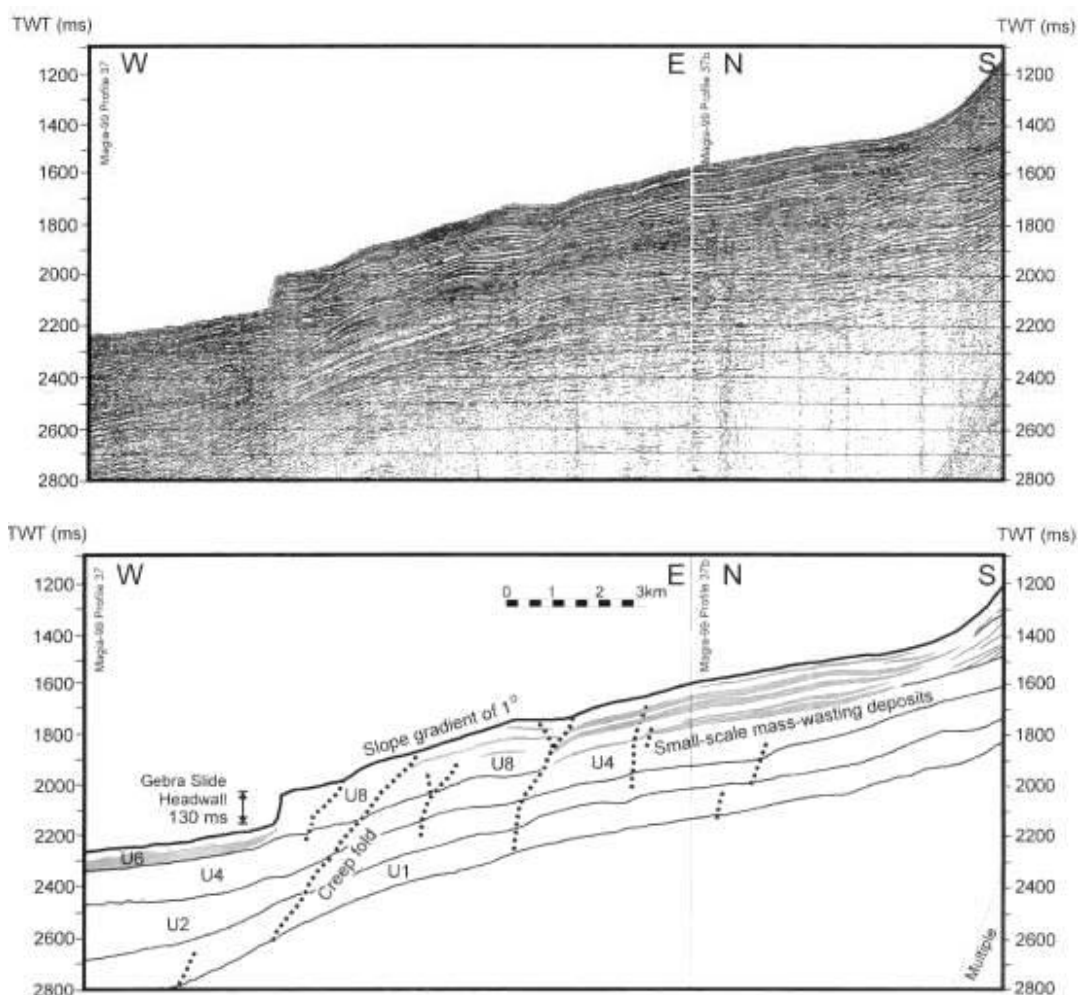


Fig. 7: Detail of MAGIA-99 profile 37 and 37b, with interpretation. For location see Fig. 3.

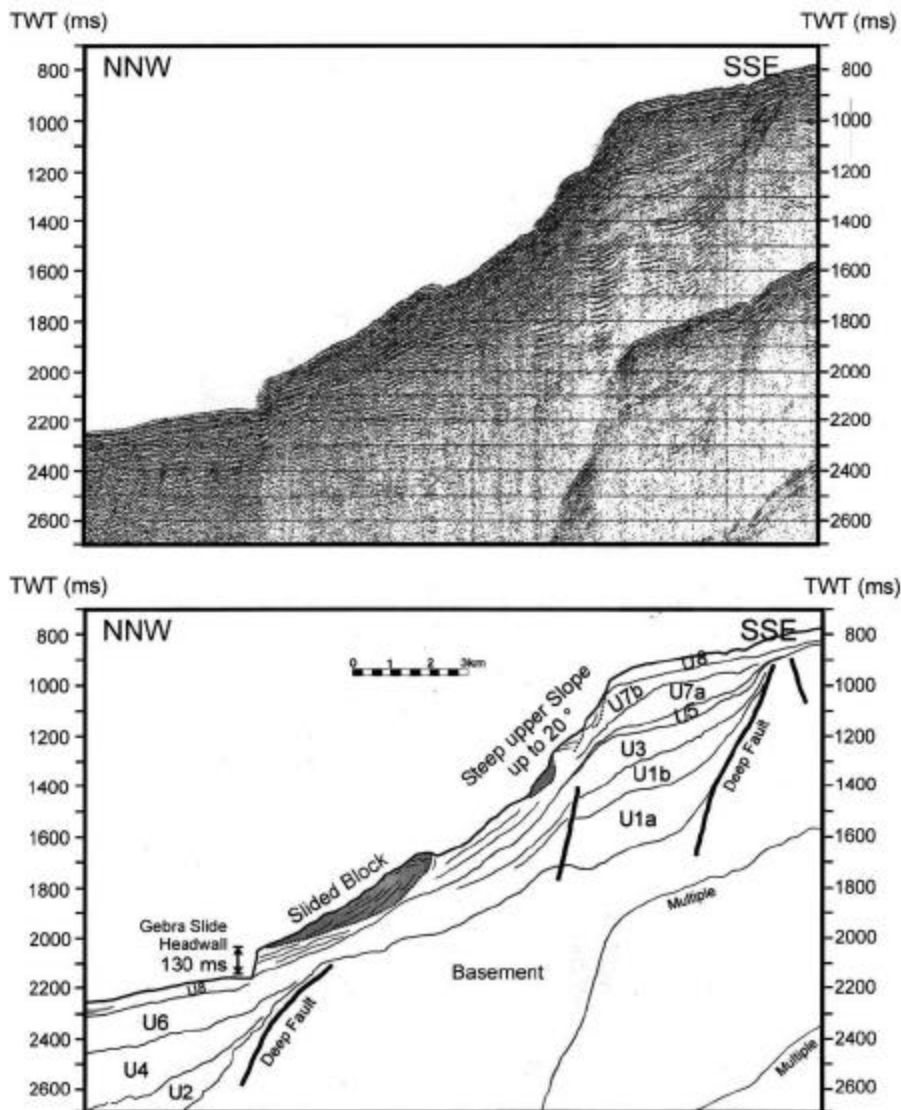


Fig. 8: Detail of MAGIA-99 profile 41, with interpretation. For location see Fig. 3.

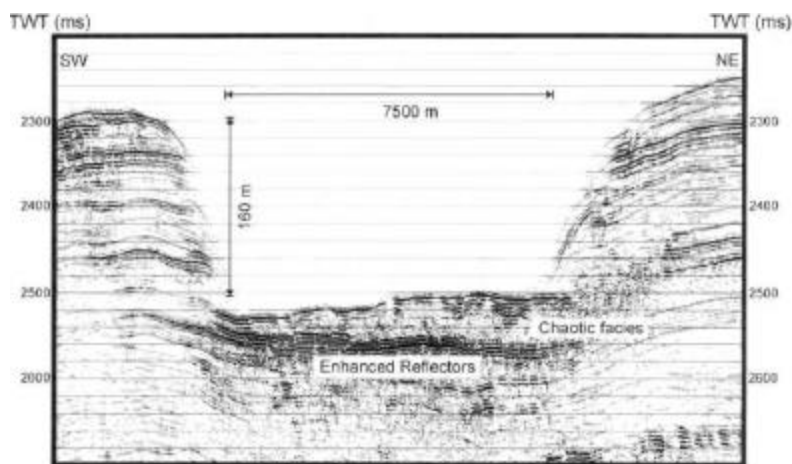


Fig. 9: Detail of MAGIA-99 profile 52. For location see Fig. 3.

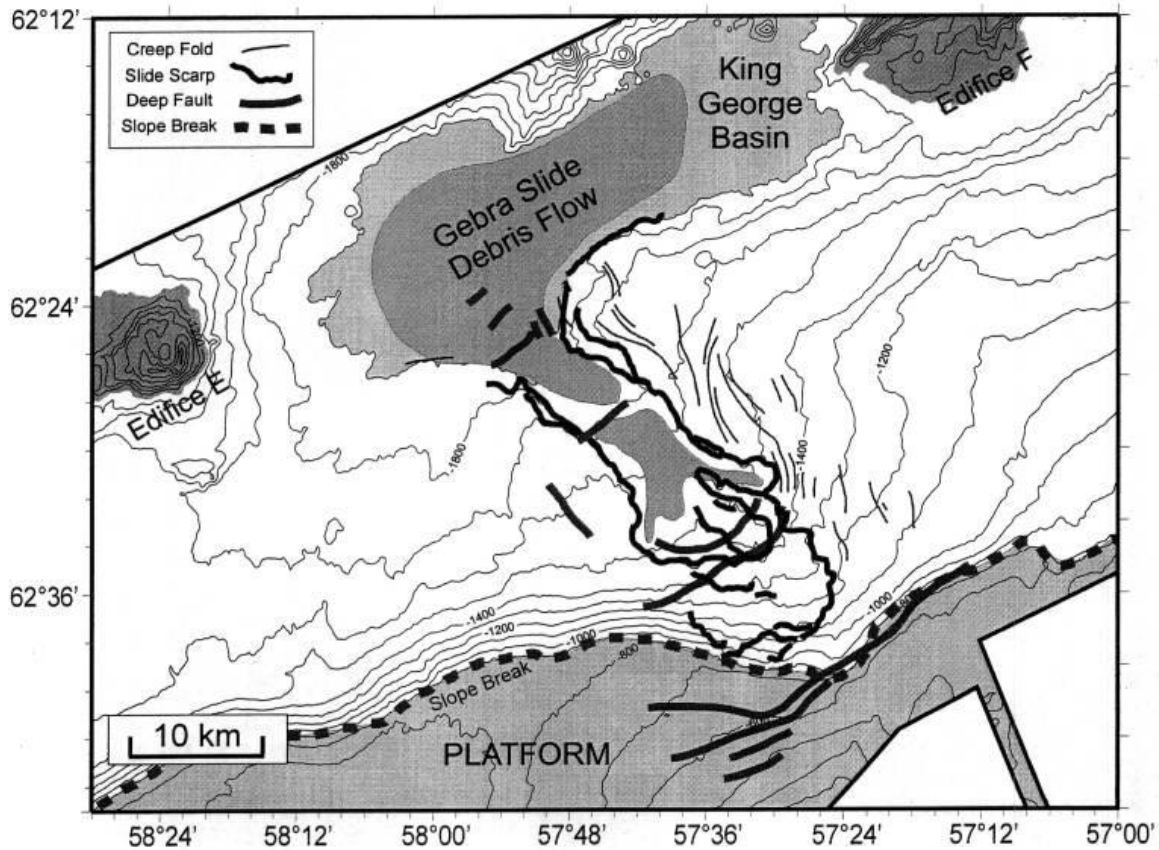


Fig. 10: Summary interpretation map of the Gebra Slide area, showing the general bathymetry, the two slide scars in the Trinity Peninsula margin and the associated buried debris-flow deposit in the King George Basin.

3.2. Seismic stratigraphy in the Gebra Slide area

The Trinity Peninsula slope and platform in the vicinity of the Gebra Slide is underlain by a thick sedimentary sequence that is composed of seismic-stratigraphic slope units U1, U3, U5 and U7, as defined by Prieto et al. [1999] (Fig. 5). Each of these units is characterized by a progradational stratified seismic facies with high-angle dipping reflections that downlap onto the underlying units [Prieto et al., 1999]. The upper boundary of these units is formed by an erosional unconformity at the upper-slope platform, which changes to a conformable surface in basinward direction. The associated depocentres of units U1, U3, U5 and U7 – i.e. the area where they have the largest preserved thickness – are located under the upper-slope platform to the northeast of the Gebra Slide scar. From there, these units pinch out both towards the continent and towards the King George Basin. Maximum thicknesses are 250 ms TWT (unit U1), 100 ms TWT (unit U3), 50 ms TWT (unit U5), 40 ms TWT (unit U7a) and 150 ms TWT (unit U7b).

Downslope from the Gebra Slide, the King George Basin is made up of seismic-stratigraphic basin-fill units U2, U4, U6 and U8 [Prieto et al., 1999]. These units are all characterized by a horizontally-stratified, high-amplitude facies with continuous reflectors. Both base and top of these units are conformable surfaces, often highlighted by a group of reflectors with even higher amplitudes. The units extend across the entire King George Basin and generally onlap against the South Shetland Islands margin and the Trinity Peninsula margin. Unit U8, however, the youngest of these basin-fill units, does not pinch out at the foot of the Trinity Peninsula margin, but is instead more or less uniformly distributed across the basin floor, the lower slope and the upper-slope platform (Fig. 5). It thus overlies basin-fill unit U6 in the basin and slope unit U7 on the slope and platform. It has an overall lens-shape, with the thickest part following the basin axis. The maximum thickness of these basin-fill units is 200-300 ms TWT (unit U2), 150 ms TWT (unit U4), 200 ms TWT (unit U6) and 130 ms TWT (unit U8).

4. EVIDENCE FOR A MULTI-PHASE INSTABILITY EVENT

From the above-presented data, it is evident that the Gebra slide scar on the Trinity Peninsula margin and the large debris-flow deposit on top of the basin-fill unit U6 downslope from the slide scar in the King George Basin, both result from the same mass-wasting event. However, there are some indications that this event might have taken place in several – at least two – phases:

- Firstly, the multi-beam bathymetry data clearly show two groups of slide scars: a main slide scar between 1500 and 2000 m, and a second, less-pronounced slide scar higher up the slope from the first one, between 1000 and 1500 m (Figs. 4, 10). We interpret the latter as being caused by a second phase of sliding, possibly as a result of headward erosion in the primary slide scar.
- Secondly, the seismic data show two separate debris-flow units (Fig. 10). The main debris-flow deposit extends across most of the King George Basin, and pinches out towards the foot of the Trinity Peninsula slope near the downslope end of the slide-scar. Upslope from there, the second, smaller and isolated debris-flow deposit is confined to the floor of the main slide scar (Fig. 10). The two debris-flow units are not attached, although they share the same basal horizon, which coincides with the base level of unit 6. We interpret them as resulting from two separate phases of mass wasting that occurred in the same glacial phase.

The hypothesis of a first massive slide event followed by a subordinate second one is also supported by a quick, rough mass-balance exercise. In a first phase, the lower slope of the Trinity Peninsula margin collapsed over an area of 160 km². The total volume of sediment that was involved in this first slide is on the order of 20 km³,

assuming an average thickness for the removed slice of 160 ms TWT (about 120 m) as suggested by our seismic data. Once moving, the slid mass probably rapidly disintegrated and evolved into a debris flow, which spread out across the flat King George Basin, over an area of 280 km². The total volume of the debris-flow deposit is about 21 km³, assuming an average thickness of 100 ms TWT (about 75 m). This implies that the main debris-flow deposit is already fully accounted for in volume by the primary slide scar and by this first phase of mass wasting. In a subsequent phase, the upper slope of the margin destabilized, presumably due to headward erosion in the primary slide scar. The total area affected by this secondary slide is only about 70 km². The resulting debris flow was channelled within the depression of the primary scar and was deposited on the flat floor of the scar on the lower slope over an area of about 35 km². Given the limited thickness of this second debris-flow unit, its volume is negligible and comparable to that of the sediment slice removed from the upper slope in the second slide.

It is not uncommon for a large-scale sub-marine slide to occur in several phases. The best-known example is probably the Storegga Slide, off the coast of Norway, for which three successive phases of destabilization have been inferred at 50-30 ka and 8-6 ka [Bugge et al., 1987]. Also the Verrill Canyon area on the Scotian Slope, Canada and successive landslides in the Canary Islands illustrate multi-phase mass-wasting processes [Masson et al., 1998; Mosher et al., 1994; Gee et al., 2001]. The Humboldt Slide, on the northern California continental margin, is interpreted as a large shear-dominated retrogressive slope failure [Gardner et al., 1999]. During the last glacial, the Svalbard-Barents Sea margin was highly instable and generated successive slope failures with a frequency varying between 95 and 170 years [Dimakis et al., 2000].

5. AGE OF THE GEBRA SLIDE

Since no deep cores are available from the Gebra slide scar or the associated debris-flow deposit - and thus no absolute dating is possible - the age of the Gebra Slide can only be derived indirectly, e.g. from seismic-stratigraphic analysis. There are some observations and lines of reasoning that can help to narrow down the potential time window:

- The seismic data show clearly that the main slide scar is cut into the distal toes of seismic-stratigraphic slope units U7, U5 and U3 (Figs. 5, 6). This implies that the slide must have taken place during or after deposition of U7, the youngest of these slope units. Following the model of Prieto et al. [1999], who attribute the formation of slope strata essentially to glacial periods (i.e. periods during which

ice sheets extend across the shelf and upper-slope platform and are grounded at the platform edge), this means that the slide must have taken place during or after the last glacial period in the area.

- The freshness of the morphology of the slide scars on the multi-beam bathymetry data indicates that the Gebra Slide has not been covered by or buried under a significant amount of post-slide slope strata, i.e. post-slide glacial-period strata. This observation implies that the slide must have taken place at the very end of or after the last glacial period.
- The seismic data also illustrate that the debris-flow deposits attributed to the Gebra Slide are totally covered by seismic-stratigraphic basin-fill unit U8, which reaches a thickness of up to about 100 m in the King George Basin (Fig. 5). According to Prieto et al. [1999], these basin-fill units are formed essentially during interglacial periods (i.e. periods during which the ice sheets have retreated far up the shelf). As the debris-flow deposits occur just below the base of unit U8, this means that the slide must have taken place at the very beginning of the last interglacial period in the area.

Our data thus indicate that the Gebra slope instability event took place around the transition between the last glacial period and the current interglacial period. According to Banfield and Anderson [1995], the ice-sheet retreated from the Central Bransfield Basin upper-slope platform at around 13500-14500 yrs BP. According to Pudsey et al. [1994], open marine sedimentation started shortly before 11000 yrs B.P. on the shelf off Anvers Island, to the southwest of Bransfield Basin. The shallower and largely sediment-free shelf cleared much later, perhaps around 6000 yrs. B.P. (Canals et al., in prep.). On our seismic data, the recentmost seismic-stratigraphic interglacial unit U8 is essentially developed on the King George basin floor (over 100 m of thickness), but it also extends, although much thinner (only about 32 m), on the slope and upper-slope terrace. The difference in thickness between the basin-floor setting and the upper-slope terrace setting is attributed to a difference in the predominant sedimentation process: mainly hemipelagites on the upper-slope terrace, and a mixture of hemipelagites and turbidites on the basin floor. Based on ¹⁴C-measurements on piston cores from the Bransfield Basin, Harden et al. [1992] calculated a hemipelagic sediment accumulation rate on a 1000-yr time scale from 0.24 cm/yr for the northwestern flank near Livingston Island to 0.49 cm/yr at a water depth of 550 m near the upper slope of the South Shetland Islands margin. Applied to our 32 m of hemipelagic interglacial deposits (and extrapolated without correction for compaction), this yields an age for the onset of the present-day interglacial sedimentation regime of about 6500-13500 yrs. B.P.

An early interglacial age (i.e. transition from glacial to interglacial period) for the Gebra slope collapse agrees with several other studies of large-scale sub-marine

slope instabilities along glaciated margins. While the build-up of the slope-prograding glacial strata is generally attributed to sustained, but relatively small-scale debris-flow activity from the ice-sheet grounding line during glacial periods [e.g. Alley et al., 1989; Aksu et al., 1992; Laberg and Vorren, 1995], the larger-scale, more catastrophic failure of these glacial strata is usually believed to occur in a later phase, after deglaciation and during the interglacial periods [Bugge et al., 1987; Bart et al., 1999; Laberg et al., 2000]. Based on analyses of maximum ice loading events for the Scotian slope, Mulder and Moran [1995] suggest that the change in ice loading (e.g. during retreat of the ice sheets) rather than high sedimentation rates, is the dominant mechanism for large-scale instability events on glacial margins.

6. POSSIBLE TRIGGER MECHANISMS

Various potential controlling factors have been proposed to explain the occurrence of large-scale slope instabilities along continental margins: (1) build-up of excess pore pressure due to high sedimentation rates; (2) loading by a static weight (i.e. the loading of a grounded ice sheet); (3) seepage of shallow methane gases or destabilisation of gas hydrates; (4) oversteepening of the margin; (5) erosion at the toe of the slope; (6) tectonic setting; and (7) earthquakes [Bugge et al., 1987; Mosher et al., 1994; Mulder and Moran, 1995; Dimakis et al., 2000]. Below, we will tentatively evaluate the potential of each of these controlling factors for having triggered the Gebra Slide.

Build-up of excess pore pressure due to high sedimentation rates. Probably the main cause of sub-marine sliding along continental margins is the build-up of excess pore pressure in fine-grained sediments as a result of rapid sedimentation. High-latitude margins are characterized by very high sedimentation rates, particularly during glacial periods. Recent studies on the Bear Island Fan (NE North Atlantic) yielded sediment accumulation rates of up to 60 cm/yr within a 5 km wide ice-proximal zone during the last glacial period [Laberg and Vorren, 1995; Dowdeswell and Siegert, 1999; Dimakis et al., 2000]. As a consequence of this extremely rapid loading, the Bear Island Fan underwent severe slope failure (note that these failures occurred during glacial times, in contrast to those of the Gebra Slide). Sedimentation rates in Bransfield Basin have most likely been much smaller, a.o. due to the more restricted, tectonically compartmentalized glacial drainage basins of Trinity Peninsula (Canals et al., in press). None of the glacial-period slope-prograding units U3, U5 and U7 reach a thickness of more than 110 ms TWT (about 90 m; unit U7). Assuming that the ice sheet was grounded at the platform edge only briefly – e.g. 3000-5000 yrs [Vorren et al., 1998] – during each of these glacial periods, we can estimate a maximum

sedimentation rate. For unit U7 this yields a maximum average glacial sediment accumulation rate of 3.1-1.9 cm/yr, which is an order of magnitude higher than the sedimentation rates during interglacial periods (0.06-0.49 cm/yr)[Harden et al., 1992], but also an order of magnitude lower than the sedimentation rates calculated for the Bear Island Fan, and therefore most likely not sufficient to build up a significant excess in pore pressure within these deposits and to generate the observed large-scale slope failure [Dimakis et al., 2000]. It is, however, not excluded that locally, e.g. in the vicinity of the grounding line at the mouth of a glacial trough and for short periods of time, sedimentation rates were temporarily higher than the above average, which could have generated high pore pressures in a thin slice of sediments. This process could easily have lead to small-scale mass wasting [Dowdeswell et al., 1998; Elverhøi et al., 1997], and could thus explain the presence of the numerous thin debris-flow-like lenses that are incorporated in the strata at the foot of the steep upper slope.

Loading/unloading by an advancing/retreating grounded ice sheet. Our data clearly show that the main Gebra Slide occurred at a water depth of 1500-2000 m, affecting only the distal toes of the glacial-period prograding-slope strata. This is far below the maximum grounding depth of the ice sheets during glacial periods. For example, Canals et al. [2000] inferred a maximum grounding depth of 900 m (present-day water depth) for a 1 km thick ice sheet during the Last Glacial Maximum in the Western Bransfield Basin, which is in agreement with earlier estimates of Banfield and Anderson [1995]. Although we are aware that ice-sheet loading on a continental shelf may induce far-field pore-pressure effects [Mulder and Moran, 1995], we believe that such loading/unloading effects should primarily have had an impact on the steeper, thicker – and thus more rapidly accumulated and inherently more instable – upper-slope deposits, closer to grounding zone.

Destabilisation of gas hydrates or seepage of shallow methane gases. Bottom-simulating-reflectors indicative for the presence of gas hydrates have been reported from the Pacific Margin of the South Shetland Islands [Lodolo et al., 1993], but not from within the Central Bransfield Basin despite the very extensive seismic coverage. Also, none of the available multi-beam bathymetry and seismic data from the Trinity Peninsula margin show traces of pockmarks, acoustic blanking, acoustic wipe-out zones, enhanced reflectors or velocity pull-downs that could indicate the presence of shallow gas. However, on some of the seismic data from the basin-floor parts of Bransfield Basin some indications can be seen for gas or fluid accumulations or migration in the vicinity of the volcanic edifices, but these sites are a few tens of km away from the Gebra Slide.

Oversteepening of the margin. The multi-beam bathymetry and seismic data show that the Gebra Slide affected essentially the lowest and least steep part of the slope (average slope of less than 1°), while the higher parts of the margin, which are steeper (average slope of $7-8^\circ$) and have accumulated more sediment, were only involved in the second phase of sliding, or remained entirely intact. Upslope the Gebra Slide, the steepest part of Trinity Peninsula slope is characterised by gradients of up to 20° (Fig. 8). Such an exponential slope curvature is distinctive for a glacial sedimentation environment with an ice sheet overstepping the slope break during glacial periods.

Erosion at the toe of the slope. There are no indications for erosion – e.g. by contour currents – at the foot of the Trinity Peninsula slope within the Central Bransfield Basin, which would be an additional factor of oversteepening.

Tectonic setting. Gebra Slide is located at the transition between two morphostructural segments of the Trinity Peninsula margin. Prieto et al. (in prep.) attribute the distinct morphological changes across this boundary (difference in margin orientation, slope angle and stratigraphic architecture) to a first order tectonic segmentation of the entire Bransfield Basin [see also Barker et al., 1998], and they infer a series of deep basement faults perpendicular to the margin associated with this segmentation. Surprisingly, on our seismic data, which do penetrate to the top of the basement, no trace of this fault system can be observed. We do, however, observe a number of other faults affecting this part of the Trinity Peninsula margin. These faults are generally oriented parallel to the margin, with the downthrown side towards the basin. They are part of the deep fault system described by Prieto et al. [1998]. These faults do not affect the sedimentary cover (Fig. 5). Nevertheless, the position of the main headwall of the Gebra Slide coincides exactly with one of these faults. In fact, also the position of the upper-platform break coincides with one of these margin-parallel faults, which suggests that – in one way or another – these basement structures still influence the present-day morphology (Fig. 10).

Earthquakes. The Central Bransfield Basin is a seismically highly active area. Recent seismic and volcanic activity in the basin is concentrated along the central volcanic lineament, and specially at the six large sub-marine volcanic edifices A to F [Gracia et al., 1996; 1997], at Deception Island and at Bridgeman Island. The latter has been the epicentre of many recent earthquakes with a magnitude of up to $M = 6.7$ [Jin et al., 1998]. The Gebra Slide is located within a radius of less than 30 km from this central lineament, less than 40 km from the nearest seamount F [Gracia et al., 1996], and only at 80 km from Bridgeman Island.

In addition to their seismic activity, the sub-marine volcanic edifices appear to be responsible for the enrichment of clay minerals (58 % illite, 19 % chlorite and 19 % smectite for the < 2 µm clay minerals) in the Central Bransfield Basin [Yoon et al., 1994]. We cannot rule out that certain stratigraphic levels associated with strongly increased volcanic activity can be characterised by high amounts of volcanically derived clay minerals and zeolites, which could develop into potential slip planes for both small-scale and large-scale mass-wasting events.

A few of the above-mentioned potential trigger mechanisms can be discarded (i.e. seepage of shallow methane gases or destabilisation of gas hydrates on the slope; oversteepening of the margin; erosion at the toe of the slope), and none of the others seem to have been important enough by themselves to generate the Gebra slope failure. The most likely scenario is therefore probably one involving a combination of various factors. While high sedimentation rates during the last glacial period and the unloading effect by the retreating ice sheet during deglaciation may have induced higher-than-normal pore pressures in the Trinity Peninsula margin deposits and rendered them prone to failure. Additional triggers – such as tectonic fabric and earthquakes – were probably required to destabilize them and initiate the Gebra collapse.

CHAPTER 2

A SUB-GLACIAL SEDIMENTARY SYSTEM ALONG THE NORTHERN ANTARCTIC PENINSULA FROM SEA-FLOOR AND SUB-SEA-FLOOR EVIDENCE

*CANALS, M., DOMACK, E., CASAMOR, J.L., BARAZA, J., FARRAN, M.,
DE BATIST, M., URGELES, R. & CALAFAT, A.*

1. STUDY AREA AND DATA SET

The study area is roughly similar to the one discussed in Chapter 1. It covers about 25,000 km² of the Trinity Peninsula margin in the Central Bransfield Basin, from 62°24'S to 63.06'S and from 57°21'W to 58°38'W. Water depths in the study area range from 100 to 2000 m (Fig. 11).

Also the data set used for this study – consisting of a combination of reflection seismic profiles and full-coverage multi-beam bathymetry data – is the same as discussed in Chapter 1.

2. SEA-FLOOR MORPHOLOGY

2.1. Inner continental shelf

The continental margin of the Trinity Peninsula has been dramatically sculpted by the ice during past glacial maxima, as shown by several sea-floor glacial troughs [British Antarctic Survey, 1985; Szeliga, 1990] that reveal the paths of paleo-ice-streams. Our study focuses on the deposystem associated with three of these troughs, which have been named “Lafond” (from the bay south of Cockerell Peninsula), “Laclavere” (from the Laclavere Plateau, >1000 m high, that drains into Huon Bay) and “Mott Snowfield” (from the ice cap on the very north end of the Trinity Peninsula) (Figs. 11, 12).

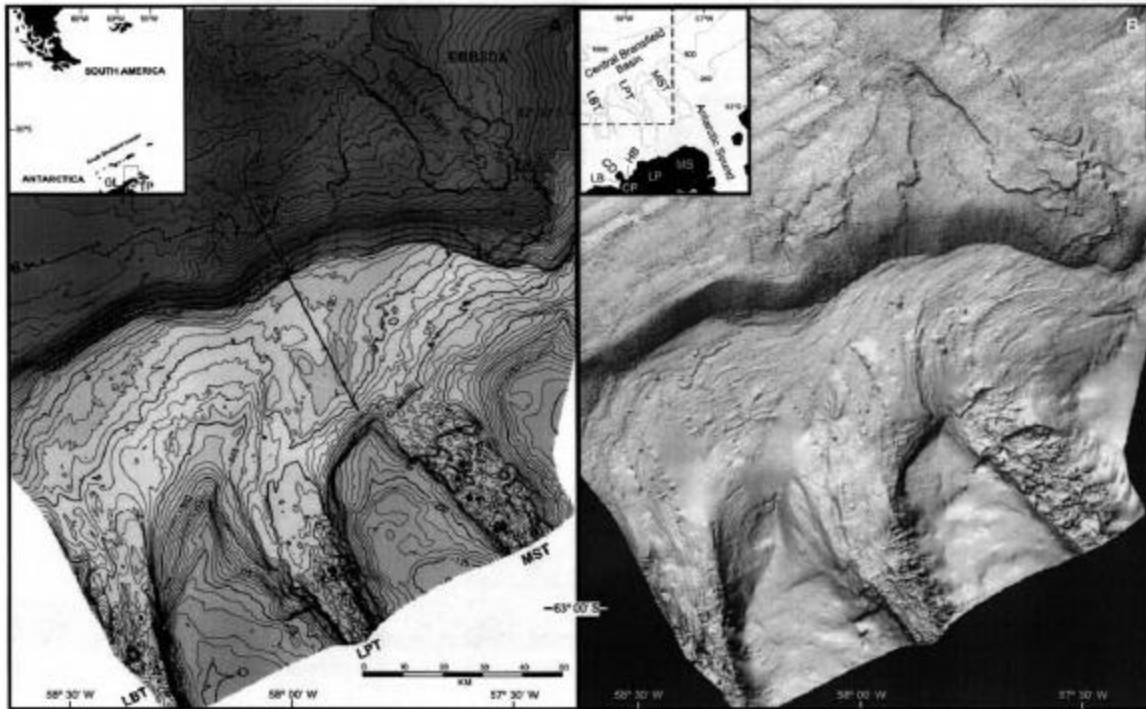


Fig. 11: Bathymetric contour map of the Trinity Peninsula margin of Central Bransfield Basin, based on multi-beam bathymetry data of the GEBRA-93, GEBRAP-96 and MAGIA-99 expeditions. Line indicates seismic profile of Fig. 13. Inset shows general location of study area. B: Shaded-relief image constructed from swath-bathymetry data.

Glacial troughs and the banks among them form a distinct inner-continental-shelf physiographic province (Fig. 11B). As a general rule, the troughs widen toward the outer shelf whereas the elongated banks between them narrow. The widths of the trough floors range from 10 to 28 km, and their upper rims are 20 to 45 km apart (Figs. 11, 12).

The Mott Snowfield Trough is markedly asymmetric, with a steeper western flank. The relief between the top of the banks (<150 m water depth) and the trough floor ranges between 200 and 350 m (Fig. 11A). The Laclavere Trough is more symmetric, with wall heights between 400 and 450 m. The sharp, steep, southwest-northeast-oriented erosional slope bounding the Mott Snowfield–Laclavere bank to the north is noteworthy. This topography clearly contrasts with the shapes of the nearby banks to the east and the west (Fig. 11). The eastern wall of the Lafond Trough, which is its only multi-beam-mapped wall, shows relief of 430 to 610 m between the top of the bank to the east and the trough floor (Fig. 11A).

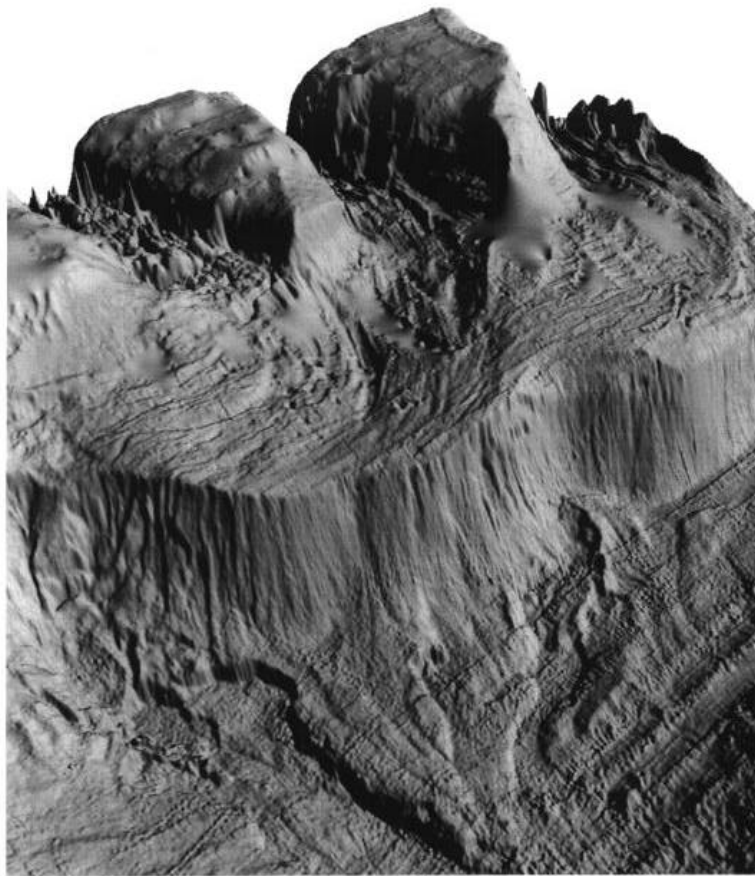


Fig. 12: *Three-dimensional view of the bathymetry of the Trinity Peninsula margin, once occupied by a sub-glacial sedimentary system.*

The trough floors display an uneven topography with local drumlins (Figs. 11, 12). Drumlins lying on deeply incised floors of glacial-valley mouths have been observed in terrestrial settings [van der Meer, 1983; Menzies and Shilts, 1996], and have recently also been reported from the Antarctic continental shelf [Anderson et al., 2001]. Drumlins exhibit such a wide complexity of form and composition that it is almost impossible to characterize what is an “ideal” drumlin [Menzies and Shilts, 1996], although some authors tend to apply this term restrictively to roughly ovoid hills of dominantly glacial debris that occur within groups or fields of several thousands.

2.2. Outer continental shelf and shelf edge

The outer shelf in the Central Bransfield Basin represents a depositional segment of the LGM sub-glacial system off the mouths of the glacial troughs entering the continental shelf. Till streamlines are indicated by sets of parallel to sub-parallel mega-scale ridges and grooves (known as “bundle structures” after Canals et al. [2000]) extending off the mouths of the above-described glacial troughs (Figs. 11, 12). However, these bundles are not as conspicuous as the western Central Bransfield Basin bundle, farther south [Canals et al., 2000]. Till deposits capped by a veneer of postglacial sediments have been sampled in several vibrocores.

The Lafond bundle markedly bends to the east, with till ridges forming a slight angle with the shelf edge, at depths between 800 and 900 m. The bundle off the intermediate Laclavere Trough is less developed than those of its two neighbors. Sea-floor morphology suggests an enhanced ice supply in this trough during glacial expansion, which caused pronounced sea-floor scouring and sediment bulldozing to the shelf edge. This interpretation is supported by the 80-m-deep elongated depression developed at the Laclavere Trough mouth (Fig. 11A) and the larger development of the shelf-edge lobe and slope debris apron (see subsequent discussion). The Mott Snowfield bundle is also markedly deflected to the east; some of its till ridges terminate in a nearly perpendicular orientation to the shelf edge at depths between 650 and 800 m (Figs. 11, 12). In the Mott Snowfield sub-glacial system, the transition from the erosional-depositional segment to the depositional segment is marked by a prominent transverse step, probably of erosional origin, followed by an equally prominent ridge at the mouth of the trough (Fig. 12). An east-southeast–west-southwest cross section across the Mott Snowfield bundle would show a set of descending morphologic steps from east to west, suggesting a thickening of the paleo–ice streams toward the southwest.

The 650–900-m-deep shelf edge is markedly sinuous, with a sediment lobe developing off the Lafond Trough bundle and a second, coalescent lobe off the

Laclavere and Mott Snowfield bundles (Figs. 11, 12). The lobate character of the shelf edge is most pronounced in front of Laclavere and Mott Snowfield bundles, thus indicating an enhanced sediment supply. These observations could be eventually applied to the interpretation of outer-shelf lobes in other Antarctic margins, such as the Pacific margin of the peninsula south of the Central Bransfield Basin.

2.3. Continental slope and base of slope

The continental slope and base-of-slope environments form the end-line of the sub-glacial system on the continental margin of the Central Bransfield Basin. The continental slope shows a mean gradient of 3.5° and local values up to 22°. The upper slope is markedly gullied, both in front of the two shelf-edge lobes and in the indentation between them (Fig. 12). The gullies are either parallel or show a downward radial pattern, are slightly incised, and less than 5 km long. A larger, coalescent debris apron exists at the lower slope and base of slope off the shelf-edge lobes (Figs. 11, 12).

The easternmost sector of the debris apron is cut by the scarp-bounded Gebra Slide (see also Chapter 1; Fig. 11A), a southeast-northwest-oriented depression that opens to the 2000-m-deep, flat-bottomed Central Bransfield Basin floor. Scarps and detached blocks are also observed on the slope debris apron west of the Gebra Slide (Figs. 11, 12). The scarps at the head and walls of the Gebra Valley and on the debris apron are interpreted as landslide scars whereas the individual blocks could be the result of downslope translational slab gliding [Prior and Coleman, 1984]. Extensive slides have been attributed to the input of sediments to the upper-continental slope by glaciers during periods of maximum ice advance, when the grounding line was located at or very close to the shelf edge in the Norwegian Sea-Barents Sea margin [Elverhoi et al., 1997; Vorren et al., 1998].

The location of the Gebra Valley suggests that shelf-edge re-entrants could behave as “instability corridors.” This possibility points toward the origin of the observed sinuosity of the shelf edge. Salients correspond to outer-shelf bundle structures supplied by inner-shelf glacial troughs, and reentrants correspond to preferred shelf-edge and slope instability zones. However, instability due to slope failure is probably more apparent where it is not masked by abundant sediment supply, as is the case for reentrants. The distinct development of the various sections of the debris apron again suggests a higher sediment supply from Laclavere and Mott Snowfield troughs compared with that of Lafond Trough. Outer-shelf and slope systems have been identified as major depositional centers for glacially eroded sediments [Myhre and Eldholm, 1988; Vorren et al., 1991]. Fan- or delta-like base-of-slope protrusions (trough-mouth fans) in front of glacial troughs crossing the continental shelf have

been observed on numerous glaciated margins, where they are associated with intense debris-flow activity [Vorren et al., 1998].

From the ice divide on the spine of the Antarctic Peninsula down to the Central Bransfield Basin floor, the overall length of the deposystem whose underwater components have been described is greater than 250 km; the maximum relief down to the shelf edge, where the ice was grounded during the LGM [Bentley and Anderson, 1998] is ~2000 m, and the basin floor is at a depth of ~3000 m [Gracia et al., 1996]. To some extent, the glacial setting in the Central Bransfield Basin during the LGM could be compared with that of the present Larsen margin east of the Antarctic Peninsula, where the ice shelf is directly nourished by valley glaciers that become unconfined over the outer shelf [Anderson and Molnia, 1989].

2.4. Internal structure

High-resolution seismic reflection profiles illustrate the internal structure of the sub-glacial system as well as the erosional-depositional character of the various margin segments from the inner-shelf–outer-shelf transition to the base-of-slope environment (Fig. 13). The overall stratigraphic configuration of the margin is aggradational-progradational; three main domains are observed in our seismic reflection profiles. These include (1) the transitional inner-shelf–outer-shelf area where intermediate-depth reflectors dip toward the outer shelf and crop out on the sea floor or subcrop beside an area of complex internal structure toward the continent, (2) the outer shelf where a >1 s thick (two-way traveltime) progradational-aggradational wedge develops, and (3) the continental slope where the outer-shelf wedge pinches out and partly ponded slope units can be seen to connect with both outer-shelf units and base-of-slope units (Fig. 13).

Inner-shelf erosion would be favored by uplift, as suggested by convex-up reflection geometries (Fig. 13) and by the exposure of acoustic basement at the innermost continental shelf [Barker and Austin, 1998]. The accommodation space left on what is now the outer shelf filled with the sediments forming the progradational wedge of province (domain 2). Owing to this progradational character, and to the general depositional setting, we assume that it consists mainly of sediments contributed during glacial and transitional periods under sub-glacial conditions [Dowdeswell et al., 1996]. The ice streams of Lafond, Laclavere, and Mott Snowfield glacial troughs would have played a major role in bulldozing sub-glacial debris to the outer shelf [Rearic et al., 1990]. It is to be noted that the ridges and grooves of the bundles in the study area have lower relief (5–8 m) than those described by Canals et al. [2000] in the western Central Bransfield Basin.

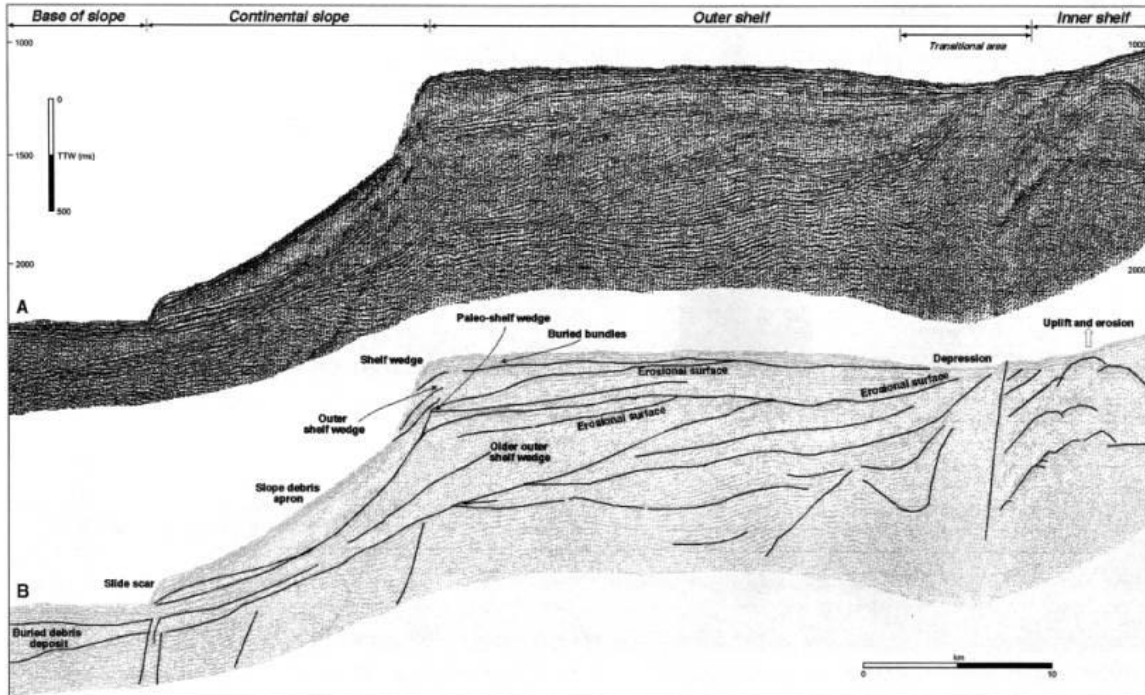


Fig. 13: Characteristic seismic profile across Trinity Peninsula Margin, with interpretation. For location see Fig. 11.

Of particular interest are the seismic facies of the uppermost stratigraphic unit on the outer continental shelf and slope. Sea-floor undulations are observed near the shelf edge over small diffraction hyperbolas and a transparent to semistratified seismic facies (Fig. 13). Following a marked morphologic step off the shelf edge, a semistratified to stratified, ponded unit caps the continental slope before ending at the basin floor through a second marked morphologic step that corresponds to a slide scar (Figs. 11, 13). Laterally, the seismic facies of this upper-slope unit becomes more stratified as shown by seismic reflection profiles a few miles east and west of the one illustrated in Fig. 13. This unit corresponds to the slope debris apron observed on the multi-beam bathymetry images (Figs. 11, 12).

Both the superficial expression of the various segments of the sedimentary system on the present-day sea floor and their excellent preservation, together with the interpretation of the most recent depositional units, are indicative of the system's young age. We therefore interpret that the last time the sedimentary system was active was during the LGM. On the basis of studies by Pudsey et al. [1994] and Banfield and Anderson [1995] we hypothesize that the ice shelf cleared the outer shelf not before 14,000 yr B.P. and probably much later because of the topographic character of the Central Bransfield Basin [Gracia et al., 1996], which would help to preserve a confined ice shelf. The shallower, scoured, and largely sediment-free

inner shelf cleared much later, perhaps by ca. 6000 yr B.P. if deglaciation ages of the Central Bransfield Basin [Barcena et al., 1998] and nearby areas are considered [Hjort et al., 1997; Pudsey et al., 1994; Herron and Anderson, 1990]. This late regional retreat has favored preservation of sub-ice landforms without significant reworking, sediment blanketing, and morphologic smoothing.

3. MODEL OF THE SEDIMENTARY SYSTEM

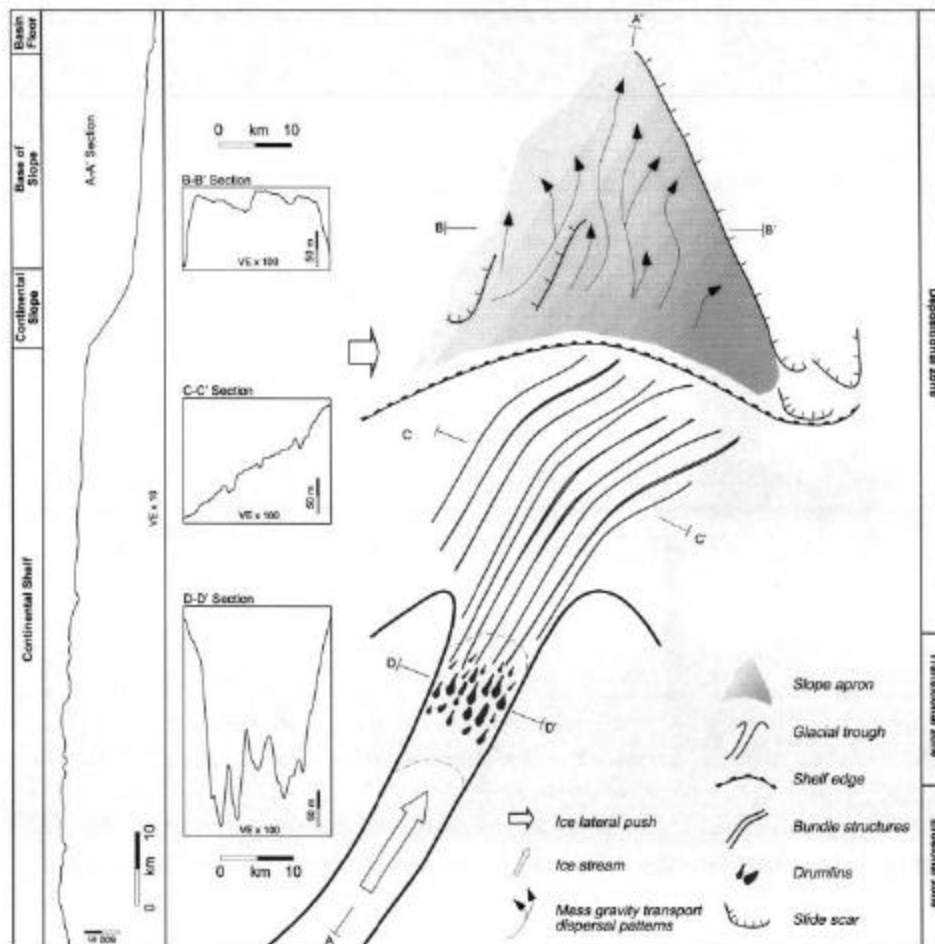


Fig. 14: Sub-glacial sedimentary-system model of the Trinity Peninsula continental margin.

The observations made allow us to propose a sedimentary-system model for marine-based, sub-glacial settings. This model includes four segments, which occur in sequence from the head of the glacier to the deep basin (Fig. 14). In the Central Bransfield Basin, the three of these segments now situated below sea level (e.g., those illustrated in Fig. 13) are supported by our own data, whereas the definition of the uppermost, onshore segment is inferred from observations on low-relief mountain

settings [Benn and Evans, 1998]. The segments are described as follows:

1. The *onshore and coastal erosional segment* (following Benn and Evans [1998] extends from the ice divide in the Antarctic Peninsula spine, where the heads of the (tidewater) marine-based glaciers flowing down to the coastline are located, to the coastal embayments and innermost continental shelf. Erosion occurs at the ice-base–bedrock contact. Tectonic uplift may play a significant role in the development of an erosional segment and favor fast downslope ice flow.
2. The *inner-shelf erosional-depositional segment* has shallow banks and deeply incised, U-shaped troughs occupied by large ice streams during glacial maxima. This segment displays evidence for both erosion and deposition. Till deposits are essentially thin and discontinuous, and their distribution may reflect debris streaming between obstructions [Boulton, 1987]. Trough floors with drumlins may develop locally within the glacial troughs (Fig. 12). The lodgment-till wedge is initiated in this zone, where ice substrate shifts from bedrock to overconsolidated sediment.
3. The *outer-shelf depositional segment* is characterized by continuous till cover where streamlined bundles develop. Deposition occurs in the sediment layer separating the ice base from bedrock or older sediments. The outer limit of this zone consists of a sinuous, lobed shelf edge that marks the ice grounding line on top of basal till. On the whole continental shelf there is no morphologic evidence indicating any grounding line in a position other than the shelf edge.
4. The *slope and base-of-slope depositional segment* occupied by a debris apron is largely formed from shelf-edge ice bulldozing and mass-wasting processes under a floating ice shelf offshore of the grounding line. That mass-wasting processes are common on the slope debris apron is shown by the many slide scars interpreted from multi-beam bathymetry data and seismic profiles (Figs. 11, 12, 13). The debris apron represents the deep-sea end-line of the sub-glacial system. We interpret the debris apron of the Central Bransfield Basin to have been formed during the LGM, when the whole basin was covered by a continuous ice shelf fed by the ice streams draining the Western Antarctic Peninsula and, to a lesser extent, the South Shetland Islands.

CHAPTER 3
DEVELOPMENT OF A NEW
DEEP-TOW REFLECTION SEISMIC ACQUISITION SYSTEM

HENRIET, J.P., GUIDARD, S. & VERSTEEG, W.

1. INTRODUCTION

The Renard Centre of Marine Geology (RCMG) of Ghent University has ventured to develop an innovating methodology for very-high-resolution seismic investigations of Antarctic margins, or of any type of continental margin where adverse sea states (ice, rough seas) may prohibit such practice. It became a whole challenge for a medium-sized academic research team, not really backed by engineering resources such as those available in major oceanographic institutions. However, through various failures and successes in concept design, construction and yearly sea tests, and through support from a number of additional funding resources, a rugged and advanced operational system with a large, multi-functional development potential has been realized and successfully tested. This original system is continuously being upgraded towards new functionalities and it presently attracts the attention of a wide community in margin research (AWI, GEOMAR, IFREMER, NIOZ, IODP, NEBROC II).

2. DESCRIPTION

The basic qualifications of RCMG's deep-towed seismic acquisition system are two-fold. The first one as compared to a classic surface-towed acquisition system is the submersion depth of typically a few hundreds of meters, down to 1000 m, to reach the most dynamic part of continental slopes: the outer shelf and upper slope, with its suite of incipient slope instabilities, decaying gas hydrates, deep-water carbonate mounds and cold water reefs, etc..

For this purpose a rugged umbilical with a length of 1100 m has been constructed to tow primarily seismic receivers or source-receiver configurations at the required depth (figure 15). Such single ROV-type cable provides the necessary power to the deep-towed seismic source (sparker, rail-gun, chirp sonar, etc.), as well as analogue transmission lines for data transfer and depth control, and a 6-way fibre-optic cable for optical telemetry. The second particularity of the deep-towed system is its modular design and compatibility with and complementarity to conventionally used systems,

and its potential for multi-functional applications, ranging from “proximal” “remote” sensing to ground-truthing.

The above description implies for a seismic system several possible modes of operation.

- A basic sub-tow mode of seismic profiling, with both a single-channel streamer and a seismic source (sparker) towed at a standard seismic surveying speed (3-4 knots) at a depth of 200-400 m, well below any swell influence and at a depth sufficient to avoid ghost interference in the imaging of the shallow sub-seabed (down to some 200 m) (status: developed and tested).
- The “Jumbo” configuration: a dual recording mode with a surface source (sparker, watergun), a surface-towed single-channel streamer and a sub-towed single-channel streamer (status: developed and tested).
- The “Touch-and-go” mode: a variant of the sub-tow mode, with a single-electrode sparker and multi-channel streamer lowered to the seabed by decreasing the vessel speed. The objective is seabed imaging with ultra-high resolution and characterization by refraction data or full-wave (P, S) analysis (status: developed and tested). A new seismic source (“rail-gun”) for shear wave generation, applicable in such touch-and-go mode, has been designed off-project in cooperation with the electric engineering department of Leuven University in the framework of a EU project (status: bench study).
- The deep-tow streamer mode: sailing at very low speeds (1-2 knots) allows the heavily armoured umbilical to sink under its own weight down to depths of 500–1000 m, trailing a multi-channel streamer a short height above the seabed in upper slope settings (or Antarctic outer shelf settings) (status: developed and tested). It is usually performed in a kind of deep-tow Jumbo mode, with an additional single-channel surface streamer.
- The deep-tow seismic profiling mode, as a post-project (2002) development in cooperation with IFREMER: towing of a deep-water streamer (RCMG) and deep-water chirp sonar (IFREMER) at very low speeds (1-2 knots) and at a shallow elevation above seabed.
- The seabed cable mode: a further post-project development involving a 24-channel seabed cable with 6 4C sensor groups (developed with additional funds) and an independent small shooting vessel (developed in the framework of a EU project) for amplitude-versus-offset (AVO) studies of gas migration pathways in upper slopes (new project submitted in the framework of an association with the NEBROC II – Netherlands Bremen Oceanography – Programme).

Further acquisition modes are in the bench study phase, as possible developments in the framework of future projects, e.g. integrated deep-towed seismics and side scan sonar profiling or near-seabed multi-beam bathymetry (Deep Reef Surveyor project, pre-design for new EU submission), use of the umbilical for box-coring with video control, chemical sampling and in-situ chemical profiling, as well as ROV operations (concept studies, jointly with IFREMER, Bath University and industrial partners). The multi-functional cable and its recent-most cable termination, re-designed and strengthened after a major accidental damage in the system's first Antarctic deployment open such multi-functional perspectives.

The development of RCMG's high-resolution deep-tow seismic acquisition system started in 1996 with the design, construction and testing of a pre-ANTAR project prototype. It was tested from R/V Belgica in the Celtic Sea in various modes: sub-tow, jumbo, touch-and-go. It evolved in function of the different trials, but the basic principles and objectives of the acquisition system remained virtually unchanged.

The sub-tow system with an advanced sparker design has been tested during cruises in 1997 and 1998 in Porcupine Seabight (Western Ireland). Due to the relative poor quality of the data as a result of initial technical design failures, the further development of the sub-tow sparker has been temporarily postponed to concentrate all efforts on the development of the acquisition module with deep-tow streamers, using the state of the art in near-receiver digital recording and long-range optical telemetry. Once the acquisition could reach full performance, it is straightforward to focus on and evaluate the performance of deep-tow sources.

The basic components of the deep-tow system are consequently the following (Fig. 15):

- a seismic surface source: a sparker with power supply and triggered capacitor bank, or a watergun or GI gun with compressors, etc.
- an umbilical for feeding the high voltage to the deep-towed source, and for transmitting the signals detected in the receivers to the recording unit
- a purpose-built winch with slip-ring units (power conductors, not yet optical)
- a high-frequency receiver unit (MC or SC streamer) for detecting the acoustic responses from the subsurface
- a streamer depth monitor, including the power supply for the pre-amplifier and depth transducers
- computer-based acquisition systems to digitise and record the data: initially only at the surface (Delph), later with full deep-water digital acquisition (Methusalem, Geometrics Geode)

- converters for full optical telemetry (implemented in later phase of the project)
- a high-precision positioning system (GPS, DGPS).

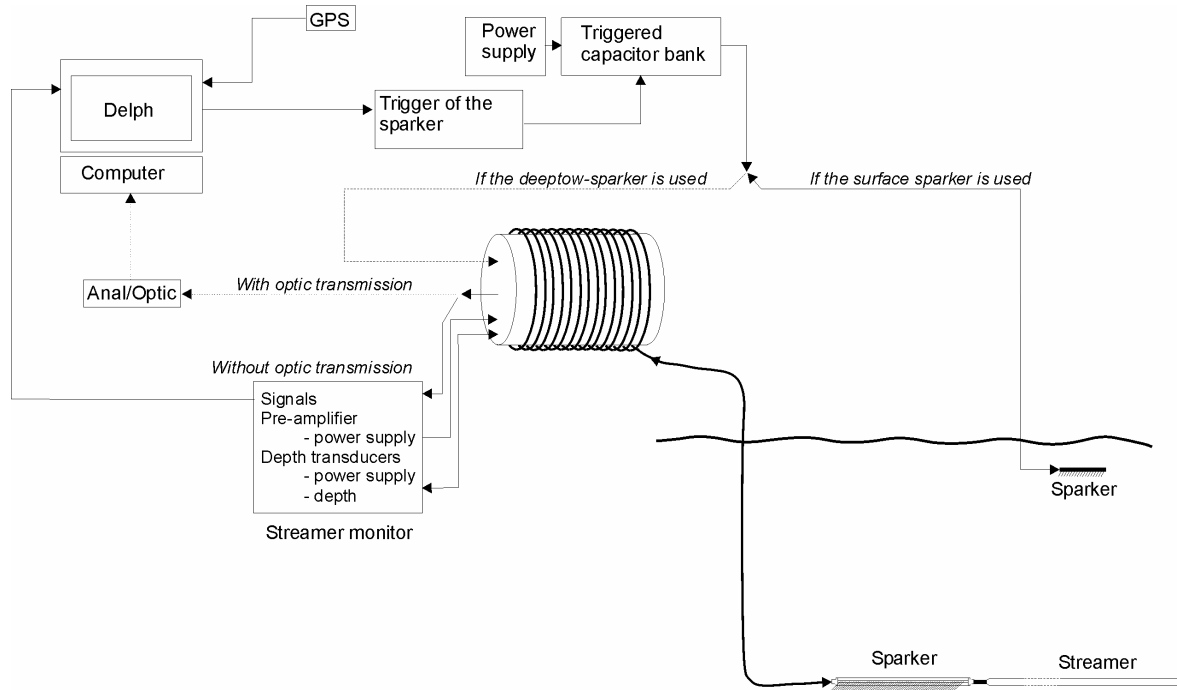


Figure 15: The main components of the RCMG deep-tow system.

The sub- or deep-tow operation mode implies that special attention has to be paid to the geometry, which can be influenced by hardly controllable movements of source and receiver. Once seismic data are acquired, geometrical corrections need to be applied prior to the data analysis and interpretation. Depth transducers built in the receiver unit provide both real time depth and attitude control and part of the input needed for the geometric corrections. When source and receiver are coupled, the movement of the source is considered to be in coherence with the movement of the streamer.

2.1. The winch

The winch is shown on Fig. 16. It is equipped with a hydraulic control unit and has a traction pull of 10 tons. Slip-ring connections are provided on the power and analogue transmission lines, and can be later implemented on the optical channels. A static box links the slip rings to the acquisition system, the command box of the winch and the power supply for the source. The mobile part of the winch includes the

drum, the cable and the rotating box, fixed on the drum. The rotating box connects the cable terminations to the slip rings.

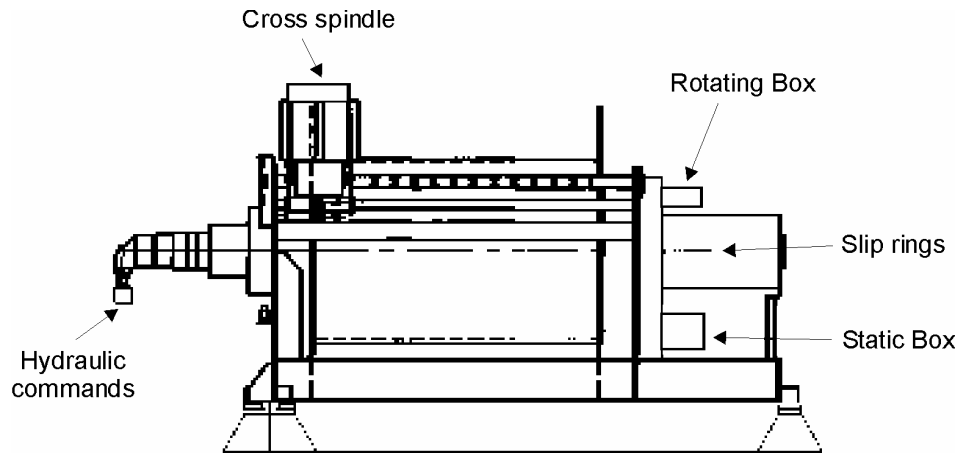


Figure 16. The winch of RCMG's sub-tow system.

2.2. The cable

The ROV-type umbilical (Fig. 17) used for the sub-tow and deep-tow systems has been built by De Regt Special Cables (The Netherlands), based on a preliminary design study by RCMG, in co-operation with the ELEN-ESAT high-energy engineering research unit of the Catholic University of Leuven. The cable has a total length of 1100 m.

The umbilical hosts two peripheral crowns totalising 15 heavy-duty power conductors (which are used for the transmission of the high-voltage) and an inner core with 6 twisted shielded quads, 6 single conductors and one 6-way fibre-optic unit.

The quads are used for data transmission and power supply to the pre-amplifiers of the streamer. Single conductors supply power to the depth sensors in the streamer and transmit the signals from the depth sensors to the surface (monitor screen). The six-string fibre-optic cable provides the telemetry string for the fully digital data transmission from the hydrophones and the sensors to the surface, or for remote depth control. The first tests with the optical transmission of the data were performed in 1999 and will be explained in paragraph 2.4.

The exterior protection and the strength element are composed of a bedding jacket of polyurethane and two layers of contra-helical steel armour with torque-balanced construction. To avoid string vibrations, a full fairing with long yarns covers the whole length of the cable.

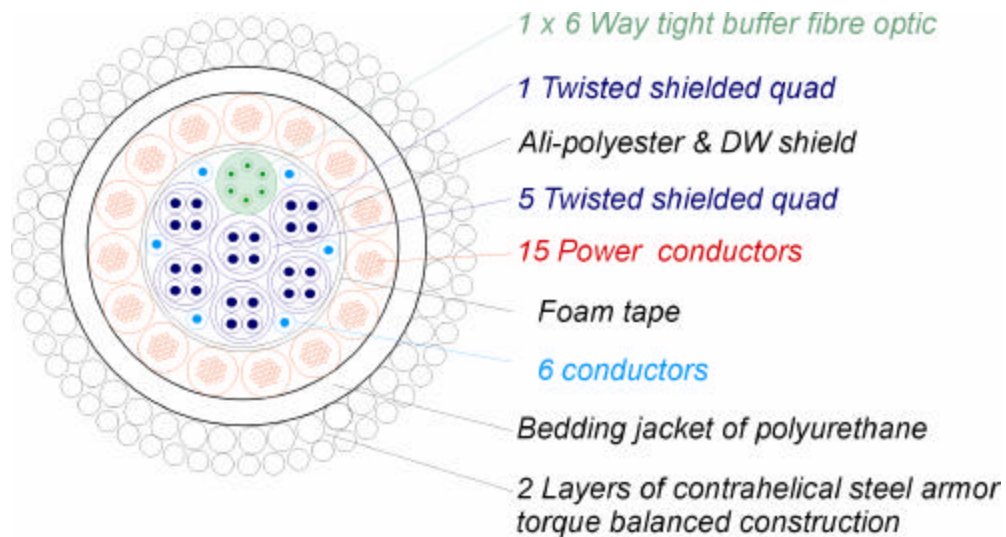


Figure 17: ROV-type umbilical built by JDR Special Cables.

2.3. The streamers

The single- and multi-channel streamers, constructed by SIG Technology Instruments, have a skin of polyurethane, specially fit for cold-water operations. They contain the different hydrophone groups and are designed to resist high pressures, up to 24 MPa (maximal depth of use is thus 2400 m, the optimum immersion depth down to 1700 m). To ensure both buoyancy and a good pressure transmission between the seawater and the hydrophones, this tube is filled with inert oil, highly dielectric, and very resistant to oxidation. The streamers are also equipped with pre-amplifiers and depth transducers. The small power demand of the pre-amplifier (10-12 V) is supplied either by a battery or by the power supply box. In the case of the multi-channel streamer, the depth transducers are located in the compartments at the head and at the tail of the section (Fig. 19). In the single-channel streamer, the depth transducer is placed in the compartment at the head of the section (Fig. 18). The 11 m long single-channel streamer contains 8 hydrophones with a spacing of 1 m. The 8-channel deep-tow streamer contains groups of 4 hydrophones, spaced over 25 cm, the group spacing being 12.5 m. The total length of this streamer is 100 m (Fig. 19).

A more rugged 16-channel streamer with group spacing of 2 m has been used for the touch-and-go applications.

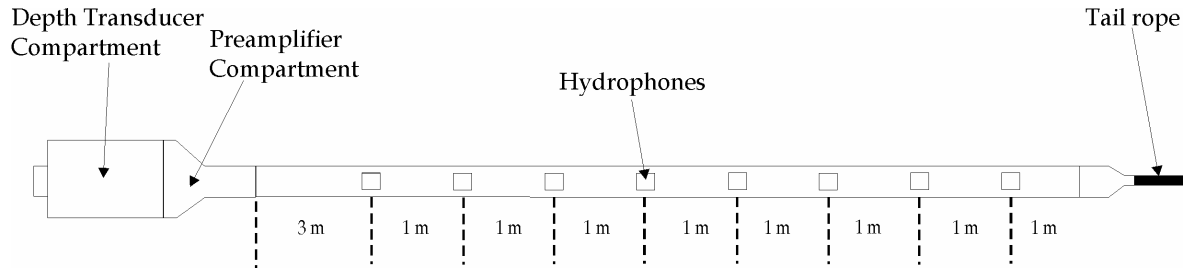


Figure 18: The single-channel streamer

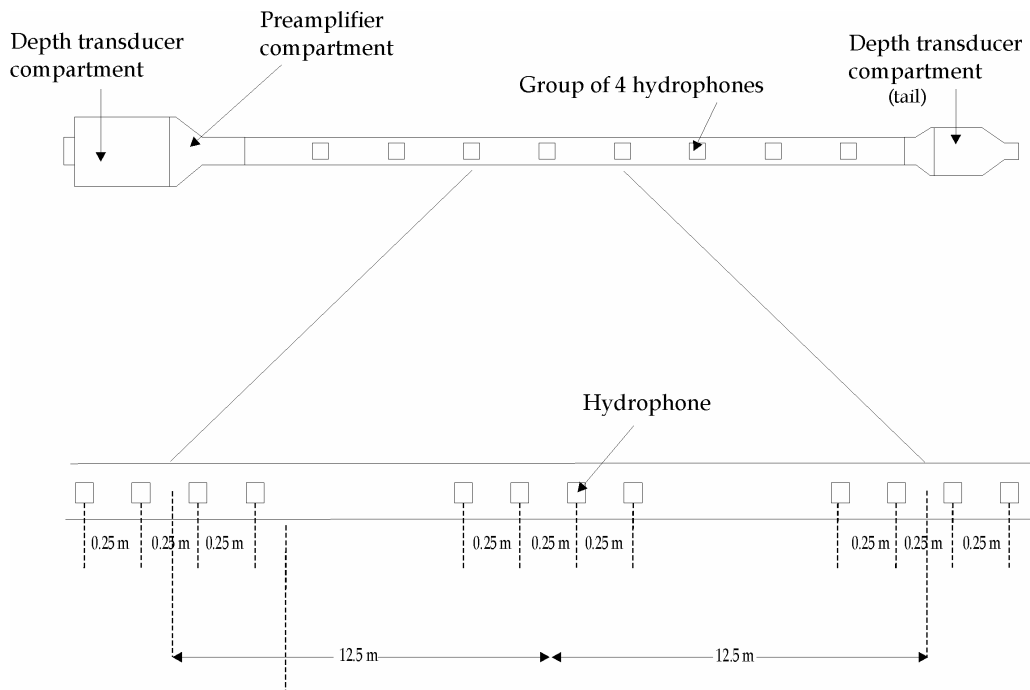


Figure 19: The multi-channel streamer.

2.4. Transmission via optic fibres

For the 1999 R.V. Belgica expedition, it had been decided to straightforwardly move into a more ambitious development, which initially had been considered at a more remote horizon:

- the full digital data acquisition immediately behind the streamer,

- to avoid the interference between the discharge from the power supply to the sparker and the transmission of the recorded data to the computer, the data transmission moved into optic fibre technology.

For this purpose, an acquisition box (Ocean Bottom Seismometer model) had been acquired and fully pressure-tested in a hyperbaric test facility in The Netherlands (Seatec). This cylinder contained an OBS-type recording system (Methusalem) and an optical transmitter, both powered by a battery (Fig. 20). Flexible connecting cables with flotation sleeves were designed and built in the Netherlands and Germany for improving the towed attitude of both sparker and streamer.

The analogue signal recorded by the deep-tow streamer was converted into an optical signal by an audio/fibre-optic multiplexer transmitter situated in the acquisition box. This optical signal was then transmitted via optic fibres through the 1100 m cable and reconverted into an analogue signal by a receiver/demultiplexer. Next, the acquisition unit (Delph) digitised the analogue signal. All pre-amplifiers, fibre-optic transmitter and down-cable seismic recorder were conceived as battery-powered units, eliminating any risk of inductive coupling through long power leads, a risk evidenced in earlier testing phases with the deep-tow system. When the deep-tow sparker is used, the whole acquisition unit is towed behind this sparker by a kevlar cable with only optical fibres as actively connected wires, which again should exclude all possible conductive electrical transient transfer.

This new sub-tow system was further equipped with a deep-sea data acquisition and recording system (the German 4-channel METHUSALEM system used in GEOMAR's advanced OBS/OBH): the analogue signal recorded by the streamer is first recorded on the "flash disk" of the Methusalem before being transmitted to the analogue/optic converter (Fig. 20).

In 2000, a new ACQ-cylinder was built. It is smaller in size and towed some 20 m from the deep-tow streamer. The purpose of this 20 m long cable is to avoid possible tow noise near the streamer resulting from the turbulence around the ACQ-cylinder.

Though basically the optical fibre transmission system should warrant a faithful - and noise-free - data transfer from the single-channel streamer to the surface, the deep-towed acquisition unit immediately behind the streamer offers a full backup of many hours of surveying, as an additional safety factor.

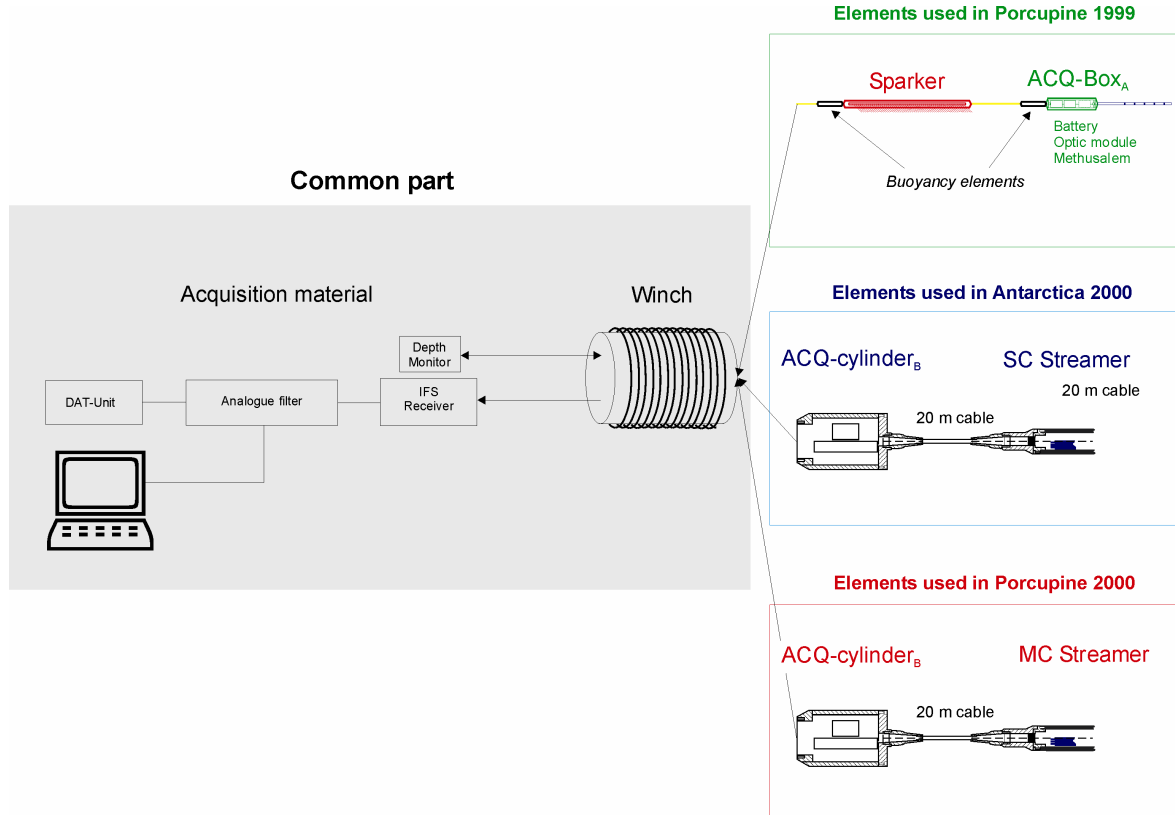


Figure 20: Sketch of the different tested configurations using the data transmission via optic fibres, up to 2000.

3. TESTING AND SEA TRIALS

Several tests have been carried out during the different phases of the construction and the optimisation of the sub-tow system. The very first series of tests were carried out with an early prototype during a pre-project high-resolution seismic survey in the Celtic Sea with R.V. Belgica in 1996. The second series of tests consisted of laboratory experiments and modelling of the cable behaviour. Two seismic surveys with R.V. Belgica in Porcupine Basin, off western Ireland, have provided the first true field testing opportunities for the prototype, resulting in a most important evolution of the deep-tow: the transmission of the data via optic fibres. These were followed by the deployment on board of R/V Polarstern in the Antarctic (cruise ANT XVII/2 in cooperation with AWI) early 2000. Beyond the present project and building upon the Antarctic experience, two more cruises were carried out in 2000, from which technical progress is reported below: a R/V Belgica cruise in Porcupine (EU project GEOMOUND) and a R/V Sonne cruise in cooperation with GEOMAR on Hydrate Ridge off Oregon (project HYDGAS). Further post-project deployments and

developments (2001) are evoked in the conclusions.

3.1. Celtic Sea (1996)

The prototype was composed of two individual single-electrode sparker sources and a 30 m long array of 16 short hydrophone groups, whereby power and data transmission lines and a steel strength element were tied in a 400 m long bundle of cables.

During this campaign, two different configurations have been tested: the so-called “Touch-and-go” and the “Jumbo” configuration, each yielding its own information.

3.1.1. The “Touch-and-go” configuration

The test procedure involved intervals of continuous high-resolution reflection profiling, smoothly alternating with a “landing” operation phase and a “take-off” phase (Fig. 21).

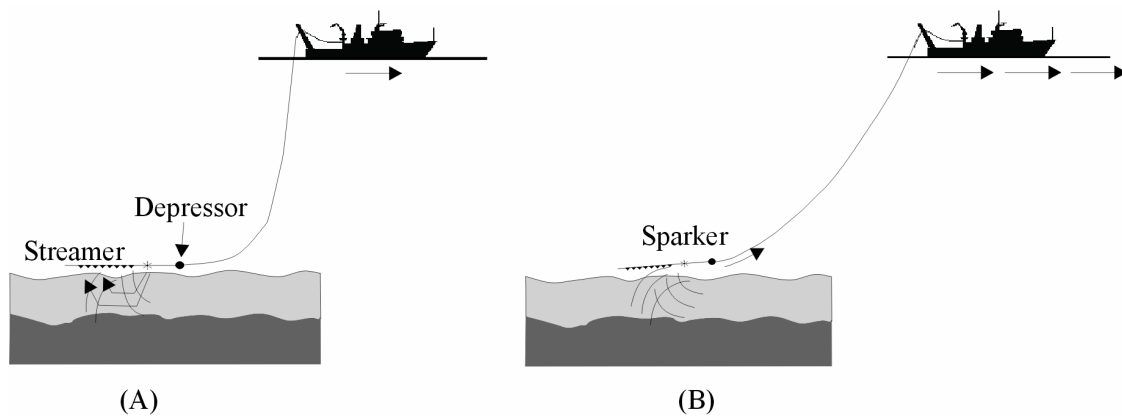


Figure 21: The “Touch-and-go” procedure. (A) Landing phase while the vessel slows down and (B) Take-off phase while the vessel accelerates.

- During the “landing “ phase, the low speed of the vessel allowed the sparker and the streamer to go down and to sweep the seabed. Such configuration is comparable to the sub-tow mode where the source and receivers are at a certain submersion depth.
- For the “take-off” phase, the speed of the vessel increased progressively and the system soon moved back into a subsurface profiling mode. This approach opens perspectives for continuous characterisation of the seabed over long profiles.

The influence of the submersion depth on the data has been evaluated. Reflection signatures have been recorded for a series of 10 shots at different submersion depths. On Fig. 22, the reflected waves at the interface air-water are shown: at the beginning of the profile the submersion depth of the system is about 120 m and at

the end about 35 m. From this figure, it is clear that the time between the reflected wave arrival and the bubble decreases when the submersion depth of the source increases. This is due to the fact that the greater hydrostatic pressure at greater depth reduces the bubble oscillation period.

This effect has an influence on the frequency content of the signal (Fig. 23). With increasing submersion depth, i.e. increasing confining pressure, the bandwidth of the sparker pulse becomes broader and the dominant frequency increases: from about 380 Hz to 660 Hz. This effect contributes to the anticipated increase in resolution obtained with the deep-tow acquisition mode when compared to that obtained with a surface-towed system.

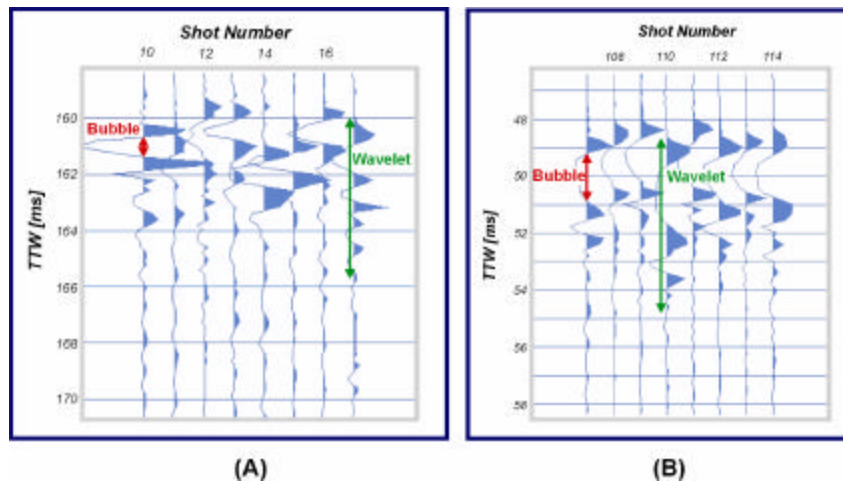


Figure 22: Reflected waves recorded for different submersion depth of the system [profile sign2506]. The depth of the system is about 120 m (A) and about 35 m (B).

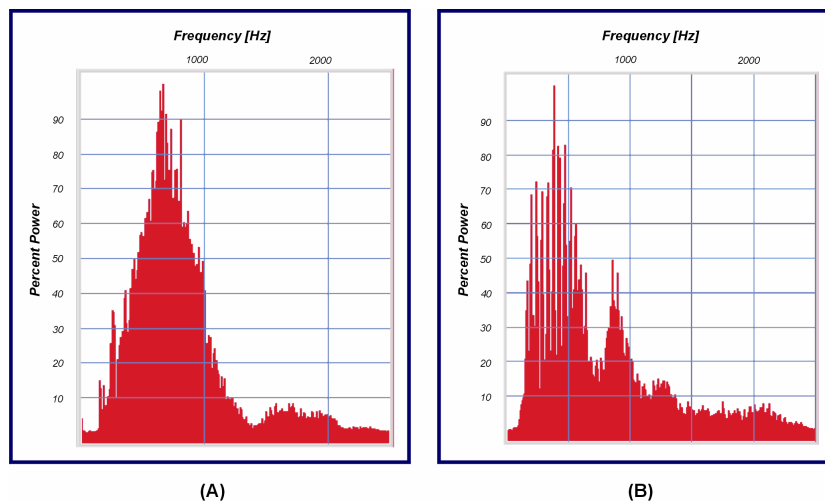


Figure 23: Signature analysis obtained with the “Touch-and-go” procedure. (A) Frequency spectrum in deep-tow mode. (B) Frequency spectrum in surface mode.

3.1.2. The “Jumbo” configuration

During the same survey, a number of seismic profiles were recorded using a quite particular acquisition geometry (*Jumbo* configuration) with surface sparker and two streamer units, one towed at the surface (near-zero offset) and the other in deep-tow mode (Fig. 24).

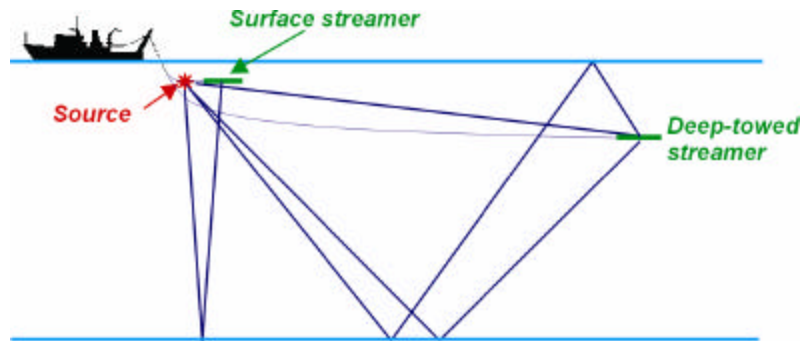


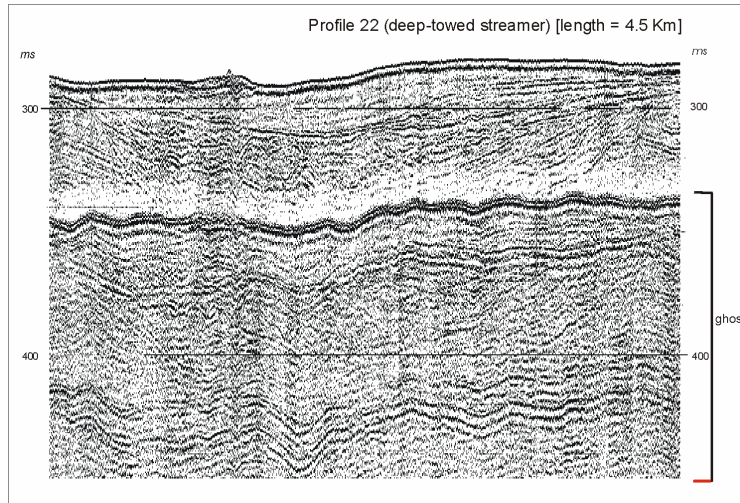
Figure 24: Illustration of the “Jumbo” configuration.

Fig. 25 shows an example of profiles acquired on the continental shelf and margin of the Celtic Sea with this configuration. On profile A, the ghost reflection – i.e. the acoustic wave generated by the source and reflected at the water-air interface – arrives shortly after the primary reflections (± 60 ms) and hereby conceals part of the information contained in the primary reflection sequence. For deeper towing depths (with a true deep-tow device), ghosts would arrive much later so that they would not interfere with any of the primary reflections. Still, ghosts are useful as they allow to calculate the vertical and horizontal position of the streamer in those cases where the direct wave has not been recorded (e.g. due to the application of a recording delay). Comparing these two records, one can notice the “compression” of the intervals between reflectors in the deep-tow image due to the larger angle of incidence of the reflected waves in the deep-tow streamer mode.

A further remark concerns the distortion of the data due to the non-constant depth of the deep-tow streamer. To correct this effect, geometrical corrections have to be applied. Such corrections imply that we virtually move the sub-tow streamer to a point situated on the surface and at a fixed distance from the shot point. This is possible by introducing a non-static header value calculated from the arrival times of two different wave fronts. The most easy and convenient way of dealing with this is by using the direct wave and the first reflected wave. However, if a recording delay is applied, the

ghost reflection can be used instead of the direct wave. It is worth emphasizing that such corrections are not real static geometrical corrections: only the position of the sea floor is corrected by applying a time shift to the whole trace. Such geometrical corrections can be applied easily in areas of flat sea-floor topography, but when the sea-floor surface is irregular other and much more complex geometrical corrections need to be applied.

(A)



(B)

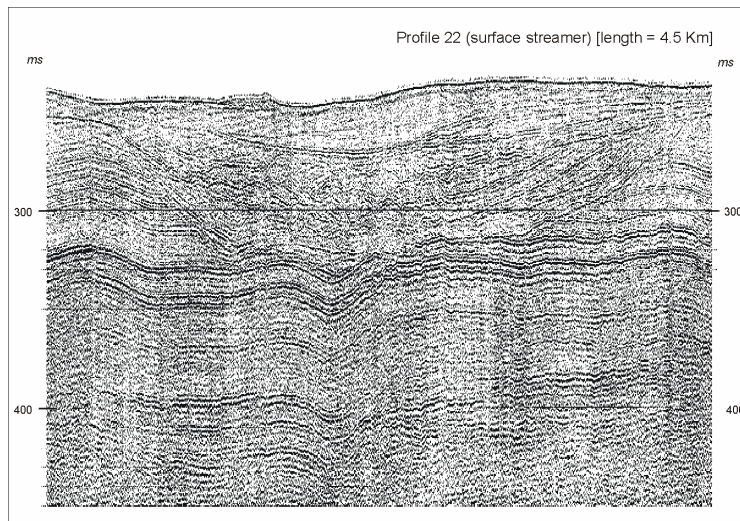


Figure 25: Profile 22 registered recorded with the Jumbo configuration (A) deep-tow record and (B) surface record.

An important point is the possibility to estimate the acoustic velocity of the shallow seabed by combining the data recorded by the two streamers (Fig. 25) [Gelfort,

1998]. The data are first stacked for a discrete series of compressional wave velocities, ranging from 1500 m/s to 1700 m/s. Next, with the help of a "movie" of different panels corresponding to a constant velocity, the coherence of individual reflectors at various depths is scrutinized. By applying the same approach to all reflectors, a vertical velocity profile is generated. Such a velocity analysis can be performed in a semi-continuous mode along a certain profile and the results projected on the reflection profile, thus offering a model of merged geology and velocity fields (Fig. 26).

Obviously, this rather unconventional method exploits the maximum of information, which can be recovered from a very simple geometry, and it cannot reach the accuracy of velocity analyses derived from full-length multi-channel streamers. It however demonstrates the potential of the "jumbo" type sub-tow method in environments, where the deployment of very long surface multi-channel streamers is questionable, e.g. by ice conditions, and it preserves the potential of generating high-resolution reflection seismic profiles.

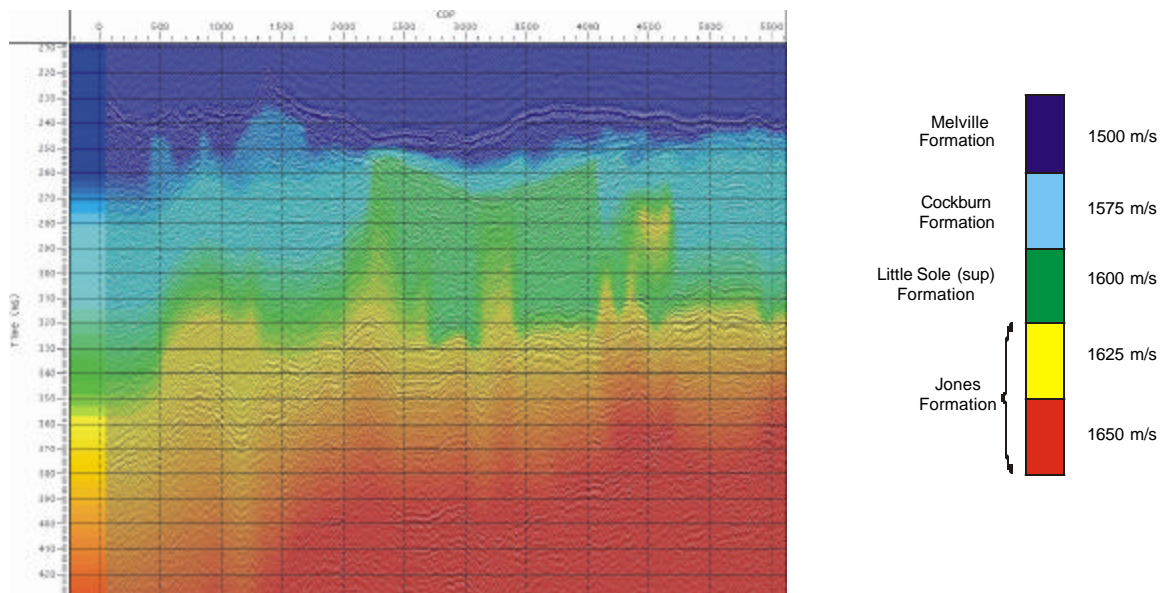


Figure 26: Acoustic velocity volume of profile 22.

3.2. Antarctica ANT XVII/2 (2000)

The ANT XVII/2 expedition of R/V Polarstern, organized in cooperation with the Alfred-Wegener-Institut für Polar- und Meeresforschung (AWI, Bremerhaven) from 8.1.2000 to 15.3.2000, offered the first opportunity for deploying RCMG's deep-tow system under real Antarctic conditions.

3.2.1. Technical information

The ANT XVII/2 expedition had from its earliest operations to cope with severe problems. After the loss of the German multi-channel streamer and of a corer, an accidental manoeuvre of the A-frame severely damaged and twisted the termination of the RCMG umbilical, even before its first deployment. It took several days and an extraordinary craftsmanship on board of R/V Polarstern to reshape a cable termination, which at least could stand sub-tow depths of 200-300m for the time of the expedition. The built-in electronics however also had suffered damage. After first repair but still negative tests, the system was checked for possible causes of failure in the electronic circuitry. Attention was also paid to the bandwidth of the system, considering the totally new characteristics of the guns, not previously available for experimentation. After trouble-shooting, it was found that the AC coupling capacitance (470 nF) of the streamer pre-amplifier output to the fibre-optic transmitter was responsible for a narrow acoustic bandwidth, filtering out the dominant frequency (120 Hz) of the GI guns (Fig. 27).

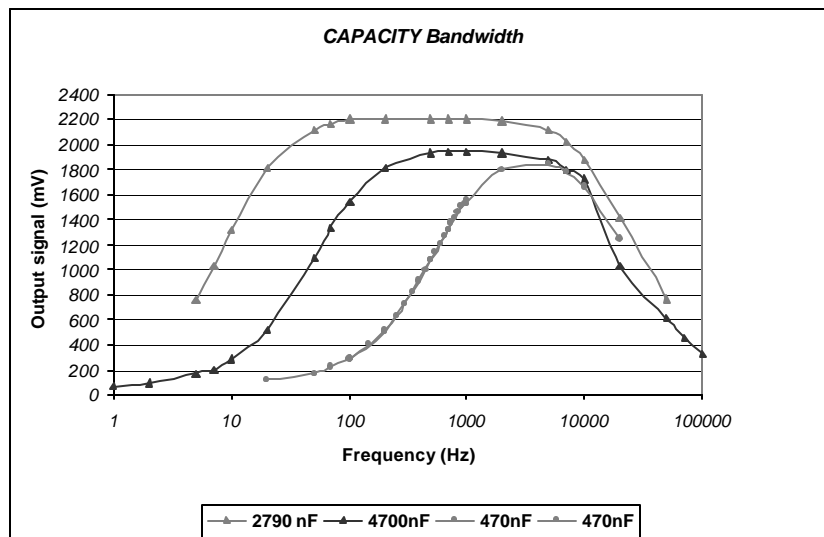


Figure 27: Bandwidth for 3 different values of the capacities.

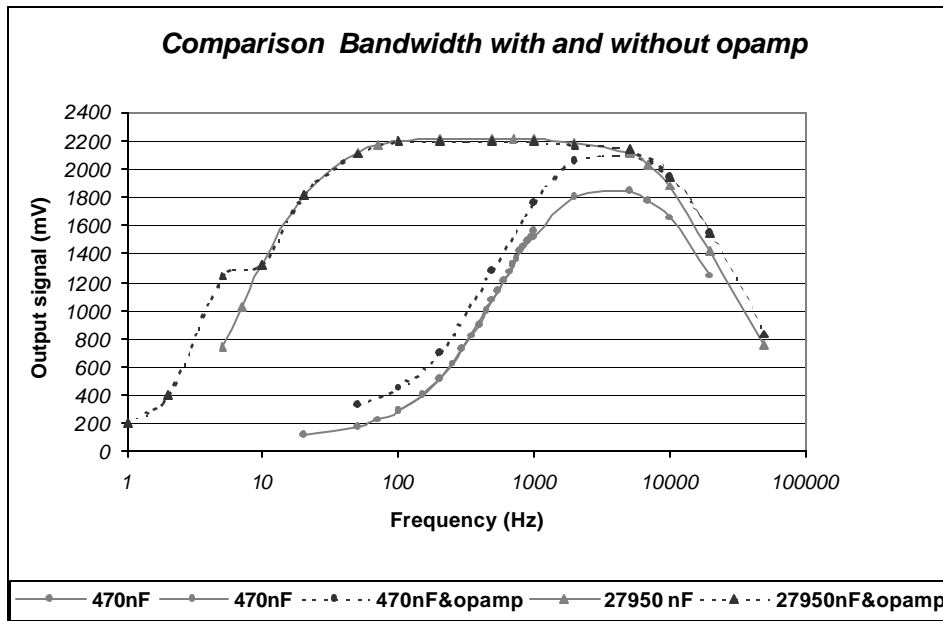


Figure 28: Influence of the Voltage follower on the bandwidth of the system.

As tests with a modified capacitance were still negative, contact was made with the streamer manufacturer. Source of problems were sought in terms of the input impedance of the fibre-optic transmitter, which together with the AC coupling capacitance of 470 nF possibly generated a low-cut filter. To decrease the output impedance of the system towards the fibre-optic transmitter a voltage follower was built and installed into the system. It appeared that such design had no major influence on the frequency behaviour of the system (Fig. 28).

Progressively, it became clear that the problems were not only technical, but the deep-water environment in the Antarctic indeed proved a true challenge. The water depth seemed to play a major role on the quality of the first data: signals were recorded in shallow water (300 m) but not deeper. Therefore it was decided to build an extra amplifier in an attempt to increase the signal's amplitude. This amplifier would replace the previously used voltage follower and AC coupling capacity.

An extra amplifier connected to the pre-amplifier gave a total gain of about 390. On Fig. 29, the gain of the extra -amplifier alone (red and the orange curves and "Y axis" on the left side) and of the total system (blue curves and "Y axis" on the right side) is shown. According to this figure, the gain of the total system amounted to some 425.

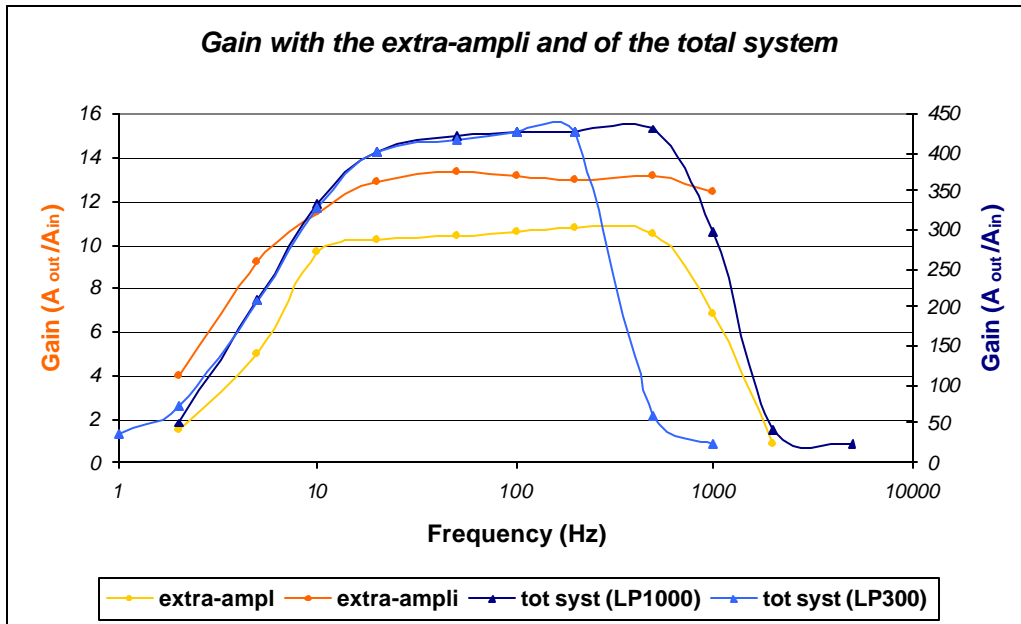


Figure 29: Comparison of the gain with the pre-amplifier alone and with the extra amplifier.

3.2.2. Results

Different tests with the extra amplifier have been performed. Because the water depth seemed to be an important parameter, it was decided to record a profile up-slope to determine this critical water depth. This turned out to be situated at about 1850 m. The high sensitivity of the surface streamer however did not allow shooting profiles in jumbo mode, i.e. with a zero offset surface streamer and a far offset deep-tow streamer.

In the Jelbart basin at the ice edge east of Neumayer, several acoustic profiles (Fig. 30) were acquired yielding sharp reflections from apparently a very hard seabed (with ghost and multiple reflections). After shooting an up-slope transit profile and three lines parallel to the ice shelf, it was decided to leave the area since not sufficient geological information could be retrieved from the acoustic sections. Continuous profiling in the area close to Atka iceport however revealed good-quality acoustic images (Fig. 31), making clear that the system is working in an appropriate way in relatively shallow water areas, and that the Jelbart basin (< 700 m water depth) is not characterized by distinct recent sediment accumulation patterns. In this area, over 130 km of seismic lines were acquired.

This line illustrates also the typical effect of a non-constant streamer submersion depth. Effectively, during the acquisition of this line, the streamer depth was about 250 m (Fig. 32). Near shot 800, due to an increase in vessel speed, the submersion of the streamer decreased from 250 m to 170 m resulting in a deformation of the recorded section: the reflected waves arrive later and the ghost is recorded earlier.

Taking into account the extremely difficult conditions met (technical accident added to harsh ice conditions in a very late season), it has been recognized that RCMG's deep-tow system has very honourably passed its first Antarctic tests. Congratulations and encouragements were received from AWI to go ahead with this development.

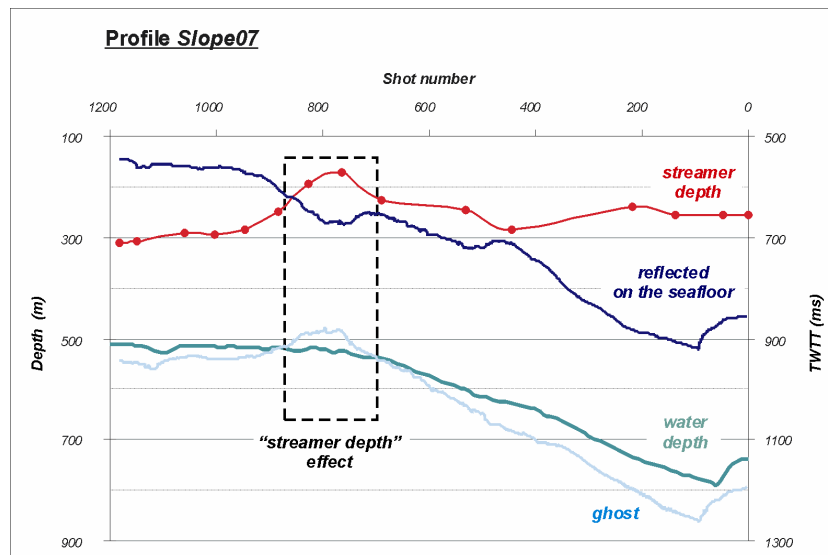


Figure 32: Correlation between the arrival time of the reflected wave and the ghost and the streamer and sea-floor depth.

3.3. Belgica 00/16 (2000)

The configuration used during this cruise, meant to continue the testing of the system building upon the Antarctic experience, was comparable to the one used in Antarctica. The only differences were the streamers and the vessel. In Antarctica, a single-channel deep-tow streamer was deployed, while in Porcupine it was a multi-channel streamer towed at a depth of about 500 m. The data were recorded in a Jumbo mode, most of them with a watergun as source. An example is shown on Fig. 33. Compared to the signals recorded with the surface streamer, the lateral resolution was enhanced (Fig. 33). Furthermore, the deep-tow data were clearly not affected by swell, which resulted in images of a higher quality. However, a new

design with a transo-fed DC, meant to be superior to the batteries, had resulted in 50 Hz interference. This would be later corrected.

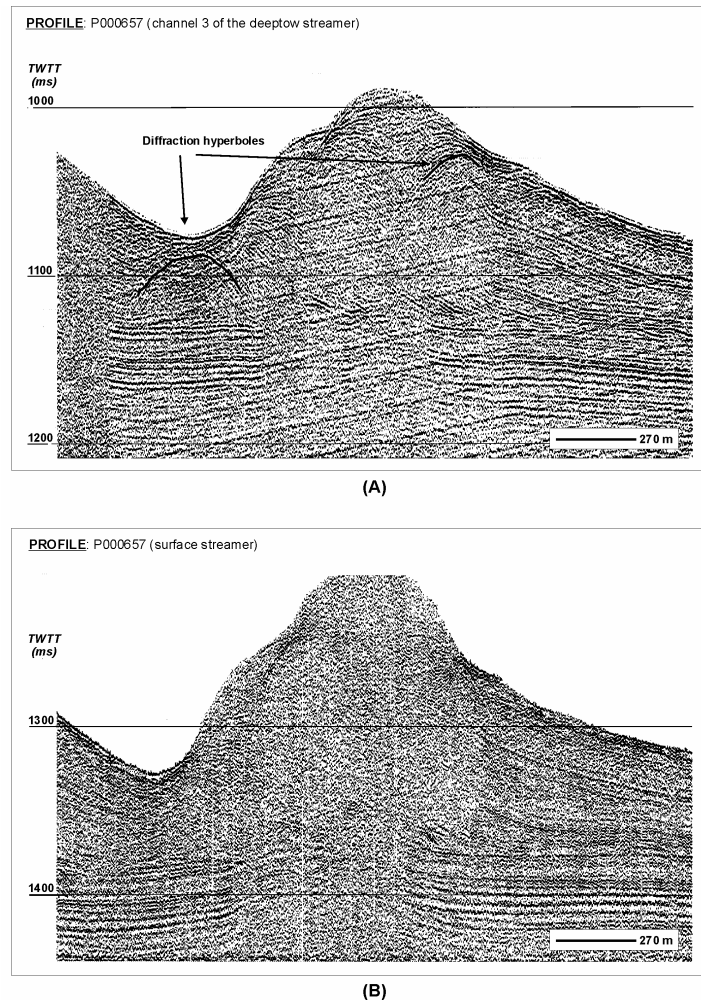
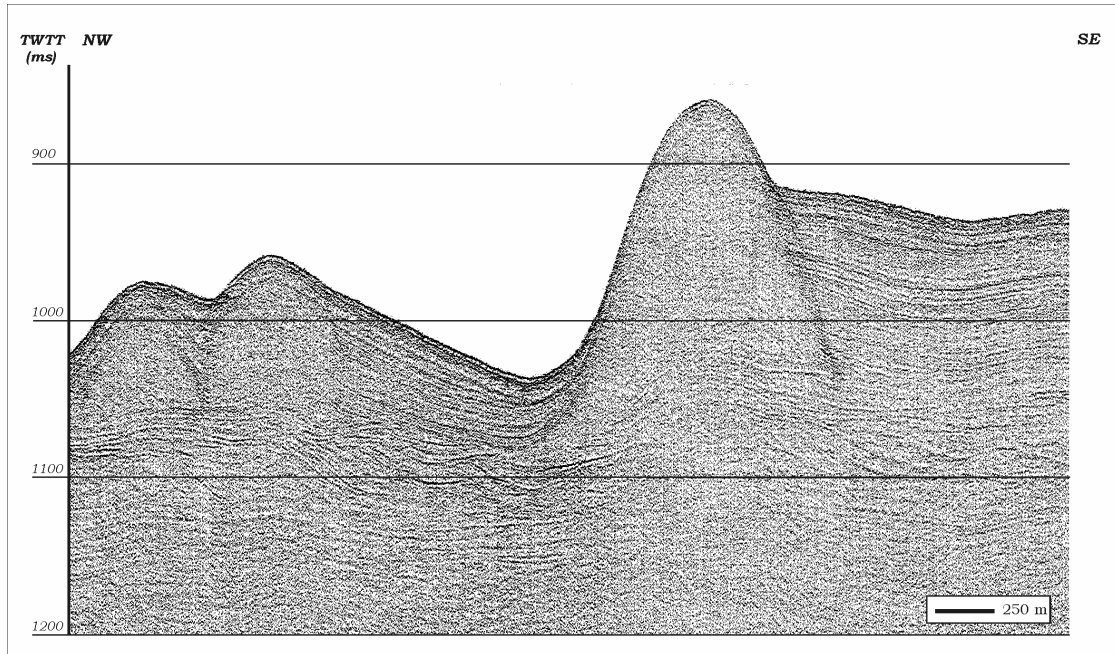


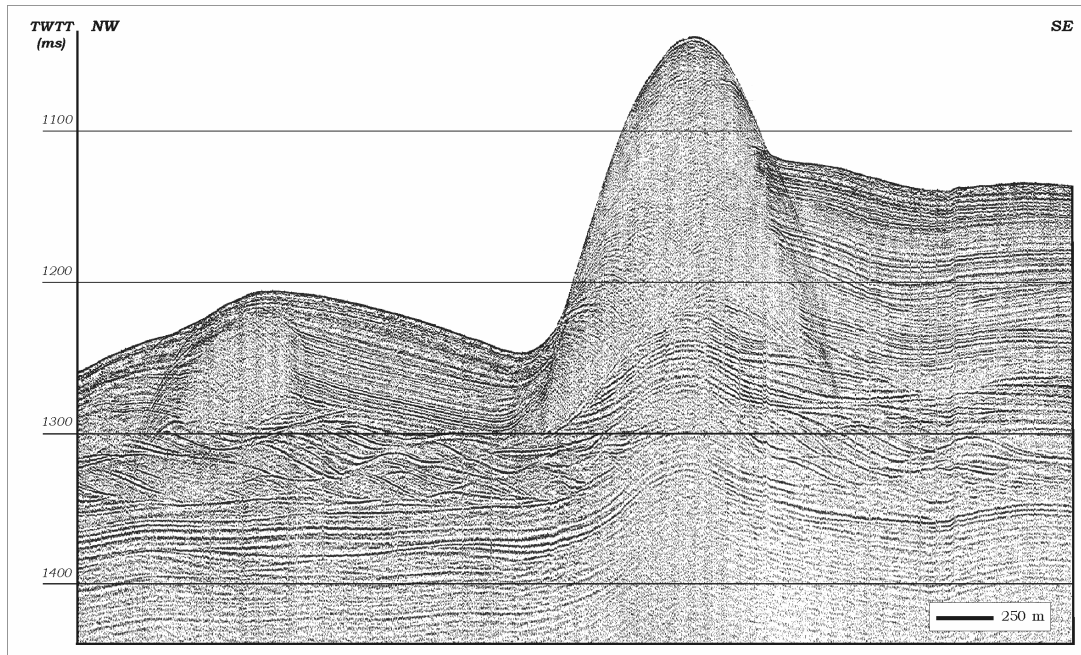
Figure 33: Profile P000657 (surface sparker) recorded by the deep-tow (A) and the surface streamer (B).

Fig. 34 displays two nearly-coincident seismic profiles recorded in the Belgica mounds: a deep-tow profile P000617 (A) with a high-frequency watergun ($\pm 100\text{-}400$ Hz) source and a surface-towed profile P000658 (B) with a very-high-frequency sparker source ($\pm 200\text{-}1000$ Hz). These seismic records clearly reveal two different kinds of semi-transparent patches or carbonate mounds. One is buried under a few meters of sediment while the other one is exposed and rises tens of metres above the seabed. They entirely lack any internal reflections, but some diffraction patterns can be recognised. The sequences beneath the base of these structures over a range of 50-100 ms TWTT are characterised by a sigmoidal facies, suggesting a

high-energy depositional environment. The quality of the deep-tow record is very promising.



(A)



(B)

Figure 34: Profile P000617 (watergun) recorded by the deep-tow (A) and Profile P000658 (sparker) recorded by the surface streamer (B).

3.4. SO-150 HYDGAS expedition (2000)

GEOMAR Kiel was highly interested in the Ghent deep-tow capacity for a survey on one of the world's richest gas-hydrate provinces, Hydrate Ridge, off Oregon. However, as there was not opportunity to embark RCMG's winch, the deep-tow components had to be fitted to the R/V Sonne's 8.000 m umbilical, which lacked optical fibres.

3.4.1. Re-design of the system

The RCMG deep-tow seismic system for HYDGAS was primarily composed of a deep-tow streamer and a newly built high-pressure ACQ-cylinder (bigger than the cylinder used for the Antarctica ANT XVII/2 and Belgica 00/16 expeditions), connected to the 8.000 m long cable of the R.V. Sonne by a GISMA-connector containing two analogue wires. To avoid noise originating from turbulence around this cylinder, it was located 20 m ahead of the streamer head (Fig. 35). The maximum operating depth of the system is about 1500 m (limitation due to the ACQ-cylinder).

Seismic signals generated by a surface source, were detected by the deep-tow streamer and amplified by a SIG pre-amplifier (X39). Originally, the data were only recorded by the Methusalem acquisition system situated in the ACQ-cylinder but, due to problems, the reflected analogue signals were later transmitted via the depth sensor cables of the 8.000 m long cable of the R.V. Sonne, straight to the Delph system. The deep-tow streamer was also equipped with depth sensors, and the analogue depth-signals were transmitted to a depth monitor in the laboratory via the GISMA-connector.

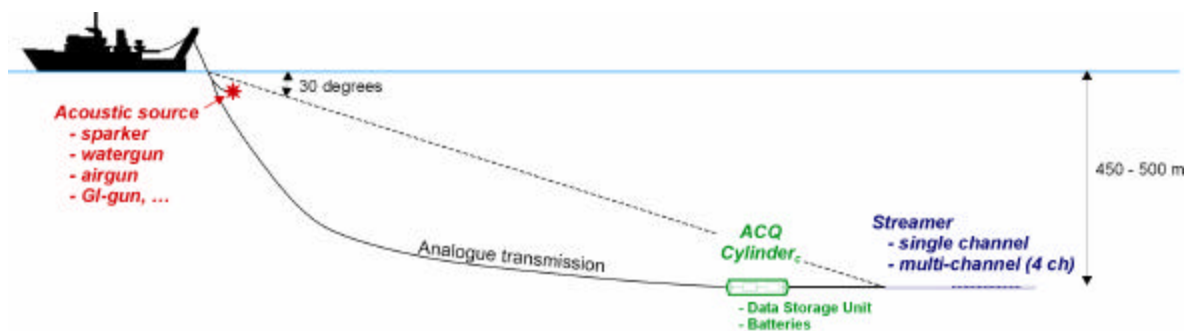


Figure 35: Acquisition with the deep-tow streamer during the R.V. Sonne for the SO-150 HYDGAS expedition in 2000.

This configuration had a primary drawback: there was no "online" control of the submersion depth of the deep-tow streamer. Owing to the wealth of previous tests, it was possible to estimate the deep-tow streamer depth as a function of cable length (vessel's speed less than 3 knots). For example, an 1100 m cable length corresponded to a submersion depth of about 500 m bsl (below sea level), with an angle of about 30° relative to the sea floor, when assuming a vessel's speed of 3.0 knots (Fig. 35).

3.4.2. Results

The objective of this expedition was to study the acoustic signatures related to gas hydrates and free gas accumulations in the sediments over a wide frequency range. Therefore, different tools were used: multi-frequency seismic profiles (sparker, watergun, GI-gun, airgun array, bolt gun) have been acquired in dual recording mode i.e. with both deep-towed and surface-towed receivers (*jumbo* configuration). Despite the geometrical corrections inherent to the deep-tow system, advantages of such records over surface-towed data are the improvement of resolution (both lateral and vertical) and enhanced signal/noise ratio. Next to that, data with larger offset can emphasise the presence of shallow gas accumulations (AVO-effect).

An example of a seismic section recorded with the *Jumbo* configuration (GI-gun - surface and deep-tow streamers) is shown in Fig. 36. Submersion depth and offset of the deep-tow streamer are respectively about 450 m and about 335 m. The depth of the deep-tow streamer is well adapted to the source characteristics and the typical sub-surface penetration depths because the ghost does not mask any relevant geological-stratigraphic information.

The effect of the larger offset with the deep-tow streamer on the BSR data can be seen on the eastern flank of Hydrate Ridge and in the basin (Fig. 37). By comparing the simultaneously recorded deep-towed vs. surface-towed acoustic sections, differences are underlined. The first one is the imaging of the sedimentary section, which obviously is more compact on the deep-tow record. This is explained by the larger angle of incidence.

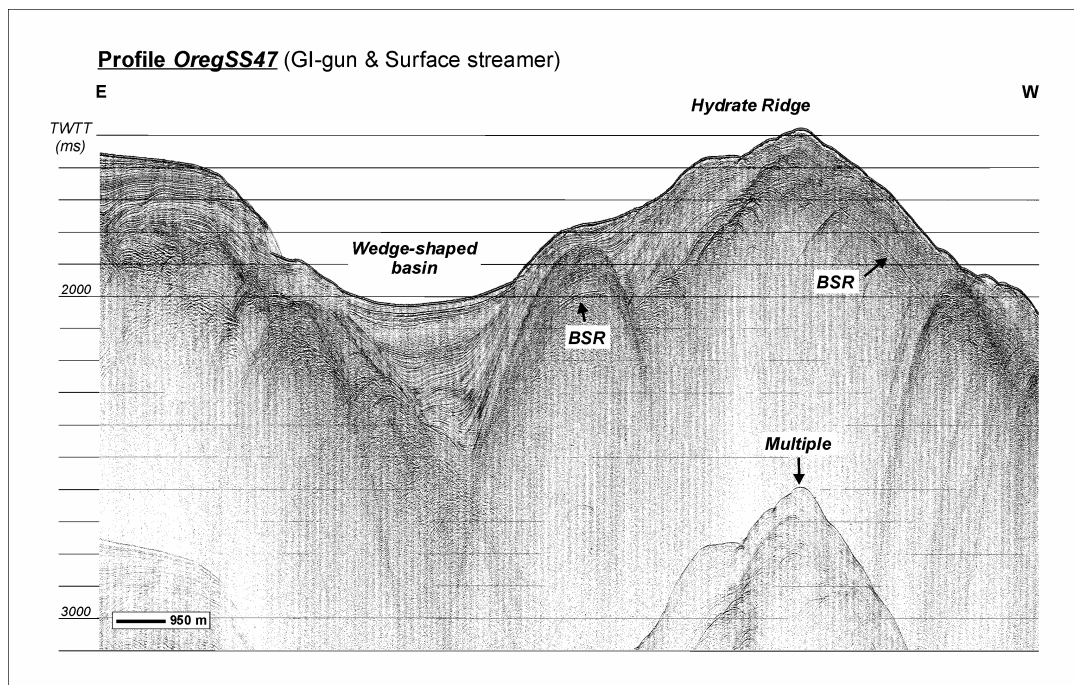
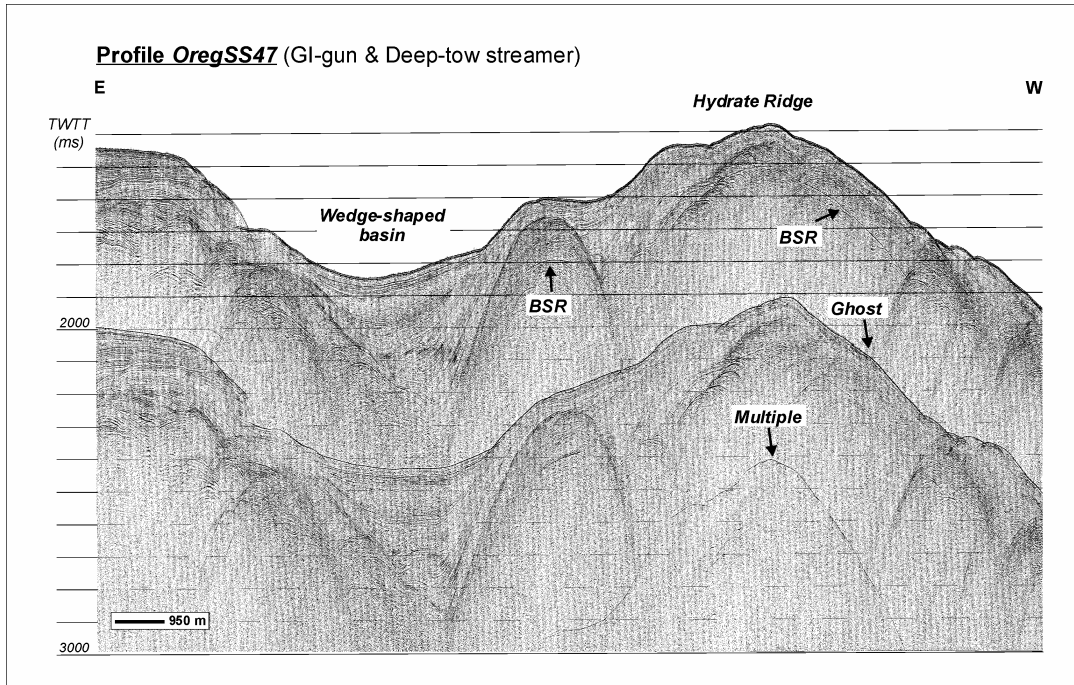


Figure 36: OREGSS47 (GI-gun) recorded by the deep-tow streamer (up) and by the surface tow streamer (down).

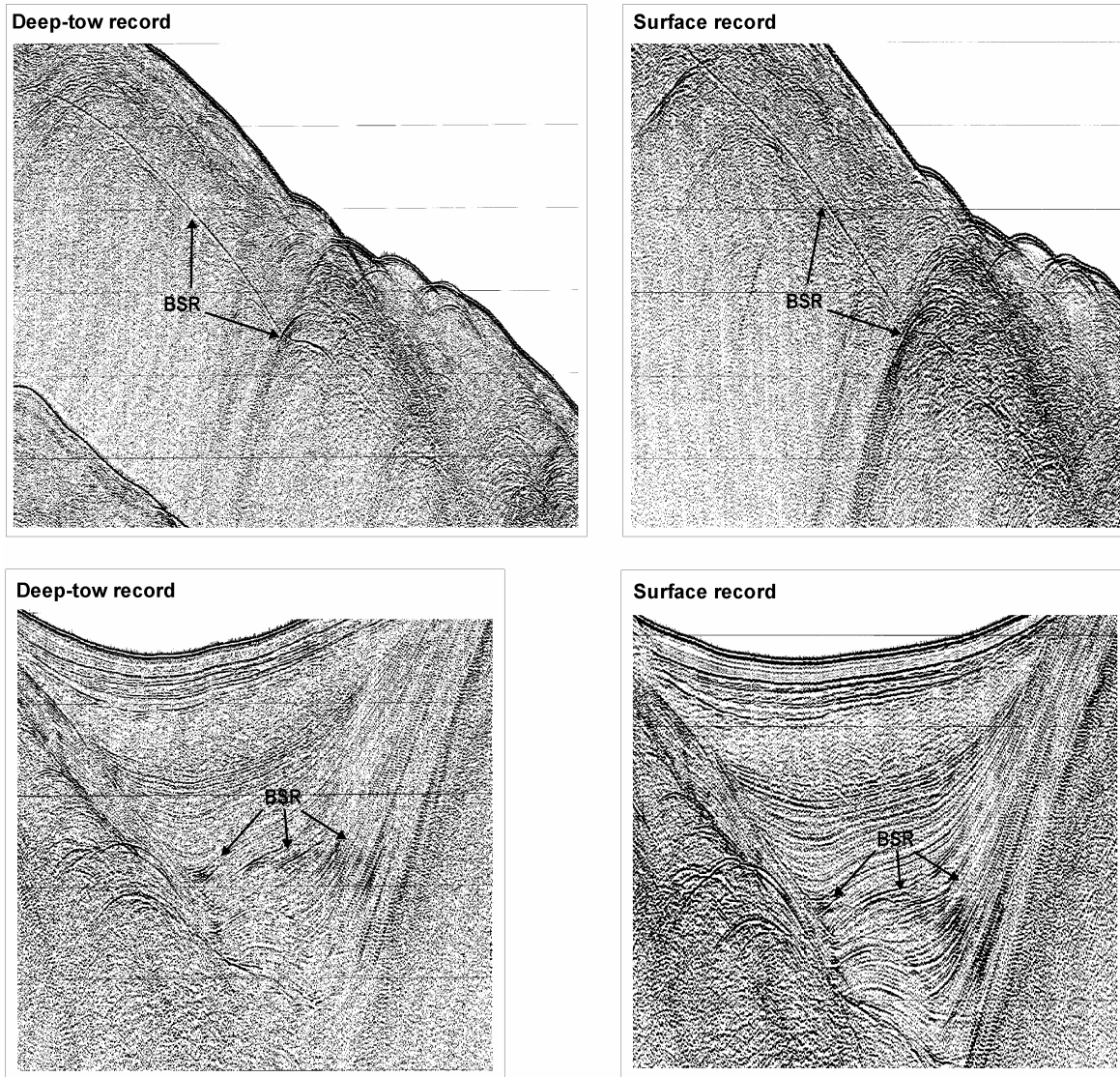


Figure 37: Zooms of Fig. 36 with the signature of the BSR recorded by both streamers on the eastern flank of the Hydrate Ridge (up) and the basin (down).

The second point concerns the resolution. On Figs. 38 and 39, different zooms taken from Fig. 36 show the improved resolution of the data and the continuity of the reflections when recorded by the deep-tow streamer.

It is worth noting that, due to the good weather and the constant vessel speed, no geometrical corrections have been applied to the data.

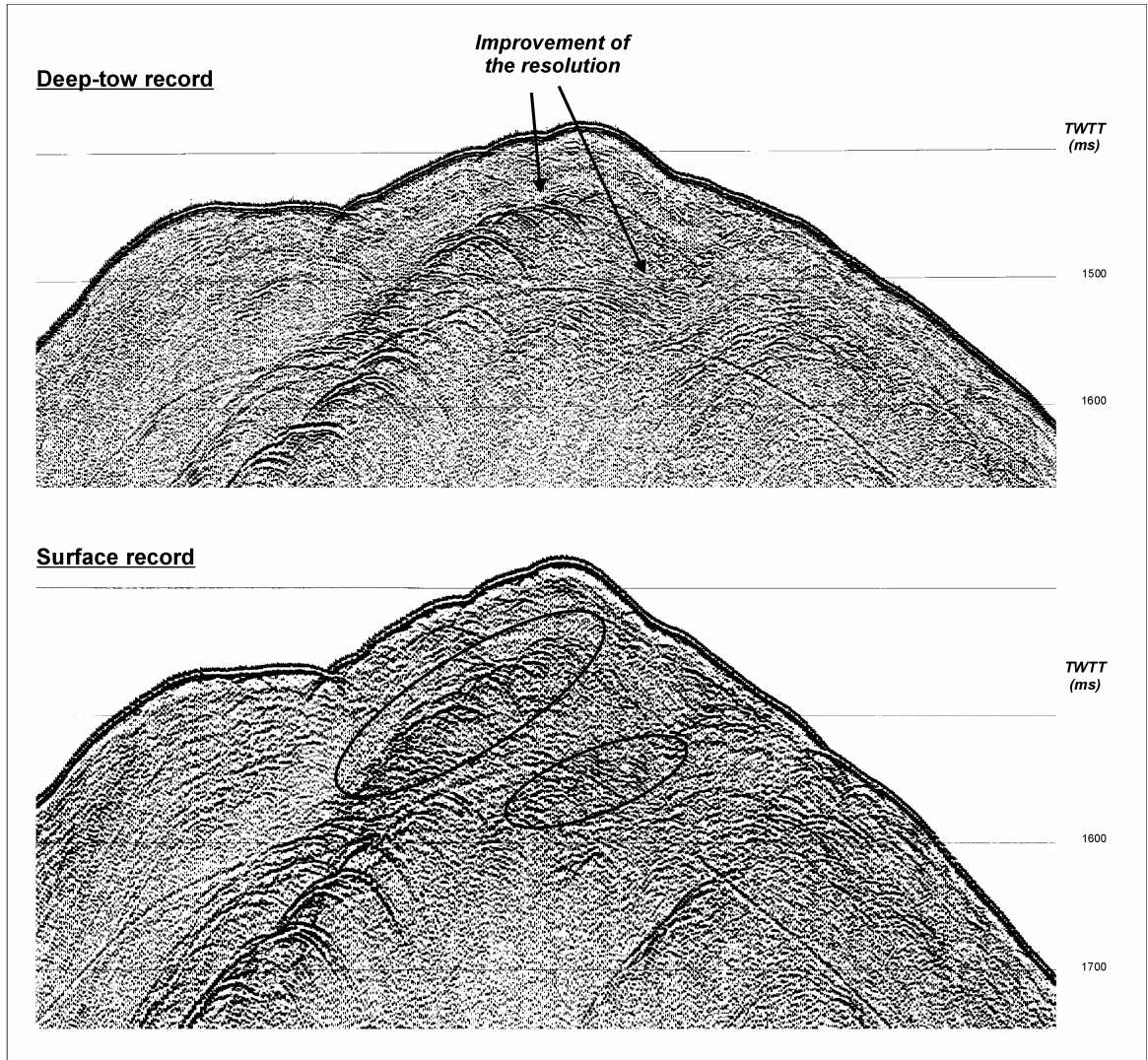
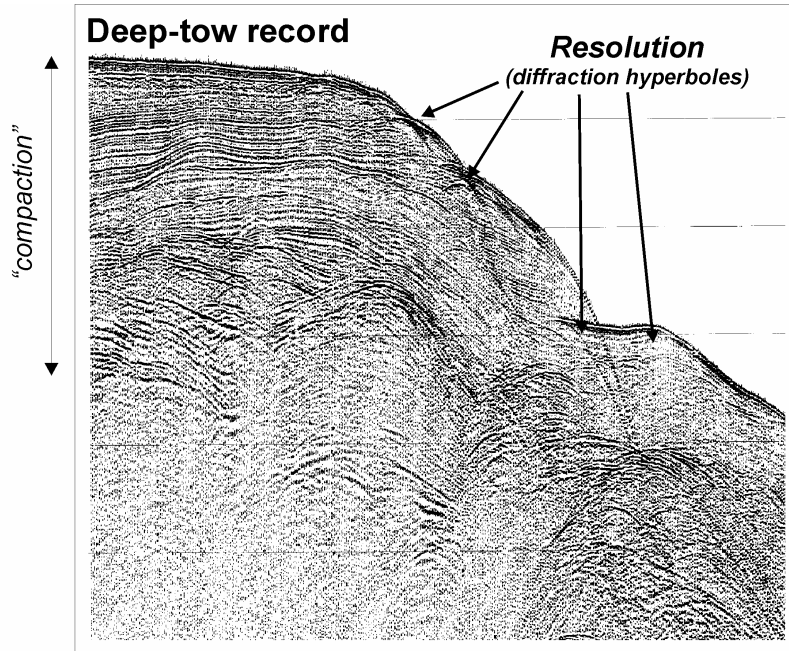
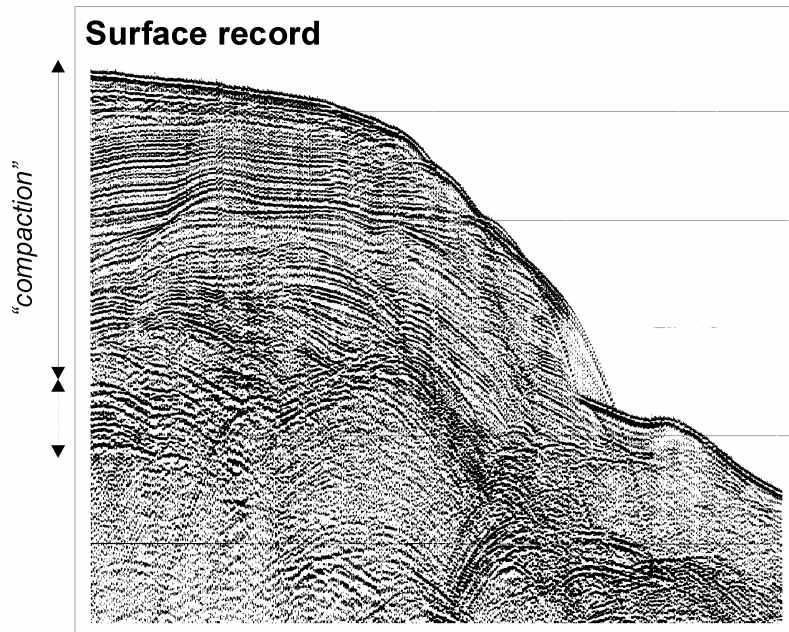


Figure 38: Zooms of Fig. 36 to show the better resolution when the data are recorded by the deep-tow streamer. (A) deep-tow streamer record (B) surface streamer record.



(A)



(B)

Figure 39: Zooms of Fig. 36 to show the better resolution and the “compaction” when the data are recorded by the deep-tow streamer. (A) deep-tow streamer record (B) surface streamer record.

4. RECENT DEVELOPMENTS

Further post-project initiatives are presently undertaken to modify and improve the deep-tow acquisition system, in order to optimise the signal/noise ratio and the sensitivity and amplification control of the analogue signals in the hydrophones. Major developments in 2001 were the implementation of an advanced 24-channels, 24-bits acquisition unit (Geometrics Geode) with full optical telemetry immediately ahead of the multi-channel streamer and the implementation of a 24-channel seabed cable with 6 groups of 4C sensors and a dedicated small shooting vessel for AVO studies (amplitude versus offset). A new project has been submitted for implementing a full set of optical slip rings on the winch, as well as a high accuracy positioning system with transducer on the deep-tow (cooperation NIOZ, AWI, Bremen University within NEBROC II project). Initial data recorded in Porcupine with the deep-tow streamer on prospective ODP sites have been labeled as “impressive” by the ESSEP panel and SCICOM of ODP.

OVERALL CONCLUSIONS

Analysis of the depositional and erosional processes controlling Antarctic shelf-to-slope sediment transport.

- We investigated a large sub-marine slide – the Gebra Slide – on the continental margin of Trinity Peninsula, Central Bransfield Basin, Antarctic Peninsula. The slide scar is clearly expressed in the multi-beam bathymetry. The total area affected by the slide is about 230 km². The associated deposit is a debris-flow deposit that extends over a total surface of about 280 km². The total volume of sediment involved in the mass movement is about 20 km³. The Gebra slide took place in two distinct phases. Indirect dating of the mass-wasting event, using seismic-stratigraphic criteria, suggests that it took place at the transition between the last glacial period that affected the area and the present-day interglacial (between 13500 and 6500 yrs. B.P.). Large slope failures like this may be an important factor controlling slope-to-basin sediment transport in periods other than glacial maxima.
- Integration of multi-beam bathymetry data and high-resolution seismic reflection profiles on the scale of the whole Trinity Peninsula margin has also allowed us to portray with unprecedented detail the sub-glacial sedimentary system of the Last Glacial Maximum in this part of the Antarctic Peninsula. The studied sedimentary

system extends 250 km, from about 1000 m above sea level to about 2000 m water depth. The data set supports a model for sub-glacial sedimentary systems during glacial periods that consists of (1) an upper ice-catchment or erosional zone on the innermost continental shelf, extending onshore; (2) a transitional erosional-depositional zone on the inner shelf with drumlins on the sea floor; (3) a depositional outer-shelf zone with mega-scale glacial lineations or "bundle structures"; and (4) a debris apron on the continental slope and base of slope formed under floating ice shelves but with debris delivery linked to grounding lines along the shelf break. This new model differs from previous ones in that (1) it is strongly supported by multi-beam mapping evidence of the modern sea floor, (2) it involves a "source to sink" approach illustrative of the continuum of processes along glacial systems, and (3) it includes and comprehensively integrates novel concepts (e.g., the streamlined outer-shelf depositional segment). The results presented outline the dramatic shift of ice cover and depositional conditions off the northern Antarctic Peninsula since the LGM.

Development of a new deep-tow reflection seismic acquisition system.

- We also developed a new multi-functional deep-tow reflection seismic acquisition system for collecting good-quality high-resolution seismic data in Antarctic waters. The system is characterised by a modular design, including a surface seismic source, an umbilical cable, a winch with slip-ring units, a MC or SC streamer sub-or deep-tow streamer, a streamer-depth monitor and a deep-water digital acquisition system. The system can be operated in various different configurations: e.g. the sub-tow profiling mode, the full deep-tow profiling mode, the "Jumbo" profiling mode using two receivers, and the "touch-and-go mode including stationary measurements on the sea floor. The system has been successfully deployed in the Antarctic and in the northeastern Pacific. The system remains under continuous development and new applications are currently being implemented and tested.

ACKNOWLEDGEMENTS

This research was carried out with the support of the Federal Office for Scientific, Technical and Cultural Affairs (OSTC), within the framework of the Belgian Antarctic Research Programme, Phase 4, Project A4/DD/G01. Part of the technical development work on the deep-tow seismic system has received additional financial support from the Special

Research Fund of the University of Gent, and of the EC Marine Science and Technology Programme through the MAST3-Project ENAM-2.

We thank the Marine Geophysics Group of the Alfred-Wegener-Institut für Polar- und Meeresforschung (Bremerhaven, GER), the Marine Geology Research Group of the University of Barcelona (ESP) and the CSIC Institute of Marine Sciences (Barcelona, ESP) for the very pleasant and stimulating cooperation and for the hospitality and facilities offered to several members of our research team during the marine-geophysical expeditions in Antarctica on board of F.S. POLARSTERN and B.I.O. HESPERIDES. We also thank GEOMAR for the invitation to participate with our newly developed deep-tow seismic system to a marine-geophysical expedition in the NE Pacific Ocean on board of F.S. SONNE. Our appreciation also goes to the captains and crews of all the research vessels (B.I.O. HESPERIDES, F.S. POLARSTERN, F.S. SONNE, R.V. BELGICA) on which we worked in the past years.

We wish to dedicate this report to the memory of Dr. J. Baraza (CSIC Institute of Marine Sciences, Barcelona), a friend and colleague who left us too soon and too fast...

REFERENCES

- AKSU, A.E. & HISCOTT, R.N., 1992. Shingled Quaternary debris flow lenses on the north-east Newfoundland Slope. *Sedimentology*, **39**, 193-206.
- ALLEY, R.B., BLANKENSHIP, D.D., ROONEY, S.T. & BENTLEY, C.R., 1989. Sedimentation beneath Ice Shelves – The View from Ice Stream B. *Marine Geology*, **85**, 101-120.
- ANDERSON, J.B. & MOLNIA, B.F., 1989. Glacial-marine sedimentation. *AAPG Short Course in Geology*, **9**, 127 pp.
- BANFIELD, L.A. & ANDERSON, J.B., 1995. Seismic facies investigation of the Late Quaternary glacial history of Bransfield Basin, Antarctica. In: Cooper, A.K., Barker, P.F. & Brancolini, G. (eds.) Geology and seismic stratigraphy of the Antarctic Margin. *AGU Antarctic Research Series*, **68**, 123-140.
- BARCENA, M.A., GERSONDE, R., LEDESMA, S., FABRES, J., CALAFAT, A.M., CANALS, M., SIERRO, F.J. & FLORES, J.A., 1998. Record of Holocene glacial oscillations in Bransfield Basin as revealed by siliceous microfossil assemblages. *Antarctic Science*, **10(3)**, 269-285.
- BARKER, D.H.N. & AUSTIN, J.A.A., 1998. Rift propagation, detached faulting, and associated magmatism in Bransfield Strait, Antarctic Peninsula. *Journal of Geophysical Research*, **103(B10)**, 24017-24043.
- BART, P.J., DE BATIST, M. & JOKAT, W., 1999. Interglacial collapse of Crary Trough Mouth Fan, Weddell Sea, Antarctica: implications for Antarctic glacial history analysis. *Journal of Sedimentary Research*, **69(6)**, 1276-1289.

- BAS (BRITISH ANTARCTIC SURVEY), 1985. Tectonic map of the Scotia Arc. 1:3,000,000. British Antarctic Survey.
- BENN, D.I. & EVANS, D.J.A., 1998. *Glaciers and glaciation*. London, Arnold Publishers, 734 pp.
- BENTLEY, M.J. & ANDERSON, J.B., 1998. Glacial and marine geological evidence for the ice sheet configuration in the Weddell Sea–Antarctic Peninsula region during the last glacial maximum. *Antarctic Science*, **10**, 309–325.
- BUGGE, T., BEFRING, S., BELDERSON, R.H., EIDVIN, T., JANSEN, E., KENYON, N.H., HOLTEDAHL, H. & SEJRUP, H.P., 1987. A giant three-stage submarine slide off Norway, *Geo-Marine Letters*, **7**, 191-198.
- CANALS, M., ACOSTA, J., BARAZA, J., BART, P., CALAFAT, A.M., CASAMOR, J.L., DE BATIST, M., ERCILLA, G., FARRAN, M., FRANES, G., GRACIA, E., RAMOS-GUERRERO, E., SANZ, J.L., SORRIBAS, J.L. & TASSONE, A. 1994. La Cuenca Central de Bransfield (NW de la Península Anártica): primeros resultados de la campana GEBRA-93. *Geogaceta*, **16**, 132-135.
- CANALS, M., DOMACK, E.W., CASAMOR, J.L., BARAZA, J., FARRAN, M., DEBATIST, M., URGELES, R. & CALAFAT, A.M., (in press). A subglacial sedimentary system off the Antarctic Peninsula: seafloor and sub-seafloor evidence. *Geology*.
- DIMAKIS, P., ELVERHOI, A., HOEG, K., SOLHEIM, A., HARBITZ, C., LABERG, J.S., VORREN, T.O. & MARR, J., 2000. Submarine slope stability on high-latitude glaciated Svalbard-Barents Sea Margin. *Marine Geology*, **162**, 303-316.
- DOWDESWELL, J.A., ELVERHOI, A., & SPIELHAGEN, R., 1998. Glacimarine sedimentary processes and facies on the Polar North Atlantic Margins. *Quaternary Science Reviews*, **17**, 243-272.
- DOWDESWELL, J.A. & SIEGERT, M.J., 1999. Ice-sheet numerical modeling and marine geophysical measurement of glacier-derived sedimentation on the Eurasian Arctic continental margins. *Geological Society of America Bulletin*, **111(7)**, 1080-1097.
- DOWDESWELL, J.A., KENYON, N.H., ELVERHOI, A., LABERG, J.S., HOLLENDER, F.J., MIENERT, J. & SIEGERT, M.J., 1996. Large-scale sedimentation on the glacier-influenced Polar North Atlantic margins: Long-range side-scan sonar evidence. *Geophysical Research Letters*, **23(24)**, 3535-3538.
- ELVERHOI, A., NOREM, H., ANDERSON, E.S., DOWDESWELL, J.A., FOSSEN, I., HAFLIDASON, H., KENYON, N.H., LABERG, J.S., KING, E.L., SEJRUP, H.P., SOLHEIM, A. & VORREN, T., 1997. On the origin and flow behavior of submarine slides on deep-sea fans along the Norwegian-Barents Sea continental margin. *Geo-Marine letters*, **17**, 119-125.
- ERCILLA, G., BARAZA, J., ALONSO, B. & CANALS, M., 1998. Recent geological processes in the Central Bransfield Basin (Western Antarctic Peninsula). In: STOKER, M.S., EVANS, D. & CRAMPS, A. (eds.) Geological Processes on Continental Margins: Sedimentation, Mass-Wasting and Stability. *Geological Society Special Publication*, **129**, 205-216.
- GAMBÔA, L.A.P. & MALDONADO, P.R., 1990. Geophysical Investigations in the Bransfield Strait and in the Bellingshausen Sea – Antarctica. In: ST.JOHN, B. (ed.) Antarctica as an exploration frontier - hydrocarbon potential, geology, and hazards. *AAPG Studies in Geology*, **31**, 13-29.

- GARDNER, J.V., PRIOR, D.B. & FIELD, M.E., 1999. Humboldt Slide – a large shear-dominated retrogressive slope failure. *Marine Geology*, **154**, 323-338.
- GEE, M.J.R., WATTS, A.B., MASSON, D.G. & MITCHELL, N.C., 2001. Landslides and the evolution of El Hierro in the Canary Islands. *Marine Geology*, **177**, 271-293.
- GELFORT, R., 1998. *Adapted processing of seismic reflection data recorded with a marine deep-tow system*. M.Sc thesis, UCNW-RUG. CEC Erasmus Project "Mercator" in marine geosciences, 124 pp.
- GRACIA, E., CANALS, M., FARRAN, M., PRIETO, M.J., SORRIBAS, J. & GEBRA TEAM, 1996. Morphostructure and evolution of the Central and Eastern Bransfield Basins (NW Antarctic Peninsula). *Marine Geophysical Researches*, **18(2-4)**, 429-448.
- GRACIA, E., CANALS, M., FARRAN, M.L., SORRIBAS, J. & PALLAS, R., 1997. Central and eastern Bransfield basins (Antarctica) from high-resolution swath-bathymetry data. *Antarctic Science*, **9(2)**, 168-180.
- HARDEN, S.L., DEMASTER, D.J. & NITTRouer, C.A., 1992. Developing sediment geochronologies for high-latitude continental shelf deposits: a radiochemical approach. *Marine Geology*, **103**, 69-97.
- HENRIET, J.P., MEISSNER, R., MILLER, H. & the GRAPE TEAM, 1992. Active margin processes along the Antarctic Peninsula. *Tectonophysics*, **201**, 229-253.
- HERRON, M.J. & ANDERSON, J.B., 1990. Late Quaternary glacial history of the South Orkney Plateau, Antarctica. *Quaternary Research*, **33**, 265-275.
- HJORT, C., INGOLFSSON, O., MOLLER, P. & LIRIO, J.M., 1997. Holocene glacial history and sea level changes on James Ross Island, Antarctic Peninsula. *Journal of Quaternary Science*, **12**, 259-273.
- IMBO, Y., DEBATIST, M., CANALS, M., PRIETO, M.J. & BARAZA, J. (submitted). The Gebra Slide: Proof of Late -Glacial mass-wasting processes on the Trinity Peninsula Margin, Antarctic Peninsula. *Marine Geology*.
- JEFFERS, J.D. & ANDERSON, J.B., 1991. Sequence stratigraphy of the Bransfield Basin, Antarctica: Implications for tectonic history and hydrocarbon potential. In: ST.JOHN, B. (ed.) Antarctica as an exploration frontier - hydrocarbon potential, geology, and hazards. *AAPG Studies in Geology*, **31**, 13-30.
- JIN, Y.K., LEE, D.K., NAM, S.H., KIM, Y. & KIM, K.J., 1998. Seismic observation at King Sejong Station, Antarctic Peninsula. *Terra Antarctica*, **5(4)**, 729-736.
- LABERG, J.S., VORREN, T.O., DOWDESWELL, J.A., KENYON, N.H. & TAYLOR, J., 2000. The Andøya Slide and the Andøya Canyon, north-eastern Norwegian-Greenland Sea. *Marine Geology*, **162(2-4)**, 259-275.
- LABERG, J.S. & VORREN, T.O., 1995. Late Weichselian submarine debris flow deposits on the Bear Island Trough Mouth Fan. *Marine Geology*, **127**, 45-72.
- LODOLO, E., CAMERLENGHI, A. & BRANCOLINI, G., 1993. A bottom simulating reflector in the South Shetland Margin, Antarctic peninsula. *Antarctic Science*, **5(2)**, 207-210.
- MASSON, D.G., CANALS, M., ALONSO, B., URGELES, R. & HUHNERBACH, V., 1998. The Canary Debris Flow: source area morphology and failure mechanisms. *Sedimentology*, **45**, 411-432.
- MENZIES, J. & SHILTS, W.W., 1996. Subglacial environments. In: MENZIES, J. (ed.) Past glacial

- environments: Sediments, forms and techniques. Oxford, Butterworth-Heinemann, pp. 15–136.
- MONTE, M., 1998. *Seismisch onderzoek op de zeebodem : analyse van bron- en detectorkarakteristieken*. M.Sc. thesis, RUG. 138 pp.
- MOSHER, D.C., MORAN, K. & HISCOTT, R.N., 1994. Late Quaternary sediment, sediment mass flow processes and slope stability on the Scotian Slope, Canada. *Sedimentology*, **41**, 1039-1061.
- MULDER, T. & COCHONAT, P., 1996. Classification of offshore mass movements, *Journal of Sedimentary Research*, **66(1)**, 43-57.
- MULDER, T. & MORAN, K., 1995. Relationship among submarine instabilities, sea level variations, and the presence of an ice sheet on the continental shelf: An example from the Verrill Canyon Area, Scotian Shelf. *Paleoceanography*, **10(1)**, 137-154.
- MYHRE, A. & ELDHOLM, O., 1988. The western Svalbard margin (74°–80°N). *Marine and Petroleum Geology*, **5**, 134–156.
- PRIETO, M.J., CANALS, M., ERCILLA, G. & DE BATIST, M., 1998. Structure and geodynamic evolution of Central Bransfield Basin (NW Antarctica) from seismic reflection data. *Marine Geology*, **149(1-4)**, 17-38.
- PRIETO, M.J., ERCILLA, G., CANALS, M. & DE BATIST, M., 1999. Seismic stratigraphy of the Central Bransfield Basin (NW Antarctic Peninsula). Interpretation of deposits and sedimentary processes in a glacio-marine environment. *Marine Geology*, **157(1-2)**, 47-68.
- PRIOR, D.B. & COLEMAN, J.M., 1984. Submarine slope instability. In: BRUNSDEN, D. & PRIOR, D.B. (eds.) *Slope instability*. Chichester, John Wiley and Sons, pp. 419–455.
- PUDSEY, C.J., BARKER, P.F. & LARTER, R.D., 1994. Ice sheet retreat from the Antarctic Peninsula Shelf. *Continental Shelf Research*, **14(15)**, 1647-1675.
- REARIC, D.M., BARNES, P.W. & REIMNITZ, E., 1990. Bulldozing and resuspension of shallow-shelf sediment by ice keels: Implications for Arctic sediment transport trajectories. *Marine Geology*, **91**, 133–147.
- STUMPFE, M., 1998. Processing of seismic data: Central Bransfield Basin, West Antarctica. Study report. CEC Erasmus Project "Mercator" in marine geosciences. 30 pp.
- SZELIGA, J., 1990. Bathymetric map of Bransfield Strait 1:700,000, Institute of Ecology, Polish Academia of Sciences, Warsaw.
- VAN DER MEER, J.J.M., 1983. A recent drumlin with fluted surface in the Swiss Alps. In: EVENSON, E.B., et al. (eds.) *Tills and related deposits: Genesis, petrology, stratigraphy*: Rotterdam, A.A. Balkema, pp. 105–110.
- VORREN, T.O., RICHARDSEN, G., KNUITSEN, S.M. & HENRIKSEN, E., 1991. Cenozoic erosion and sedimentation in the western Barents Sea. *Marine and Petroleum Geology*, **8**, 317–340.
- VORREN, T.O., LABERG, J.S., BLAUME, F., DOWDESWELL, J.A., KENYON, N.H., MIENERT, J., RUMOHR, J. & WERNER, F., 1998. The Norwegian-Greenland Sea continental margins: Morphology and Late Quaternary sedimentary processes and environment. *Quaternary Science Review*, **17**, 273-302.
- YOON, H.I., HAN, M.W., PARK, B.K., OH, J.K. & CHANG, S.K., 1994. Depositional environment of near-surface sediments, King George Basin, Bransfield Strait, Antarctica. *Geo-Marine*

Letters, 14, 1-9.